Modelling of Explosion Deflagrating Flames Using Large Eddy Simulation

By

Yinqing Wang

A Doctoral Thesis

Submitted in partial fulfillment of the requirements for the award of Doctor of Philosophy of Loughborough University

Loughborough University

March 2013

School of Aeronautical, Automotive, Chemical and Materials Engineering

Loughborough University

Abstract

Encouraged by the recent demand for eco-friendly combustion systems, advancements in the predictive capability of turbulent premixed combustion are considered to be essential. The explosion and deflagrating flame are modelled with the numerical method by applying the Large Eddy Simulation (LES) technique. It has evolved itself as a powerful tool for the prediction of turbulent premixed flames. In the LES, Sub-Grid Scale (SGS) modelling plays a pivotal role in accounting for various SGS effects. The chemical reaction rate in LES turbulent premixed flames is a SGS phenomenon and must be accounted for accurately. The Dynamical Flame Surface Density (DFSD) model which is based on the classical laminar flamelet theory is a prominent and well accepted choice in predicting turbulent premixed flames in RANS modelling.

The work presented in this thesis is mainly focused upon the implementation of a dynamic flame surface density (DFSD) model for the calculation of transient, turbulent premixed propagating flames using the LES technique. The concept of the dynamism is achieved by the application of a test filter in combination with Germano identity, which provides unresolved SGS flame surface density information. The DFSD model is coupled with the fractal theory in order to evaluate the instantaneous fractal dimension of the propagating turbulent flame front.

LES simulations are carried out to simulate stoichiometric propane/air flame propagating past solid obstacles in order to validate the model developed in this work with the experiments conducted by the combustion group at The University of Sydney. Various numerical tests were carried out to establish the confidence of LES. A detailed analysis has been carried out to determine the regimes of combustion at different stages of flame propagation inside the chamber. LES predictions using the DFSD model are evaluated and validated against experimental measurements for various flow configurations. The LES predictions were identified to be in strong agreement with experimental measurements. The impact of the number and position of the baffles with respect to ignition origin has also been studied. LES results were found to be in very good agreement with experimental measurements in all these cases.

Acknowledgements

Firstly, I wish to express my deep sense of gratitude to Dr. Salah S Ibrahim for giving me this great opportunity. I am very grateful to my supervisors, Dr. Salah S Ibrahim and Professor W. Malalasekera for their invaluable guidance throughout the course of my research work. Their keen interest and personal involvement at all stages of this work is beyond words of gratitude. Their invaluable advice and exceptionally thought-provoking discussions have improved my knowledge and helped this thesis to be in good shape.

Secondly, I am very thankful to Dr. M. Kirkpatrick for providing the basic LES code, PUFFIN. I am very grateful to Professor A.R. Masri and Mr. Ahmed Al-Aerbi for providing the experimental data used for model validation and for their invaluable advice about the progress of my work. I am thankful to Mr. Mohamed Abdel-Raheem for sharing his invaluable modelling and experimental experiences with me.

Finally, I owe thanks to my parents for the financial support they provided so I could carry out this research work. I would like to thank my wife Lingna for her hard work, continuous support and moral encouragement - without which, this work would have been impossible. I would like to thank my teachers, project supervisors and colleagues for motivating me through their aspiring discussions and great teachings, all of which have helped me to choose the correct path in my life. Last but not least, I would like to thank my family for their support in helping me to achieve this great success in my life.

Publications

1. **Wang, Y**., Ibrahim, S.S. and Malalasekera, W., (2012). On the modelling of Explosion *deflagrating flames. International symposium on safety science and technology , Nanjing, China, 45* (2012), 390-398.

Contents

Nomenclature

Latin Letters

A	Area
A_T	Turbulent flame surface area pre unit volume
A_L	Laminar flame surface area per unit volume
$\bar{A}$	Projected area of flame on its average surface per unit volume
B_i	Body forces
C_{ij}	Cross stress
C_P	Specific heat at constant pressure
C	Dimensionless coefficient in Smagorinsky model
C_{EBU}	EBU Model constant
C_I	Model coefficient in Smagorinsky mode
C_s	Smagorinsky coefficient
C_S	Model constant used in DFSD equation
c	Reaction progress variable
c_{red}	Reduced progress variable
D	Mass Diffusivity/ Fractal dimension
Da	Damköhler number
D_L	Laminar fractal dimension
D_T	Turbulent fractal dimension
E	Efficiency function
e	Specific internal energy
F	Flame thickening factor
f	Force per unit mass
G	Convolution function or G field
h	Enthalpy

I_0	Mean stretch factor	X
Ka	Karlovitz number	
k	Thermal conductivity	
L_{ij}	Leonard stress	
L_y	Length scale of wrinkle flame front	
l	Length scale	
l_t	Integral length scale	
M	Molar mass	
$\dot{m}$	Mass flow rate	
n	Constant	
Pr	Prandtl number	
Pr_t	Turbulent Prandtl number	
P_{sg}	Probability in PDF equation	
p	Pressure	
Q	Heat generation	
q_c	Chemical source term	
R	Mean reaction rate per unit surface area	
Re	Reynolds number	
R_{ij}	Sub-grid scale Reynolds stress	
R_G	Gas constant	
R_u	Universal gas constant	
S	Stress tensor	
Sc	Schmidt number	
Sc_t	Turbulent Schmidt number	
S_φ	Generic source term	
S_{ij}	Strain rate	
T	Temperature	
T_{ij}	Sub-test-scale stress tensor	
t	Time	

u	Velocity in x-direction
u'	RMS fluctuations
u'_Δ	SGS velocity fluctuation
u_k	Flame advancement by curvature effects
u_L^0	Un-strained laminar burning velocity
u_L	Laminar burning velocity
u_T	Turbulent burning velocity
$\tilde{u}$	Tangential velocity
V	Volume
v	Velocity in y-direction
w	Velocity in z-direction
W	Functional dependence
Y_{fu}	Fuel mass fraction
Y_{fu}^0	Fuel mass fraction in un-burnt mixture

Greek Symbols

α	Model constant in TFS equation
α_1	Model constant in equation 5.11
α_2	Model coefficient in equation 5.14
α_3	Model constant in equation 5.40
α_T	Thermal diffusivity
α_{ij}	Traceless tensor
β	Model coefficient simple FSD equation
β_1	Model constant in equation 5.11
β_3	Model constant in equation 5.40
β_{ij}	Traceless tensor
λ	Unresolved flame surface density
μ	Dynamic viscosity

μ'	Bulk viscosity
$\bar{\mu}_{SGS}$	SGS turbulent eddy viscosity
$\dot{\omega}_c$	Chemical reaction rate
ε	Turbulent kinetic energy
ρ	Fluid density
ρ_u	Unburned gas density
σ	Surface force
δ_{ij}	Kronecker delta
δ_L	Flame thickness
δ_c	Lower cut-off scale
δ_r	Reaction zone thickness
ϕ	Any fluid property
$\boldsymbol{\phi}$	Equivalence ratio
τ	Stress tensor
τ_{ij}^{sgs}	Residual stress
τ_t	Turbulent time scale
τ_c	Chemical time scale
τ_k	Kolmogorov time scale
τ_w	Wall shear stress
$\bar{\Delta}$	Filter width
Σ	Flame surface density
η_k	Kolmogorov scale
γ	Ratio of test filter to grid filter
Λ	Unresolved flame surface density at test filter
Ξ	Flame wrinkling factor
Γ_k	Efficiency function in ITNFS equation

Subscripts/Superscripts

fu	fuel
k	Kolmogorov
l	Laminar
o	unburned
s	Smagorinsky
sgs	Sub-grid scale
t	Turbulence

Operations

$\sim$	Favre average
$\,\widehat{}\,$	Test filter
$-$	Spatial filter
$\prime$	Fluctuations

Abbreviations

AFSD	Algebraic Flame Surface Density
ADI	Alternating-Direction-Implicit
ANN	Artificial Neural Network
BiCGStab	Bi-Conjugate Gradient Stabilized
CFD	Computational Fluid Dynamics
DFSD	Dynamic Flame Surface Density
DFM	Dynamic Fractal Model
DNS	Direct Numerical Simulation
EBU	Eddy-Break-Up

EFM   Empirical Fractal Model

FSD   Flame Surface Density

FPI   Flame Propagation of Intrinsic Low-Dimensional Manifold

GHG   Green House Gases

ISAT   In Situ Adaptive Tabulation

ITNFS   Intermittent Turbulence Net Flame Stretch

LIF   Laser Induced Florescence

LDV   Laser Doppler Velocimeter

LDA   Laser Doppler Anemometry

LEM   Linear Eddy Mixing

LES   Large Eddy Simulation

MSI   Modified Strongly Implicit

NGT   Non-Gradient Transport

Nd:YAG   Neodymium-doped Yttrium Aluminum Garnet

PDF   Probability Density Function

PIV   Particle Image Velocimetry

PLIF   Planar Laser-Induced Fluorescence

PRISM   Piecewise Reusable Implementation of Solution Mapping

PUFFIN   Particles IN Unsteady Fluid Flow

QSSA   Quasi-Steady State Assumption

RANS   Reynolds Averaged Navier-Stokes

RCCE   Rate-Controlled Constrained Equilibrium

RMS   Root Mean Square

SIMPLE   Semi-Implicit Method for Pressure Linked Equations

SGS   Sub-Grid Scale

SSM   Scale Similarity Models

TFS   Turbulent Flame Speed

ZNG   Zero Normal Gradient

List of Figures

List of Tables

Chapter 1 Introduction

1.1 Background

Following the Piper Alpha disaster and the subsequent Cullen enquiry, offshore operators now have to define the risks associated with their operations and convince the Health and Safety Executives (HSE) that these risks are As Low As Reasonably Practicable (ALARP). This approach embodies a vast array of design methodologies for structures, process engineering, construction, human factors and safety. Many of these procedures are well documented in standards which have been tested over time. However, when considering safety issues, it is necessary to ascribe probabilities to failures and events which may lead to a loss of flammable material and subsequently may lead to a fire or an explosion. The probability of an explosion has major implications on the safety of personnel on a platform both in terms of potential loss of life and the possibility of escalation of the process which could lead to a domino effect and more serious consequences. An understanding of the possible severity of an explosion is therefore a critical factor in establishing the satisfactory demonstration of ALARP. The mechanisms which enhance explosion overpressures, therefore, need to be established with some certainty in order to ensure that all aspects of safe design (structures and processes) and the safe protection of personnel are taken into account. Builders and operators of process plant require design criteria to ensure that the risk associated with an explosion from an accidental release of flammable material satisfies ALARP.

In recent years considerable effort has been devoted to the development of reliable means of assessing the vulnerability of industrial plant to fire and explosion. Examples include the Commission of European Communities (CEC) co-sponsored project MERGE - Modelling and Experimental Research into Gas Explosions (Popat et al 1996) and the Steel Construction Institute's Joint Industry Project (JIP) on blast and fire engineering. Current explosion models are either empirical or based on phenomenological CFD models and are very often tuned to particular experiments which thereby limit their range of applicability. Moreover, the effect of obstacles in the generation of turbulence and its effect on the rate of chemical reaction is inadequately treated. Since explosions are characterised by the

interaction between a compressible fluid flow and rapid chemical reactions, any realistic predictive computer model must be able to deal with both of these aspects of the problem.

In the event of an explosion, the damage caused by the initial overpressure resulting from the acceleration of the deflagrating flame front as it interacts with the surrounding media can cause considerable loss of lives and damage to property. Gaseous explosions are a class of combustion considered to be one of the most important methods of energy generation. A deep understanding of the basic phenomena and mechanisms of combustion is essential to improve the performance, reliability, safety and environmental impact of combustion systems. On the other hand, protecting the global environment and preventing ozonosphere damage are deemed the most important protection issues. Combustion processes involving chemical reactions can result in the output of poisonous gases such as Carbon monoxide (CO), Nitrogen Oxides (NO_x) and Hydrocarbons (HC). Optimising combustion systems represent significant opportunities for energy saving and they can be influenced strongly even by small improvements, such as through improved combustion systems and by understanding the physics of combustion. Much success has been achieved in the understanding of the physics of combustion following decades of continuous research, with many problems now being solved such as combustion instabilities, extinction, re-ignition and flame flow interaction etc. Combustion is a complex thermo chemical process where it is required to understand the unsteadiness and turbulence that combine to form a multifaceted problem.

Modern industries such as aerospace, automotive, ship and military still apply combustion in their field. Combustion is classified as either premixed and non-premixed with a modality of laminar or turbulent. Many of the practical combustion systems, such as spark ignition engines as shown in Figure 1.1 (Maly, 1994) and gas turbines as shown in Figure 1.2 (Encyclopaedia Britannica, Inc.), are very rapid with a high turbulence level and fast chemical reactions. Furthermore, most of the aforementioned engineering applications operate in either fully or partially premixed conditions prior to reaction.

Designing the optimisation of combustion systems demands rigorous experimental investigations, and requires expensive experimental setups, since combustor designs are

very complex. For instance, a typical gas turbine combustion structure layout, as shown in Figure 1.3 (Wikipedia), is not realistic for detailed experimental investigation due to its harsh internal flow and combustion characteristics.
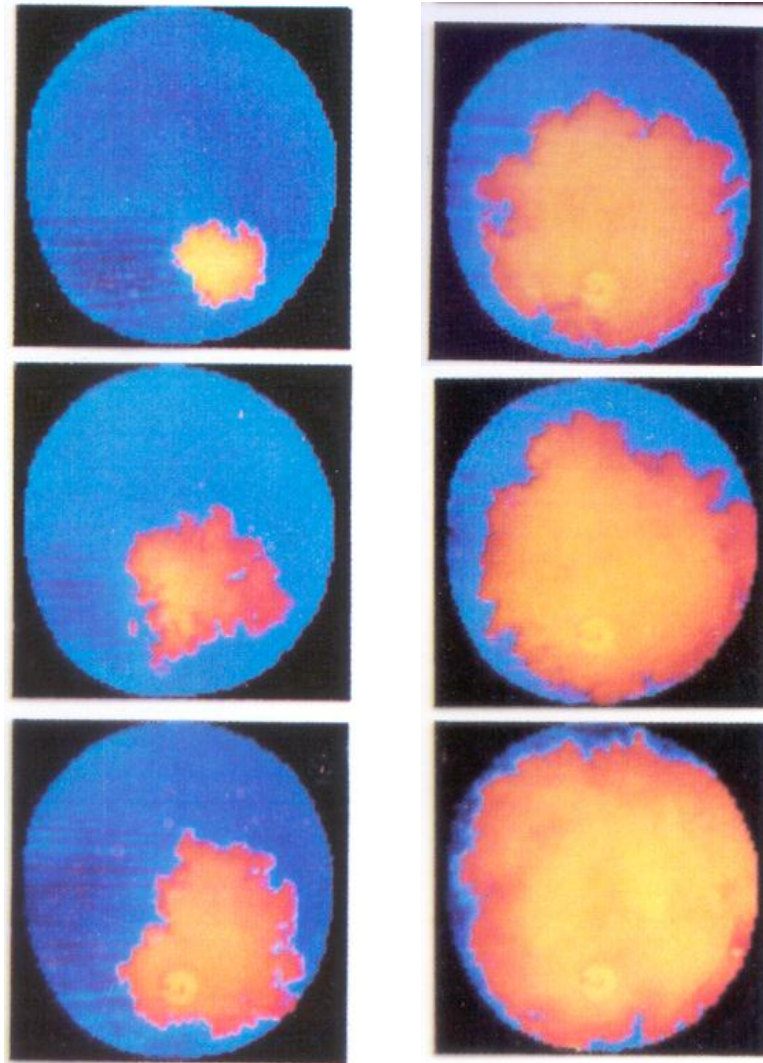
Figure 1.1 Experimental images of explosion with premixed deflagrating flames sequence propagation in a spark ignition engine (Maly, 1994).
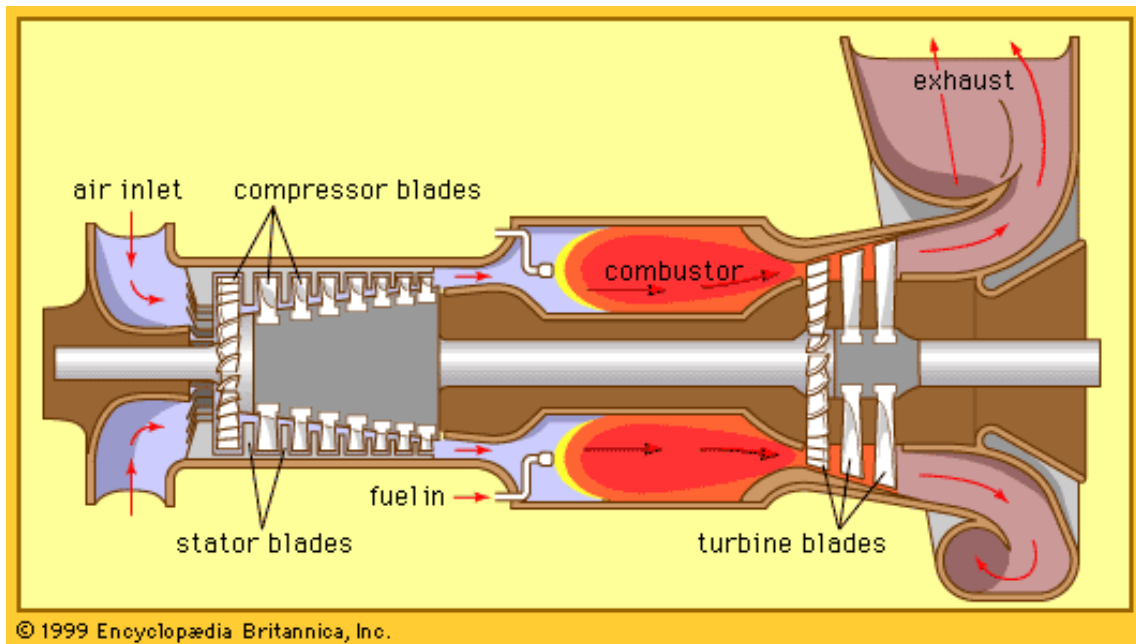
Figure 1.2 Combustion in a gas turbine engine from Encyclopaedia Britannica, Inc. (www.britannica.com/EBchecked/media/19424/Open-cycle-constant-pressure-gas-turbine-engine)
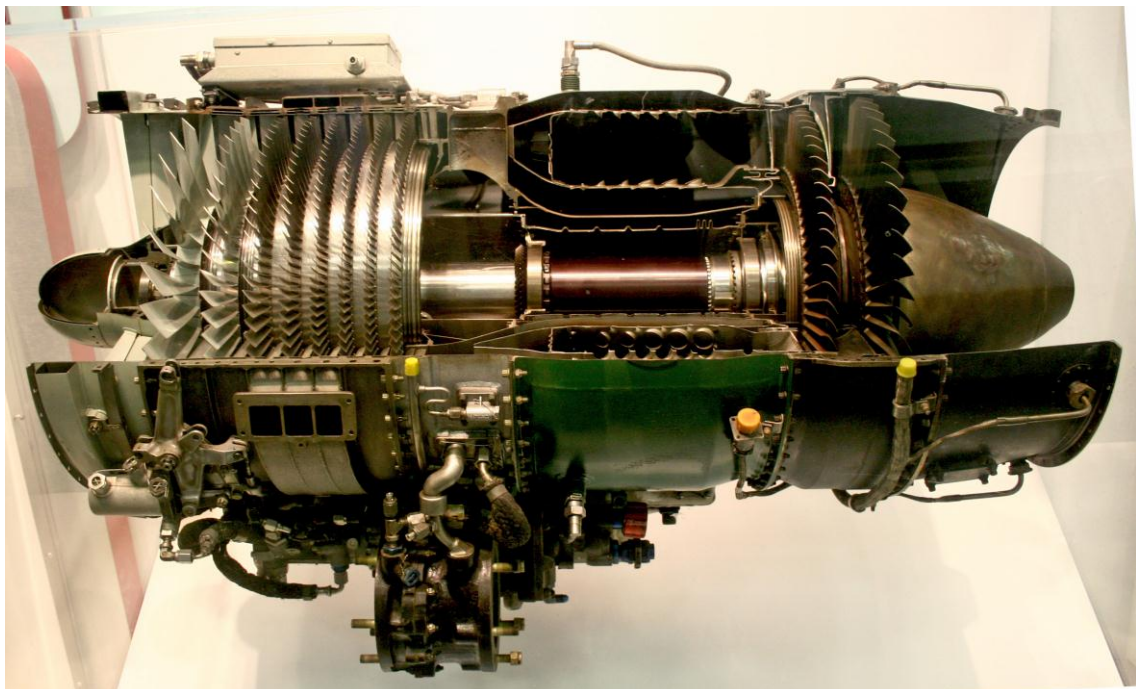
Figure 1.3 A typical axial- flow gas turbine turbojet the J85 Sectioned for display. (http://en.wikipedia.org/wiki/Gas_turbine)

A very famous example of an explosion accident happened on Sunday 11th December 2005 at the Buncefield oil depot, which is located near the M1 motorway on the edge of Hemel Hempstead, England (Figure 1.4). The gaseous explosion generated an overpressure due to rapid flame acceleration and its interactions with the local equipment, such as different shaped of obstacles, and the resulting damage caused was enormous and highly hazardous. The investigation and reconstruction of such large-scale explosion experiments in industrial scale vessels are very expensive, difficult and risk creating.

Figure 1.4 Accidental explosions at Buncefield oil depot, Hemel Hempstead (Courtesy of Royal Chiltern Air Support Unit,

http://www.buncefieldinvestigation.gov.uk/images/gallery/casu02big.jpg)

Consequently, computational or numerical modelling provides a potential alternative to difficult and expensive experimental investigations. As in the aforementioned applications, numerical modelling plays a control role in the safe design of on and off shore chemical/fuel processing storage plants. Computational Fluid Dynamics (CFD) is strongly recognised as part of the extensively Computer Aided Engineering (CAE) computing tools used in the industry. CFD predicts the fluid flow in complicated cases, in terms of mass transfer, flow of heat, phase change, chemical reaction, and mechanical movement etc.

Actual experiments are time consuming and very expensive in general and not practicable in explosion cases due to its complexity. For example, internal combustion is unfeasible for detailed experimental investigation because of the harsh conditions established internally. These internal conditions raise unanswered questions to the investigators, which are important to the understanding and improvement of the design of the system. Also CFD provides a deeper understanding of the processes involved in the instability mechanisms, enabling the design of passive or active control strategies.

Computational modelling tools have been proved to be excellent alternatives and the methods are adequately developed in the field of fluid dynamics, metrology and health engineering even for complex non-reacting flow problems. Nonetheless, when turbulence is involved in the reacting flow problems, the progress made is less satisfactory leaving many outstanding research issues. With the successful prediction of non-reacting flow applications, there are three computational modelling techniques available for current application: Direct Numerical Simulations (DNS), Reynolds Averaged Navier Stokes (RANS) equations and Large Eddy Simulations (LES).

Among the three numerical techniques, DNS is the most accurate method for all scales of the turbulent flow field that need to be resolved in the computation. The chemical and fluid dynamics of the reacting gas mixture can be described by conservation equations for mass, momentum, energy and chemical species with the thermodynamic equations. DNS includes solving the transport equation down to the smallest important physical scales. The smallest scales are highly computational, with molecular diffusion making the velocity and state variables smooth, such as the resolution on the computational mesh. However, despite significant improvement in computational resources, the application of DNS is limited to low Reynolds number flows due to the cost and computational resources involved. Hence, the application of DNS to real combustion systems, where the flows are complex and involve higher Reynolds numbers, is unpractical in the freeseeable future. The computational resources required by a DNS would exceed the capacity of the most powerful computers currently available. However, direct numerical simulation(DNS) is a useful tool in fundamental research into turbulence.

On the other hand, Large Eddy Simulation (LES) is now accepted as a feasible computational tool despite the added computational cost, as compared with the RANS technique. Several recent works by Charlette et al. (2002), Knikker et al. (2004), Fureby et.al. (2005), Masri et al. (2006) and Pitsch (2006) confirmed the high fidelity of LES in predicting the key characteristics of turbulent combustion. LES has a clear advantage over classical Reynolds averaged based methods in its capability of accounting for the time varying nature of the flow, and this is particularly important in transient processes such as swirling flow or transient propagating premixed flames. LES also allows for detailed description of turbulent chemistry interactions, which is a common failure in RANS. The ever increasing speed of computers is reducing the high computational requirement of LES and shifting the focus towards developing adequate sub grid scale models for combustion. The development of such SGS models is imperative in both premixed and non-premixed combustion and the focus of this present work is only on the premixed combustion.

1.2 Motivation

A major objectives of this study is to develop and validate a model for turbulent premixed combustion which is capable of predicting the correct flame acceleration rates and over-pressures in explosions. An explosion is characterised by the interaction between a compressible fluid flow and rapid exothermic chemical reactions and any realistic model must be able to deal with both aspects of the problem. Reliable prediction of the interaction between accelerating flames and solid obstacles of different geometries requires a realistic description of both the turbulent flow and chemical reactions that take place during the course of flame propagation.

The work carried out in this study establishs validated physical submodels for the interactions between propagating flames, flow turbulence and solid obstacles in a realistic explosion chamber. In addition, it will provide a thorough understanding of the mechanisms by which explosion over-pressures (magnitude and timing) are produced under various obstacle configurations. The developed submodels should provide safety engineers and scientists with an accurate predictive tool for the safe design of chemical processing plant.

1.3 Objectives of the present investigation

In this study, the LES modelling technique is used to develop a turbulent premixed combustion model for explosion applications. The flame surface density (FSD) model for combustion is developed, tested and incorporated in an in-house LES code within the Department of Aeronautical and Automotive Engineering. The code is capable of computing compressible flows in complex geometries. Initially, the developed model has been tested to predict the behaviour of accelerating flames in geometries with single obstacles. Having established the reliability of the baseline numerical model, it is used to study flame interactions with more complex solid obstacle geometries.

The dynamic flame surface density (DFSD) combustion model was originally developed by Knikker et al. (2004) and was tested on experimentally extracted reaction progress variable information from OH images of a premixed flame over a triangular stabiliser. In this work, this concept is applied to the explosion and numerically implemented in an existing LES code. A novel DFSD model has been evaluated for a laboratory-scale explosive premixed combustion chamber Hall et al. (2009), with a specific emphasis on predicting the deflagrating premixed flames characteristics and their interactions with repeated obstacles.

The specific objectives of this investigation can be given as following points and methodology by Figure 1.5 :

➢ Conduct transient LES simulations of explosion flames deflagrating over repeated solid obstacles in a laboratory scale explosion chamber (Hall et al. 2009). The simulations use a developed novel dynamic flame surface density (DFSD) model for the chemical reaction rate.

➢ To confirm the maturity of the LES methodology, extensive grid independency tests, blockage ratio, ignition source, various shape solid obstacles and various flow configurations were performed. The developed model has been incorporated in an in-house LES code in order to evaluate the aforementioned flow configurations and hence achieve a level of confidence.

➢ Perform detailed analysis in order to identify the influence of the number and position of obstacles inside the chamber on the generated overpressure, flame position and speed, which help to understand an accidental explosion scenario. Subsequently the DFSD model is expected to contribute towards the advancement of the LES prediction capabilities of turbulent premixed combustion.

➢ The important issue at the focus of this study, is to establish the influence and importance of combustion in the wake of obstacles representative of offshore plant and process equipment (i.e. pipework, pressure vessels etc.)
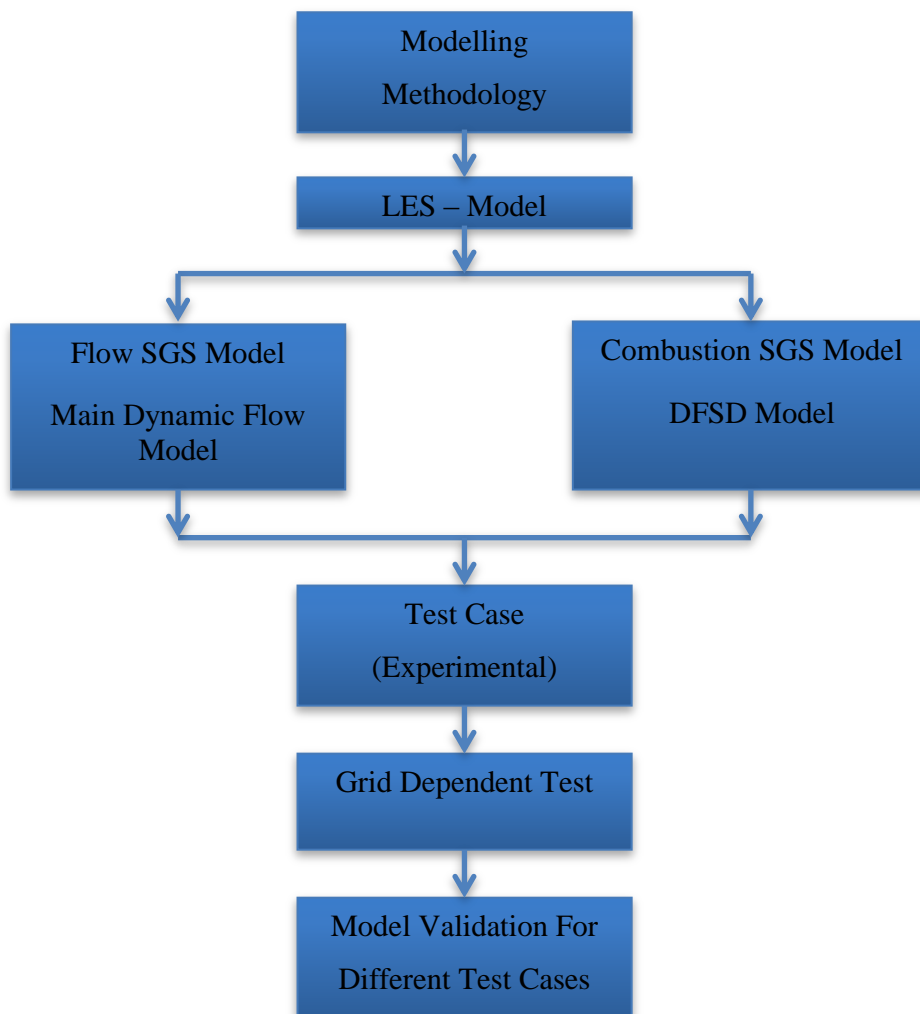
Figure 1.5 The Methodology used to achieve the main aim of the current work.

1.4 Thesis Outline

Chapter 1- INTRODUCTION

This chapter describes the motivation and specific objectives defined in modelling dynamic sub grid scales (SGS) for LES simulations of chemical reaction and flow in explosion combustion systems. The number of numerical approaches and their capabilities for predicting turbulent reacting flows are briefly described. The rest of the thesis layout is as follows.

Chapter 2 - LITERATURE REVIEW

Outlines the breakthrough in premixed combustion research and highlights the various SGS models available to account for the chemical reaction rate. A brief discussion is provided to review the characteristics of combustion through various regimes.

Chapter 3 - GOVERNING EQUATIONS

Governing equations for turbulent premixed combustion are presented in their instantaneous and filtered form. The Favre filtering technique is briefly explained with an overview of the closure problem encountered while applying the filter.

Chapter 4 - THE FLOW MODEL

An overview of the LES approach for modelling turbulent flows, various types of filtering techniques and available filters are presented and discussed. The LES methodology has been described with details of the closing strategies employed for sub grid scale stresses and scalar fluxes.

Chapter 5 - THE COMBUSTION MODEL

This describes the premixed combustion model used here. The dynamic flame surface density (DFSD) model and its incorporation in the in house LES code are presented. Details

of the empirical and dynamic fractal models employed in calculating the fractal dimensions are also outlined.

Chapter 6 -THE EXPERIMENT TEST CASES

This describes the test cases employed in the work for explosion model validation. A detailed description of the influencing factors in designing this test chamber and the novelty of the chamber are explained. A detailed overview of the experimental ignition system and the utilised measurement techniques are introduced. Classification of the various test case configurations in terms of the number of obstacles and their position in the chamber are explained. A typical experimental sequence is detailed to outline the procedure followed.

Chapter 7 - THE NUMERICAL MODEL

This chapter explains the Numerical implementation of the filtered governing equations outlined in Chapter 3. The implementation of the spatial discretisation and time advancement schemes through finite volume methodology are discussed. A detailed description of the initial and boundary conditions and the working procedure are also presented.

Chapter 8 – RESULTS VALIDATION AND DISCUSSIONS

In this chapter, the numerical domain used and the various grid resolutions employed in the LES simulations. The LES simulations are presented and discussed. The LES results obtained using the dynamic flame surface density model for explosion chemical reaction rate are presented and examined for grid independency. Firstly the LES results obtained using dynamic formulation for the model controlling parameters are presented and validated. Secondly, the LES modelling of explosion delegating flames using dynamic flame surface density models are presented and analysed for various complex flow configurations. Flame characteristics from various flow configurations are analysed and presented in a turbulent premixed combustion regime diagram.

Chapter 9 – CONCLUSIONS AND RECOMMENDATIONS FOR FUTURE WORK

This summarises the conclusions from this research work with its key contributions towards improved prediction capabilities. It also suggests directions for further improvement.

Chapter 2   Literature Review

This chapter reviews important breakthroughs in the experimental and numerical techniques for the turbulent premixed combustion research associated in understanding the explosion turbulent propagating flames. A brief discussion is provided in this section to review the characteristics of premixed flames through various turbulent combustion regime diagrams. Section 2.2 describes various modelling techniques of the RANS and LES models available to account for the chemical reaction rate in computational modelling.

2.1 Explosion Flames

Explosion premixed turbulent flames are often characterised by their ability to propagate towards the fresh gases. Once the flame is initiated due to an the ignition source, the chemical reaction advances through the gas with a relatively thin-localised flame front until all the fuel is exhausted. Unlike laminar flames, in turbulent flames the flame propagation speed is not equal to the incoming gas velocity. The turbulent flame speed has been identified as depending on many parameters such as turbulence levels, mixture reactivity, the surface area of the flame and flame stretch etc. On the other hand, if the flame propagation is due to thermal conduction i.e. transporting energy from hot burnt matter to a cold fuel mixture, it is known as deflagration. If the flame propagates due to a shock wave i.e. increasing the temperature by virtue of compressing the fuel mixture, it is known as detonation. The deflagration may transform into detonation depending on the boundary conditions, the length and width of the chamber and the generated overpressure etc. Alternatively, the presence of solid obstructions in the explosion environment eventually leads to a higher flame acceleration with high overpressure, which has severe consequences in many engineering applications. As described in Chapter 1, simulation of explosion scenarios using numerical modelling techniques would help in designing an efficient combustion system. However, the success of any numerical combustion model depends mainly on the competence of the employed chemical reaction rate model in accounting for the chemical reaction rate. Hence, the development and evaluation of combustion models are very important with ever growing industrial needs and demands for essentially, efficient combustion systems.

The main focus of this thesis is to develop and evaluate the dynamic formulation of a flame surface density model for turbulent premixed combustion. The developed model is evaluated and validated for a laboratory scale premixed combustion chamber established at The University of Sydney by Prof. Masri's combustion group (Kent et al., 2005), where highly resolved experimental data has been obtained. This rectangular chamber has built- in solid obstacles to enhance the turbulence level and to increase the flame propagating speed, which eventually lead to stronger interactions between the flame and the solid obstacles. These interactions were found to create turbulence both by vortex shedding and local wake/recirculation. As the flame propagates past the solid obstacles, it wraps on itself, which eventually increases the flame surface area available for combustion. More details of the combustion chamber and the various flow configurations considered in the present study are outlined in Chapter 6.

Several experimental and numerical studies have been performed in the past, using laboratory scale chambers, to evaluate the effect of the chamber size, with or without obstacles on accelerating flames (Williams, 1985i, Aldredge et al., 1998, Bradley, 2002, Lee and Lee, 2003, Akkerman et al., 2006, Bauwens et al., 2007). A large number of these experimental studies were aimed at understanding the flame-turbulence interactions in vented explosion chambers with in-built solid obstructions (Moen et al., 1980, Hjertager et al., 1988, Starke and Roth, 1989, Fairweather et al., 1996, Masri et al., 2000, Bradley et al., 2001). The chambers used by Moen et al. (1980), Moen et al. (1982), Hjertager et al. (1988) and Bradley et al. (2001) to study the flame interaction issues, yielded limited data because they involved large-scale experiments that did not lend themselves easily to detailed measurements. Starke and Roth (1989), Phylaktou and Andrews (1991), Fairweather et al. (1996), Lindstedt and Sakthitharan (1998), Masri et al. (2000) and Ibrahim and Masri (2001) have used laboratory scale chambers utilising simple geometrical configurations that were adaptable to complex diagnostics and the subsequent validation of numerical models. All these studies have involved the use of a variety of obstacles (square/circle/triangular/wall baffles) in the path of propagating flames. However, the exact mechanism that correlates flame structure, speed and resulting overpressure are not well understood yet. Masri et al. (2000) reported the influence of the size and shape of the solid obstacles and found that both the blockage ratio, as well as the shape of obstacles, influences the flame structure and propagation rate. Lindstedt and Sakthitharan (1998) and Fairweather et al. (1999) reported the interaction of flames with baffles and extracted a high quality flame structure, mean and

fluctuating velocity data using expensive experimental setups. Numerical studies have been reported on a variety of confined and semi-confined chambers using RANS and LES approaches (Patel et al., 2002, Pitsch and Duchamp de Lageneste, 2002, Kirkpatrick et al., 2003, Fureby et al., 2005, Masri et al., 2006). Masri et al. (2006) performed LES studies on a 20 litre volume and found it to be impractical due to the long LES computational times. Hence, an alternative design that preserved the same physics and optical access, yet with a reduced volume of less than a litre was developed by Kent et al. (2005), and that geometry was used by Gubba et al. (2011) with numerical studies. After this, a similar design, with the same combustion chamber volume, and having an alternative big square solid obstacle, was developed by et al. (2009). This geometry is used in the present study.

Considerable progress has been made in the modelling of turbulent premixed flames using LES methodology within the last 20 years. Modelling of the chemical reaction rate plays a major role and a variety of modelling approaches are available. However, drawbacks still exist due to the complex nature of turbulent premixed flames, insufficient experimental data for validations and failure to predict flames over a range of turbulent premixed combustion regimes and flow configurations. The majority of models are derived from the popular and simple laminar flamelet concepts, where chemistry is separated from turbulence. Some of these models are briefly discussed in the following sections.

2.1.1 Explosion Characteristics

The explosion of flammable gas or vapour is a very complex thermo chemical fluid flow phenomenon, which is usually associated with a rage of turbulence, chemical, time and length scales. Analyses lead to turbulent combustion diagrams where various regimes are identified and delineated introducing non-dimensional characteristic numbers. These diagrams indicate whether the flow contains flamelets, pockets or distributed reaction zones depending on the turbulence, characterising turbulence by rms velocity u' and its integral length scale l_t. In the case of laminar-premixed flames, the flame will propagate with a speed equal to the incoming gas velocity. In the case of turbulent premixed flames, though the turbulent flame speed is observed the turbulent propagation speed S_T is larger than the

corresponding laminar flame speed S_L. The thickness of the turbulent flame brush δ_T is greater than the laminar flame thickness δ_L.

As observed by Damköhler (1940), the turbulent flame speed S_T is linked to the flame front wrinkling and independent of Reynolds number. When $Re > 6000$, the turbulent eddies are comparable with the tube diameters, and much larger than the laminar flame front thickness. The large eddies do not increase the diffusivities and the small eddies do, but they distort the otherwise smooth laminar flame front. The influence of these folds in the flame front in creases the flame front area per unit cross section of the tube, and as a consequence, the apparent flame speed is increased without any change in the instantaneous local flame structure itself. Damköhler proposed the relation for S_T as

$$\frac{S_T}{S_L} = \frac{A_T}{A_L}$$ (2.1)

where $\frac{A_T}{A_L}$ is the ratio of the surfaces of turbulent laminar flames and corresponds to the wrinkling of the flame front due to turbulent motions. Turbulent combustion involves various lengths, velocity and time scales describing the turbulent flow field and chemical reactions. The Damköhler number is one of the classical non-dimensional numbers, which corresponds to the large eddies, and is defined as the ratio of the turbulent time scale τ_t

$$Da = \frac{\tau_t}{\tau_c}$$ (2.2)

In turbulent premixed flames, the chemical time scale τ_c may be estimated as the ratio between the flame thicknesses δ_L and the laminar flame speed S_T. The turbulent timescale corresponds to the integral length scale l_t and is estimated as $\tau_t = \frac{l_t}{u'}$ when u' is the rms velocity. Then the Damköhler Number becomes

$$Da = \frac{\tau_t}{\tau_c} = \frac{l_t}{\delta_L}\frac{S_L}{u'}$$ (2.3)

when the velocity u'/S_L and the length scale l_t/δ_L ratios are identified.

Classical turbulent combustion diagrams are derived on the basis of two reduced number known as the Damköhler number equation (2.2) and the Korlovitznumber (Ka). The

Karlovita number, Ka, corresponds to the smallest eddies and is the ratio of the chemical time scale to the Kolmogorov time and is expressed as

$$Ka = \frac{\tau_c}{\tau_K} = \frac{u'(\eta_k)/\eta_k}{S_L^o \delta} = \left(\frac{l_t}{\delta}\right)^{-1/2} \left(\frac{u'}{u_L}\right)^{3/2} = \left(\frac{\delta_L}{\eta_k}\right)^2 \qquad (2.4)$$

Using the Damköhler and Karlovitz numbers, various combustion regimes may be identified in terms of l_t/δ and velocity u'/S_L^o ratios as described in Table 2.1. For $Ka < 1$, the chemical time scale is shorter than any turbulent time scales and the flame thickness is smaller than the smallest turbulent scale, the Kolmogorov scale. In this regime, the flame front is thin, has an inner structure close to a laminar flame and is wrinkled by turbulence motions. This thin flame regime or flamelet regime may be divided into two regions, depending on the velocity ratio u'/S_L^o. For the case when $u' < S_L^o$, the speed of turbulent motions is too low to wrinkle the flame front up to the flame interactions. This regime is identified as a wrinkled flamelet regime. If $u' > S_L^o$, the turbulent motion velocities become larger than the flame speed, turbulent motions become able to wrinkle the flame front up to the flame front interactions leading to the formation of pockets of fresh and burnt gases. This regime is identified as a thin flame regime with pocket or corrugated flamelet regimes.

For $\tau_k < \tau_c < \tau_t$ ($Ka > 1$ and $Da > 1$) the turbulent integral time scale is still larger than the chemical time scale but the Kolmogorov scales are smaller than the flame thickness and are able to modify the inner flame structure. The flame can no longer be identified as a laminar flame front but is still a wrinkled flame. This regime is known as the 'thickened flame regime' or the 'distributed reaction zone'. According to the Karlovitz number, the stretch induced by the Kolmogorov scale becomes larger than the critical 'flame stretch' S_L^o/δ possibly leading to flame quenching.

For $Da < 1$, turbulent motions have shorter characteristic times than the chemical reaction time τ_c, mixing is fast and the overall reaction rate is limited by chemistry; this regime is the 'well-stirred reactor' limit. The line separating corrugated flamelets and distributed reaction regimes corresponds to the condition $Ka = 1$ and is known as the Kilmov-Williams criterion.

These regimes may be plotted on a combustion diagram as a function of lengths l_t/δ and velocities u'/S_L^o ratios as shown in Figure 2.1, using log-log scale.

$Ka < 1\ (Da > 1)$	$Ka > 1$ and $Da > 1$	$Da \ll 1$
Flamelets	Thickened flames	Well stirred reactor
Flame is thinner than all turbulent scales	Small turbulent scales may enter the flame front	All turbulent time scales are smaller than the chemical time scale

Table 2.1 Classical regimes of explosion turbulent premixed combustion.
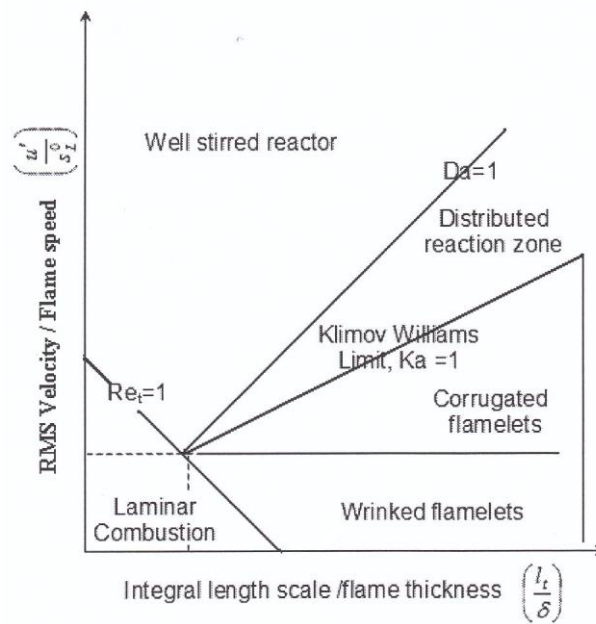
Figure 2.1 Classical Turbulent combustion diagram, Peters (1988).
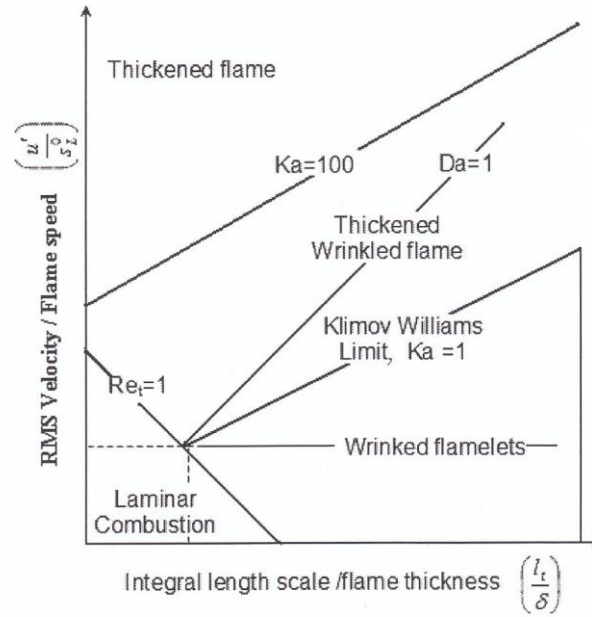
Figure 2.2 Modified turbulent combustion diagram, Peters (2000).

Peters proposed a modified combustion diagram to identify the combustion regimes with flame thickness δ, and reaction zone thickness, $\delta_r (\delta_r \ll \delta)$ as shown in Figure 2.2. A thin flame regime can be identified when $\delta < \eta_k$. The thickened-wrinkled flame regime and the thickened flame regime can be identified when $\delta < \eta_k$. For larger values of the Damköhler number ($Da \gg 1$), the flame front is thin and its structure is not affected by turbulent motions. This regime is called the flamelet regime or the 'thin wrinkled flame regime'. As the turbulence level increases, turbulent structures become able to affect the preheat zone of the flame, and this is known as the 'thickened-wrinkled flame regime'. If the turbulence level continues to increase (and the Damköhler number continues to decrease), turbulent motions become sufficiently strong to affect the whole flame structure. It is called the 'thickened flame regime'. The regimes are separately shown in Figure 2.3, Figure 2.4 & Figure 2.5 respectively.
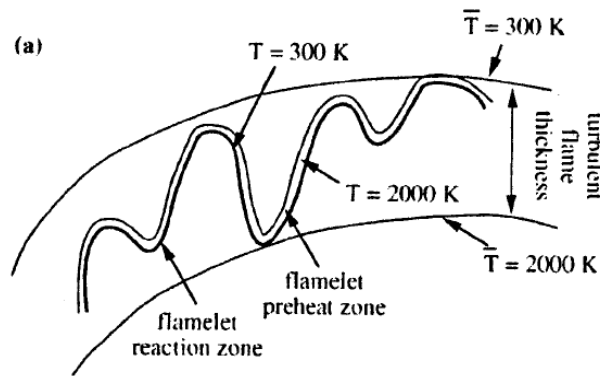
Figure 2.3 Flamelet regime or thin wrinkled flame regime, Poinsot & Veynante (2005).
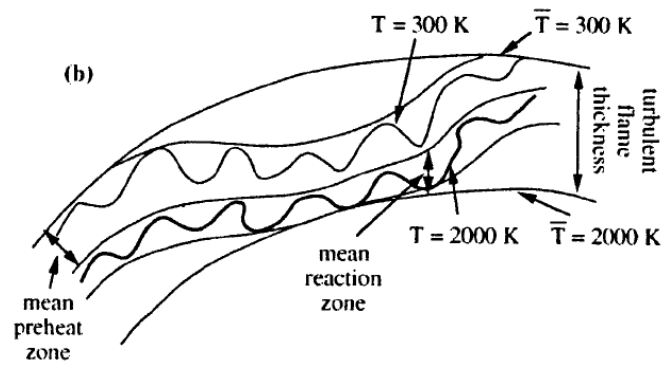
Figure 2.4 Thickened-wrinkle flame regime, Poinsot & Veynante (2005).
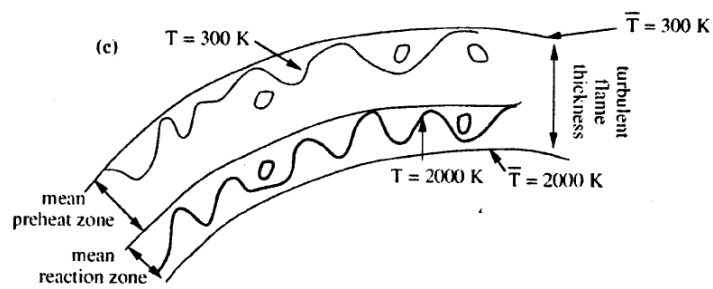
Figure 2.5 Thickened flame regime, Poinsot & Veynante (2005).

2.1.2 Regimes of Turbulent Premixed Combustion in LES

The regime diagrams reported above are treated as classical turbulent combustion diagrams and similar diagrams can be constructed for LES premixed flames using the filter size Δ as the length scale and the sub-filter velocity fluctuation u'_Δ as the velocity scale. Such a representation introduces both physical and modelling parameters into the diagram. A change in the filter size, however, also leads to a change in the sub-filter velocity fluctuation. This implies that the effect of the filter size, which is a numerical or model parameter, cannot be studied independently. In response to this issue, an LES regime diagram for characterising sub-filter turbulence/flame interactions in premixed turbulent combustion was proposed by Pitsch *et al.* (2002), and recently extended by Pitsch (2005). This diagram is shown in Figure 2.6. In contrast to the RANS regime diagrams Δ/l_F and the Karlovitz number Ka are used as the axes of the diagram. The Karlovitz number describes the physical interaction of flow and combustion on the smallest turbulent scales. The sub-filter Reynolds, Damköhler numbers and the Karlovitz number relevant to the diagram are defined as

$$Re_\Delta = \frac{u'_\Delta \Delta}{S_L l_F}, Da_\Delta = \frac{S_L \Delta}{u'_\Delta l_F}, and \ Ka = \frac{l_F^2}{\eta^2} = \left(\frac{u'^3_\Delta l_F}{S_L^3 \Delta}\right)^{1/2} \tag{2.5}$$

where η is the Kolmogorov scale. In LES, the Karlovitz number is a fluctuating quantity, but for a given flow field and chemistry it is fixed. The effect of changes in the filter size can therefore easily be assessed at constant Ka number. An additional benefit of this regime diagram is that it can be used equally well in DNS if Δ is associated with the mesh size. In the following, the physical regimes are briefly reviewed and the relevant issues for LES are discussed.
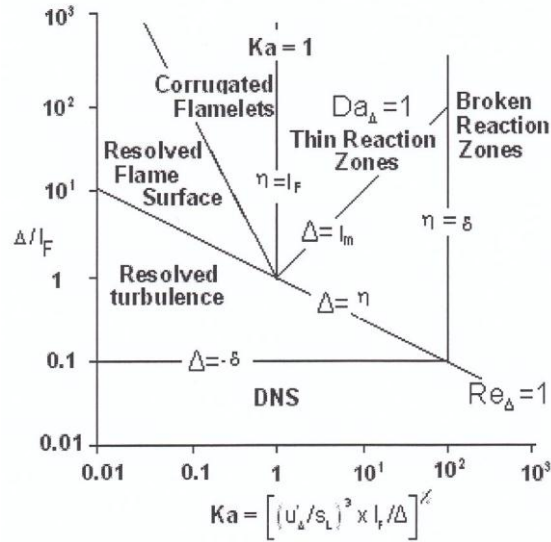
Figure 2.6 Regimes diagram for LES of premixed turbulent combustion, Pitsch (2005).

The three regimes with essentially different interactions of turbulence and chemistry are the corrugated flamelet regime, the thin reaction zones regime and the broken reaction zones regime. In the corrugated flamelet regime, the laminar flame thickness is smaller than the Kolmogorov scale, and hence $Ka < 1$. Turbulence will therefore wrinkle the flame, but will not disturb the laminar flame structure. In the thin reaction zones regime, the Kolmogorov scale becomes smaller than the flame thickness, which implies $Ka > 1$. Turbulence then increases the transport within the chemically inert preheat region. In this regime, the reaction zone thickness δ is still smaller than the Kolmogorov scale. Because the reaction zone, which appears as a thin layer within the flame, can be estimated to be an order of magnitude smaller than the flame thickness, the transition to the broken reaction zones regime occurs at approximately $Ka < 100$. The thin reaction zone retains a laminar structure in the thin reaction zones regime, whereas the preheat region is governed by turbulent mixing, which enhances the burning velocity. In the broken reaction zones regime, the Kolmogorov scale becomes smaller than the reaction zone thickness. This implies that the Karlovitz number, based on the reaction zone thickness, Ka_δ, becomes larger than one.

Most technical combustion devices operate in the thin reaction zones regime, because mixing is enhanced at higher Ka numbers, which leads to a higher volumetric heat release and shorter combustion times. The broken reaction zones regime is usually avoided in fully

premixed systems. In this regime, mixing is faster than the chemistry, which leads to local extinction. This can cause noise, instabilities, and possibly global extinction. However, the broken reaction zones regime is significant, for instance, in a partially premixed system. In a lifted jet diffusion flame, stabilisation occurs by partially premixed flame fronts, which burn fastest at conditions close to stoichiometric mixture. Away from the stoichiometric surface toward the centre of the jet, the mixture is typically very rich and the chemistry slow. Hence, the Ka number becomes larger. This behaviour has been found in the analysis of the DNS results of a lifted hydrogen/air diffusion flame, Mizobuchi *et al.* (2002).

The effect of changing the LES filter width can be assessed by starting from any one of these regimes at large Δ/l_F. As the filter width is decreased, the sub-filter Reynolds number, Re_Δ, eventually becomes smaller than one. Then the filter size is smaller than the Kolmogorov scale, and no sub-filter modelling for the turbulence is required. However, the entire flame including the reaction zone is only resolved if $\Delta < \delta$. In the corrugated flamelets regime, if the filter is decreased below the Gibson scale l_G, which is the smallest scale of the sub-filter flame-front wrinkling, the flame-front wrinkling is completely resolved. It is apparent that in the corrugated flamelet regime, where the flame structure is laminar, the entire flame remains on the sub-filter scale, if Δ/l_F is larger than one. This is always the case for LES.

In the thin reaction zones regime, the preheat region is broadened by the turbulence. Peters (2000) estimated the broadened flame thickness from the assumption that the timescale of the turbulent transport in the preheat zone has to be equal to the chemical timescale, which for laminar flames leads to the burning velocity scaling given in the beginning of this section. From this, the ratio of the broadened flame thickness l_m and the filter size can be estimated as proposed by Pitsch (2005):

$$\frac{l_m}{D} = \left(\frac{u'_\Delta l_F}{S_L \Delta}\right)^{3/2} = Ka\frac{l_F}{D} = Da_D^{-3/2} \tag{2.6}$$

Hence, the flame is entirely on the sub-filter scale as long as $Da_\Delta > 1$, and is partly resolved otherwise.

It is important to realise that the turbulence quantities, especially u'_Δ, and hence most of the non-dimensional numbers used to characterise the flame/turbulence interactions, are fluctuating quantities and can significantly change in space and time, To give an example, the variation of these quantities from a specific turbulent stoichiometric premixed methane/air flame simulation is shown in Figure 2.6. This simulation was done for an experimental configuration with a normal Ka number of $Ka = 1$, based on experimentally observed integral scales. The simulated conditions correspond to flame F3 of Chen *et al.* (1996), and details of the simulation can be found in Pitsch et al. (2005). For a given point in time, the Ka number has been evaluated using appropriate sub-filter models for all points on the flame surface. Because of the spatially varying filter size, but also because of heat losses to the burner, which locally lead to changes in l_F, there is a small scatter in Δ/l_F. Although the flame is mostly in the thin reaction zones regime, there is a strong variation in the Ka number, ranging from the corrugated to the broken reaction zones regime. Figure 2.7 and Figure 2.8 are demonstrating recently of ours LES simulation of combustion regimes by Gubba (2009).
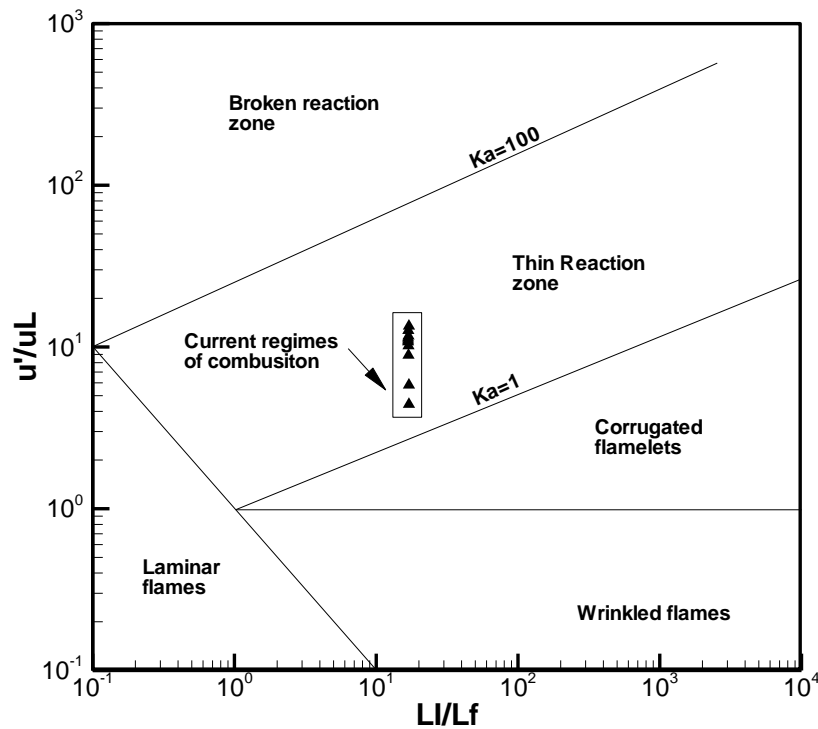
Figure 2.7 Estimates for configuration 9 of the LES simulation presented are fitted in to regimes of combustions as turbulent premixed combustion reported by Peters (2000)
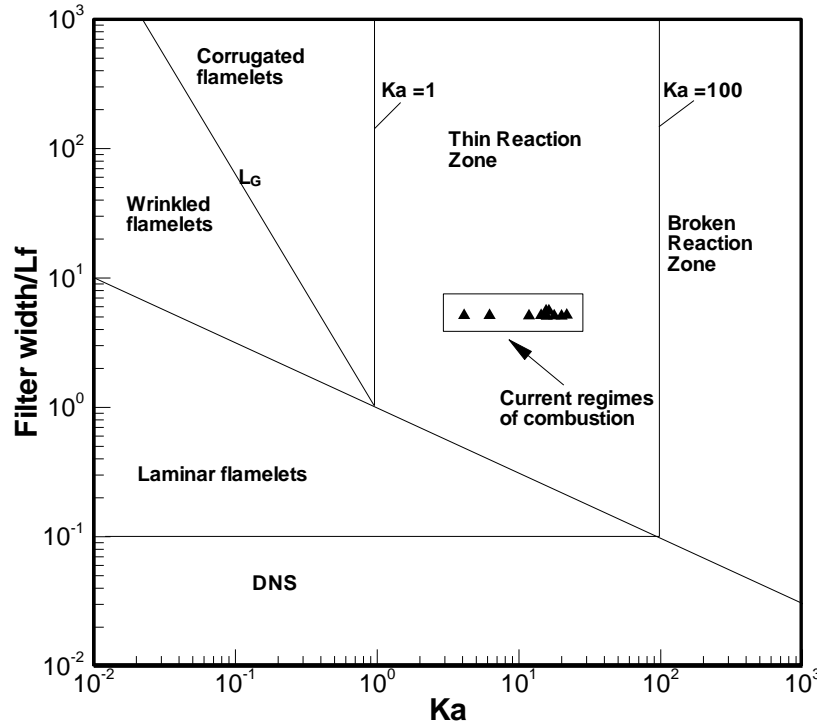
Figure 2.8 Estimates for configuration 9 of the LES simulation presented are fitted in to regimes of combustions as LES turbulent premixed combustion reported by Pitsch (2005)

2.2 CFD Model for Explosion

Modelling the reaction rate in turbulent premixed flames is highly challenging due to its non-linear relation with chemical and thermodynamic states, and is often characterised by propagating reaction layers thinner than the smallest turbulent scales. The major difficulty in modelling the reaction rate is due to the variation of thermo chemical variables through the laminar flame profile, which is typically very thin (Veynante and Poinsot, 1997). This issue is strongly affected by turbulence, which causes flame wrinkling and thereby forming the most complex three way thermo-chemical-turbulence interactions. However, assuming a single step irreversible chemical reaction and neglecting the Zeldovich instability (thermal diffusion), i.e. considering the unit Lewis number will reduce the complexity of the whole system. The various modelling approaches that are available can be found in the literature (Poinsot and Veynante, 2005). Some of these models are briefly discussed in the following sections.

2.2.1 Early Modelling Approaches

As aforementioned earlier, modeling of chemical reaction rate in turbulent premixed combustion is very complex and there are various modeling approaches ranging from simple to complex available in the literature. Most of these approaches have been initially developed for RANS modelling and then extended to LES.

2.2.1.1 Turbulent Flame Speed Relating Models

The chemical reaction rate can be simply modelled by the overall turbulent flame speed s_T as a function of the ratio of turbulent flame surface area to laminar flame surface area. Abdel-Gayed et al. (1985) have shown this in equation 2.7, by correlating various experimental measurements of turbulent premixed flames.

$$\frac{s_T}{s_L} = 1 + \alpha \left(\frac{u'}{s_L}\right)^n \tag{2.7}$$

where α and n are two model constants close to unity and u' is the turbulent velocity. Since the turbulent flame speed is not a well defined quantity and is known to be dependent on many physical and chemical parameters, turbulent flame speed closure is quite questionable (Gouldin et al. 1996).

2.2.1.2 Eddy Break Up (EBU) Model

The Eddy-Break-Up (EBU) model, originally proposed by Spalding (1971), is based on a phenomenological analysis of turbulent combustion assuming high Reynolds numbers. And it is considered that chemistry does not play any explicit role while turbulent motions control the reaction rate. The reaction zone is viewed as a collection of fresh and burnt gaseous pockets transported by turbulent eddies and is expressed as:

$$\bar{\dot{\omega}}_c = C_{EBU}\bar{\rho}\frac{\varepsilon}{k}\frac{\tilde{Y}_F}{Y_F^0}\left(1 - \frac{\tilde{Y}_F}{Y_F^0}\right) \tag{2.8}$$

where Y_F^0 is the fuel mass fraction in fresh gases, k and ε are respectively the turbulent kinetic energy and its dissipation rate, and C_{EBU} is a model constant.

This model is attractive because the reaction rate is simply written as a function of known quantities without any additional transport equation. Nevertheless, this reaction rate does not depend on chemical characteristics. The eddy break-up model also tends to overestimate the reaction rate, especially in highly strained regions. In the LES context the model has been fully evaluated. Kim et al. (2006) have reported results by using the EBU model for gas turbine flame holder stabilised flames for various equivalence ratios, with an additional transport equation for turbulent kinetic energy and an algebraic equation for dissipation rate. Their studies are found to predict the stabilised flame very well, except for a few deviations from experimental data at the stoichiometric condition. Therefore, it can be concluded that the success of EBU models with or without sub-models or additional transport equations, is variable.

2.2.1.3 Probability Density Function (PDF) model

The application of probability density function (PDF) methods to LES was first suggested by Givi (1989), and has subsequently been explored by Pope (1985), Madnia and Givi (1993), Gao and O'Brien (1993), and Cook and Riley (1994), and others. The method is mainly applicable to non-premixed combustion, but it has been applied to premixed combustion by Möller *et al.* (1996). In PDF methodology, the flame front/flow field is described based on statistical properties and probability theories. These methods have close tie-ups in deriving sub-models in flame tracking and flame surface density approaches. There are several methods to describe flow/flame probability functions such as presumed PDF, where a shape is assumed by solving a PDF balance equation; joint PDF, where the probability of a set of variables are either solved using a transport equation or modelled; and finally, conditional PDF, where PDF is used based on certain local conditions.

The fundamental idea of the PDF method is based on describing the statistical property of thermo-chemical variables. For instance, if ϕ represents an arbitrary thermo-chemical variable of interest the PDF in LES can be defined as:

$$P_{sg}(\theta; x, t) = \iiint \delta\big(\theta - \phi(x', t)\big) G(x' - x) dx' \tag{2.9}$$

where θ is the statistical random variable associated with ϕ, and $\delta\big(\theta - \phi(x', t)\big)$ is the fine grained density of the variable θ. The value $P_{sg}(\theta; x, t) d\theta$ is the probability of the LES filter-weighted fraction of fluid around x that has ϕ in the range $[\theta, \theta + d\theta]$. The

advantage of the PDF approach is that the reaction rate term can be closed exactly through the simple relation as:

$$\bar{\bar{\omega}}(x,t) = \int \dot{\omega}(\theta) P_{sg}(\theta; x, t) d\theta \qquad (2.10)$$

Using PDF models has produced good results in comparison with DNS data for non-premixed combustion (Möller et al., 1996, Reveillon and Vervisch, 1997, Colucci et al., 1998 and Cook and Riley, 1998), and successfully predicted premixed combustion using a presumed PDF approach, assuming a multidimensional normal distribution for the scalar variables. With this success, PDF of turbulent premixed flames has become an alternative method to predict flames in various combustion regimes. But the shape of the initial PDF may need to be obtained either from experimental data or DNS data.

2.2.1.4 Flame Tracking (G-equation) Approach

The flame Tracking G-equation approach proposed by Williams (1985ii) is based on the flamelet modelling assumptions and uses a level-set method to describe the evolution of the flame front as an interface between the unburned and burned gases. In this approach the flame thickness is set to zero and the flame front is described as a propagating surface tracked by the level surface of a scalar field G.

$$\frac{\partial G}{\partial t} + u.\nabla G = w|\nabla G| \qquad (2.11)$$

where w is the local relative propagation velocity of the flame. Pitsch (2006) argued that this approach is not modelling the flame front, instead a numerical method, can resolve the flame front. Several studies reported, successful prediction of turbulent flames using the G-equation in RANS and LES. Yakhot (1988) was the first to suggest this equation to be used in LES combustion. Following Yakhot (1988), several authors (Kim and Menon, 2000, Pitsch and Duchamp, 2002 and Huang et al., 2003) proposed an LES formulation of the G-equations and applied it to various combustion chambers such as ramjet (Menon and Jou, 1991), IC engines (Naitoh et al., 1992), Bunsen burner experiments (Pitsch and Duchamp, 2002) etc.

Pitsch (2005) argued that the G-equation for the filtered flame front used in the above studies, did not consider the special character while filtering the G-equation, which has

caused an inconsistency with generalised scaling symmetry. Pitsch (2005) derived a new filtering technique for the G-equation and reported that the filtered G-equation (equation 2.12) is valid in corrugated flamelet and the thin reaction zones.

$$\frac{\partial \breve{G}}{\partial t} + \hat{u}.\nabla \breve{G} = -(u_L + u_K)n.\left|\nabla \breve{G}\right| \tag{2.12}$$

where n is the flame front normal vector, u_L and u_K describes laminar flame propagation and flame advancement by curvature effects respectively, which requires sub-models to close. Pitsch (2006) proposed models for u_L and u_K based on the production dissipation balance assumption and found this to fit well in LES, with certain drawbacks near the flame holder, where the flame is not fully established. Also he described that G in the above equation is not the filtered G-field, but a level set representing the flame front position. This clears the concerns raised by Hawkes and Cant (2000) regarding this approach in tracking the level set of the flame front. However, the G-equation employed in the above studies still appears to have some drawbacks.

Modelling the flame structure is a major challenge in the G-equation, as the flame surface can only be tracked and not resolved in numerical space. This can be achieving by the sub-models derived either from experiments or DNS data. The filtered G-equation (2.12) does not include any diffusion terms, which may lead to numerical difficulties. Finally, there is no theoretical lower limit for the radius of the flame front curvature. As the flame front propagates, cusps can form with a zero radius of curvature (Pope, 1988), which cannot be resolved on the computational mesh. Cusps are not expected for the filtered LES field since these would be smeared out by the filtering process. This problem is usually overcome in an ad-hoc manner by the introduction of artificial diffusion (Piana et al., 1997).

2.2.1.5 Artificially Thickened flame modelling

As previously mentioned for the above modelling approach, the premixed flame is very thin i.e. is approximately 0.1 to 1mm (Colin et al., 2000) and cannot be resolved on the LES numerical grid. This difficulty in resolving the flame on the numerical grid, associated with the stiffness of the progress variable has led to the development of an alternative approach of "thickened flame modelling" by Butler and O'Rourke (1977), which was originally for laminar flame calculations. This method has been extended to LES by Veynante and

Poinsot (1997) and Thibaut and Candel (1998) for turbulent premixed flames. The basic idea of this approach is the thickening of the flame brush by a factor F, and a division of the reaction rate by the same factor, while keeping the laminar flame speed constant, so that its structure is resolved by LES.

$$s_L^0 \propto \sqrt{D_{th}B} \; ; \quad \delta_L^0 \propto \frac{D_{th}}{s_L^0} = \sqrt{\frac{D_{th}}{B}} \tag{2.13}$$

The flame speed s_L^0 and the flame thickness δ_L^0 are expressed here, where D_{th} is the thermal diffusivity and B is the pre-exponential constant. If the thermal diffusivity is increased by a factor F while the pre-exponential constant is decreased by F, the flame thickness δ_L^0 is multiplied by F while the flame speed is maintained. The advantages of the approach are that it is simple to implement and, due to the Arrhenius law, it can handle some effects associated with ignition and flame-wall interaction processes (Colin et al., 2000). This approach models both the reaction rate and sub-grid transport terms simultaneously.

The flame thickening approach seems to be very attractive for flows in which the turbulence flame interactions are governed mainly by very large scale flow structures. However, there are several drawbacks when this is applied to many common scenarios. Firstly, this approach assumes implicitly that the reaction rate is controlled by chemistry rather than by diffusive processes, and hence the use of detailed chemical kinetics is recommended for better accuracy (Poinsot et al., 1991). This is numerically unattractive compared to the laminar flamelet approach where fast chemistry is considered, and the reaction is assumed to be controlled by transport processes. Secondly, the thickening of the flame decreases the sensitivity towards turbulent motions. Therefore the turbulent and chemical time scales are altered, which need to be accounted separately. Turbulent eddies smaller than the size of the thickened flame is found to have no significant effect in stretching the flame (Poinsot et al., 1991). This effect was observed for the thickened flame model in comparison with DNS results by Veynante and Poinsot (1997). Thirdly, the sensitivity of the laminar flame velocity to stretch and curvature is increased by the transformation since the Markstein length is proportional to the flame thickness. The thickened flame will react to a stretch of *k/F,* as the actual flame would react to a stretch of *k*. This may influence flame quenching and may be prone to quench thickened flames much more easily.

To counteract the over-response of the flame stretch, an efficiency function E, relating the actual flame stretch to the stretch felt by the thickened flame has been proposed by Meneveau and Poinsot (1991) based on DNS results. Similarly, Charlette et al., (2002) developed a dynamic model based on local flame conditions to overcome the over-response of the flame stretch in thickened flame modelling.

2.2.2 Flame Surface Density Technique

Flame surface density modelling technique of turbulent deflagrating premixed flames provides a means to introduce chemical and turbulence time scales by considering a thin laminar flame in a turbulent flow field. The key goal behind laminar flamelet modelling is to incorporate various flamelet stretch mechanisms to account for the effective turbulence time scales by assuming that the heat release will only occur within the thin reaction zone. Much of the flamelet modelling literature focuses on deriving the effective turbulent burning velocity (e.g. Abdel-Gayed et al., 1987). An alternative modelling strategy has been pursued for the flamelet regime since the introduction of the Bray-Moss-Libby (BML) model (Bray et al., 1985). This model has been extended from its preliminary form since first introduction in premixed turbulent combustion by Bray and Moss (1977), into the Bray-Moss-Libby (BML) model (Bray et al., 1981, Libby and Bray, 1981), and is the subject of many interesting research works thereafter. BML models are derived based on a combination of statistical approaches using probability density functions (PDF) and physical analysis. This combination has led to the development of both complex and simple models using probability functions. For instance, Bradley et al. (1992) used a classical presumed PDF model by assuming a weak flamelet, which considers reduced chemistry through the parameterisation of detailed chemistry. On the other hand, following BML analysis, the mean chemical reaction rate can be simply modelled by analysing the flamelet and using modelling tools as (Bray et al., 1985):

$$\dot{\omega}_c = \rho_u u_L^0 I_0 \Sigma \tag{2.14}$$

where $\dot{\omega}_c$ is the chemical reaction rate, ρ_u is the unburned gas density, I_0 is the mean stretch factor and Σ is the flame surface density (FSD), defined as flame surface to volume ratio. Modelling the chemical reaction rate using the above approach requires models for FSD and the mean flame stretch factor. Several models and empirical correlations for the valuation of

flame stretch I_0 can be found in the literature. For example, Bray (1990) identified flame stretch as a function of Karlovitz number. Bradley et al. (1992) identified flame stretch as a function of Karlovitz and Lewis numbers, and Bray and Cant (1991) deduced an analytical expression from DNS data as a function of Markstein and Karlovitz numbers.

The flame surface density, Σ in equation (2.14), represents the balance between turbulence, which wrinkles the flame, and laminar flame propagation, which smoothes out the flame wrinkles (Bray and Peters, 1993). The flame surface density can be computed by either solving a transport equation (Pope, 1988, Candel and Poinsot, 1990, Cant et al., 1991) or via an algebraic model (Bray, 1990, Trouvé and Poinsot, 1994). Various models available to compute FSD have been evaluated in the RANS frame-work (Duclos et al., 1993, Prasad and Gore, 1999), which is a central problem in establishing a good flamelet model. Duclos and Veynante (1993) reported that solving a transport equation for FSD in its exact form is highly difficult due to the excessive computational times involved. However, solving a transport equation for the flame surface density has been the subject of many works in RANS and LES (Prasad and Gore, 1999, Hawkes and Cant, 2001, Patel et al., 2003) and sub models have been developed through phenomenological arguments (Darabiha et al., 1986, Borghi, 1990). Although solving a transport equation for the flame surface density is an attractive option, this will result in several unclosed terms which need to be closed by appropriate sub-models and restricted to handle extreme cases, where coupling between the flow-field and flame front is intense.

Resolving the uncertainties involved in the extensive modelling of unclosed terms, which are in solving the transport equation for Σ through instigating for an algebraic expression for Σ, is the main focus of the present study. Bray et al. (1985) proposed a simple model to calculate Σ as, $\bar{c}(1 - \bar{c})/L_y$, where $\bar{c}$ is the reaction progress variable and L_y is the length scale associated with the wrinkled flame. The length scale, Ly can be modelled by assuming it to be proportional to the integral length scale (Abu-Orf and Cant, 2000) or by an additional transport equation (Lindstedt and Váos, 1999). Gouldin et al. (1989i) and Weller et al. (1998) derived an expression for Σ based on fractal theory by viewing the turbulent flame as a fractal surface within the lower and outer cut-off scales, and found this to be in good agreement (Veynante and Vervisch, 2002) with experimental data for $\Sigma/[\bar{c}(1 - \bar{c})]$.

Various other studies (Pope, 1988, Duclos et al., 1993, Veynante et al., 1996) can be found in the literature, modelling the flame surface density either by balancing the production, transport and annihilation terms or developing a correlation from experimental data. On the other hand, Σ can be modelled using turbulent flame speed (TFS) closure as a ratio between the turbulent flame surface area per unit volume A_T to its projection on its average surface per unit volume $\bar{A}$. The ratio of $A_T/\bar{A}$ can be modelled by following the prominent observation of Damköhler (1940). Recently, this approach has been used by Muppala et al. (2005) in RANS and by Aluri et al. (2006) in LES to predict various turbulent premixed flames.

Most of these flamelet models have been successfully transformed from the framework of RANS to LES, and have been applied to a variety of practical problems such as V-flames (Chan and Li, 2005), SI engines (Richard et al., 2007), gas turbines and Ramjets (Menon and Jou, 1991) etc. Boger et al. (1998) deduced a simple algebraic model suitable for LES of turbulent premixed flames. This model has been used by Kirkpatrick et al. (2003) and Masri et al. (2006) to predict the turbulent deflagrating flame in an obstructed explosion chamber, and found this to be predicting outcomes reasonably well. However, their studies under- predicted explosion overpressures, flame position and structures. Masri et al. (2006) reported that using a complex model for flame surface density would provide more accurate predictions for the flame characteristics.

Inspired by the works of Masri et al. (2006), the present study intends to apply a dynamic flame surface density model to the modelling of explosion. In this work, the dynamic FSD model of Knikker et al. (2004) is used initially to predict the turbulent deflagrating flames in various flow configurations. Subsequently, the present work concludes (see Chapter 8) that the model constant is not universal and depends on many physical parameters such as the LES filter width, fuel/air mixture, turbulence etc. Hence, a model is developed based on the wrinkling flame theory and tests are performed to evaluate the self-scaling capabilities of this model. The concept of the dynamic flame surface density model, which was proposed by Hawkes (2000) and Knikker et al. (2002) is developed and evaluated. This model follows the dynamic procedure of Germano et al. (1991) and the similarity concept of Bardina et al. (1980). The dynamic flame surface density model, presented in Chapter 5,

has been linked with flame wrinkling theory in order to dynamically evaluate the model coefficient. This procedure is followed to calculate the fractal dimension of the turbulent premixed flame, which has been the subject of many interesting research works (Mandelbrot, 1975, Gouldin, 1987, Kerstein, 1988, Gouldin et al., 1989i and, Hilton et al., 1989ii) in the past. Recently, Fureby (2005) used an empirical model in LES, based on the original developments of North and Santavicca (1990). This model is also tested, here, and evaluated against the fractal dimension model developed by Knikker et al. (2004) in calculating the dynamic model coefficient.

2.3 Summary

In this chapter, some of the fundamentals and characteristics of explosion flames have been described. Various regimes of turbulent premixed combustion have been discussed in general and also in the LES context. Various reaction rate modelling techniques and approaches suitable for RANS and LES were presented and discussed. A brief history and evolution of the flamelet model, employed in this study for the mean chemical reaction rate, was presented. A survey of a wide range of experimental and numerical studies, which have employed similar forms for the explosive combustion chamber employed in the present investigation, has been presented. Some of the interesting features and drawbacks of the existing models were also presented and discussed.

Chapter 3   The Governing Equations

Modelling the instantaneous explosion scenario is governed by the equations for the conservation of mass, momentum, energy, the reaction progress variable (c) and the equation of state, which governs turbulent premixed flames. In this chapter, all the equations are derived in the Cartesian coordinate system by choosing a control volume to provide better understand. Energy and transport equations for the reaction progress variables are derived for a one-dimensional system and then implemented in the three dimensional system. Turbulent explosion reaction flow prediction is normally related through the form of the averaging equation, which is briefly described. Besides this, the application of the Favre averaging equation is covered by the instantaneous governing equation and shows unclosed terms. The filtered governing equations used in the current study are also summarised and presented in this chapter.

3.1 Conservation Equations

The instantaneous conservation equation governing fluid flows can be applied to the infinitesimal control volume fixed in space and represents the conservation laws of physics. The governing equations presented in the following sections are derived for the Cartesian coordinate system by considering the following assumptions.

- ➢ Low Mach number
- ➢ Soret and Dufour effects are neglected
- ➢ Unity Lewis number
- ➢ Newtonian fluid
- ➢ Negligible bulk viscosity from the Stokes hypothesis
- ➢ Ideal gases
- ➢ Fully premixed reactants with one step irreversible chemistry

3.1.1 Conservation of Mass in a Multi Component System

Consider the rectangular volume of $\Delta x \Delta y \Delta z$ in a fluid flow and involving the mass conservation of the species A. In the control volume, the species A could be produced by the chemical reaction rate ω_A (kg/m^{3}s).

The rate of increase of the mass of species A in a fluid element is given by:

$$\frac{\partial}{\partial t}(\rho_A \Delta x \Delta y \Delta z) = \frac{\partial \rho_A}{\partial t}\Delta x \Delta y \Delta z \tag{3.1}$$

Accordingly the mass flow rate of species A across the x direction is $\dot{m}_{Ax}|_x \Delta y \Delta z$, and the output of species A across the face at $x + \Delta x$ is given by

$$\dot{m}_{Ax}|_{x+\Delta x}\Delta y \Delta z = \dot{m}_{Ax}|_x \Delta y \Delta z + \frac{\partial \dot{m}_{Ax}}{\partial x}\Delta x \Delta y \Delta z \tag{3.2}$$

The chemical reaction rate of species A with in the control volume is

$$\omega_A \Delta x \Delta y \Delta z \tag{3.3}$$

According to (3.2) the input of species A in the y and z direction is given as $\dot{m}_{Ay}\big|_y \Delta x \Delta z$ and $\dot{m}_{Az}|_z \Delta x \Delta y$ respectively, and the output of species A in the y and z direction is given as

$$\dot{m}_{Ay}\big|_{y+\Delta y}\Delta x \Delta z = \dot{m}_{Ay}\big|_y \Delta x \Delta z + \frac{\partial \dot{m}_{Ay}}{\partial y}\Delta x \Delta y \Delta z \tag{3.4}$$

$$\dot{m}_{Az}|_{z+\Delta z}\Delta x \Delta y = \dot{m}_{Az}|_z \Delta x \Delta y + \frac{\partial \dot{m}_{Az}}{\partial z}\Delta x \Delta y \Delta z \tag{3.5}$$

So the mass conservation for the species A in the control volume, as showing Figure3.1, leads to:
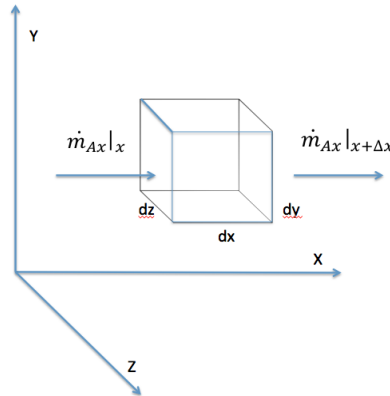
Figure 3.1 Region of volume dx, dy, dz fixed in space through which a fluid is flowing

$$-\frac{\partial \rho_A}{\partial t}\Delta x \Delta y \Delta z + \omega_A \Delta x \Delta y \Delta z$$

$$= \left(\dot{m}_{Ax}|_x \Delta y \Delta z + \frac{\partial \dot{m}_{Ax}}{\partial x}\Delta x \Delta y \Delta z + \dot{m}_{Ay}\Big|_y \Delta x \Delta z + \frac{\partial \dot{m}_{Ay}}{\partial y}\Delta x \Delta y \Delta z \right.$$

$$\left. + \dot{m}_{Az}|_z \Delta x \Delta y + \frac{\partial \dot{m}_{Az}}{\partial z}\Delta x \Delta y \Delta z \right)$$

$$- \left(\dot{m}_{Ax}|_x \Delta y \Delta z + \dot{m}_{Ay}\Big|_y \Delta x \Delta z + \dot{m}_{Az}|_z \Delta x \Delta y \right)$$

$$(3.6)$$

The above equation counteracts some terms which all divide by $\Delta x \Delta y \Delta z$, thus:

$$-\frac{\partial \rho_A}{\partial t} + \omega_A = \frac{\partial \dot{m}_{Ax}}{\partial x} + \frac{\partial \dot{m}_{Ay}}{\partial y} + \frac{\partial \dot{m}_{Az}}{\partial z} \qquad (3.7)$$

Also the equation in (3.7) can be expressed in vector format as

$$\frac{\partial \rho_A}{\partial t} + (\nabla \dot{m}_A) = \omega_A \qquad (3.8)$$

Similarly for species B, the conservation equation can be written as

$$\frac{\partial \rho_A}{\partial t} + (\nabla \dot{m}_B) = \omega_B \qquad (3.9)$$

Adding the species continuity equations (3.8) and (3.9) leads to the continuity equation of a mixture. Substituting $\omega_A + \omega_B = 0$ and $\dot{m}_A + \dot{m}_B = \rho V$ will mean a simplification of the expression to the following form of continuity equation as

$$\frac{\partial \rho}{\partial t} + \nabla(\rho V) = 0 \qquad (3.10)$$

Equation (3.10) is for the unsteady, compressible and three-dimensional mass conservation equation, which can be simplified as per the specifications.

3.1.2 Conservation of Momentum in a Multi Component System

Newton's second law states that the rate of change of momentum of a fluid particle equals the sum of the forces on the particle. Considering the infinitesimal control volume of

$\Delta x \Delta y \Delta z$ in space and writing down the momentum and force terms acting on the control volume gives:

Rate of increase of momentum in control volume = Net rate of momentum in control volume + Sum of forces acting on control volume

The net momentum flux in the x-direction is

$$= \left[\rho u^2 - \left(\rho u^2 + \frac{\partial(\rho u^2)}{\partial x} dx \right) \right] dydz + \left[\rho uv - \left(\rho uv + \frac{\partial(\rho uv)}{\partial y} dy \right) \right] dxdz$$
$$+ \left[\rho uw - \left(\rho uw + \frac{\partial(\rho uw)}{\partial z} dz \right) \right] dxdy$$

(3.11)

Simplifying the above equation gives:

$$= - \left[\frac{\partial(\rho u^2)}{\partial x} + \frac{\partial(\rho uv)}{\partial y} + \frac{\partial(\rho uw)}{\partial z} \right] dxdydz \qquad (3.12)$$

The net increase of the rate of momentum in the control volume in x - direction is

$$= \frac{\partial(\rho u)}{\partial t} dxdydz \qquad (3.13)$$

The forces acting on the control volume are of two types

    1.Surface forces   Pressure forces and Viscous forces

    2.Body forces   Gravitational force

                               Centrifugal force

                               Coriolis force

                               Electromagnetic force

In a mixture of N species, the body forces acting on the species may differ. Thus for a multi component system, the body forces are defined as:

$$B_i = \rho \sum_{k=1}^{n} (y_k f_k)_i \qquad (3.14)$$

when f_k is the force per unit mass on the kth species.

$$dF_i = df_i + B_i dxdydz \qquad (3.15)$$

The surface forces acting the control volume are as shown in Figure 3.2.
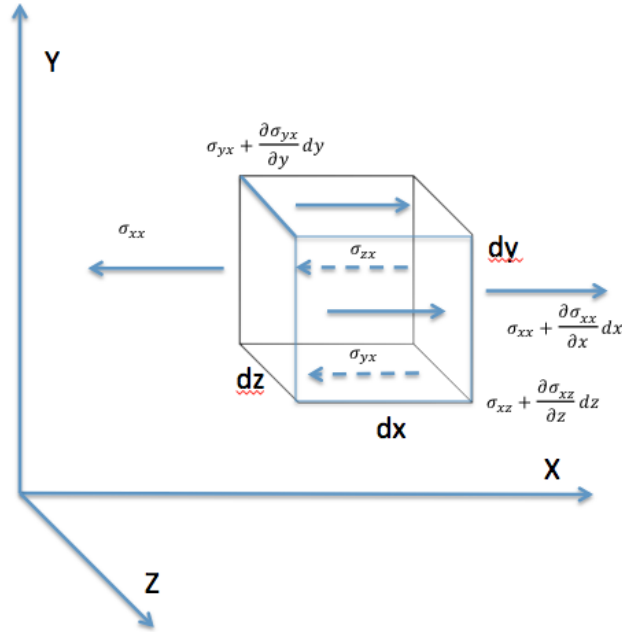
Figure 3.2 Surface stress components acting on the fluid particle in the x-direction

The surface force in the x-direction can be written and summarised as

$$df_x = \left[\frac{\partial \sigma_{xx}}{\partial x} + \frac{\partial \sigma_{xy}}{\partial y} + \frac{\partial \sigma_{xz}}{\partial z}\right] dxdydz \qquad (3.16)$$

So the surface forces in the y and z directions are:

$$df_y = \left[\frac{\partial \sigma_{xy}}{\partial x} + \frac{\partial \sigma_{yy}}{\partial y} + \frac{\partial \sigma_{yz}}{\partial z}\right] dxdydz \qquad (3.17)$$

$$df_z = \left[\frac{\partial \sigma_{xx}}{\partial x} + \frac{\partial \sigma_{xy}}{\partial y} + \frac{\partial \sigma_{xz}}{\partial z}\right] dxdydz \qquad (3.18)$$

Summarising the momentum equation in the x-direction by using equations (3.12), (3.13) and (3.16) leads to:

$$\frac{\partial (\rho u)}{\partial t} dxdydz = -\left[\frac{\partial (\rho u^2)}{\partial x} + \frac{\partial (\rho uv)}{\partial y} + \frac{\partial (\rho uw)}{\partial z}\right] dxdydz + B_i dxdydz$$

$$+ \left[\frac{\partial \sigma_{xx}}{\partial x} + \frac{\partial \sigma_{xy}}{\partial y} + \frac{\partial \sigma_{xz}}{\partial z}\right] dxdydz$$

$$(3.19)$$

the above equation can be simplified as follows:

$$\frac{\partial(\rho u)}{\partial t} + \frac{\partial(\rho u^2)}{\partial x} + \frac{\partial(\rho uv)}{\partial y} + \frac{\partial(\rho uw)}{\partial z} = \frac{\partial \sigma_{xx}}{\partial x} + \frac{\partial \sigma_{xy}}{\partial y} + \frac{\partial \sigma_{xz}}{\partial z} + B_i \qquad (3.20)$$

Equation (3.20) is the momentum in the x-direction. This can be written in vector format as below, which is convenient for expressing the momentum in any direction.

$$\rho \left(u_j \frac{\partial u_i}{\partial x_j} + \frac{\partial u_i}{\partial t} \right) = \frac{\partial \sigma_{ij}}{\partial x_j} + B_i \qquad (3.21)$$

$$\rho \left(u_j \frac{\partial u_i}{\partial x_j} + \frac{\partial u_i}{\partial t} \right) = \frac{\partial \sigma_{ij}}{\partial x_j} + \sum_{k=1}^{n}(y_k f_k)_i \qquad (3.22)$$

For the stress strain relationship, the stress tensor can be written as

$$\sigma_{ij} = -p\delta_{ij} + \left(\mu' - \tfrac{2}{3}\mu\right)\frac{\partial u_k}{\partial x_k}\delta_{ij} + \mu\left(\frac{\partial u_i}{\partial x_j} + \frac{\partial u_j}{\partial x_i}\right) \qquad (3.23)$$

Substituting the stress tensor (3.23) into the momentum equation (3.22) leads to the Navier-Stokes equation.

$$\rho \left(u_j \frac{\partial u_i}{\partial x_j} + \frac{\partial u_i}{\partial t} \right) = \frac{\partial}{\partial x_j}\left[-p\delta_{ij} + \left(\mu' - \tfrac{2}{3}\mu\right)\frac{\partial u_k}{\partial x_k}\delta_{ij} + \mu\left(\frac{\partial u_i}{\partial x_j} + \frac{\partial u_j}{\partial x_i}\right)\right] + B_i \qquad (3.24)$$

Using the Stokes hypothesis, we can substitute bulk viscosity $\mu' = 0$ in equation (3.24)

$$\rho \left(u_j \frac{\partial u_i}{\partial x_j} + \frac{\partial u_i}{\partial t} \right) = -\frac{\partial p}{\partial x_j} + \frac{\partial}{\partial x_j}\left\{\mu\left[\left(\frac{\partial u_i}{\partial x_j} + \frac{\partial u_i}{\partial x_i}\right) - \tfrac{2}{3}\delta_{ij}\frac{\partial u_k}{\partial x_k}\right]\right\} + B_i \qquad (3.25)$$

Substituting $S_{ij} = \frac{1}{2}\left(\frac{\partial u_i}{\partial x_j} + \frac{\partial u_i}{\partial x_i}\right)$ and $S_{kk} = \frac{\partial u_k}{\partial x_k}$ in equation (3.25) mean it can be simplified as:

$$\frac{\partial \rho u_i}{\partial t} + \frac{\partial(u_i u_j)}{\partial x_i} = -\frac{\partial p}{\partial x_j} + \frac{\partial}{\partial x_j}\left[2\mu\left(S_{ij} - \tfrac{1}{3}\delta_{ij}S_{kk}\right)\right] + B_i \qquad (3.26)$$

3.1.3 Conservation of Energy in a Multi Component System

The energy transport equation is used to evaluate the temperature T for the chemical reaction flow. Many forms of this equation exist, having static temperature, static enthalpy, stagnation enthalpy or internal enthalpy as the principal variables. The law of the conservation of energy for the fluid is shown in Figure 3.3.

$$
\underbrace{\left\{\begin{array}{c}\text{Rate of}\\\text{accumulation}\\\text{of internal}\\\text{and}\\\text{kinetic}\\\text{energy}\end{array}\right\}}_{\text{I}}=\underbrace{\left\{\begin{array}{c}\text{Net rate of}\\\text{influx of}\\\text{internal}\\\text{and}\\\text{kinetic}\\\text{energy}\\\text{by}\\\text{convection}\end{array}\right\}}_{\text{II}}+\underbrace{\left\{\begin{array}{c}\text{Net rate of}\\\text{heat}\\\text{addition}\\\text{due to heat}\\\text{flux}\end{array}\right\}}_{\text{III}}+\underbrace{\left\{\begin{array}{c}\text{Rate of}\\\text{heat}\\\text{added by}\\\text{heat}\\\text{source}\end{array}\right\}}_{\text{IV}}+\underbrace{\left\{\begin{array}{c}\text{Net rate of}\\\text{work done}\\\text{on system by}\\\text{surroundings}\end{array}\right\}}_{\text{V}}
$$
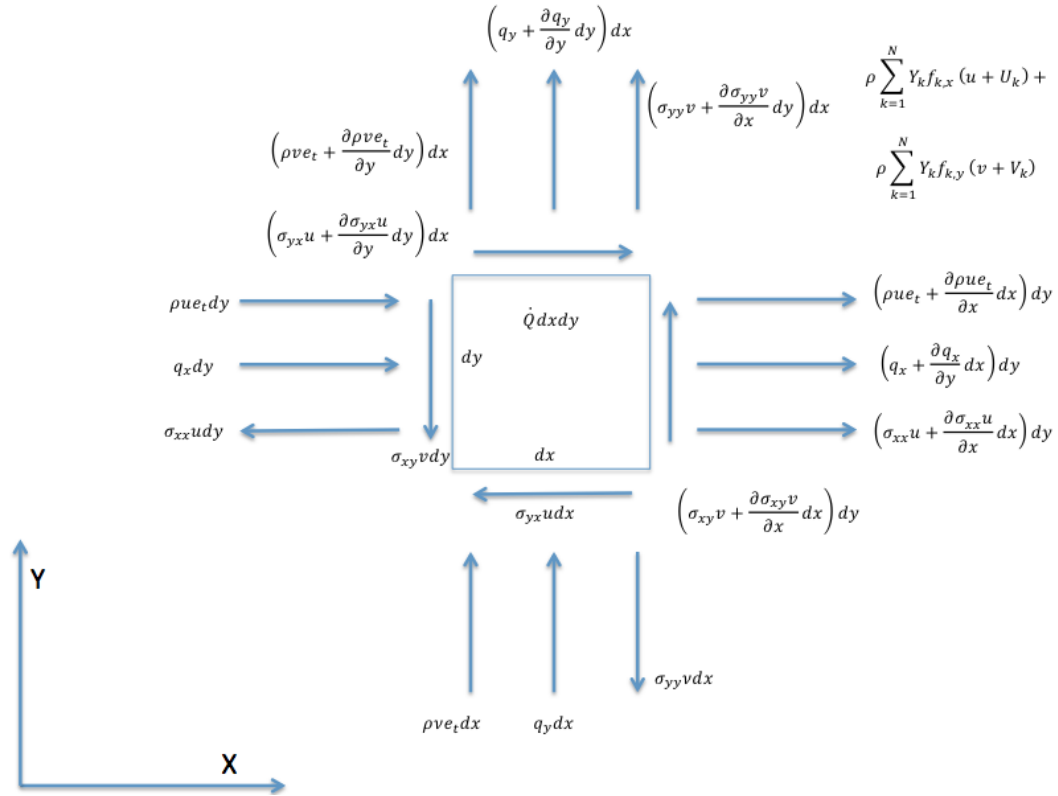
Figure 3.3 Terms in the energy flux balance for a two-dimensional flow

$$
\underbrace{\frac{\partial}{\partial t}(\rho e_t)}_{\text{I}}
$$

$$
=\underbrace{-\frac{\partial}{\partial x}(\rho u e_t)-\frac{\partial}{\partial y}(\rho v e_t)}_{\text{II}}-\underbrace{\left(\frac{\partial q_x}{\partial x}+\frac{\partial q_y}{\partial y}\right)}_{\text{III}}+\underbrace{\dot{Q}}_{\text{IV}}
$$

$$
\underbrace{+\rho\sum_{k=1}^{N}Y_k f_{k,x}(u+U_k)+\rho\sum_{k=1}^{N}Y_k f_{k,y}(v+V_k)+\frac{\partial\sigma_{xx}u}{\partial x}+\frac{\partial\sigma_{yx}u}{\partial y}+\frac{\partial\sigma_{yy}v}{\partial y}+\frac{\partial\sigma_{xy}v}{\partial x}}_{\text{V}}
$$

41

$$(3.27)$$

where U_k, V_k are the relative mass diffusion velocity components.

The specific internal energy, e, is defined as:

$$e = h - \frac{p}{\rho} = \sum_{i=1}^{N} h_i Y_i - \frac{p}{\rho}$$

$$(3.28)$$

The stored energy per unit mass, e_t, is defined as

$$e_t = e + \frac{u_i u_i}{2}$$

$$(3.29)$$

with h_i defined as:

$$h_i = \Delta h_{f,i}^o + \int_{T^o}^{T} C_{p,i} dT$$

$$(3.30)$$

Generalising the energy equation (3.27) for three dimensional space, thus leads to the following:

$$\frac{\partial}{\partial t}(\rho e_t) + \frac{\partial}{\partial x}(\rho u e_t) + \frac{\partial}{\partial y}(\rho v e_t) + \frac{\partial}{\partial z}(\rho w e_t)$$

$$= -\left(\frac{\partial q_x}{\partial x} + \frac{\partial q_y}{\partial y} + \frac{\partial q_z}{\partial z}\right) + \dot{Q} + \frac{\partial \sigma_{xx} u}{\partial x} + \frac{\partial \sigma_{yx} u}{\partial y} + \frac{\partial \sigma_{zx} u}{\partial z} + \frac{\partial \sigma_{xx} v}{\partial x}$$

$$+ \frac{\partial \sigma_{yx} v}{\partial y} + \frac{\partial \sigma_{zx} v}{\partial z} + \frac{\partial \sigma_{xx} w}{\partial x} + \frac{\partial \sigma_{yx} w}{\partial y} + \frac{\partial \sigma_{zx} w}{\partial z} + \rho \sum_{k=1}^{N} Y_k f_{k,x} (u + U_k)$$

$$+ \rho \sum_{k=1}^{N} Y_k f_{k,y} (v + V_k) + \rho \sum_{k=1}^{N} Y_k f_{k,z} (w + W_k)$$

$$(3.31)$$

writing the above equation in vector tensor notation, gives the following:

$$\frac{\partial}{\partial t}(\rho e_t) + \frac{\partial}{\partial x}(\rho u_i e_i) = -\frac{\partial q_i}{\partial x_i} + \dot{Q} + \frac{\partial \sigma_{ji} u_i}{\partial x_i} + \rho \sum_{k=1}^{N} Y_k f_{k,i} (u_i + V_{k,i})$$

$$(3.32)$$

Substituting the continuity equation on the left hand side of equation (3.32) means it can be simplified as follows:

$$\rho \frac{\partial e_t}{\partial t} + \rho u_i \frac{\partial e_t}{\partial x} = -\frac{\partial q_i}{\partial x_i} + \dot{Q} + \frac{\partial \sigma_{ji} u_i}{\partial x_i} + \rho \sum_{k=1}^{N} Y_k f_{k,i} (u_i + V_{k,i})$$

$$(3.33)$$

The above equation is with the Euler form of the energy equation. From the Euler energy equation subtracting the mechanical energy equation, and then simplifying and adding the mechanical energy equation, we arrive at the following equation:

$$\rho \frac{D}{Dt}\left(h + \frac{u_i u_i}{2}\right) - \frac{Dp}{Dt} = u_i \frac{\partial \sigma_{ji}}{\partial x_i} + \dot{Q} - \nabla \cdot q + \rho \sum_{k=1}^{N} Y_k f_k \cdot (u + V_k) + \Phi \qquad (3.34)$$

where the dissipation by viscous stress, Φ, can be written as:

$$\Phi = \tau_{ij} \frac{\partial u_i}{\partial x_j} \qquad (3.35)$$

Using (3.23) and $h_t = h + \frac{u_i u_i}{2}$

means the energy equation can be written as

$$\rho \frac{Dh_t}{Dt} - \frac{Dp}{Dt} = u_i \frac{\partial}{\partial x_j}\left[-p\delta_{ij} + \left(\mu' - \frac{2}{3}\mu\right)\frac{\partial u_k}{\partial x_k}\delta_{ij} + \mu\left(\frac{\partial u_i}{\partial x_j} + \frac{\partial u_j}{\partial x_i}\right)\right] + \dot{Q} - \nabla \cdot q$$

$$+ \rho \sum_{k=1}^{N} Y_k f_k \cdot (u + V_k) + \Phi$$

$$(3.36)$$

substituting the bulk viscosity $\mu' = 0$ from Stokes theorem and writing τ_{ij} as:

$$\tau_{ij} = -\frac{2}{3}\mu \frac{\partial u_k}{\partial x_k}\delta_{ij} + \mu\left(\frac{\partial u_i}{\partial x_j} + \frac{\partial u_j}{\partial x_i}\right) = \sigma_{ij} + p\delta_{ij} \qquad (3.37)$$

simplifies the equation as

$$\rho \frac{Dh_t}{Dt} - \frac{Dp}{Dt} = -u_i \frac{\partial p}{\partial x_j}\delta_{ij} + u_i \frac{\partial \tau_{ij}}{\partial x_j} + + \dot{Q} - \nabla \cdot q + \rho \sum_{k=1}^{N} Y_k f_k \cdot (u + V_k) + \Phi \quad (3.38)$$

expressing the above (3.38) give as:

$$\rho \frac{\partial h_t}{\partial t} + \rho u_i \frac{\partial h_t}{\partial x_i} - \frac{\partial p}{\partial t} - u_i \frac{\partial p}{\partial x_i}$$

$$= -u_i \frac{\partial p}{\partial x_j}\delta_{ij} + u_i \frac{\partial \tau_{ij}}{\partial x_j} + \dot{Q} - \nabla \cdot q + \rho \sum_{k=1}^{N} Y_k f_k \cdot (u + V_k) + \tau_{ij} \frac{\partial u_i}{\partial x_j}$$

$$(3.39)$$

the above equation can be simplified by introducing:

$$u_i \frac{\partial p}{\partial x_j} \delta_{ij} = u_i \frac{\partial p}{\partial x_j} \text{ and } \frac{\partial(\tau_{ij}u_i)}{\partial x_j} = u_i \frac{\partial \tau_{ij}}{\partial x_j} + \tau_{ij} \frac{\partial u_i}{\partial x_j}$$

this gives the simplified form of the energy equation

$$\rho \frac{\partial h_t}{\partial t} + \rho u_i \frac{\partial h_t}{\partial x_i} - \frac{\partial p}{\partial t} = \frac{\partial(\tau_{ij}u_i)}{\partial x_j} + \dot{Q} - \nabla \cdot q + \rho \sum_{k=1}^{N} Y_k f_k \cdot (\mathrm{u} + \mathrm{V}_k) \tag{3.40}$$

Also, the energy equation can be expressed in many ways, which is useful for modelling problems. By substituting $\tau_{ij} = 2\mu\left(S_{ij} - \frac{1}{3}\delta_{ij}S_{kk}\right)$ in the equation (3.40) this gives:

$$\rho \frac{\partial h_t}{\partial t} + \rho u_i \frac{\partial h_t}{\partial x_i} = \frac{\partial p}{\partial t} + 2\mu\left(S_{ij} - \frac{1}{3}\delta_{ij}S_{kk}\right) : \frac{\partial u_i}{\partial x_j} + \dot{Q} - \nabla \cdot q + \rho \sum_{k=1}^{N} Y_k f_k \cdot (\mathrm{u} + \mathrm{V}_k) \tag{3.41}$$

Substituting $q_j = -k \frac{\partial T}{\partial x_j} = -\frac{\mu}{\mathrm{Pr}_l} \frac{\partial h}{\partial x_j}$, where Pr_l=laminar Prandtl number $= \frac{C_p \mu}{k}$, in equation (3.41) gives another form of the energy equation as follows:

$$\rho \frac{\partial h_t}{\partial t} + \rho u_i \frac{\partial h_t}{\partial x_i}$$

$$= \frac{\partial p}{\partial t} + 2\mu\left(S_{ij} - \frac{1}{3}\delta_{ij}S_{kk}\right) : \frac{\partial u_i}{\partial x_j} + \dot{Q} + \frac{\partial}{\partial x_j}\left(\frac{\mu}{\mathrm{Pr}_l} \frac{\partial h}{\partial x_j}\right) + \rho \sum_{k=1}^{N} Y_k f_k$$

$$\cdot (\mathrm{u} + \mathrm{V}_k)$$

$$\tag{3.42}$$

3.1.4 Reaction Progress Variable Equation / (Transport Equation)

In the premixed explosion flames, the chemical state of the mixture can be assumed to be a single irreversible step of reaction between the reactants and the products, which is given in terms of a reaction progress variable c defined such that it is zero where the mixture is unburned and unity where it is fully burned. The mathematical expression of the reaction progress variable is defined as:

$$c = 1 - \frac{Y_{fu}}{Y_{fu}^o} \tag{3.43}$$

Y_{fu} is the local fuel mass fraction and Y_{fu}^o is the fuel mass fraction in the unburned mixture. A transport equation for c is arrived at as below:
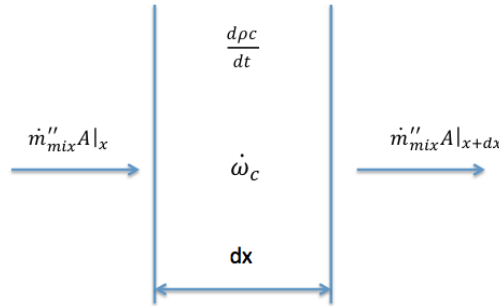
Figure 3.4 One-dimensional control volumes showing the parameter

Figure 3.4 shows the one dimensional control volume as a plane layer of dx thick. A mixture of unburned fuel and oxidiser flows into the control volume as a result of combined action of bulk flow and diffusion. With in the control volume, the mixture's reaction progress variable can be created or destroyed as a result of the chemical reaction. The net rate of increase in the mixtures reaction progress variable of fuel within the control volume relates to the mass fluxes and the reaction rate as follows

$$\begin{bmatrix} \text{Rate of increase} \\ \text{of fraction of} \\ \text{reaction} \\ \text{progress} \\ \text{variable} \\ \text{with in the} \\ \text{control volume} \end{bmatrix} = \begin{bmatrix} \text{Mass flow of} \\ \text{unburned mixture} \\ \text{into the control} \\ \text{volume in terms} \\ \text{of reaction} \\ \text{progress variable} \end{bmatrix} - \begin{bmatrix} \text{Mass flow of} \\ \text{mixture out of the} \\ \text{control volume} \\ \text{in terms of} \\ \text{reaction} \\ \text{progress variable} \end{bmatrix} + \begin{bmatrix} \text{Production rate} \\ \text{due to} \\ \text{chemical reaction} \end{bmatrix}$$

$$Adx \frac{dpc}{dt} = \dot{m}''_{mix}A|_x - \dot{m}''_{mix}A|_{x+dx} + \dot{\omega}_c Adx \tag{3.44}$$

the mixture mass flux is given as:

$$\dot{m}''_{mix} = c(\dot{m}''_{ub} - \dot{m}''_b) - \rho D_{ub,b}\frac{dc}{dx} \tag{3.45}$$

$D_{ub,b}$ is the diffusion coefficient for unburned to burned gases. $\dot{\omega}_c$ is the chemical reaction rate. Using this expression the above equation can be written as:

$$Adx \frac{dpc}{dt} = A\left(c\dot{m}''_{mix} - \rho D_{ub,b}\frac{dc}{dx}\right)_x - A\left(c\dot{m}''_{mix} - \rho D_{ub,b}\frac{dc}{dx}\right)_{x+dx} + \dot{\omega}_c Adx \tag{3.46}$$

Dividing through by $A\Delta x$ and taking the limit as $\Delta x \to 0$, equation (3.46) becomes:

$$\frac{dpc}{dt} = -\frac{\partial}{\partial x}\left(c\dot{m}''_{mix} - \rho D_{ub,b}\frac{dc}{dx}\right) + \dot{\omega}_c \tag{3.47}$$

Rewriting equation (3.47) in multiple coordinates after substituting the Schmidt number, $Sc = \frac{\mu}{\rho D_{ub,b}}$, leads to:

$$\frac{\partial \rho c}{\partial t} + \frac{\partial(\rho u_j c)}{\partial x_j} = \frac{\partial}{\partial x_j}\left(\frac{\mu}{Sc}\frac{\partial c}{\partial x_j}\right) + \dot{\omega}_c \tag{3.48}$$

3.1.5 The Equation of state

In general, for a closed system of known material at a volume V and temperature T, there will be one set of values of n_i for which the system is in chemical equilibrium. Then $n_i^* = n_i^*(V,T)$, when the values n_i^* are the equilibrium values. The equation of state for a system in equilibrium becomes $P = P(V,T,n_1^*,n_2^*,\cdots n_N^*)$. From Dalton's law of partial Pressures, a mixture of thermally perfect gases in the thermodynamic equilibrium can be written as follows:

$$P = \frac{1}{V}\sum_{i=1}^{N} n_i^* R_u T = \sum_{i=1}^{N} n_i R_u T \tag{3.49}$$

3.2 Favre Averaging

Turbulent flows consist of random fluctuations in the various flow properties such as density, temperature, velocities etc., as mentioned in section 3.1.2. In the case of reacting flows, the density is subjected to fluctuations due to thermal heat release. In order to account for these fluctuations some sort of statistical averaging is required, where all the quantities are expressed as the sum of mean and fluctuating parts. Conventional Reynolds-averaging, or time averaging, will only take into consideration velocity and pressure fluctuations in the fluid flow. This is appropriate for steady turbulence, which on average does not vary with time. Using Reynolds averaging in unsteady, reacting problems leads to several complexities, which eventually involve the explicit modelling of the velocity density correlation due to high fluctuations, and is thus not recommended.

Alternatively, Favre averaging, or mass weighted averaging, accounts for the density and temperature fluctuations in addition to the velocity and pressure fluctuations, when the medium is a compressible fluid. In Favre averaging, all the instantaneous values of the velocity and scalars, except for pressure and density, are decomposed in to steady and fluctuating parts as:

$$\phi = \tilde{\phi} + \phi'' \tag{3.50}$$

where ϕ is the generic flow property, $\tilde{\phi}$ is the mass weighted mean, defined as $\tilde{\phi} = \overline{\rho\phi}/\bar{\rho}$, and ϕ'' is the superimposed fluctuations. The Favre mean is shown by a tilde, while the fluctuation about the Favre mean is given by a double prime. Additionally, $\overline{\rho u_i''} = 0$ and $\overline{\rho\phi''} = 0$, while $\overline{\phi''} \neq 0$ and $\overline{u_i''} \neq 0$. Insertion of this decomposed form of the governing equations, with sub sequent ensemble averaging, results in the Favre averaged equation for the mean flow quantities as shown in next section.

3.2.1 Favre Averaged Governing Equations

Favre averaging applied to the governing equations shown in Equations 3.10, 3.26, 3.41 and 3.48 induces the following set of equations, which must be closed by modelling the unclosed terms:

♦ Conservation of mass:

$$\frac{\partial \bar{\rho}}{\partial t} + \frac{\partial (\rho \tilde{u}_i)}{\partial x_i} = 0 \tag{3.51}$$

♦ Conservation of momentum:

$$\frac{\partial (\bar{\rho}\tilde{u}_i)}{\partial t} + \frac{\partial (\rho \tilde{u}_i \tilde{u}_j)}{\partial x_i} = -\frac{\partial \bar{P}}{\partial x_i} + \frac{\partial}{\partial x_j}\left[2\bar{\mu}\left(\tilde{S}_{ij} - \tfrac{1}{3}\delta_{ij}\tilde{S}_{kk}\right)\right] + \tilde{B}_i - \frac{\partial \tau_{ij}}{\partial x_j} \tag{3.52}$$

$$\tilde{S}_{ij} = \frac{1}{2}\left(\frac{\partial \tilde{u}_i}{\partial x_j} + \frac{\partial \tilde{u}_i}{\partial x_i}\right) \tag{3.53}$$

$$\tau_{ij} = \bar{\rho}\overline{u_i''u_j''} = \bar{\rho}\left(\widetilde{u_i u_j} - \tilde{u}_i \tilde{u}_j\right) \tag{3.54}$$

♦ Conservation of energy:

$$\frac{\partial \bar{\rho}\tilde{h}}{\partial t} + \frac{\partial (\bar{\rho}\tilde{u}_j \tilde{h})}{\partial x_j} + \frac{\partial \left(\overline{\rho u_j'' h''}\right)}{\partial x_j} = \frac{\partial \bar{P}}{\partial t} + 2\bar{\mu}\left(\tilde{S}_{ij} - \tfrac{1}{3}\delta_{ij}\tilde{S}_{kk}\right):\frac{\partial \tilde{u}_i}{\partial x_j} + \frac{\partial}{\partial x_j}\left(\frac{\bar{\mu}}{\Pr}\frac{\partial \tilde{h}}{\partial x_j}\right) + \bar{q}_c \tag{3.55}$$

$$\bar{q}_c = \Delta h_f^o \bar{\omega}_c Y_{fu}^o \tag{3.56}$$

♦ Reaction progress variable equation:

$$\frac{\partial \bar{\rho}\tilde{c}}{\partial t} + \frac{\partial(\bar{\rho}\tilde{u}_j\tilde{c})}{\partial x_j} + \frac{\partial\left(\overline{\rho u_j'' c''}\right)}{\partial x_j} = \frac{\partial}{\partial x_j}\left(\frac{\bar{\mu}}{Sc}\frac{\partial \tilde{c}}{\partial x_j}\right) + \bar{\dot{\omega}}_c \tag{3.57}$$

♦ The equation of state:

$$\bar{P}/\bar{\rho} = MR\tilde{T} \tag{3.58}$$

By observing the above Favre averaged governing equations, it can be shown that some of the transport terms, such as Reynolds stress and heat flux, cannot be closed in the solution space. Nevertheless, these terms are very important for closing the equations and must be obtained by modelling. Some of the closing strategies are discussed in Chapter 4.

3.3 Summary

In this chapter, the governing conservation for the explosion turbulent premixed flames are presented and discussed. The Favre averaging technique for flows with variable density has been demonstrated, which generally applies in turbulent reacting flows. A summary of the Favre averaged equations used in the current study has also been presented.

Chapter 4   The Flow Model

This chapter reviews the modelling of turbulent flows by applying the large eddy simulation technique, and discusses the main issues that have to be accounted for before implementation. The fundamental components of this, such as the spatial filtering technique, the mathematical description of the filters and the decomposition of the velocity components are briefly described. The governing equations detailed in the previous chapter are spatially filtered using the box filter and are presented with unclosed terms. Some models and methodologies available to close the sub-grid scale momentum fluxes and the choice of model considered in the present simulations are discussed. The commonly used gradient transport model is implemented to account for the sub-grid scalar turbulent fluxes in the filtered energy and reaction progress variable equations. The sub-grid scale reaction rate can be modelled based on the modelling strategies discussed in Chapter 2. A short discussion is presented in this chapter and a more detailed discussion can be found in Chapter 5, which is dedicated to the modelling of the Sub-Grid-Scale (SGS) reaction rate.

4.1 Large Eddy Simulation

Numerical modelling of turbulent flows usually involves defining the flow properties in terms of the mean and the fluctuation, corresponding to the instantaneous values associated with turbulence. The way these quantities are predicted or calculated will, in general, calibrate the accuracy of the numerical approaches. Large Eddy Simulation (LES) modelling lies between direct numerical simulations (DNS), in which the whole of the turbulence spectrum is resolved, and Reynolds-averaging approaches, in which the Reynolds-averaged Navier-Stokes (RANS) equations are solved in conjunction with a turbulence model to give a solution for the time-averaged flow-field. While DNS gives a high degree of accuracy, the computational requirements are such that, in the foreseeable future, the use of this technique will remain limited to a range of simple, low-Reynolds number flows.

The RANS approach requires computer resources and has been applied to a wide range of

complex flows with varying degrees of success. The accuracy of a RANS simulation depends on how well the flow conforms to the assumptions of the model, and generally model parameters must be 'tuned' if acceptable accuracy is to be achieved. Modelling the whole spectrum of flow turbulence scales poses great difficulty, which was eventually piloted to develop the concept of LES. In the LES approach, the large scales explicitly resolved are in fact equal to those of the DNS large scales and give both an instantaneous and statistical information of the flow, while the effect of small scales are modelled. Since, only the sub-grid, dissipative scales which are usually expected to be universal and homogeneous are modelled, the accuracy of the LES solution is less dependent on the accuracy of the model. Hence, LES demands greater computational resources than RANS, as are involved in resolving the large eddies.

Large eddy simulations (LES) is an extremely powerful and highly reliable modelling technique and has been proved to be so for the last couple of decades, following the pioneering works of Smagorinsky (1963) and the first successful application to turbulent channel flows by Deardorff (1970). Since then, LES has been applied to many fluid flow dynamics domains such as turbulence transition modelling, forecasting weather conditions, understanding the aerodynamics of vehicles and combustion dynamics etc. LES is basically a numerical technique, which separates large eddies from small eddies by the application of a low-pass filtering technique. Also, it is used to solve the partial differential equations responsible for most of the transportation of mass, momentum and energy, and for governing turbulent fluid flow, which is able to predict instantaneous flow characteristics and resolve turbulent flow structures. In LES the large scale motions of the flow are calculated, while the effect of the smaller universal scales are modelled using a sub-grid scale (SGS) model. In order to differentiate small eddies from large ones, a reference or cut-off length has to be determined. Those scales that are of a characteristic size greater than the cut-off length are called large or resolved scales, and the others are called small or Subgrid scales. This means that larger eddies are directly affected by the boundary conditions and must be computed. By contrast, the small-scale turbulence is more nearly isotropic and has universal characteristics; it is thus more amenable to modelling. The difficulty comes from the fact that many parameters contribute to the definition of the effective scale-separation operator. (Ferziger 1977).

LES typically uses non-linear eddy viscosity to model the effect of the SGS, or unresolved turbulence, on the resolved field. Separating the scales in the exact solution into two categories can do this, one is the resolved scale and the other is the subgrid scale as shown in .
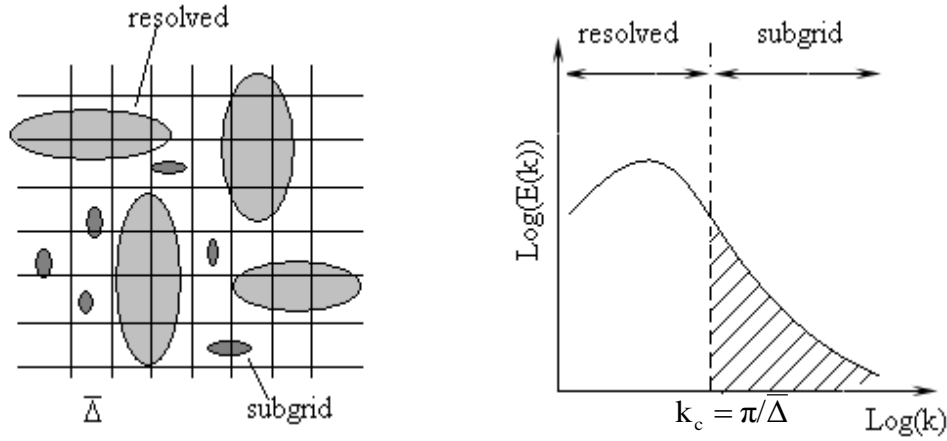
Figure 4.1 Schematic view of the simplest scale separation operator, Sagaut (2006)

The classical Smagorinsky eddy viscosity model, though widely used by turbulence modellers, is found to fail for various reasons. The Smagorinsky model failed to predict the energy backscatter to the resolved scales and was found to have an improper asymptotic behavior regarding the Smagorinsky model coefficient. These failures have been rectified by the development of the dynamic procedure (Germano et al., 1991), which to calculates the Smagorinsky model coefficient using local instantaneous flow conditions, and is detailed in the following sections of this chapter. The procedure typically involves the application of a test filter to the velocity field to extract information from the resolved scales based on the scale similarity ideas of Bardina et al. (1980), which are then used to calculate the coefficient. Ghosal et al. (1995) and Piomelli and Liu (1995) extended this using a localised dynamic procedure to calculate the model coefficient. Moin et al. (1991) extended the Germano dynamic procedure for compressible flows, which has been found to be successful in predicting the model coefficient and energy backscatter, and continues to be used with much remarkable advancement (Kirkpatrick et al., 2003 and Malalasekera et al., 2007).

The other challenge of LES is to separate the large scales from the small ones. This can be achieved by separating the scales in the exact solution by defining a cut-off length based on Ferziger (1977) and Rogallo and Moin (1984) in spectral space, or by applying the spatial filter of Leonard (1979) in physical space. The scales that are of a characteristic size which is greater than the chosen cut-off length are called large or resolved scales, and the others are called small or sub-grid scales (SGS). However, defining the cut-off length and the scale-separation mathematical operator are very difficult tasks in LES. The difficulty comes from the fact that many parameters contribute to the definition of the effective scale-separation operator.

4.2 Spatial Filtering

Scales are filtered either in physical space or spectral space by applying a scale high-pass filter, i.e. low-pass in frequency, to the exact solution. The sub-grid scale fluctuations below the chosen cut-off scale are modelled by assuming they are isotropic. The application of scale separation or spatial filtering in LES can be mathematically represented by a convolution product, first attributable to the work of Leonard (1979), and can be defined for any flow variable $\phi(x, y, z, t)$ to separate large eddies from flow motions as:

$$\bar{\phi}(x, y, z, t) = \int_v G(x - x', y - y', z - z')\phi(x', y', z', t)dx'dy'dz' \tag{4.1}$$

In the above equation G is a filter function, which is associated with the cut-off length Δ in space, generally taken in between Kolmogorov and integral length scales. Eddies of size larger than Δ are classified as large eddies, while those smaller than Δ are classified as small eddies which need to be modelled. The integration is carried out over the entire computational domain v. Selection of the correct spatial filter in equation (4.1) is very important in LES as it must commute with differentiation, once filtered Navier-Stokes equations are developed for the flow field. The most commonly used filter functions are the cut-off filter (Fourier), the Gaussian filter and the box filter as shown below:

I) The cut-off filter is defined as:

$$G(x - x') = \frac{sin[k_c(x - x')]}{k_c(x - x')} \tag{4.1}$$

$$G(k) = \begin{cases} 1 & if \ |k| \leq k_c = \pi/\bar{\Delta} \\ 0 & otherwise \end{cases} \tag{4.2}$$

A cut-off filter is applied in spectral space and is generally known as the ideal low-pass filter, in which flow contributions greater than the cut-off wave number (k_c) are removed without affecting the contributions of the small wave numbers.

II) The Gaussian filter is defined as:

$$G(x - x') = \left(\frac{6}{\pi\bar{\Delta}^2}\right) exp\left(\frac{-6|x-x'|^2}{\bar{\Delta}^2}\right) \tag{4.3}$$

The Gaussian filter, which is generally applied in physical space, is widely used for homogeneous and inhomogeneous turbulence in the direction of homogeneity, often with separate cut-off scales in each direction.

III) The Box or top-hat filter is the other most commonly used implicit spatial filter applied in physical space, with a characteristic cut-off scale of $\bar{\Delta}$, generally defined in terms of grid spacing. Since this filter wipes out the small scales by a filtering operation, this is also considered as a smooth filter and is typically defined as:

$$G(x - x') = \begin{cases} \frac{1}{\bar{\Delta}} & if \ |x - x'| \leq \frac{\bar{\Delta}}{2} \\ 0 & otherwise \end{cases} \tag{4.4}$$

In the present work, the top-hat filter is employed as it naturally fits into the finite volume discretisation. The filtered governing equations in finite volume format can be simply rewritten by the application of the equivalent box filter width of:

$$\bar{\Delta} = (\Delta x \Delta y \Delta z)^{1/3} \tag{4.5}$$

where Δx, Δy and Δz denote the width of a computational cell in the three co-ordinates. The accuracy of LES simulations depends on many factors, and yet the filter width is one of the most important. The choice of the filter width is critical to resolve the appropriate amount of energy in the computational domain. For example, Figure 4.1 illustrates the use of two different filter widths in obtaining the filtered velocity. It is clear that the use of a larger filter width has resulted in a smoother curve compared to that of the smaller filter width.

Using a large filter width may save computational time; however, Figures 4.2 and 4.3 confirm the loss of information while using the large filter width. In a conceptual study, Pope (2004) hypothesises that the solution may reach an intermediate asymptote when the filter width lies within the inertial sub-range. However, using a box filter (equation 4.5) simplifies the difficulty of choosing appropriate cut-off scales, yet is associated with the grid resolution employed. In general, the above filters can be classified into two categories as either implicit or explicit filters. Both filtering approaches have their own advantages and disadvantages. However, most of the LES simulations reported so far have been carried out using the implicit filtering technique (Schumann, 1989), due to its simplicity and ability to fit naturally into the discretisation schemes employed. Another advantage is that the definition of the discrete unknown amounts to an implicit filtering, i.e. any scales smaller than the grid are automatically discarded. This facilitates the implicit filter's ability to fit naturally into the numerical discretisation and the notations look similar to that of the RANS technique.
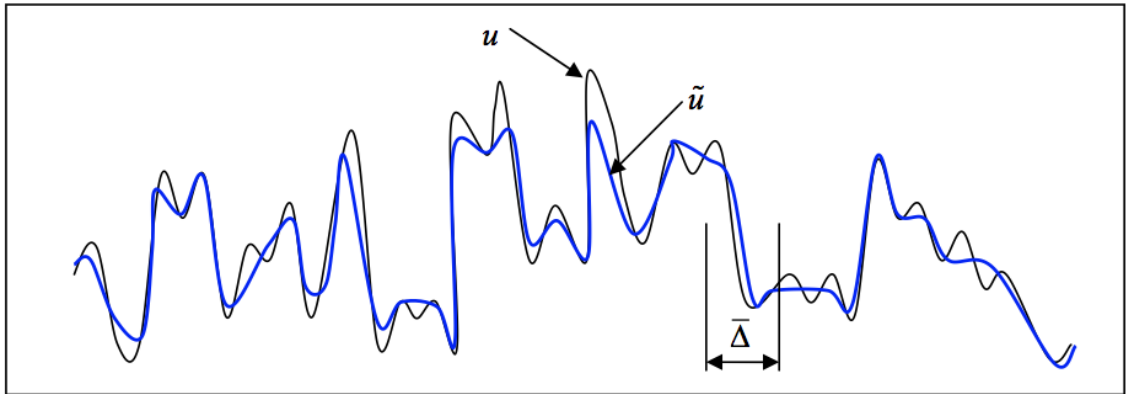
Figure 4.2 Top-hat filter applied on the velocity signal u(x) with a narrow filter.
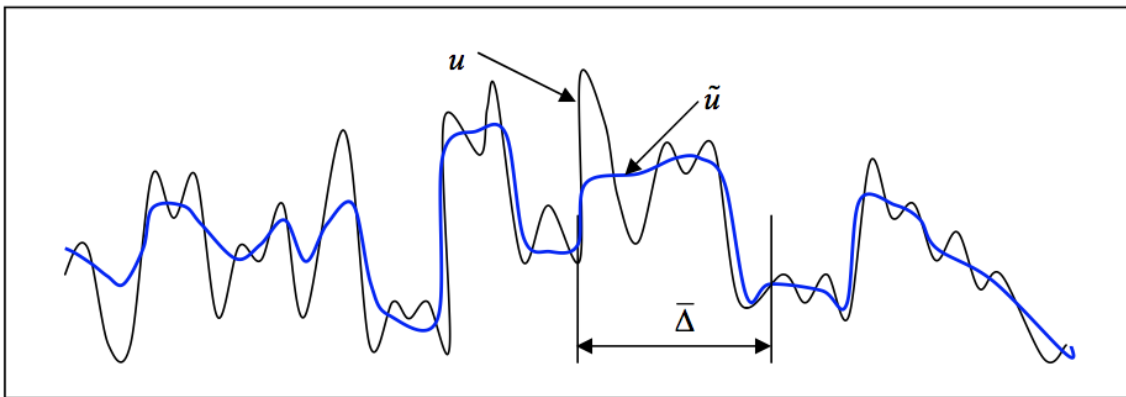
Figure 4.3 Top-hat filter applied on the velocity signal u(x) with a wide filter.

4.2.1 Filtered Governing Equations

As described with regards to the Favre filter in the previous chapter, the turbulent reacting flows are associated with large density variations which must be properly taken into account, and considering these sub-grid density fluctuations in filtered conservation equations seems to be possible by the application of Favre-filtering. Similar to equation (4.1), equation (4.6) shows a Favre, or mass weighted, spatial filter in LES:

$$\bar{\rho}\tilde{\phi}(x,t) = \int_v \rho G(x - x')\phi(x',t)dx' \tag{4.6}$$

Applying equation (4.6) and filtering the conservation equations leads to the Favre-filtered conservation equations, and the Favre-filtered equations are similar to the equations (3.51) to (3.58) shown previously.

The Favre-filtered Continuity equation is given as:

$$\frac{\partial \bar{\rho}}{\partial t} + \frac{\partial (\rho \tilde{u}_i)}{\partial x_i} = 0 \tag{4.7}$$

The Favre-filtered Navier-Stokes equation is given as:

$$\frac{\partial (\bar{\rho}\tilde{u}_i)}{\partial t} + \frac{\partial (\rho \tilde{u}_i \tilde{u}_j)}{\partial x_i} = -\frac{\partial \bar{P}}{\partial x_i} + \frac{\partial}{\partial x_j}\left[2\bar{\mu}\left(\tilde{S}_{ij} - \tfrac{1}{3}\delta_{ij}\tilde{S}_{kk}\right)\right] + \tilde{B}_i - \frac{\partial \tau_{ij}^{sgs}}{\partial x_j} \tag{4.8}$$

where the filtered strain rate tensor $\tilde{S}_{ij}$ is defined as

$$\tilde{S}_{ij} = \frac{1}{2}\left(\frac{\partial \tilde{u}_i}{\partial x_j} + \frac{\partial \tilde{u}_i}{\partial x_i}\right) \tag{4.9}$$

The filtered NS equation given in (4.8) yields an unclosed term, τ_{ij}^{sgs}, due to the decomposition of non-linear convective terms, which must be closed using the models available from simple linear eddy viscosity based on complex second moment closures, where the transport equations are solved. In LES, the term τ_{ij}^{sgs} is generally referred to as the residual stress and represents the impact of the unresolved velocity components on the resolved ones. Mathematically, these terms arise from the non-linearity of the convection term, which does not commute with the linear filtering operation. In the present work, this term is modelled by the widely used, classical Smagorinsky turbulence model based on linear eddy viscosity:

$$\tau_{ij}^{sgs} = \bar{\rho}\overline{u_i'' u_j''} = \bar{\rho}(\widetilde{u_i u_j} - \tilde{u}_i \tilde{u}_j) \tag{4.10}$$

The Favre-filtered Energy equation is given as:

$$\frac{\partial \bar{\rho}\tilde{h}}{\partial t} + \frac{\partial(\bar{\rho}\tilde{u}_j\tilde{h})}{\partial x_j} + \frac{\partial\left(\overline{\bar{\rho}u_j''h''}\right)}{\partial x_j} = \frac{\partial \bar{P}}{\partial t} + 2\bar{\mu}\left(\tilde{S}_{ij} - \frac{1}{3}\delta_{ij}\tilde{S}_{kk}\right)\!:\!\frac{\partial \tilde{u}_i}{\partial x_j} + \frac{\partial}{\partial x_j}\left(\frac{\bar{\mu}}{\text{Pr}}\frac{\partial \tilde{h}}{\partial x_j}\right) + \bar{q}_c \quad (4.11)$$

The above equation (4.11) needs to be closed for SGS scalar fluxes, $\overline{\bar{\rho}u_i''h''} = \bar{\rho}(\widetilde{u_i h} - \tilde{u}_i\tilde{h})$ and the filtered energy source term. The modelling of scalar fluxes is quite a challenge compared to the modelling of momentum fluxes, since they are of a dissipative nature. Also, the SGS residual stresses shown in equation (4.10) are assumed to be isotropic, but SGS scalar fluxes are anisotropic in nature and involve sharp variations due to the large density variations.

The Favre-filtered reaction progress variable equation is given as:

$$\frac{\partial \bar{\rho}\tilde{c}}{\partial t} + \frac{\partial(\bar{\rho}\tilde{u}_j\tilde{c})}{\partial x_j} + \frac{\partial\left(\overline{\rho u_j''c''}\right)}{\partial x_j} = \frac{\partial}{\partial x_j}\left(\frac{\bar{\mu}}{\text{Sc}}\frac{\partial \tilde{c}}{\partial x_j}\right) + \bar{\omega}_c \quad (4.12)$$

The above Favre-filtered reaction progress variable equation outputs two unclosed terms, which are both sides of the last term. The left hand side of the equation is due to the scalar fluxes, similar to the of Navier-Stokes equation, which can be decomposed to $\overline{u_j''c''} = \widetilde{u_j c} - \tilde{u}_j\tilde{c}$. This is often modelled based on the gradient diffusion and turbulent eddy viscosity hypothesis. The other term is the right hand side of the equation of the filtered chemical reaction rate $\bar{\omega}_c$, which represents the SGS mean chemical reaction rate. Because the turbulent flame thickness is thinner than the LES grid and most of the turbulent combustion is a sub-grid phenomenon, it must be accounted for appropriately.

4.3 Modelling of SGS Residual stresses

The modelling of the SGS residual stresses, τ_{ij}^{sgs}, is a primary concern of any SGS model which accounts for the local and instantaneous momentum transportation effects of small scales on large scales and vice versa. It may not always be essential for the SGS models to show the detailed interaction between resolved and small scales, but correct representation of the energy at the correct location is expected. A brief outline of important modelling strategies is given below.

4.3.1 Residual Stress Decomposition

Equation (4.8) shows the sub-grid stress, τ_{ij}^{sgs}, resulting from the commutation of Favre filtering on the convective term of the Navier-Stokes equation, which must be closed by modelling as a function of known resolved values. Ferziger (1982) identified that the models developed following the Leonard decomposition of the velocity field into mean and fluctuating quantities are effective and efficient in accounting for sub-grid scale effects. Hence, the velocity component in the *i* direction can be decomposed as:

$$u_i = \widetilde{u_\iota} + u_i'$$ (4.13)

where u_i' is the sub-grid scale component of u_i. Following on from the above, decomposition of the equation:

$$\widetilde{u_\iota u_j} = \widetilde{\widetilde{u_i}\widetilde{u_j}} + \widetilde{u_i'\widetilde{u_j}} + \widetilde{\widetilde{u_i}u_j'} + \widetilde{u_i'u_j'}$$ (4.14)

Then rearranging the above equation as:

$$\widetilde{u_\iota u_j} = \widetilde{u_i}\widetilde{u_j} + L_{ij} + C_{ij} + R_{ij}$$ (4.15)

where:

$$L_{ij} = \widetilde{\widetilde{u_\iota}\widetilde{u_j}} - \widetilde{u_i}\widetilde{u_j}, \; C_{ij} = \widetilde{u_i'\widetilde{u_j}} + \widetilde{\widetilde{u_\iota}u_j'} \text{ and } R_{ij} = \widetilde{u_i'u_j'}$$ (4.16)

Rewrite equation (4.10) as:

$$\tau_{ij}^{sgs} = \widetilde{u_\iota u_j} - \widetilde{u_\iota}\widetilde{u_j} = \bar{\rho}(L_{ij} + C_{ij} + R_{ij})$$ (4.17)

In the above equation, L_{ij} is the Leonard stress, C_{ij} is the cross stress and R_{ij} is the sub-grid scale Reynolds stress. The Leonard stress represents interactions between the resolved scales that result in sub-grid scale contributions. The cross terms represent interactions between resolved and unresolved scales, whereas the sub-grid scale Reynolds stress represents interaction between the small unresolved scales.

Various approaches (Smagorinsky, 1963, Lilly, 1967, Deardorff, 1970, Schumann, 1975 and Bardina et al., 1980) have been delineated in the literature to model the above stress

terms, based on either explicit or implicit filtered resolved values. Among the available solutions, representation of these turbulent stresses through the use of simplified linear models based on the eddy viscosity approach are well known and widely used. The classical model of this category as introduced by Smagorinsky (1963) gives the historical point of view, and has been subjected to many changes later on. The introduction of the dynamic modelling concept by Germano et al. (1991) has spurred significant progress in the sub-grid scale modelling of non-equilibrium flows (see section 4.5). In dynamic modelling, model coefficients are determined as the calculation progresses, based on the energy contents of the smallest resolved scales rather than input a priori as in the standard Smagorinsky model. A detailed discussion of this method is given in the following section.

4.3.2 The Smagorinsky Model

The Smagorinsky (1963) model was the first to propose an approach that was introduced by Boussinesq (1877), which is a similar model for turbulent stresses using scalar eddy viscosity in LES, and is still widely employed in turbulence modelling today. The Smagorinsky model assumes that the anisotropic part of the residual stress tensor is inline and proportional to the anisotropic part of the resolved strain tensor, while the normal stresses are isotropic. This model assumes that the scales in unresolved turbulence are approximately in equilibrium with energy being cascaded down from the large scales. Hence, the SGS stress tensor, τ_{ij}^{sgs}, can be modelled as:

$$\tau_{ij}^{sgs} - \tfrac{1}{3}\delta_{ij}\tau_{ij}^{sgs} = -2\bar{\mu}_{SGS}\left(\tilde{S}_{ij} - \tfrac{1}{3}\delta_{ij}\tilde{S}_{kk}\right) \tag{4.18}$$

where $\bar{\mu}_{SGS}$ is the eddy viscosity, which can be expressed as a function of the filter size and the strain rate as:

$$\bar{\mu}_{SGS} = \bar{\rho}C\bar{\Delta}^2\left|\tilde{S}\right| \tag{4.19}$$

where $\left|\tilde{S}\right| = \sqrt{2\tilde{S}_{ij}\tilde{S}_{ij}}$ and C is a dimensionless coefficient which often used to be specified in classical models as the Smagorinsky coefficient $C_s = \sqrt{c}$. The isotropic part of the SGS stress tensor in equation (4.18), τ_{ij}^{sgs}, is modelled using the relation of Yoshizawa (1986) as:

$$\bar{\mu}_{SGS} = 2\bar{\rho}C_I\bar{\Delta}^2\left|\tilde{S}\right| \tag{4.20}$$

where the model coefficient C_I is very small and usually expected to be around 0.01. The classical Smagorinsky model is quite simple and widely used, despite having certain drawbacks. One of its major drawbacks is a prior requirement to specify the model coefficient, though it is dependent on local flow conditions. For example, Lilly (1967) suggested a value of $C_s \approx 0.23$ for homogeneous isotropic turbulence, Deardorff (1970) used a value of 0.1 in turbulent channel flow simulations, where as for the same flows Piomelli et al. (1988) found that 0.0065 was an optimal value. Rogallo and Moin (1984) and Germano et al. (1991) identified that the C_s value ranges between 0.1 and 0.25 and there is no general agreement on how it influences the flow.

Over the time period, the model cannot predict the correct asymptotic behavior near a wall and thus requires treatment. Simulations of transitional wall boundary flows show that the model over-damps the flow, leading to incorrect prediction of the growth rates of the initial disturbance. Due to the dissipative nature of the model, Piomelli et al. (1990) identified that the model over-predicts dissipation by 35% in laminar channel flows. Also it has been identified by Piomelli et al., (1990) that it fails to predict the energy transfer from small to large scales, which is generally known as energy backscatter and is important in certain flows. Finally, the model does not vanish in a fully resolved "laminar" flow, even though $\widetilde{u_i \widetilde{u}_j} = \widetilde{u}_i \widetilde{u}_j$.

4.3.3 The Dynamic SGS Flow Model

In order to overcome the limitations outlined in the previous section, several researchers have employed procedures (Ferziger, 1993, Fureby et al., 1997) to calculate the appropriate model coefficient, and these have been found to be in good agreement with the Smagorinsky model. Motivated by its simplicity, Germano et al. (1991) developed a dynamic procedure to calculate the model coefficient, C_s, using local instantaneous flow conditions. The procedure involves the application of a test filter (^) to the equations, and then extraction of information from the smallest resolved scales, which is then used to calculate the coefficient.

This procedure was found to be a great success in predicting the correct model coefficient and was extended to compressible flows by Moin et al. (1991); it used in the present simulations to calculate the model coefficient. The central idea of the dynamic procedure concerns using information from the smallest resolved scales to model the sub-grid scales effects. In order to obtain information from the smallest resolved scales, a test filter is used, generally represented by $\hat{\bar{\Delta}}$, which is larger than the grid filter $\bar{\Delta}$, which is then applied to the velocity field. Application of the test filter to the filtered Navier-Stokes equations results in the sub-test scale stress tensor analogous to the sub-grid-scale stress tensor.

$$T_{ij} = \widehat{\overline{u_i \tilde{u}_j}} - \widehat{\overline{u_i}}\,\widehat{\tilde{u}_j} \tag{4.21}$$

Employing the test filter to equation (4.13) and rearranging it, will result in the resolved turbulent stress as shown below:

$$\mathcal{L}_{ij} = \widehat{\overline{\tilde{u}_i \tilde{u}_j}} - \widehat{\tilde{u}_i}\,\widehat{\tilde{u}_j} \tag{4.22}$$

The resolved turbulent stresses also known as Leonard stresses, represent the contribution of the Reynolds stresses by scales whose length is intermediate between the test and grid filter width. Identifying the relation between equations (4.17), (4.21) & (4.22) and then rearranging them, will result in what is called the Germano identity:

$$\mathcal{L}_{ij} = T_{ij} - \hat{\tau}_{ij}^{sgs} \tag{4.23}$$

The Germano identity in the above equation (4.23) can be used to compute, explicitly, the sub-grid scale stresses at the test and grid levels, T_{ij} and τ_{ij}^{sgs}.

$$T_{ij} - \tfrac{1}{3}\delta_{ij}T_{kk} = -2\bar{\rho}C\hat{\Delta}^2 \left|\hat{\tilde{S}}\right| \left(\hat{\tilde{S}}_{ij} - \tfrac{1}{3}\delta_{ij}\hat{\tilde{S}}_{kk}\right) = -C\alpha_{ij} \tag{4.24}$$

$$\tau_{ij}^{sgs} - \tfrac{1}{3}\delta_{ij}\tau_{kk}^{sgs} = -2\bar{\rho}C\bar{\Delta}^2 |\tilde{S}| \left(\tilde{S}_{ij} - \tfrac{1}{3}\delta_{ij}\tilde{S}_{kk}\right) = -C\beta_{ij} \tag{4.25}$$

where the traceless tensors are given by:

$$\alpha_{ij} = -2\bar{\rho}C\hat{\Delta}^2 \left|\hat{\tilde{S}}\right| \left(\hat{\tilde{S}}_{ij} - \tfrac{1}{3}\delta_{ij}\hat{\tilde{S}}_{kk}\right) \tag{4.26}$$

$$\beta_{ij} = -2\bar{\rho}C\bar{\Delta}^2 |\tilde{S}| \left(\tilde{S}_{ij} - \tfrac{1}{3}\delta_{ij}\tilde{S}_{kk}\right) \tag{4.27}$$

Substituting equation (4.24) and (4.25) into the anisotropic part of equation (4.23) will give:

$$\mathcal{L}_{ij}^a = C\left(\hat{\beta}_{ij} - \alpha_{ij}\right) \tag{4.28}$$

A scalar equation for the model coefficient C, obtained by the above equation and contracted with the $\tilde{S}_{ij}$ tensor, is given as:

$$C = \frac{\mathcal{L}_{ij}^{a}\tilde{S}_{ij}}{(\hat{\beta}_{ij}-\alpha_{ij})\tilde{S}_{ij}} \qquad (4.29)$$

The equation above can obtain C, but the fact that the terms within the bracket could become zero, may create a problem. To overcome this problem, C was considered to vary in only the y-direction, normal to the wall. As this equation is a tensor, it can only be satisfied in some average sense, which can be carried in the y-direction where the test filter is not applied. This results in the expression for C being given as:

$$C(y,t) = \frac{\left(\mathcal{L}_{ij}^{a}\tilde{S}_{ij}\right)_{y}}{\left(\hat{\beta}_{ij}\tilde{S}_{ij}-\alpha_{ij}\tilde{S}_{ij}\right)_{y}} \qquad (4.30)$$

Since, equation (4.28) is a set of five independent equations, it is rare for a single value of C to be obtained simultaneously. To assuage the situation, Lilly (1992) proposed a tensor M_{ij} instead of $\tilde{S}_{ij}$ in equation (4.28), which locally minimises the sum of the square of residuals as:

$$\mathcal{L}_{ij} = \tfrac{1}{3}\delta_{ij}\mathcal{L}_{kk} = 2CM_{ij} \qquad (4.31)$$

where $M_{ij} = \left(\hat{\bar{\Delta}}/\bar{\Delta}\right)^{2}\hat{\bar{\rho}}\left|\hat{\bar{S}}\right|\hat{\bar{S}}_{ij} - \widehat{\bar{\rho}|\bar{S}|\bar{S}}_{ij}$, which is obtained by explicitly evaluating the stressor at the test scale, and comparing locally by subtracting the test-scale average of equation (4.25) from (4.24). Rearranging equation (4.31) for C yields:

$$C = \frac{\mathcal{L}_{ij}M_{ij}-\tfrac{1}{3}\mathcal{L}_{ll}M_{mm}}{2\bar{\Delta}^{2}\left(M_{ij}M_{ij}-\tfrac{1}{3}M_{ll}M_{mm}\right)} \qquad (4.32)$$

Hence, the Smagorinsky model coefficient can be obtained using the dynamic procedure at every spatial grid point and time by considering the localised flow conditions, which have the correct behavior near to a solid wall and in laminar flow and also allows for energy backscatter. However, the model coefficient was found to fluctuate in space and time, and some form of averaging is usually required to avoid stability problems. Typically, L_{ij} and M_{ij} are averaged in spatially homogeneous directions in space. This requires the flow to have at least one homogeneous direction. However, if there is no direction in which to perform averaging, alternative approaches may be used, such as the localised models of Ghosal et al. (1992) and Piomelli and Liu (1995), the dynamic mixed models of Zang et al.

(1993) and the relaxation procedure of Breuer and Rodi (1994) i.e. the co-efficients from the previous time step are used.

4.3.4　Scale Similarity Models

Bardina (1980) first proposed the concept of the scale similarity and this was expected to overcome the previously mentioned drawbacks of the eddy viscosity models. The key idea of scale similarity is to identify and correlate the smallest resolved scales to the sub grid scales of the flow. Filtering the decomposed velocity component in equation (4.13) gives:

$$\bar{u}_i' = \bar{u}_i - \bar{\bar{u}}_i \tag{4.33}$$

This can reasonably be estimated to be equal to the largest contributions of u_i' and the smallest i contributions of $\bar{u}_i$. Furthermore, this equality will facilitate velocity decompositions such that:

$$\overline{u_i u_j} \approx \overline{\bar{u}_i \bar{u}_j} \ and \ \overline{u_i' \bar{u}_j} \approx \bar{u}_i' \bar{\bar{u}}_j \tag{4.34}$$

which in turn facilitates the to modelling of the residual stress given in equation (4.17) as:

$$\tau_{ij}^{sgs} = \rho \left\{ \underbrace{\overline{\bar{u}_i \bar{u}_j} - \bar{\bar{u}}_i \bar{\bar{u}}_j}_{L_{ij}} + \underbrace{K_C \left[(\bar{u}_i - \bar{\bar{u}}_i)\bar{\bar{u}}_j + (\bar{u}_j - \bar{\bar{u}}_j)\bar{\bar{u}}_i \right]}_{C_{ij}} + \underbrace{K_R (\bar{u}_i - \bar{\bar{u}}_i)(\bar{u}_j - \bar{\bar{u}}_j)}_{R_{ij}} \right\} \tag{4.35}$$

where the model coefficients K_C and K_R in the above equation should be carefully chosen such that the expression observes Galiean (Zang etal., 1993, Salvetti and Banerjee, 1995 and Horiuti, 1997). The scale similarity models (SSM) allow back scatter, as the transfer of energy from small to large scales, and does not impose alignment between the SGS stress tensor and the strain rate. Piomelli etal. (1996) identified that the scale similarity models in conjunction with the dynamic procedure perform quite well for low order finite difference or finite volume methods.

4.4 Modelling of SGS Scalar Fluxes

Modelling sub-grid scalar fluxes in turbulent reacting flames is highly challenging due to their non-linear relation with chemical and thermodynamic states. The major difficulty in modelling is due to the anisotropic behaviour of scalar fluxes. This is strongly affected by the turbulent velocity fields, through the large increase in specific volume and viscosity, which causes large temperature rises in reacting flows. Modelling could be further complicated due to the large pressure gradients and density variations associated with heat release, which may cause non-gradient transport (NGT) or counter gradient diffusion.

Several models are available in the literature to account for SGS scalar fluxes, such as the simple gradient transportation assumption, the scale similarity model (Fureby and Möller, 1995), the linear eddy model (LEM) (Kerstein, 1991) etc. In a recent LES analysis, Boughanem and Trouvé (1998) revealed that the gradient or counter gradient diffusion of scalar fluxes are observed to be similar to RANS. However, unresolved scalar fluxes are identified to be less in LES, which supports the idea that the use of the simple model will have fewer consequences on the end solution. To support this observation, Boger and Veynante (2000) performed LES of turbulent premixed flames on a V-shaped flame holder using the simple gradient transport assumption, and were able to recover counter gradient transport at resolved scales without any extra effort, which is not the situation in RANS. Hence, in the present simulations the simple gradient transport model in equations (4.12) and (4.13) for scalar fluxes is adopted. Hence:

$$\bar{\rho}\overline{u_j'' h''} = \frac{\bar{\mu}_{SGS}}{\mathrm{Pr}_t}\frac{\partial \tilde{h}}{\partial x_j} \tag{4.34}$$

$$\bar{\rho}\overline{u_j'' c''} = \frac{\bar{\mu}_{SGS}}{\mathrm{Sc}_t}\frac{\partial \tilde{c}}{\partial x_j} \tag{4.35}$$

where Pr_t is the turbulent flow Prandtl number, Sc_t is the turbulent flow Schmidt number and $\bar{\mu}_{SGS}$ is the SGS eddy viscosity.

4.5 Modelling of The Chemical Reaction Rate

Modelling the chemical reaction rate is another challenging task in LES premixed turbulent combustion for explosions, as it is generally involved in complex thermo-chemical-turbulence interactions. One major difficulty is predicting the random, non-linear behaviour of the chemical reaction rate as a function of the available scalar variables. Another challenge, especially in the LES of the laminar flame thickness, which is typically thinner than the characteristic flow turbulence length, is that the scale is much smaller than a typical LES filter width. Hence it is a prerequisite of any SGS combustion model in LES, to address the above issue with an accurate, yet computationally efficient model. One way of modelling the filtered mean chemical reaction rate term is by solving the transport equations of the detailed or reduced chemical kinetic mechanism of the fuel. This generally includes tens of species and several hundred elementary reactions. Solving these transport equations directly in RANS itself is quite complex and solving them in LES is impossible. Nevertheless, several alternative strategies are available to implement the detailed chemistry effects. These include techniques such as the following: the "skeletal mechanism" obtained due to the elimination of inconsequential species from the detailed chemical mechanism, "dimension reduction techniques" due to low-dimensional manifold systems such as QSSA (quasi-steady state assumption), RCCE (rate-controlled constrained equilibrium) FPI (flame propagation of intrinsic low-dimensional manifold), "storage and retrieval systems" such as look-up tables, repro-modelling, artificial neural network (ANN), in situ adaptive tabulation (ISAT), piecewise reusable implementation of solution mapping (PRISM) finally, adaptive chemistry technique. All of the above techniques require extraordinary computational resources.

However, the mean chemical reaction rate term can be simply modelled by considering a single step, irreversible chemistry, which is widely used due to the long turbulent time scales compared to the chemical time scale (Bray, 1981) in turbulent premixed combustion for explosion and greatly reduces the complexity of the whole system of equations. Several modelling strategies are available and the briefly delineated in section 2.2. For example the laminar flamelet based models gained wide attention due to their flexibility in decoupling chemistry from turbulence. There has been some recent interest in FSD models as they are fundamentally based on the laminar flamelet concepts, which view the reaction zone as a

collection of propagating reaction layers thinner than the smallest scales of turbulence and where the laminar flame structures propagate locally at the laminar burning velocity. The FSD, defined as the local flame surface area per unit volume, may be computed using either an algebraic model or by solving a transport equation for the FSD. Algebraic models are simple, yet well established and are similar to the Bray-Moss-Libby (BML) approach in the context of RANS. These models are considered in the present study to account for the filtered mean chemical reaction rate term with a dynamic formulation for the flame surface density, which is described in Chapter 5.

4.6 Summary

This chapter summarises the use of the LES concept for turbulent premixed flames. A brief history of the LES, and the developments initiated since Smagorinsky (1963) have been detailed. The spatial filtering technique distinguishes LES from other modelling techniques, and has been discussed with a variety of filters. Compression of the implicit and explicit filtering was briefly discussed and applied to the governing equations described in the previous chapter. Modelling strategies to close the resulting unclosed terms from the Favre-filtered governing equation were discussed. For momentum fluxes, classical and dynamic modelling techniques were described. More details of chemical reaction rate model development is discussed in the next chapter.

Chapter 5　The Combustion Model

The turbulent premixed combustion model, based on the Flame surface density (FSD) approach to LES, is presented and discussed in this chapter. Knikker et al. (2004) have made efforts in developing a dynamic formulation for the FSD of premixed turbulent flames. Gubba et al. (2007) has implemented and validated a dynamic flame surface density (DFSD) model in an LES code PUFFIN (Kirkpatrick et al, 2003) developed jointly with the university of Sydney. The FSD models are well established in the context of LES and are the subject of many interesting developments. The present work is carried out by implementing and validating the DFSD model for explosions with different solid shapes and using the modified version of the combustion chamber. In this chapter, a brief introduction to the flamelet and flame surface density concepts is given. A short survey of the available algebraic models and the exact transport equation of FSD in LES are described in this section. Details of a simple algebraic FSD model derived based on DNS data and its use with a self-scaling model coefficient are explained in section 5.2. Section 5.3 presents the concept and development of the dynamic FSD (DFSD) model, together with the dynamic evaluation of the fractal dimension and the flame wrinkling theory of Weller et al. (1998). Finally, section 5.4 provides brief details of the fractal concept and the empirical and dynamic fractal models used in the present simulations to calculate the fractal dimensions of turbulent premixed flames. The available outer and inner cut-off scale models and their choice in the present work are also presented and discussed.

5.1 Introduction of FSD Modelling

The concept of Flame Surface Density (FSD) models in RANS was well established but relatively new in the LES framework. The FSD models proposed in this work are similar to those of RANS and can be derived from the laminar flamelet fundamentals. Many of the turbulent premixed applications are based on the laminar flamelet assumptions; the reaction flame front is viewed as a collection of asymptotically thin, wrinkled, propagating layers between fresh and burnt gases. At the limit of a high Damköhler number, these layers can be assumed to propagate at local laminar flame speed. Hence, these layers can be

considered as laminar flamelets. The concept of the laminar flamelet in turbulent premixed combustion greatly reduces the complexity of the problem by decoupling turbulence form chemistry. Following the laminar flamelet concept, the wrinkling of the flame front surface by turbulence can be described by the mean flame-surface area per unit volume i.e. flame surface density, Σ. Hence, the filtered mean chemical reaction rate in equation (4.12) can be expressed as a function of the FSD, Σ given as:

$$\overline{\dot{\omega}_c} = R\bar{\Sigma} = (\rho_u S_d)_s \bar{\Sigma} \tag{5.1}$$

In equation (5.1), R is expressed as $(\rho_u S_d)_s$, which is the surface averaged, Favre filtered displacement speed of the propagating flame into the fresh gases. Assuming that the individual flamelet is propagating with the laminar flame speed u_L, into the fresh gases having density ρ_u, the mean reaction rate can be modelled as $\rho_u u_L$.

The filtered FSD, $\bar{\Sigma}$ in the above equation is accounted for via either solving a transport equation, known as the Σ equation or by using an empirical algebraic expression. The Σ transport equation was first formulated by Marble and Broadwell (1977) and further developed by Pope (1988). The transport equation developed by Pope (1988) is based on filtering the basic equation with a filter width sufficiently larger than the grid spacing such that the thin turbulent dynamic premixed flame is smeared out sufficiently to be resolved on an LES grid. Hawkes and Cant (2001) provided a transport equation for FSD, similar to the typical RANS equation, which includes resolved contributions neglected by the typical RANS equations. However, this equation has resulted in several unclosed terms, leading to excessive computational requirements (reaching the DNS limit for fully resolved flows (Pitsch, 2005)) during computation. The exact, unclosed equation proposed by Hawkes and Cant (2001) is presented below and its details are available in the original publication, given as:

$$\frac{\partial \Sigma}{\partial t} + \frac{\partial (\tilde{u}_i \Sigma)}{\partial x_i} + \frac{\partial \{\langle (\bar{u}_i)_s - \tilde{u}_i \rangle \Sigma\}}{\partial x_i} = \overline{(a_T)_s} \Sigma - \frac{\partial \overline{\langle (wN_i)_s \rangle \Sigma}}{\partial x_i} + \overline{\left(w \frac{\partial N_k}{\partial x_k} \right)_s} \Sigma \tag{5.2}$$

FSD can be alternatively modelled by an empirical algebraic model, by considering the balance between the production and the destruction of the flame surface density in the transport equation. Boger et al. (1998) were the first to develop a simple algebraic model for

FSD in LES, based on the widely used DNS database of infinitely thin planar flames using a Gaussian filter. This model is simple and very similar to the BML model in the context of RANS. This model has been used by several researchers to model turbulent premixed flames (see for example; Kirkpatrick et al. (2003), Masri et al. (2006) and Richard et al. (2007)), and is given as:

$$\bar{\Sigma} = 4\frac{\tilde{c}(1-\tilde{c})}{L_{\Sigma}} \tag{5.3}$$

where $\tilde{c}$ is the filtered reaction progress variable and L_{Σ} refers to the flame wrinkling scale formulated as $\bar{\Delta}/\beta$. The model coefficient, β in the above equation can be either considered as a constant or modelled based on a flame wrinkling factor.

Another model similar to the BML and EBU expressions proposed by Charlette et al. (1999), including a term to account for the resolved flame surface density, can be given as:

$$\bar{\Sigma} = |\nabla\bar{c}| + a\Gamma_k\left(\frac{\delta_L}{\bar{\Delta}}, \frac{\sqrt{2k/3}}{u_L}\right)\frac{\sqrt{k}}{u_L}\frac{\tilde{c}(1-\tilde{c})}{L_{\Sigma}} \tag{5.4}$$

where Γ_k is the efficiency function of the Intermittent Turbulence Net Flame Stretch (ITNFS) model of Meneveau and Poinsot (1991), k is the sub-grid kinetic energy and a is a model constant.

Angelberger et al., (1998) proposed another model based on sub-grid RMS fluctuations which is expressed as:

$$\bar{\Sigma} = |\nabla\bar{c}| + a\Gamma_k|\nabla\bar{c}|\left(\frac{\delta_L}{\bar{\Delta}}, \frac{u'}{u_L}\right)\frac{u'}{u_L} \tag{5.5}$$

Weller et al. (1998) and Tabor and Weller (2004) used an additional equation to solve for the flame surface wrinkling factor, Ξ in their work as follows:

$$\Xi = \frac{\bar{\Sigma}}{|\nabla\bar{b}|} \tag{5.6}$$

where $|\nabla\bar{b}|$ is the area of the grid scale surface and the flame surface density is derived using the conditional filtering method.

Knikker et al. (2004) proposed a dynamic flame surface density model following their *a priori* work (Knikker et al., 2002) in deriving a mathematical formulation for LES. Although this model was never implemented numerically, it was tested on the data extracted from experimental OH images and found to work well with LES. The work presented in this thesis is carried out by employing two different models for Σ, the first is a simple algebraic FSD (AFSD) model (i.e. equation 5.3) and the second is a dynamic FSD (DFSD) model described in the following sections. Details of the numerical implementation of the DFSD model are provided in Chapter 7.

5.2 The Algebraic Flame Surface Density (AFSD) Model

As introduced in the above section, Boger et al. (1998) were the first to deduce an algebraic expression for FSD for use in LES codes. A 3-D DNS database developed by Boughanem and Trouvé (1998) has been used for decaying isotropic, homogeneous turbulence, with the assumption of an evolving thin flame front into the fresh gases. The key idea behind their expression is in identifying the sub-grid surface density, Σ (i.e. the sub-grid flame surface per unit volume) of the flame surface defined by $c = c^*$ and the conditionally averaged displacement speed of the propagating flame of the surface c^* into the fresh gases, $\overline{(R)}_s$ as:

$$\bar{\Sigma} = \int_{-\infty}^{\infty} |\nabla \bar{c}| \delta(c - c^*) G(x - x') dx' \tag{5.7}$$

$$\overline{(R)}_s = (\rho_u S_d) \tag{5.8}$$

A generalised sub-grid flame surface density and displacement speed, which do not depend on a specific c^* isosurface, are defined as:

$$\Sigma_{gen} = \int_1^0 \bar{\Sigma} \, dc^* = \overline{|\nabla c|} \tag{5.9}$$

$$(R)_s = \frac{1}{\Sigma_{gen}} \int_1^0 \overline{(R)}_s \, dc^* = \frac{\overline{R|\nabla c|}}{\Sigma_{gen}} \tag{5.10}$$

Following the laminar flamelet concepts, and assuming the reaction zone to be very thin, the sub-grid flame surface density Σ of $c = c^*$ isosurface is no longer dependent on the isosurface chosen and becomes equal to the generalised flame surface density Σ_{gen}. The

displacement speed $(R)_s$ can be approximated as $\rho_u u_L$ by considering that the laminar flamelets are steadily propagating. Boger et al. (1998) have validated this approximation for turbulent premixed combustion by filtering the DNS data. The laminar flame speed in the above equation is calculated by the following expression of Metghalchi and Keck (1980) and Metghalchi and Keck (1982), which accounts for the effects of local pressure and temperature, and is given as:

$$u_L = u_L^o \left(\frac{T_R}{T_o}\right)^{\alpha_1} \left(\frac{P}{P_o}\right)^{\beta_1} \tag{5.11}$$

where u_L^o is the reference or un-strained laminar burning velocity taken as being 0.45 m/s for a stoichiometric propane/air mixture, T_o and P_o are the reference temperature and pressure of 298.15 K and 1.01 bar respectively, T_R is the reactant temperature, and α_1, β_1 are constants calculated from the following expressions of Metghalchi and Keck (1980) and Metghalchi and Keck (1982), and can be given as:

$$\alpha_1 = 2.18 - 0.8(\phi - 1.0) \tag{5.12}$$

$$\beta_1 = -0.16 + 0.22(\phi - 1.0) \tag{5.13}$$

where ϕ is the mixture equivalence ratio. However, Poinsot et al. (1995) identified that the process of filtering will average the effects of variations in the flame strain and the curvature on the flame speed.

Boger et al. (1998) chose $c^* = 0.8$ to define the flame surface and introduced a reduced progress variable, c_{red} which is 0 if $c \leq c^*$ otherwise it is 1. Accordingly, they extracted a simple expression for $\bar{\Sigma}$ from DNS:

$$\bar{\Sigma} = 4\alpha_2 \frac{\tilde{c}_{red}(1 - \tilde{c}_{red})}{\bar{\Delta}} \tag{5.14}$$

where α_2 is the model coefficient, analytically derived by assuming an infinitely thin flame front (i.e. $|\nabla c| = \delta(c - c^*)$):

$$\alpha_2 = \sqrt{\frac{6}{\pi}} \, \Xi \tag{5.15}$$

In the above expression, α_2 becomes 1.4 for a unity sub-grid scale flame wrinkling factor, Ξ. Alternatively, Boger et al. (1998) proposed another expression similar to equation (5.14) by replacing c_{red} with c, which is the instantaneous value of the reaction progress variable:

$$\bar{\Sigma} = 4\beta \frac{\tilde{c}(1-\tilde{c})}{\bar{\Delta}} \tag{5.16}$$

where β is a model coefficient which has a value equal to α_2 in equation (5.14) for sufficiently large values of $\bar{\Delta}/L_f$, i.e. infinitely thin flames compared to the grid width. The above expression has a similar format to as the Bray-Moss-Libby (BML) expression for flame surface density in RANS (Bray et al., 1989) and only accounts for the so called resolved contributions. The ratio $\Delta/4\beta$ represents the wrinkling length scale of the sub-grid flame surface.

Normally, the model coefficient β is not universal and is known to be dependent on many physical parameters such as grid resolution, turbulence levels and chemistry. A range of values for the model coefficient, β, in RANS and LES ranging from 1.0 to 2.6 can be found in the literature. Hence, choosing a constant value for β resembles the Eddy-Break-Up (EBU) model in RANS, which is inappropriate and alters the solution based on model the coefficient. To avoid the problems associated with selecting a value for β, it can be solved by the following two options:

    I.   Choosing a constant value either by doing parametric studies based on appropriate filter width and chemistry or iterating/tuning in order to get the qualitative agreement with experimental values.

    II.   Deriving a self-scalable model for the model coefficient β using local flame characteristics.

As in the first option above, we can use a constant value for β. However, fine-tuning to achieve the desired results in LES is inadvisable. Hence, this has been carried out initially using a constant value for β from the parametric studies of Kirkpatrick (2002) and Masri et al. (2006), who derived a simple expression capable for use as a self-scale model coefficient based on the local flow conditions as shown in next section.

5.2.1 Modelling β coefficient using a flame Wrinkling Factor

The model coefficient, β, can be modelled using a wrinkling flame factor as observed in equation (5.15) rather than choosing unity. The sub-grid flame wrinkling factor Ξ in equation (5.15) is defined as the ratio between the flame surface density and its projection in the normal direction of the flame propagation (Knikker et al., 2004). Identifying the flame surface as a fractal surface between the inner and outer cut-off scales leads to:

$$\Xi = \left(\frac{\bar{\Delta}}{\delta_c}\right)^{D-2} \tag{5.17}$$

In the above equation, Δ is the filter width considered as the outer cut-off scale, δ_c is the inner cut-off scale and D is the fractal dimension. In deriving the fractal dimension in equation (5.17), we have used an empirical relation (see section 5.4.1) based on sub-grid velocity fluctuations, which is based on the fractal properties of the sub-grid flame surface area (Kronenburg and Bilger, 2001). However, it has not yet been experimentally determined whether the sub-grid flame surface area is fractal or not, since the flame wrinkling process may not be scale-independent. However, this approach has been implemented successfully in the thickened flame modelling (Charlette et al., 2002). The critical assumption involved in choosing such an expression for the wrinkling flame factor is that vortices of all sizes between the outer and inner cut-off scales contribute to the wrinkling of flame surfaces. In general, the outer cut-off length represents the largest eddies of integral length scales and the inner cut-off length represents eddies of the size of Kolmogorov length scales. In LES, the filter width, Δ, is generally considered as the outer cut-off scale and for the inner cut-off scale there are several expressions available in the literature related to the Gibson scale, the Kolmogorov scale, or the laminar flame thickness as discussed in section 5.4.3. The inner cut-off scale is assumed to be equal to three times the laminar flame thickness following the work by Knikker et al. (2004). Hence, β is calculated as:

$$\beta = \sqrt{\frac{6}{\pi}}\,\Xi = \sqrt{\frac{6}{\pi}}\left(\frac{\bar{\Delta}}{\delta_c}\right)^{D-2} \tag{5.18}$$

5.3 The Dynamic Flame Surface Density (DFSD) Model

The limitation of the AFSD model, as outlined in the above section, is that it can only account for the resolved contributions, using a model constant which is not universal. To overcome this limitation, Hawkes (2000) proposed a dynamic model for the flame surface density, and Knikker et al. (2002) developed a conceptual similarity FSD model, involving a combination of the test filter application and similarity ideas (Bardina et al. 1980) to account for the SGS reaction rate. This approach has been coupled with the fractal theory to identify the flame surface as a fractal surface and to determine the model constant, C_s, which is given in equation (5.32) below. However, this model has failed to determine the fractal dimension, D. The similarity FSD model has been tested against experimental data published by Nottin et al. (2000). The data were extracted from OH images obtained from planar laser-induced fluorescence (PLIF) measurements of propane/air turbulent premixed flames. The FSD model was successful in predicting the specific regions where the sub-grid scale contribution to the flame surface density is high. However, this model failed to calculate the fractal dimension dynamically, which resembles the failure of the AFSD model in using the constant model coefficient.

To overcome this limitation, a DFSD model has been developed by Knikker et al. (2004). The main idea is based on modelling the unresolved FSD by applying the Germano identity (4.23) to the flame surface density, and modelling the fractal dimension dynamically. In this approach, a flame wrinkling factor, Ξ, is introduced as a ratio of the flame surface density to its projection in the normal direction of the flame propagation as:

$$\Xi = \frac{\int_v |\nabla c| G(x-x')dx'}{N \cdot \int_v |\nabla c| n G(x-x')dx'} = \frac{\overline{|\nabla c|}}{|\nabla \bar{c}|} = \frac{\bar{\Sigma}}{|\nabla \bar{c}|} \tag{5.19}$$

where n and N are the normal vectors to the instantaneous c and to the filtered $\bar{c}$ isosurface pointing towards the unburnt gases. Knikker et al. (2004) identified that the gradient of the filtered progress variable $|\nabla c|$ becomes zero due to the highly wrinkled nature of the flame front. To avoid this problem, they assumed the flame to be locally planar and to be an infinitely thin surface. They defined a sharp progress variable c_l using the Heaviside function and expressed $|\nabla \bar{c}|$ as $|\nabla \bar{c}_l| = \Pi(\bar{c}_l, \bar{\Delta})$, which becomes zero only far away from the flame front. This facilitates the redefinition of the flame wrinkling factor, Ξ, as:

$$\Xi = \frac{\overline{\Sigma}}{\Pi(\bar{c},\overline{\Delta})} \tag{5.20}$$

Knikker et al. (2004) coupled the above equation with fractal theory to identify the flame surface as a fractal surface between the inner and outer cut-off scales. In the present analysis, Δ and δ_c are considered as the outer and inner cut-off scale respectively. Hence, the wrinkling factor at the outer cut-off scales can be presented as:

$$\Xi(\overline{\Delta}) = \left(\frac{\overline{\Delta}}{\delta_c}\right)^{D-2} \tag{5.21}$$

In this approach, the term of the mean filtered flame surface density $\overline{\Sigma} = \overline{|\nabla c|}$ (in equation 5.19), can be split into two terms as resolved and unresolved:

$$\overline{\Sigma} = \overline{|\nabla c|} = \underbrace{\Pi(\bar{c},\overline{\Delta})}_{Resolved} + \underbrace{f\left(\bar{c},\overline{\Delta},\Pi(\bar{c},\overline{\Delta})\right)}_{Unresolved} \tag{5.22}$$

The resolved term in the above equation is evaluated using the expression given by Knikker et al. (2002), and the unresolved term is calculated as:

$$\lambda = \overline{\Sigma} - \Pi(\bar{c},\overline{\Delta}) = \overline{|\nabla c|} - \Pi(\bar{c},\overline{\Delta}) \tag{5.23}$$

γ can be defined as a ratio of the test filter to the grid filter, i.e. $\hat{\overline{\Delta}}/\overline{\Delta}$, such that the test filter $\hat{\overline{\Delta}}$ is greater than the grid filter $\overline{\Delta}$. Applying the test filter to the flame surface density (5.22) leads to:

$$\hat{\overline{\Sigma}} = \widehat{\overline{|\nabla c|}} = \underbrace{\Pi\left(\hat{\bar{c}},\hat{\overline{\Delta}}\right)}_{Resolved@testfilter} + \underbrace{\left[\widehat{\overline{|\nabla c|}} - \Pi\left(\hat{\bar{c}},\hat{\overline{\Delta}}\right)\right]}_{Unresolved@testfilter} \tag{5.24}$$

From the above equation, the unresolved flame surface density contributions at the test filter level can be written as:

$$\Lambda = \left[\widehat{\overline{|\nabla c|}} - \Pi\left(\hat{\bar{c}},\hat{\overline{\Delta}}\right)\right] \tag{5.25}$$

Following the similarity ideas (Bardina et al., 1980), assuming that the sub-grid scale contribution of the unresolved flame surface density at the test filter is the same as that at the grid filter, and relating λ and Λ by using the Germano identity (Germano et al., 1991) leads to:

$$\Lambda - \hat{\lambda} = \left[\widehat{\overline{|\nabla c|}} - \Pi\left(\hat{\bar{c}},\hat{\overline{\Delta}}\right)\right] - \left[\widehat{\overline{|\nabla c|}} - \widehat{\Pi(\bar{c},\overline{\Delta})}\right] \tag{5.26}$$

$$\Lambda - \hat{\lambda} = \left[\widehat{\Pi(\bar{c},\bar{\Delta})} - \Pi\left(\hat{\bar{c}},\hat{\bar{\Delta}}\right) \right] \tag{5.27}$$

The sub-grid scale flame surface density contributions from the above equation can be added to the resolved flame surface density (5.24) with a model coefficient C_s in order to obtain the total flame surface density. Hence the flame surface density can be expressed as:

$$\bar{\Sigma} = \Pi(\bar{c},\bar{\Delta}) + C_s \left[\widehat{\Pi(\bar{c},\bar{\Delta})} - \Pi\left(\hat{\bar{c}},\hat{\bar{\Delta}}\right) \right] \tag{5.28}$$

Using equation (5.20) & (5.21), the two terms in the unresolved equation (5.28) may be expressed as:

$$\widehat{\Pi(\bar{c},\bar{\Delta})} = \hat{\bar{\Sigma}} \left(\frac{\bar{\Delta}}{\delta_c} \right)^{D-2} \tag{5.29}$$

$$\Pi\left(\hat{\bar{c}},\hat{\bar{\Delta}}\right) = \hat{\bar{\Sigma}} \left(\frac{\hat{\bar{\Delta}}}{\delta_c} \right)^{D-2} \tag{5.30}$$

The above terms can be combined with the similarity concept in order to derive the model coefficient C_s:

$$C_s = \frac{\widehat{\Pi(\bar{c},\bar{\Delta})} - \Pi\left(\hat{\bar{c}},\hat{\bar{\Delta}}\right)}{\Pi\left(\hat{\bar{c}},\hat{\bar{\Delta}}\right) - \Pi\left(\hat{\hat{\bar{c}}},\hat{\hat{\bar{\Delta}}}\right) - \widehat{\widehat{\Pi(\bar{c},\bar{\Delta})}} + \widehat{\Pi(\bar{c},\bar{\Delta})}} \tag{5.31}$$

The above equation can be simplified by using equation (5.30) by identifying the sub-grid scale flame surface as a fractal surface (Knikker et al., 2004) as:

$$C_s = \frac{1}{1 - \gamma^{2-D}} \left[\left(\frac{\bar{\Delta}}{\delta_c} \right)^{D-2} - 1 \right] \tag{5.32}$$

In the above equation, δ_c is the lower cut-off scale, taken to be equal to three times of the laminar flame thickness following Knikker et al. (2004). The fractal dimension, D, can be calculated using either the empirical relation (North and Santavicca, 1990 and Fureby et al., 2005) described in section 5.4.1, or calculated dynamically by similarity to Germano identity with the fractal theory for wrinkled flames as in section 5.4.2.

The above model for C_s with the fractal model described in section 5.4.1 has been tested by Knikker et al. (2004) for experimentally extracted data of PLIF-OH images (Nottin et al., 2000). Good predictions were obtained for the global mean flame surface density together with realistic values for the fractal dimension. In the Gubba et al. (2007) investigation, this

dynamic flame surface density model is implemented in an in-house LES code PUFFIN (Kirkpatrick, 2002) and the numerical predictions are validated against some of the experimental data from a laboratory scale premixed combustion chamber.

5.4 Modelling of the Fractal Dimension

In this section, two models, based on the classical fractal theory, are presented and discussed to examine the fractal nature of turbulent premixed flames. Since the successful introduction of the fractal theory by Mandelbrot (1975) in homogeneous, isotropic turbulence, fractal concepts have been widely used for various diverse applications (Batty, 1985). The application of the fractal concept to turbulent premixed flames has been a subject of interest, while understanding the flame structure has been examined by many researchers such as Gouldin (1987) and Kerstein (1988). Gouldin (1987) characterised the turbulent flame surface as a passive scalar surface dominated by the fractal nature of turbulent flow field. Kerstein (1988) represented the turbulent flame structure as a fractal surface based on the dynamic similarity of the flame front. However, both studies have concluded with a value of 2.37 for the fractal dimension, D for turbulent premixed flames. Later, North and Santavicca (1990) carried out an extensive experimental study of a freely propagating turbulent premixed flame over a wide range of turbulent Reynolds and Damköhler numbers. From their experimental observations, they devised a heuristic, empirical relation as a function of turbulence intensity and laminar flame speed.

The basic principle of fractal theory is to identify and characterise the flame front structure as a fractal surface, which cannot be described by conventional methods. Since turbulent flames come under the category of naturally occurring fractals as shown in Figure 5.1, there exists a wide range of self-similar shapes and forms of different scales between outer and inner cut-off scales as shown in Figure 5.2. The similarity between the different size scales implies that the dynamic processes operating at each scale of similar size is the same, and facilitates the calculation of the fractal dimension of the fractal surface. As mentioned earlier, Mandelbrot (1975) was the first to suggest a value of 2.5 to 2.67 for D in the case of isotropic, homogeneous turbulence, but subsequent experiments (Lovejoy, 1982, Sreenivasan and Meneveau, 1986) and mathematical analysis (Hentschel and Procaccia,

1984) suggested a value of 2.35 to 2.41. However, Gouldin (1987) considered an intermediate value of 2.37 based on experimental studies of clouds and jet boundaries in free shear flows in his turbulent premixed modelling studies. Kerstein (1988) also suggested the same value for D, while deriving it using the dynamic similarity approach. Hence, it is evident that there exist various values for fractal dimensions based on intuitive arguments, experimental analysis or mathematical derivation in the literature.

Numerical modelling of turbulent premixed flames, based on fractal theory, generally requires a value for the fractal dimension of the fractal surface, which can be either modelled, based on local flow conditions or a prior value can be taken as an input. Nevertheless, most of the current research studies are found to follow the later approach due to either a loss of information in numerical simulations or to avoid the complexity of the whole problem. However, in the present work, the fractal dimension of the turbulent premixed flame front is modelled using two different models, namely, the empirical fractal model (EFM) of North and Santavicca (1990) and the dynamic fractal model (DFM) of Knikker et al. (2004). The first is based on an empirical relation, parameterised based on the local flow conditions, while the second is based on the outcome of the recent mathematical derivation of the dynamic evaluation and Germano identity of the resolved filtered flame surface density at the test and grid filter. These two models are presented and discussed in the following two sections.
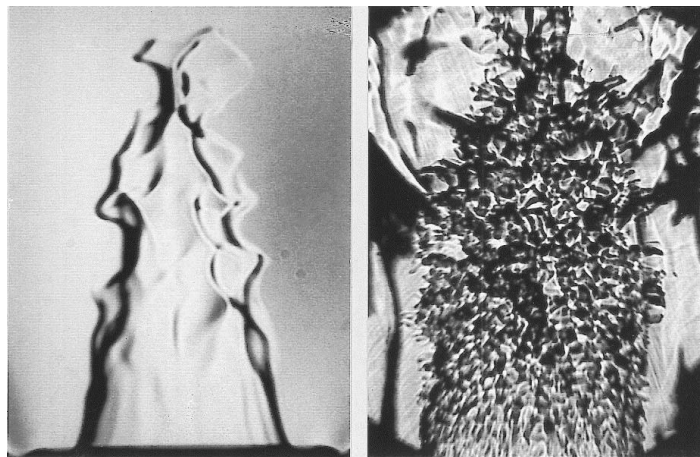
Figure 5.1 Instantaneous Schlieren images of a typical lean premixed flame at different pressures showing the fractal nature of the flame (Kobayashi et al., 1996).
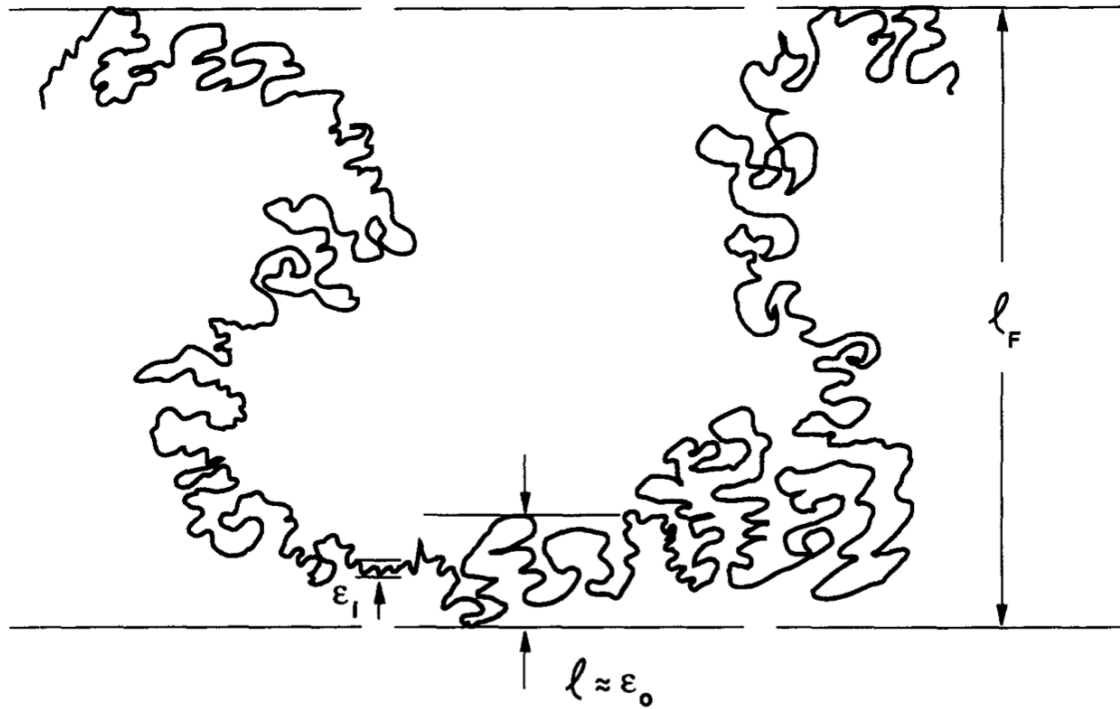
Figure 5.2 Fractal nature of the flame front showing various length scales (Gouldin, 1989i).

5.4.1 Empirical Fractal Model (EFM)

North and Santavicca (1990) considered various turbulent premixed flame configurations over a wide range of Reynolds and Damköhler numbers, such as rod-stabilised V-flames (Dandekar and Gouldin, 1981), rim stabilised conical flames (Murayama and Takeno, 1989), edge stabilised oblique flames (Gulati and Driscoll, 1985) and wall stabilised stagnation flames (Cho et al., 1988). They also developed a pulsed-flame flow reactor, which is able to generate a freely propagating turbulent premixed flame over a wide range of conditions. After careful examination of the images taken of the experimental flame, it was observed that the fractal dimension increases with increasing turbulence intensity and decreasing laminar flame speed. This phenomenon is explained in the following way:

> "the turbulent velocity fluctuations act to convectively distort the flame front at
> a rate proportional to the characteristic velocity scale, u' and the laminar
> burning process acts to smooth the flame surface at a rate proportional to the
> laminar burning speed, u_L " [See (North and Santavicca, 1990)].

They quantified this equilibrium situation as the wrinkling of the flame within the turbulent fractal limit i.e. D_T, due to the convective process by u', as a measure of the distortion of

the flame sheet by turbulent motions and the smoothing of the flame within the laminar fractal limit i.e. D_L, due to the control of the burning process by u_L, to eliminate the flame wrinkles. Based on the combined, equilibrium effects of the turbulent intensity and laminar burning speed, they parameterised a model to evaluate the fractal dimension as follows:

$$D = \frac{D_L}{\frac{u'}{u_L}+1} + \frac{D_T}{\frac{u_L}{u'}+1} \tag{5.33}$$

It is evident from the above equation that the fractal dimension, D, is automatically clipped between the chosen lower and upper fractal limits for a particular flame. However, these values are not definite and depend on the flow configuration. In the present investigation, the laminar fractal limit, D_L, and the turbulent fractal limit, D_T, are considered as 2.19 and 2.35 respectively, following the recent analysis of the wrinkling length scales of propane/air flames by Patel and Ibrahim (1999). Fureby et al. (2005) has successfully implemented this empirical model in the LES modelling of propane/air turbulent flames in a dump combustor by replacing u' with the SGS velocity fluctuations, u'_Δ as follow:

$$D = \frac{D_L}{\frac{u'_\Delta}{u_L}+1} + \frac{D_T}{\frac{u_L}{u'_\Delta}+1} \tag{5.34}$$

It is evident from the above equation that the use of the SGS velocity fluctuation instead of the turbulence intensity is quite clear, and does not require any further explanation in the case of LES. Using the equation (5.34), one can calculate the fractal dimension at every grid point for each time step.

5.4.2 Dynamic Fractal Model (DFM)

The dynamic fractal model (DFM) can be considered as a continuation of the DFSD model described in section 5.3, which identified the fractal dimension of the turbulent premixed flame. Considering the flame kernel as a fractal surface, the fractal dimension, D, is extracted by coupling the wrinkling flame factor (equation 5.20) with the Germano identity (Germano et al., 1991), while conserving the averaged filtered flame surface at the test and grid filter as follows:

$$\Xi(\bar{\Delta})\widehat{\Pi(\bar{c},\bar{\Delta})} = \Xi\left(\hat{\bar{\Delta}}\right)\Pi\left(\hat{\bar{c}},\hat{\bar{\Delta}}\right) \tag{5.35}$$

Using equations (5.21) and (5.29) the above expression can be rewritten as:

$$\left(\frac{\bar{\Delta}}{\delta_c}\right)^{D-2} \widehat{\bar{\Sigma}\left(\frac{\bar{\Delta}}{\delta_c}\right)^{2-D}} = \left(\frac{\hat{\bar{\Delta}}}{\delta_c}\right)^{D-2} \hat{\bar{\Sigma}}\left(\frac{\hat{\bar{\Delta}}}{\delta_c}\right)^{2-D} \tag{5.36}$$

The above expression can be solved for the fractal dimension, *D*, for each time step at every grid point in the computational domain. However, some form of averaging is usually required to avoid numerical stability issues, similar to that used to dynamically evaluate the Smagorinsky constant. Hence, the volume average of equation (5.36) is carried out for every time step as follow:

$$\left[\left(\frac{\bar{\Delta}}{\delta_c}\right)^{D-2} \widehat{\bar{\Sigma}\left(\frac{\bar{\Delta}}{\delta_c}\right)^{2-D}}\right] = \left[\left(\frac{\hat{\bar{\Delta}}}{\delta_c}\right)^{D-2} \hat{\bar{\Sigma}}\left(\frac{\hat{\bar{\Delta}}}{\delta_c}\right)^{2-D}\right] \tag{5.37}$$

Rearranging the above equation results in:

$$\left(\frac{\hat{\bar{\Delta}}}{\bar{\Delta}}\right)^{D-2} = \frac{\left[\widehat{\Pi(\bar{c},\bar{\Delta})}\right]}{\left[\Pi(\hat{\bar{c}},\hat{\bar{\Delta}})\right]} \tag{5.38}$$

Applying the logarithm on both sides of the above equation and rearranging will lead to:

$$D = 2.0 + \frac{\log\left(\left[\widehat{\Pi(\bar{c},\bar{\Delta})}\right]/\left[\Pi(\hat{\bar{c}},\hat{\bar{\Delta}})\right]\right)}{\log\left(\hat{\bar{\Delta}}/\bar{\Delta}\right)} \tag{5.39}$$

The above equation can be solved at each grid point in the computational domain at every time step. To alleviate the ill-posed problems caused by strong local variations or to avoid irrelevant values, the maximum value of the fractal dimension is clipped to 2.5 in simulations. It is worth mentioning at this stage that the empirical model described in section 5.4.1 can be applied to any turbulent premixed flame situation, as the turbulent intensity and the laminar burning velocity information can easily be extracted. Where as the DFM can only be applied in conjunction with the dynamic flame surface density procedure described in section 5.3, and applying it in the present work, where the values of $\Pi(\bar{c}, \bar{\Delta})$ at the grid and test filter, at every grid point in time are available.

5.4.3 Outer and Inner Cut-off Scales

It is evident from the above fractal models that there is a necessity to define correct outer and inner cut-off scales, which facilitates the evaluation of the correct fractal dimension of

the flame. In the case of EFM, the outer cut-off scale is important since it is required to determine the SGS velocity fluctuations based on the filter width used in LES studies. Similarly, in the case of DFM, it is evident that the wrinkling flame factor and the flame surface density in equation (5.35) are derived based on the filter width, which is considered as the outer cut-off scale. In the case of LES studies, it is appropriate to consider the filter width, Δ, as the outer cut-off scale. Hence, in the present simulations, the filter width has been considered as the outer cut-off scale.

The inner cut-off scale, commonly representing the smallest scale of the wrinkling flame, is predominant in evaluating the overall reaction rate apart from the fractal dimension. There are several hypotheses available in choosing appropriate inner cut-off scales based on physical and intuitive arguments. However, the interaction between the smaller turbulent eddies and the local flame front are not well established in defining the inner cut-off scale through experiments (North and Santavicca, 1990). Among the available, predominantly used cut-off scales are the Kolmogorov length scale (Gouldin, 1987), the Gibson scale (Peters, 1988) and the laminar flame thickness (Murayama and Takeno, 1989, Knikker et al., 2002 and Knikker et al., 2004).

The Kolmogorov scale is the smallest physical length scale in any turbulent flow and it has been widely exploited by Gouldin (1987), who identified that the smoothing action in numerical simulations will generally wipe out the information regarding the smallest scales and increases the inner cut-off scale. Also, at high values of u'/u_L, the Kolmogorov scale can become smaller than the laminar flame thickness (North and Santavicca, 1990). Whereas Peters (1988) identified the Gibson scale as the smallest scale, which remains in the reaction region long enough to alter the flame structure and is appropriate to be considered as the inner cut-off scale. However, Murayama and Takeno (1989) argued that it is impossible for an object to have wrinkles smaller than its thickness, which eventually implies that the laminar flame thickness should be appropriate to be considered as the inner cut-off scale while using laminar flamelet concepts. Experimental studies of Gülder and Smallwood (1995) support this concept by relating the inner cut-off scale as, $\delta_c \propto \delta_L$. Gülder and Smallwood (1995) proposed a relation based on DNS data by considering the chemistry effects as follow:

$$\delta_c = \delta_L\left(\alpha_3 + Ka^{\beta_3}\right) \tag{5.40}$$

In the above equation, Ka is the Karlovitz number, and α_3 and β_3 are model constants. Equation (5.40) can be applicable for u'/u_L values between 0.5 and 6.2. However, Gubba et al. (2009) identified that u'/u_L values reach a maximum of 13.4, hence the above relation may not be useful in defining the appropriate inner cut-off scale. A similar opinion has been expressed by Fureby (2005) who used a model based on the sub-grid scale wrinkling length scale as the inverse of the surface averaged curvature of the flame as $\delta_c = |\langle\nabla\cdot n\rangle|^{-1}$. However, Knikker et al. (2002 and 2004) used an inner cut-off scale equal to three times the laminar flame thickness, which they identified as being able to predict good results from experimental extractions. Accordingly, a lower cut-off scale equal to three times the laminar flame thickness is used in the present work.

5.5 Summary

This chapter mainly describes the various models that have been considered and developed for turbulent premixed combustion. The existing challenges in accounting for the mean chemical reaction rate in turbulent premixed flames using the flame surface density model are presented and discussed. One of the main challenges in LES for turbulent premixed combustion was accounting for the unresolved flame surface density, which can either be obtained by solving the exact FSD equation or by modelling using the dynamic procedure. It was identified that solving the exact equation in RANS itself used to be complex, and that solving it in LES will lead to many unclosed terms. Alternatively, a dynamic flame surface density (DFSD) model based on the Germano identity and the similarity concept by Knikker et al. (2004), has been implemented in the current work.

Prior to the DFSD model, it was concluded that the dynamic evaluation of the model coefficient in the algebraic FSD model might be the best choice. However, it was identified that the application of the Germano identity in deriving the model coefficient fails, and alternatively a model based on the flame wrinkling factor was identified. Using this model revealed that the flame wrinkling model is capable of self scaling the model coefficient, based on the local flow conditions and is a much better option than using a constant value. However, this study also identifies that algebraic FSD can be further improved by

calculating the unresolved flame surface density by additional formulation. Consequently, the DFSD model based on the simple FSD has been the best available option, and a detailed derivation was provided. The DFSD derivation provides certain challenges in calculating the fractal dimension and a model for the lower cut-off scale. Two models were used to calculate the fractal dimension based on experimental studies and dynamic similarity ideas respectively with a choice of the lower cut-off scale. However, following the simple experimental method, it is concluded that the lower cut-off scale corresponding to the laminar flame thickness would result in the best predictions and hence is used in the present study. The DFSD validation has been carried out by comparisons with available experimental data for the following parameters as overpressure, flame position, flame speed and reaction rate etc.

Chapter 6   The Numerical Model

In this research work, an available in-house LES code, PUFFIN is used. The code was originally developed by Kirkpatrick (2002) and thereafter extended through joint collaboration with The University of Sydney for compressible flows (Kirkpatrick et al., 2003). Following this, Gubba (2007) implemented a dynamic flame surface density model for combustion. The code was developed using sophisticated, state of the art programming techniques in FORTRAN 90, which is capable of handling 2D and 3D, non-reacting and reacting flows, using LES numerical simulations of various industrial flow problems. Also, it has been extended to compute, non-premixed (Ranga-Dinesh, 2007) and partially premixed (Ravikanti, 2008) industrial problems as well. However, the work presented in this thesis is mainly in relation to explosion premixed flames and aims to give confidence in using DFSD models for unsteady turbulent flames, especially for flame propagation over multiple solid obstacles. The model findings are validated against available experimental measurements. This chapter describes various numerical aspects and solution methodologies implemented in the LES numerical code.

In the entire numerical simulation tool, the primary concern is to outline the partial differential equations, governing the fluid flow, as described in Chapters 3 and 4. The governing equations are then carefully discretised, to achieve error free and more accurate numerical results. Finally, spatially discretised equations are solved in computational space and time, which is very important to achieve results of the desired accuracy, within the available computational resources. The numerical code uses a finite volume spatial discretisation methodology, on a forward staggered, non-uniform, Cartesian grid, which is detailed in the following section. Spatial discretisation of the individual terms in a generic governing equation using finite volume methodology is discussed here. Various aspects of the code, such as the time advancement scheme, pressure correction scheme, the solver and the typical solution iteration procedure, are described. The details of the outflow and the solid boundary conditions employed in the present investigation are also presented and discussed.

6.1 The Finite Volume Method

In the finite volume method, the computational domain is divided into a finite number of control volumes (CVs). The conservation equations described in Chapters 3 and 4 for turbulent premixed flames are numerically integrated in each of these CVs, which eventually leads to a set of simultaneous algebraic equations, whose solution is an approximation to the solution of the continuous equations at a set of discrete points or nodes. The centroid of the individual control volume is generally considered as a node, and the solution at this node represents the solution within the control volume. One main advantage of the finite volume methodology is that it can accommodate any type of grid, which is quite suitable for complex geometries. Also, as discussed in Chapter 4, the application of the box filter in LES naturally fits into the finite volume formulation.

Hence, the work presented here uses the finite volume methodology, based on a forward, staggered Cartesian grid and defines the boundaries of the rectangular finite volumes as shown in Figure 6.1. Scalars such as pressure and the reaction progress variable are calculated at the scalar nodes as shown in Figure 6.1. However, the velocity components are calculated at the velocity nodes, i.e. the centroid of the scalar cell faces, forming a staggered grid, which means that the velocity cells are staggered with respect to the scalar cells. The staggering of the velocity avoids physically non-realistic predictions for oscillating pressure fields. Also, since the velocities are generated at the scalar cell faces, it has the added advantage of avoiding the interpolation of velocities for scalar transport computations. Extension of the grid shown in Figure 6.2 in 3D uses the same structure in the z direction, with an additional velocity component in the z direction, i.e. w.
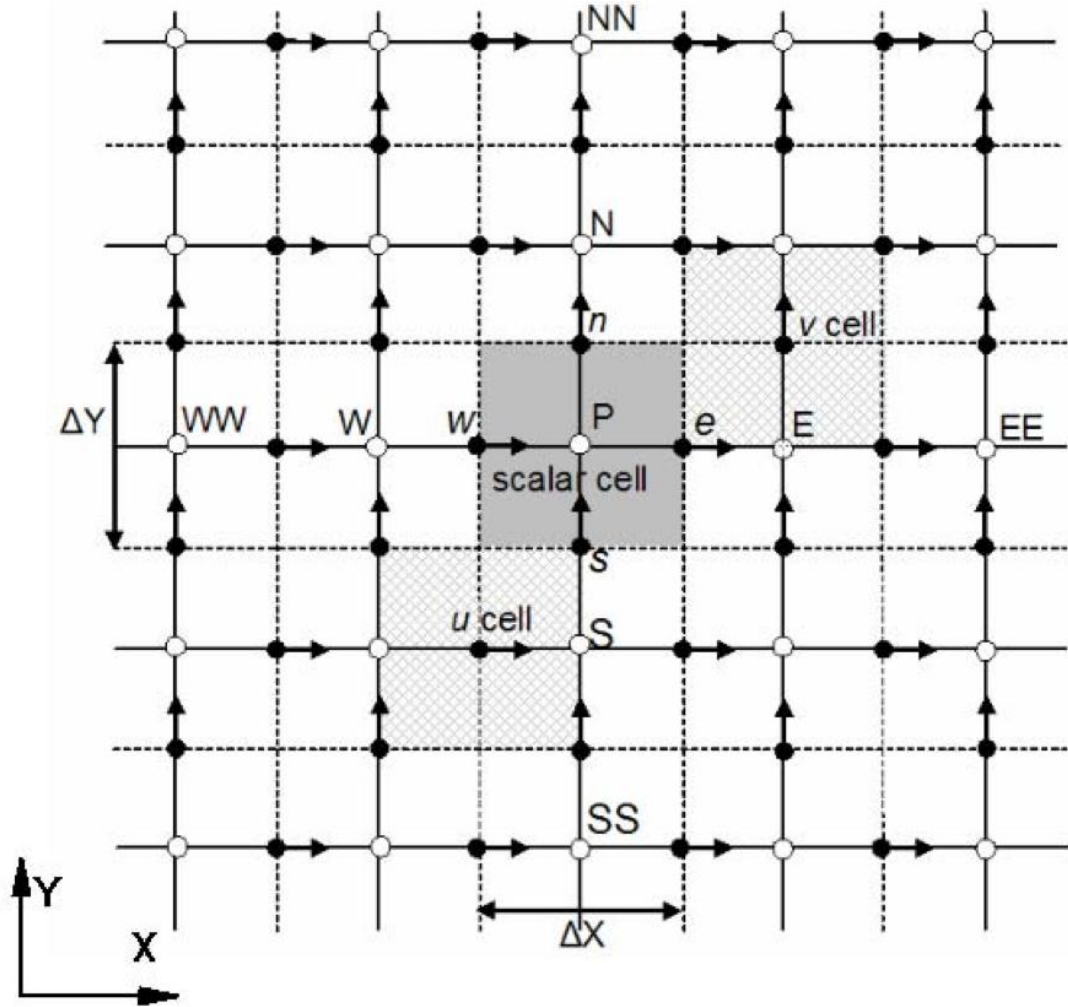
Figure 6.1 Two-dimensional forward staggered grid. The circles are scalar nodes, the horizontal arrows are the nodes of the u velocity component and vertical arrows are the nodes of the v velocity component. Examples of u, v and scalar cells are highlighted.

6.2 Discretisation of the conservation Equations

The conservation equations of mass, momentum, energy and the reaction progress variable detailed in Chapters 3 and 4 are in a similar format and therefore can be expressed using a generic variable ϕ as:

$$\frac{\partial(\rho\phi)}{\partial t} + \frac{\partial(\rho u_j \phi)}{\partial x_j} = \frac{\partial}{\partial x_j}\left(\Gamma \frac{\partial \phi}{\partial x_j}\right) + S_\phi \qquad (6.1)$$

For instance, in the above equation, ϕ equals one to represent continuity, u represents the momentum in x-direction, and thus equation (6.1) can be rearranged as:

$$\frac{\partial(\rho\phi)}{\partial t} = -\frac{\partial(\rho u_j \phi)}{\partial x_j} + \frac{\partial}{\partial x_j}\left(\Gamma\frac{\partial\phi}{\partial x_j}\right) + S_\phi \tag{6.2}$$

In the above equation, Γ is the diffusion coefficient and S_ϕ is the source term. Equation (6.2) is integrated over a control volume V bounded by an arbitrary shape such that:

$$\int_V \frac{\partial(\rho\phi)}{\partial t} dV = -\int_V \frac{\partial(\rho u_j \phi)}{\partial x_j} dV + \int_V \frac{\partial}{\partial x_j}\left(\Gamma\frac{\partial\phi}{\partial x_j}\right) dV + \int_V S_\phi dV \tag{6.3}$$

The convection and diffusion terms in the above equation can be transformed into surface integrals by using the Gauss divergence theorem, which yields the integral form of the equation as follows:

$$\frac{\partial}{\partial t}\int_V (\rho\phi) dV = -\int_S \rho u_j \phi dS_j + \int_S \Gamma\frac{\partial\phi}{\partial x_j} dS_j + \int S_\phi dV \tag{6.4}$$

The differential surface area vector dS has a magnitude equal to the area of the segment of the surface, and the direction corresponds to the direction of the outward normal to the segment. The terms in equation (6.4) represent an unsteady term on the left hand side, and advection, diffusion and the source terms on the right hand side respectively. Spatial discretisation of equation (6.4) involves approximating the volume and surface integrals within the finite volume to obtain a set of simultaneous linear algebraic equations in ϕ.

A schematic representation of the 2D forward staggered grid shown in Figure 6.1 elucidates the details of a scalar cell P for which the integrals are to be calculated and surrounded by its northern (N), eastern (E), southern (S) and western (W) neighbours and one level away from it as north of northern(NN), east of eastern (EE), south of southern (SS) and west of western (WW). Figure 6.2 extends this structure in 3D for the same scalar and shows neighbouring cells in the z direction as up (U) and down (D), which can be extended thereafter as the upper of up (UU) and the down of down (DD). The surfaces separating two cells are denoted as A_n, A_e, A_s, A_w, A_u and A_d, and the associated fluxes are F_n, F_e, F_s, F_w, F_u and F_d. Small letters e, n etc. refer to the points at the centroid of the respective cell faces. In the following section, nb is used as a generic subscript for the neighbour cell and f is a generic subscript for a quantity evaluated at a cell face. To reduce the complexity of the notation, the fluxes are given for a particular face such as the east or north face. All results can be applied in a similar manner to the other faces.
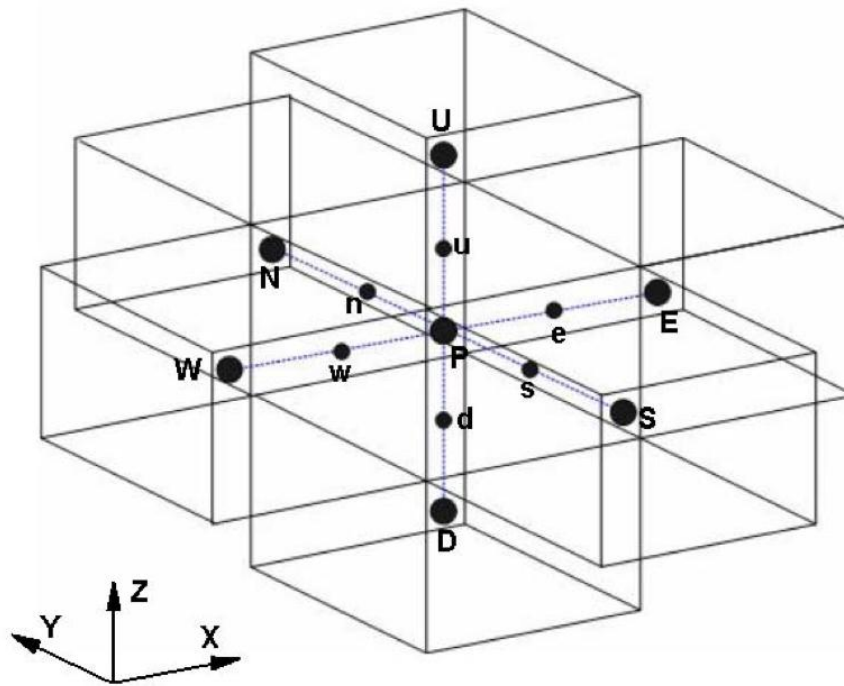
Figure 6.2 Three dimensional view of a finite volume cell and its neighbours.
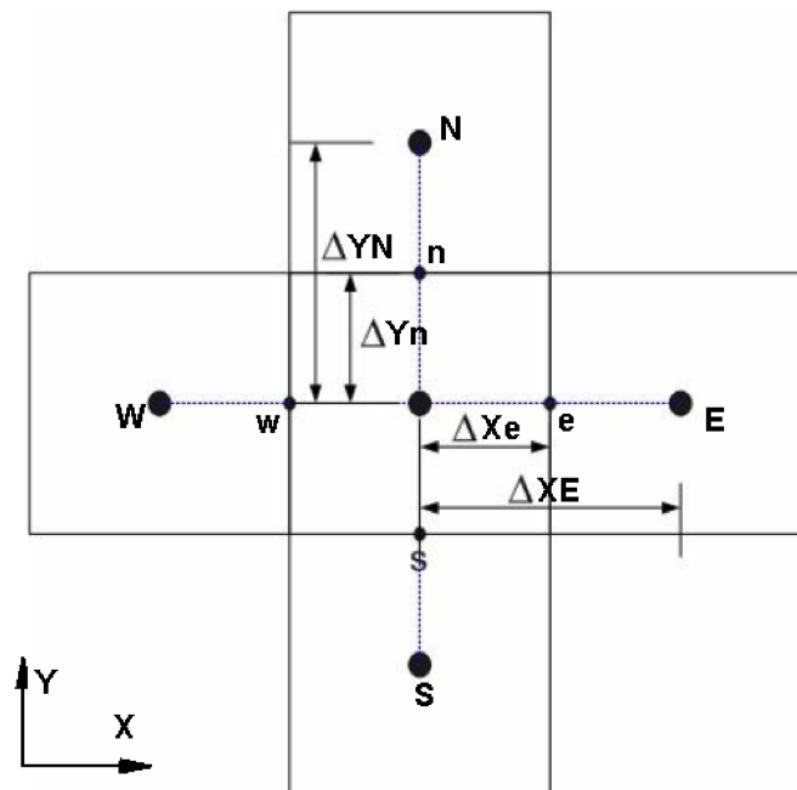
Figure 6.3 A finite volume cell and its neighbour in the xy plane.

6.2.1 The Unsteady Term

The unsteady term on the left hand side of the conservation equation (6.4) can be discretised by considering the value of ϕ at the central node, which is considered to represent the value throughout the control volume. Using the central difference approximation for the time derivative at $n + 1/2$ it can be derived as:

$$\int_V \frac{\partial(\rho\phi)}{\partial t} dV = \frac{(\rho\phi)^{n+1}-(\rho\phi)^n}{\Delta t} \Delta V \tag{6.5}$$

where n is the time level. The value n indicates that the values are taken at the start of the current time step, whereas $n + 1$ indicates the end of the time step.

6.2.2 The Convection Term

The convective fluxes are very important in any turbulent reacting flows, and hence their description is essential in numerical simulations. In order to achieve appropriate numerical stability and accuracy, a special treatment for the convective fluxes is required. Numerical discretisation employed for convective fluxes is explained as follows:

Considering a control volume and representing the convective fluxes as:

$$\int_S \rho u_j \phi dS_j = \sum_{n,e\ldots} F_{conv} \tag{6.6}$$

the convection flux across a cell face is given by:

$$F_{conv} = (\rho u_{normal} \Delta A \phi)_f \tag{6.7}$$

where u_{normal} is the velocity component normal to the surface A and ΔA is the area of the face. The convection for the east face can be written as:

$$F_{conv} = (\rho u \Delta A)_e \phi_e \tag{6.8}$$

The application of weighted, linear interpolation of the neighbouring cells at the centre of the face leads to:

$$\phi_e = (1 - \theta)\phi_P + \theta \phi_E \tag{6.9}$$

Here the weighting factor for the interpolation is:

$$\theta = \frac{\Delta x_e}{\Delta x_E} \tag{6.10}$$

where Δx_e and Δx_E are the distances from the node P to the face of the centroid e and the east neighbor node E, as shown in Figure 6.3.

In the staggered grid, it is required to find the convective velocity, u_e, at the face, and the density, ρ_e, at the face depending on whether the variable ϕ is a scalar or velocity component. When ϕ is a scalar, the convective velocity is available, as u is established at the cell face. However, density must be interpolated using an equation similar to (6.9) such as:

$$\rho_e = (1 - \theta)\rho_P + \theta \rho_E \tag{6.11}$$

Contrarily, when ϕ is a velocity component, linear interpolation is required to find the convective velocity, however ρ is directly available. Finally the resulting formulation for the convection fluxes can be described using a second order central difference scheme as follows:

$$F_{conv} = (\rho u \Delta A)_e [(1 - \theta)\phi_P + \theta \phi_E] \tag{6.12}$$

This linear interpolation based numerical scheme used to calculate the variables at the cell faces of the finite volumes is equivalent to a second order central difference scheme in the finite difference method. This scheme is second order accurate, computationally efficient and simple to implement. This accuracy is desirable for LES since numerical damping acts as an extra un-quantified contribution to the eddy viscosity and contaminates the effects of the sub-grid scale model. However this scheme tends to give solutions containing non-physical oscillations, or 'wiggles', in areas of the field containing high gradients. The convection terms in the scalar equations are particularly problematic due to the large gradients, which often occur in the scalar fields. Because scalars are often coupled with the velocity field through density, the wiggles which result from the use of the central difference for the scalar convection terms cause problems with the numerical stability of the overall solution. Hence this scheme is hardly suited for scalar transport, especially when it has to remain bounded. For example, the reaction progress variable is limited to a range from 0 to 1. From this scheme, wiggles may lead to unphysical results such as predictions of reaction progress variables outside the range 0 to 1, which do not yield any sensible

meaning. For this reason, the convection term for the scalar equation is discretised using non-centred schemes such as QUICK by Leonard (1979) or SHARP by Leonard (1987).

QUICK is a third order upwind scheme and can reduce numerical oscillations by introducing fourth order dissipation. Quadratic interpolation is used to find the value ϕ at the centre of the cell faces. The formula for the east face can be written as:

$$\phi_e = [(1 - \theta)\phi_P + \theta\phi_E] - \tfrac{1}{8}CRV \times \Delta x_E^2 \qquad (6.13)$$

Here the upwind biased curvature term is defined as:

$$CRV = \frac{\phi_P - 2\phi_E + \phi_{EE}}{\Delta x_E^2}, \quad u < 0 \qquad (6.14)$$

$$CRV = \frac{\phi_E - 2\phi_P + \phi_W}{\Delta x_E^2}, \quad u > 0 \qquad (6.15)$$

The double subscript such as *EE* refers to the cell east of the eastern neighbour as described in section 6.2. The weighting factor, θ, can be calculated from equation (6.10). The first term in equation (6.13) is the value of ϕ at the cell face calculated using linear interpolation. The second term is an upwind biased curvature term which makes the overall interpolation quadratic.

The linear interpolation term accounts for the non-uniform grid through the weighting factor, θ, while the curvature terms have no grid weighting included. Castro and Jones (1987) have shown that the uniform grid formula for QUICK gives negligible errors for grid expansion ratios $r_x = \Delta x_i + 1/\Delta x_i$ between 0.8 and 1.25. Substituting equation (6.13) into equation (6.5) gives the convective flux of ϕ across the east face as:

$$F_{conv} = (\rho u \Delta A)_e \{[(1 - \theta)\phi_P + \theta\phi_E] + S_{QUICK}\} \qquad (6.16)$$

where S_{QUICK} is given as:

$$S_{QUICK} = -\tfrac{1}{8}CRV \times \Delta x_E^2 \qquad (7.17)$$

The source term S_{QUICK} indicates the curvature of the field. In PUFFIN, the term S_{QUICK} is included as part of the source term S_ϕ.

However, the QUICK scheme can reduce the wiggles but does not remove them completely. In this case, another scheme called SHARP (Leonard, 1987), which is a modification to QUICK, is used. SHARP introduces a second order diffusion where local conditions are such that oscillations will not occur, thereby ensuring that the solution remains monotonic. An outline of this scheme can be found in Leonard (1987). Finally, the summation of the convective fluxes across all faces can be added and described as:

$$\int_S \rho u_j \phi dS_j \approx \sum (\rho u \Delta A)_f \left[(1-\theta)\phi_P + \theta_f \phi_{nb} + \sum S_{QUICK} \right] \qquad (6.18)$$

6.2.3 The Diffusion Term

The diffusive flux is proportional to the gradient, ϕ, across a cell face, f, and is given as:

$$F_{diff} = \left[\Gamma \Delta A \left(\frac{\partial \phi}{\partial n} \right) \right]_f \qquad (6.19)$$

where n is the direction normal to the face, Γ is the kinematic diffusion coefficient and ΔA is the area of the face. The flux at the centre of the east cell face is then computed from the values at the two neighbour points and their distance from the central difference approximation as:

$$F_{diff} = (\Gamma \Delta A)_e \frac{\phi_E - \phi_P}{\Delta x_E} \qquad (6.20)$$

The diffusion coefficient at the centre of the face Γ_e is calculated by linear interpolations, in the same way as the density calculation in the preceding section of the convection term. Summation of the diffusive fluxes across all faces can be described as a discrete diffusion operator as:

$$\int_S \Gamma \frac{\partial \phi}{\partial x_j} dS_j \approx \sum \frac{(\Gamma \Delta A)_e}{\Delta x_E} (\phi_{nb} - \phi_P) \qquad (6.21)$$

Note at this stage, that the discrete diffusion operator does not suffer from numerical instability as observed in the case of convective fluxes. Therefore, no special treatment is required for the diffusion terms in the conservation equation.

6.2.4 The Source Term

the source terms are different for each variable in the individual conservation equations and dependent on the variable being transported. For instance, in the case of the momentum equation, the source term represents the effect of the pressure gradient and the gravitational force. Whereas in the case of the energy equation, the source term includes contributions due to pressure work, viscous dissipation and flow dilatation as well as a chemical source term. The chemical source term is also presented in the reaction progress variable equation.

Spatial discretisation of the source term in all the transport equations proceeds in the same manner. They are calculated by evaluating the function representing the source term, S_ϕ, at the node and multiplying by the volume of the cell as:

$$\int_V S_\phi dV \approx S_{\phi P} \Delta V \tag{6.22}$$

the gradients are evaluated using second order central differences, while the interpolations utilise a linear profile similar to that used in evaluating the convection and diffusion terms. In general, source terms can be expressed as a combination of implicit and explicit components as:

$$S_{\phi P} \Delta V = S_{imp} \phi_P + S_{exp} \tag{6.23}$$

The implicit component of the above equation is integrated using the implicit time advancement scheme, whereas the explicit component is integrated using the explicit time advancement scheme. The time advancement schemes employed in the present work are described in section 6.3.

6.2.5 The Complete Discretised Conservation Equation

It is evident from the above sections, that the complete discretised conservation equation for a generic variable, ϕ, can simply written by summing the individual discretised terms as:

$$\frac{(\rho\phi)^{n+1} - (\rho\phi)^n}{\Delta t}\Delta V$$

$$= \left\{\sum (\rho u \Delta A)_f \left[(1 - \theta_f)\phi_P + \theta_f\phi_{nb}\right]\right\}^{(n-2,n-1,n,n+1)}$$

$$+ \left[\sum \frac{(\Gamma\Delta A)_e}{\Delta x_E}(\phi_{nb} - \phi_P)\right]^{(n-1,n,n+1)} + \left(S_{imp}\phi_P\right)^{(n-1,n,n+1)}$$

$$+ \left(S_{exp}\right)^{(n-1,n,n+1)}$$

$$(6.24)$$

Here the brackets { } with superscripts $(n - 2, n - 1, n, n + 1)$ represent a weighted average of the term evaluated at the listed time intervals, which gives an estimate of the term at the $(n + 1/2)$ time level, which will be discussed in the next section. Collecting the coefficients and rearranging the above equation results in the final form equation which can be given as:

$$A_P^{n+1}\phi_P^{n+1} = \sum_{nb}(A_{nb}^{n+1}\phi_{nb}^{n+1}) + S_{imp}\phi_P^{n+1} + S_{exp}^{n+1}$$

$$+ \left[\sum_{nb}(A_{nb}^n\phi_{nb}^n) - A_P^n\phi_P^n + S_{imp}\phi_P^n + S_{exp}^n\right]$$

$$+ \left[\sum_{nb}(A_{nb}^{n-1}\phi_{nb}^{n-1}) - A_P^{n-1}\phi_P^{n-1} + S_{imp}\phi_P^{n-1} + S_{exp}^{n-1}\right]$$

$$+ \left[\sum_{nb}(A_{nb}^{n-2}\phi_{nb}^{n-2}) - A_P^{n-2}\phi_P^{n-2} + S_{exp}^{n-2}\right]$$

$$(6.25)$$

where the coefficients corresponding to the node, A_P, and its neighbours, A_{nb}, are formed due to the contributions from the convection and diffusion terms. More details of spatial discretisation methods can be found in Kirkpatrick (2002) and Kirkpatrick et al. (2003).

6.3 The Time Advancement Scheme

The discretised transport equation described in the above section must be solved in space and time in order to simulate reacting flows. To obtain time-accurate and unsteady

simulations, time integration schemes are developed using second and third order numerical accuracy. The time integration schemes for scalar equation uses the Crank-Nicolson scheme and the momentum equations are advanced using either Crank-Nicolson or the second- and third- order hybrid Adams-Bashforth scheme.

6.3.1 Time Integration of the Scalar Equation

In the present work, the Crank-Nicolson scheme is employed to achieve the time integration of the scalar equation. The time dependent conservation equation, integrated in time using the Crank-Nicolson scheme can be written as:

$$
\frac{(\rho\phi)^{n+1} - (\rho\phi)^n}{\Delta t}\Delta V
$$
$$
= -\frac{1}{2}[H^{n+1}(\phi^{n+1}) + H^n(\phi^n)] + \frac{1}{2}[L^{n+1}(\phi^{n+1}) + L^n(\phi^n)]
$$
$$
+ \frac{1}{2}\left(S_{imp}^{n+1}\phi^{n+1} + S_{imp}^n\phi^n\right) + \frac{1}{2}\left(S_{exp}^{n+1}\phi^{n+1} + S_{exp}^n\phi^n\right)
$$

$$(6.26)$$

where H is the discrete convection term, expressed as:

$$
H(\phi) = \sum(\rho u \Delta A)_f \left[(1 - \theta_f)\phi_P + \theta_f\phi_{nb}\right]
$$
$$(6.27)$$

L is the discrete diffusion term, expressed as:

$$
L(\phi) = \sum \frac{(\Gamma\Delta A)_e}{\Delta x_E}(\phi_{nb} - \phi_P)
$$
$$(6.28)$$

and $S_{imp}\phi$ and S_{exp} are the discrete implicit and explicit source terms respectively. It is to be note that S_{imp} is a coefficient of ϕ rather than a function of ϕ.

In the above equation (6.26), each term is evaluated at the n and $n + 1$ time levels, and employs linear interpolation to estimate their value at $(n + 1/2)$. Therefore, this scheme is second order accurate. At least two iterations of the scalar equation per time step are required due to the contributions of terms containing ϕ^{n+1} to the explicit source term

which result from the use of the QUICK and SHARP spatial discretisation schemes. It should be noted at this stage that in turbulent premixed combustion, density and diffusivity vary significantly in time. Hence to maintain the stability of the solution, a number of outer iterations of the entire time advancement scheme per time step are required to ensure that the values of ρ^{n+1} and Γ^{n+1} are second order accurate. This non-oscillatory criterion for the Crank-Nicolson scheme can be achieved by enforcing a condition on time as:

$$\Delta t \leq \frac{(\Delta x)^2}{\Gamma} \qquad (6.29)$$

While the above criterion poses a rather stringent limitation on the improvement that could be achieved on spatial accuracy, it results from an error term in the Taylor series expansion, which contains the second derivative in space $\partial^2 \phi / \partial x_i^2$. However, this term i is relatively small in most flow problems and the scheme remains stable for considerably large time steps.

6.3.2 The Time Integration of Momentum Equations

Time integration of the momentum equations uses either the Crank-Nicolson or the second and third order hybrid Adams schemes. In the hybrid schemes, Adams-Bashforth methods are used for the advection terms and Adams-Moulton methods for the diffusive terms. The momentum equations are integrated by using the Crank-Nicolson scheme and can be expressed as:

$$\frac{\rho^{n+1}u^* - \rho^n u^*}{\Delta t}\Delta V$$
$$= -\frac{1}{2}(H^{n+1}u^* + H^n u^n) + \frac{1}{2}(L^{n+1}u^* + L^n u^n) + \frac{1}{2}\left(S_{imp}^{n+1}u^* + S_{imp}^n u^n\right)$$
$$+ \frac{1}{2}\left(S_{exp}^{n+1}u^* + S_{exp}^n u^n\right) - Gp^{n-\frac{1}{2}}$$

$$(6.30)$$

It is evident from the above equation, that it has a similar form to the scalar equation employing the Crank-Nicolson scheme (equation 6.26). However, an additional term can be noticed, added as a pressure gradient term $Gp^{n-\frac{1}{2}}$, which considers $n - \frac{1}{2}$ to be the time level concerning the pressure correction scheme, which will be discussed in the next section.

Here the approximate velocity obtained before the pressure correction step at the $n + 1$ time level is specified with the superscript u^*.

The advection terms in the momentum equations are integrated using the explicit time advancement scheme, as Crank-Nicolson requires several iterations to retain second order accuracy. In PUFFIN, second and third order hybrid schemes are used such that advection terms are treated explicitly using an Adam-Bashforth scheme, while the diffusion term is treated implicitly using Adams-Moulton. The additional terms, such as gravitational terms, are treated explicitly using Adams-Bashforth.

The second order Adams-Bashforth/Adams-Moulton scheme for the momentum equations can be written as:

$$\frac{\rho^{n+1}u^* - \rho^n u^*}{\Delta t}\Delta V$$
$$= -\frac{1}{2}(3H^n u^n + H^{n-1}u^{n-1}) + \frac{1}{2}(L^{n+1}u^* + L^n u^n)$$
$$+ \frac{1}{2}\left(S_{imp}^{n+1}u^* + S_{imp}^n u^n\right) + \frac{1}{2}\left(3S_{exp}^n u^n + S_{exp}^{n-1}u^{n-1}\right) - Gp^{n-\frac{1}{2}}$$

$$(6.31)$$

and the third order Adams-Bashforth/Adams-Moulton scheme can be written as:

$$\frac{\rho^{n+1}u^* - \rho^n u^*}{\Delta t}\Delta V$$
$$= -\frac{1}{12}(23H^n u^n - 16H^{n-1}u^{n-1} + 5H^{n-2}u^{n-2})$$
$$+ \frac{1}{12}(5L^{n+1}u^* + 8L^n u^n - L^{n-1}u^{n-1})$$
$$+ \frac{1}{12}\left(5S_{imp}^{n+1}u^* + 8S_{imp}^n u^n - S_{imp}^{n-1}u^{n-1}\right)$$
$$+ \frac{1}{12}\left(23S_{exp}^n u^n - 16S_{exp}^{n-1}u^{n-1} + S_{exp}^{n-2}u^{n-2}\right) - Gp^{n-\frac{1}{2}}$$

$$(6.32)$$

The non-linear advection terms and explicit source terms in this case are calculated at previous time steps, in which all the necessary information is known. Hence these schemes do not require any iteration procedure, as in the Crank-Nicolson scheme, to maintain their accuracy. However, when the density and viscosity vary significantly, for instance such as in the "turbulent premixed propagating flame", the iteration of the overall solution procedure is required to include the correct value for the density in the unsteady term and for the viscosity in the diffusion term at the $n + 1$ time step. The advection term within one time step has to be limited to at least satisfy the Courant number, $C = u_i \Delta t / \Delta x_i < 1.0$. Simply put, this criterion requires that, within a time step, information may only travel to the neighbour cell but no further. For advection terms, the maximum time step is proportional to the characteristic convection time $\Delta x_i / u_i$, which is usually described in terms of the Courant number. For the diffusion term, the maximum usable time step is proportional to the characteristic diffusion time $\Delta x_i^2 / v$. However, Adams methods require some treatment for the initial steps when no information about the previous time step is available. Therefore, the Crank-Nicolson method is used for the initial time steps to enable the calculation of the $n - 1$ and $n - 2$ source terms for the Adams schemes.

6.3.3 The Pressure Correction Equations

In the present study, the pressure correction of unsteady compressible flow simulations has been carried out using the fractional step method, based on the incompressible flow pressure correction of Vankan (1986) and Bell and Colella (1989), which has been recently extended by Kirkpatrick (2002) for compressible flows. It is well known that in the case of compressible reacting flows, pressure and density remain coupled through the state equation and large density variations exist. Hence, it is essential to correct the velocity, density and pressure simultaneously by enforcing the mass conservation of the fluid flow. Since density depends on both pressure and temperature, an iterative method is required to correct it. Accordingly, considering the mth iteration of the time step from $t = n$ to $t = n + 1$, the transport equations of the energy and reaction progress variables are solved for the temperature field T^m. An approximate density field ρ^* for the mth iteration is then found using the equation of the state with the temperature T^m and the pressure from the previous iteration P^{m-1} as:

$$\rho^* = \frac{RT^m}{P^{m-1}} \tag{6.33}$$

The momentum equations for the three velocity components are then integrated using ρ^* and P^{m-1} to find an approximate solution for the velocity field u_i^* as:

$$\frac{(\rho^* u_i^*)^{n+1} - (\rho u_i)^n}{\Delta t} = \Upsilon(u_i^*, u_i^n) - \frac{1}{2}\left(\frac{\delta P^n}{\delta x_i} + \frac{\delta P^{m-1}}{\delta x_i}\right) \tag{6.34}$$

where Υ is an operator representing the remaining terms in the momentum equation. In order to correct u_i^*, P^{m-1} and ρ^*, mass conservation is thus enforced through the obtained velocity field as:

$$\frac{(\rho^m u_i^m)^{n+1} - (\rho u_i)^n}{\Delta t} = \Upsilon(u_i^*, u_i^n) - \frac{1}{2}\left(\frac{\delta P^n}{\delta x_i} + \frac{\delta P^m}{\delta x_i}\right) \tag{6.35}$$

which eventually satisfies the conservation of mass as follows:

$$\frac{\rho^m - \rho^n}{\Delta t} + \frac{\delta(\rho^m u_i^m) P^n}{\delta x_i} = 0 \tag{6.36}$$

Subtracting equation (6.34) from (6.35) gives:

$$\rho^m u_i^m - \rho^* u_i^* = -\frac{\Delta t}{2}\frac{\delta p'}{\delta x_i} \tag{6.37}$$

where the pressure correction is defined as:

$$p' = p^m - p^{m-1} \tag{6.38}$$

Taking the divergence of equation (6.37) yields:

$$\frac{\delta(\rho^m u_i^m)}{\delta x_i} - \frac{\delta(\rho^* u_i^*)}{\delta x_i} = -\frac{\Delta t}{2}\frac{\delta^2 p'}{(\delta x_i)^2} \tag{6.39}$$

Substituting equation (6.36) in the above results in:

$$\frac{\rho^m - \rho^*}{\Delta t} + \frac{\rho^* - \rho^n}{\Delta t} + \frac{\delta(\rho^* u_i^*)}{\delta x_i} - \frac{\Delta t}{2}\frac{\delta^2 p'}{(\delta x_i)^2} = 0 \tag{6.40}$$

Finally, writing the density correction in terms of the pressure correction using the state equation gives:

$$\rho^m - \rho^* = \frac{p'}{RT^m} \tag{6.41}$$

Substituting equation (6.41) in (6.40) results in the pressure correction equation as follows:

$$\frac{p'}{\Delta t R T^m} - \frac{\Delta t}{2}\frac{\delta^2 p'}{(\delta x_i)^2} = -\left[\frac{\rho^* - \rho^n}{\Delta t} + \frac{\delta(\rho^* u_i^*)}{\delta x_i}\right] \tag{6.42}$$

Once the pressure correction is evaluated, it is used to correct the pressure, velocity and density as follow:

$$P^m = P^{m-1} + p' \tag{6.43}$$

$$\rho^m = \rho^* + \frac{p'}{R T^m} \tag{6.44}$$

$$u_i^* = \frac{1}{\rho^*}\left(\rho^m u_i^m + \frac{\Delta t}{2}\frac{\delta p'}{\delta x_i}\right) \tag{6.45}$$

Hence, the pressure correction equation is spatially discretised in a similar manner to the discretisation of the generic transport equation described in the earlier sections. Integrating equation (6.42) over a control volume and then applying the Divergence theorem gives:

$$\frac{p'}{\Delta t R T^m}\Delta V - \frac{\Delta t}{2}\sum\left(\Delta A \frac{\delta p'}{\delta x_i}\right)_f = -\left[\frac{\rho^* - \rho^n}{\Delta t}\Delta V + \sum(\rho^* u_i^* \Delta A)_f\right] \tag{6.46}$$

where the summation is performed over each of the faces of area ΔA, and ΔV is the volume of the cell. Second order central differences are used to calculate the gradients $\delta p'/\delta x_i$. It is important to use the same discretisation for the pressure gradient in the momentum equation and the pressure correction in the pressure correction equation (6.42). This minimises the projection error and ensures convergence if an iterative scheme is used.

The boundary condition for the pressure correction equation at solid boundaries uses the zero-normal gradient condition, since the mass flux across these boundaries is constant. However for outflow boundaries, a special treatment is required to reduce the pressure reflections as discussed in later sections of this chapter.

6.3.4 Solution of the Algebraic Equations

The system of algebraic equations, obtained through numerical discretisation, is generally solved using linear equation solvers. The flow simulation code, PUFFIN, has two solvers, namely the Alternating-Direction-Implicit (ADI) solver and the Bi-Conjugate Gradient

Stabilised (BiCGStab) solver with a Modified Strongly Implicit (MSI) pre-conditioner. Current work has been carried out using BiCGStab to solve the momentum, scalar and pressure correction equations, which is more efficient and requires ten times fewer iterations to achieve the same level of convergence by ADI (Kirkpatrick, 2002).

Convergence of the solvers is measured using the L_2 norm of the residual (the L_2 norm is a vector norm that is commonly encountered in vector algebra and vector operations such as dot product). The residual was set to be less than 10^{-10} for the solution of the momentum and scalar equations, which typically require one or two sweeps of the solver to obtain convergence. At each time step, a number of iterations of the pressure/velocity correction steps are generally required to ensure adequate mass conservation.

The pressure correction equation is solved for all iterations with a condition: either to reduce the residual to 10% of its original value, or the BiCGStab solver has performed 7 sweeps. Each sweep of the solver includes 2 sweeps of the pre-conditioner. The solution is then used to correct the pressure and velocity field and the divergence of the corrected velocity field is calculated. The process is repeated until the L_2 norm of the divergence error is less than the pre-set value. Typically, 6 to 8 projections are required to attain the minimum divergence error.

6.3.5 Typical Iteration Procedure

In the case of unsteady, compressible reacting flows, where density and pressure variations are predominant, it must be ensured that the pressure, density and velocity are corrected simultaneously by enforcing mass conservation. The overall solution procedure for each time step follows a process similar to that of Kirkpatrick (2002) for compressible flows; however, the combustion modelling capabilities in LES have been enhanced using dynamic modelling of flame surface density (FSD). A typical iteration procedure requires information at current and previous time steps represented by superscripts *n* and *n-1* respectively. In the following, superscript *k* refers to the iteration cycle within the time step,

and the superscript 0 indicates the initial guess for the first iteration with a time step i.e. $k = 0$.

Step 1: Predict or choose appropriate initial values for the variables at time = 0. In the present work, a straightforward choice is adopted by choosing the solution values at the current time level as:

$$u_k^0 = u_k^n, \ \phi_k^0 = \phi_k^n \tag{6.47}$$

Step 2: Solve the scalar transport equations to obtain provisional values, which will facilitate a better estimate of the density early in the iteration process.

Step 3: Calculate the fluid properties such as temperature, density and molecular viscosity according to the combustion model implemented.

Step 4: Update the scalar field information, based on the new density available from the preceding step and solve for the momentum equation.

Step 6: Solve the pressure correction equation.

Step 7: Correct the pressure, velocity and density fields.

Step 8: Check the mass conservation error and repeat steps 6 and 7 as required.

Step 9: Calculate the eddy viscosity.

Step 10: Calculate dp/dt, S_{kk}, etc.

Typically 8 to 10 outer iterations of this procedure are required to obtain satisfactory convergence at each time step. The time step is limited to ensure that the Courant number (CFL number), C, remains less than 0.5 by enforcing a limit on the time advancement, δt, as follows:

$$C = \frac{\delta t u_i}{\delta x_i} \tag{6.48}$$

However, to avoid un-realistic times an extra condition has been imposed such that the upper limit for δt is 0.3 ms. The solution for each time step requires around 8 iterations to converge, with residuals for the momentum equations of less than 2.5e-5 and scalar equations less than 2.0e-3. The mass conservation error is less than 5.0e-8.

6.3.6 Numerical Implementation of the DFSD models

The flame surface density models have been detailed and implemented in the LES code, PUFFIN, to calculate the sub-grid scale reaction rate and other numerical parameters such as the model coefficients and fractal dimensions. The SGS reaction rate calculated by these models will be added to the source term of the reaction progress variable equation at every grid point and at each time step. All the models are programmed in a separate subroutine and invoked during step 1 and 4, while calculating and updating the scalar field iteration. It should be noted that for every time step, 8 to 10 outer iterations and several inner iterations are required to achieve the desired accuracy. At each of these inner and outer iterations, the reaction rate is calculated from the reaction progress variable information that has been stored.

From the equations (5.16), (5.17), (5.22), (5.32), (5.34) and (5.39), it is evident that the information required is the filtered reaction progress variable, the filter width, the test filter width, the laminar flame width and the SGS velocity fluctuations. It is worth mentioning here that most of the information, except the SGS velocity fluctuations, is available at step 2 at time = 0, and can be calculated without any difficulty. However, calculating the fractal dimension at the initial step using equation (5.34) may be slightly difficult due to the unavailability of the SGS velocity at that time. However, due to the upper and lower fractal limitations in equation (5.34), initial values will be within these limits and will be used as

an initial guess. Since the solution requires a minimum number of outer iterations, the fractal dimension in the case of (5.34) will be reasonable at the initial time step

6.4 Boundary Conditions

The mathematical model and the numerical scheme appropriate boundary conditions are important for successful LES predictions. From a mathematical point of view, the imposition of exact boundary and initial values are a prerequisite for a unique solution of the set of partial differential equations to be solved. In the present investigation, the problem considered is the propagation of the turbulent premixed flame, evolving from a stagnant condition in a rectangular chamber having multiple solid obstacles. Solving premixed flames requires the boundary conditions for all the dependent variables such as density, velocity, pressure, temperature and the reaction progress variable. Since the density is dependent on the pressure and temperature, the boundary condition for the density can be specified from the pressure and temperature. Continuity requires that mass conservation be satisfied over the complete domain at all times, and the boundary conditions for the velocity field must therefore ensure that given as:

$$\int_\Omega \frac{\partial \rho}{\partial t} dV + \int_S \rho u_i n_i S = 0 \tag{6.49}$$

For the combustion configuration under investigation, we imposed outflow boundary conditions at the outlet (top) of the chamber and solid wall boundary conditions for the rest of the walls (four vertical and one bottom) and the solid obstacles. The details of these boundary conditions are described in the following sections. The investigations of various outflow boundary condition cases are shown in Chapter8.

6.4.1 Outflow Boundary Conditions

The outflow boundary conditions generally use a zero normal gradient (ZNG) condition or a convective outlet boundary condition. The use of a zero gradient condition at an outflow boundary is generally given by:

$$\frac{\partial \phi}{\partial n} = 0 \tag{6.50}$$

where $\partial/\partial n$ denotes the gradient taken normal to the outflow boundary. Alternatively, the convective boundary condition is also given by:

$$\frac{\partial \phi}{\partial t} + U_b \frac{\partial \phi}{\partial n} = 0 \qquad (6.51)$$

where U_b is the bulk velocity across the boundary. It is very important in the case of a compressible flow that the pressure wave generated within the chamber must be allowed to leave smoothly without reflection. Since the pressure field is dependent on the velocity field, the boundary conditions applied for the velocity will determine the pressure wave behaviour. The outflow boundary conditions described in equations (6.50) & (6.51) work well when the dominant force on the fluid flow is due to advection and diffusion. However, in the present case (as shown in next Chapter 7 for a description of the test case), due to the compressible nature of the propagating flame, the dominant force is the pressure gradient resulting from pressure waves radiating from the chamber. Consequently, both the above boundary conditions would result in significant pressure reflections. Hence, to overcome this problem, Kirkpatrick (2002) developed a new non-reflecting boundary condition for velocity, analogous to the commonly used convective boundary condition in incompressible LES as:

$$u_i = \left(u_{i-1} - \frac{\Delta x_i}{C} \frac{\partial u_{i-1}}{\partial t}\right) \frac{R_{i-1}^3}{R_i^3} \qquad (6.52)$$

where u_i is the velocity on the boundary, *ui-1* is the velocity in the adjacent cell within the domain, Δx_i is the distance between the two nodes, R_i and R_{i-1} are the distance from the two nodes to the centre of the open end of the chamber and C is the speed of sound, which is convective velocity. To ensure that this boundary condition is accurate, the numerical domain has to be extended with far-field boundary conditions from the outlet of the chamber.

6.4.2 Solid Boundary Conditions

The natural boundary condition for velocity at solid wall boundaries is to set the normal and tangential velocity components to zero at the wall. These conditions correspond to the impermeable and the no-slip conditions ideally. At the domain boundaries coinciding with a stationary impermeable wall, the no-slip condition can be applied as:

$$u_i(x,t) = 0 \qquad (6.53)$$

It is very important in the case of turbulent reacting flows, that the near wall treatment should be accurate enough to account for the boundary layer effects. In general, the flow near the wall exhibits itself substantially differently than away from it, due to the shear forces within the vicinity of the wall. The predominant structures capable of determining the flow properties within this region are of the order of boundary layer thickness. Hence, in high Reynolds flows, it is very important to employ a fine grid in the domain near the wall, which eventually reaches the DNS limit in order to resolve the energy carrying scales. Refining the grid near the wall in LES is not possible due to computational limitations, and alternative methods, such as wall functions, are required to model the overall dynamics of the near wall effects. Hence, in the present investigation, the wall shear is calculated by the $1/7^{th}$ power-law wall function of Werner and Wengle (1991) as follows:

$$\tau_w = W(\tilde{u}, y) \qquad (6.54)$$

where τ_w is the wall shear stress, W is a functional dependence, y is the distance of the grid point from the wall and $\tilde{u}$ is the tangential velocity at y. Solid boundary conditions with this wall function are applied at the bottom, vertical walls, and for solid obstacles in the chamber.

6.5 Summary

This chapter describes the various numerical aspects of the LES simulation code. The code uses the finite volume methodology, which generally allows complex geometries to form grids and be solved successfully. Spatial discretisation and numerical implementation of a generic transport equation of variable ϕ have been detailed. Several challenges are discussed while dealing with the individual terms of the generic equation. Since the fluid flow numerically marches into time, the time advancement of the spatially discretised equations is very important for accurate predictions. In the mainly, the Crank-Nicholson time advancement scheme is discussed as it was used for momentum and other scalar equations. Pressure correction is critical as the fluid flow involved is mainly unsteady, compressible, which is generally involved in large density variations and is directly coupled with pressure via the state equation. Hence, the new methodology developed is used to

correct the pressure, velocity and density fields simultaneously by enforcing mass conservation. Various linear solvers available in the present numerical code were briefly outlined and the choice of BiCGStab to solve the system of linear equations has been explained. A typical iteration procedure used by the model is outlined with the possible modifications carried out, while accounting for the chemical reaction rate of the propagating flame. The various boundary conditions, such as solid and outflow, used in the present study are also presented and discussed.

Chapter 7   The Experiment Test Cases

This chapter presents a description of the experimental test cases that are used for model validation in the present investigation. The importance of the experimental turbulent flames and the influencing factors are described relative to the design of any experimental combustion configuration. The novel chamber established at the University of Sydney is an amended version and third inline to test turbulent premixed propagating flames. This chamber has a reconfigurable capability and obstructions, which facilitated the generation of a number of different flow configurations. A general introduction and some technical details of the various measuring techniques and the Laser ignition system are provided. Next, the typical experimental procedure and sequence of operations are detailed. Finally, a numerical domain with initial conditions and ignition details are discussed along with the various grids employed in the numerical simulations.

7.1 Influencing Factors in Designing the Explosion Chamber

Turbulence has been an unsolved problem for many decades using the available analytical and experimental techniques; a turbulence-flame interactions complicated by premixed turbulent flames is one of the very interesting and most challenging areas of research. In this regard, with the advancement of numerical prediction tools and computational power, numerical techniques have become an alternative method of solving turbulent fluid flow and combustion problems. In order to capture the correct physical and chemical properties of fluid flow problems, it is compulsory to validate the numerical model, the method and the technique against a valid experimental test case. Since the introduction of laser technology for the flow measurements in combustion studies, such as Laser Induced Florescence (LIF), Laser Doppler Velocimeter (LDV), Laser Doppler Anemometry (LDA) and Particle Image Velocimetry (PIV), extracting the more accurate information regarding turbulence intensity and various other flow parameters has been made possible. However, the major challenge is to quantify these measurements of turbulence and its interactions with a flame in a transient process of approximately, 10 to 20 ms duration.

As described in the first Chapter, turbulent premixed flames have significant practical importance in real engineering applications. Experimental studies of turbulent premixed flames have been carried out by several researchers with a variety of chambers and turbulence generating devices as detailed in Chapter 2. The work presented here mainly aims to simulate a real explosion situation, where multiple solid obstacles are presented in the path of a propagating flame, which is expected to facilitate understanding of some of the remaining key challenges such as complex feedback systems formed due to flame-flow interactions, local quenching due to abnormal flame stretch, flame dynamics with respect to position and number of obstacles etc. However, one of the objectives of this work is the application of the DFSD model against experimental studies, which is expected to give predictions of the combustion characteristics.

Hence, one of the main objectives of the current work was to develop the explosion chamber, so that could provide sufficient optical access for measurements and made affordable for computational modelling. It is worth mentioning here, that the original experimental chamber used by the combustion groups at both Loughborough and the University of Sydney (Masri et al., 2000, Ibrahim and Masri, 2001 and Masri et al., 2006) was a large chamber of 20 litres in volume, and was found to be impractical for LES modelling studies due to the expensive computational cost. Hence, an alternative design (Kent, Masri et al., 2005), that preserved the same physics and optical access, yet with a reduced volume of less than one litre was adopted. However, some of the experiments with various shapes of obstacles (Ibrahim and Masri, 2001) used with the big chamber of 20 liters to evaluate against a similar of numerical domain (as shown in section 7.4) and to demonstrate the explosion phenomenon in this study.

Essentially the present experimental combustion chamber is designed to represent many of the most realistic situations of the propagating turbulent premixed flames in a confined chamber, such as in an accidental explosion situation, an SI engine, bluff body combustion etc. Understanding the turbulence generation, the flame propagation speed and the flame interactions will help to design a better combustion device. This allows the analysis of the relationship between turbulence levels and flame surface density, and the associated influence/dependence of the flame front structure on turbulent burning rates to be related to other real world applications such as the prevention of loss and damage in case of accidental

explosions in built-up areas. One important factor influencing the design of any experimental chamber is that it should be easily applicable for model validations and numerical simulations. This requires well defined initial and boundary conditions and also the physical size must be affordable for numerical simulations in order to resolve the length scales (Masri et al., 2006). Additionally, good optical access is required to allow the imaging experiments to be easily performed. Considering the factors stated above, the experimental chamber designed in this investigation was a simple rectangular chamber with a provision to hold a maximum of three baffle plates and a solid obstacle in the path of the propagating flame.

7.2 Experimental Setup

As described in the preceding section, the experimental setup adopted in this investigation was originally developed by Kent, et al. (2005) at The University of Sydney. The early stage of the large chamber vessel consisted of a box, 545 mm in height, with a square cross section of 195x195 mm giving a total volume of 20 liters (Ibrahim and Masri, 2001). In Figure 6.1, several obstructions were mounted within the chamber and these were centered at 150 mm from the ignition end. The iteration (Masri and Ibrahim, 2007) of the combustion chambers is used in similar experimental investigations. Figures 7.2 and 7.3 illustrate the schematic representation of the vessel used in this study. The combustion chamber is a Perspex square prism, with internal dimensions of 50 x 50 mm, and an overall length of 250 mm giving an experimental volume of 0.625L. The external prism is constructed from 20 mm thick Perspex walls, which are used to enclose the thinner 5 mm Perspex combustion chamber. The external prism encapsulates the inner chamber rigidly and adds additional strength in order to withstand the shock waves encountered during the explosion. The external and internal prisms are placed in-between a Perspex base plate and an open vented aluminum top plate, and the entire rig is then held firmly together using draw bolts.
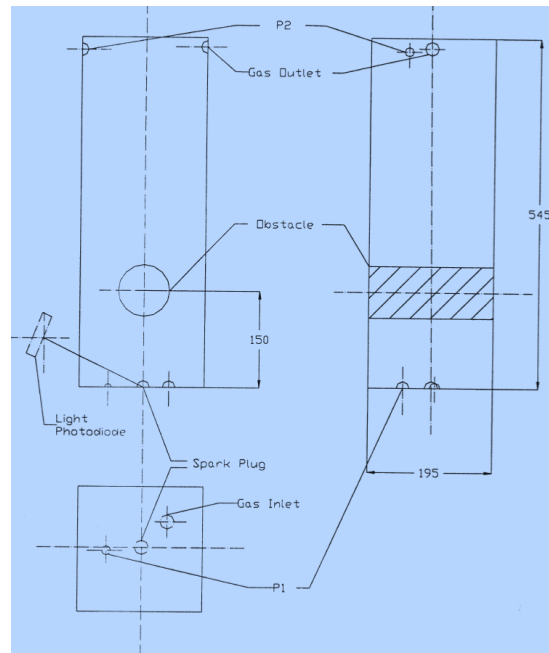
Figure 7.1 Schematic of the experimental rig used for early the stage 20 liters explosion chamber. (Dimensions in mm)
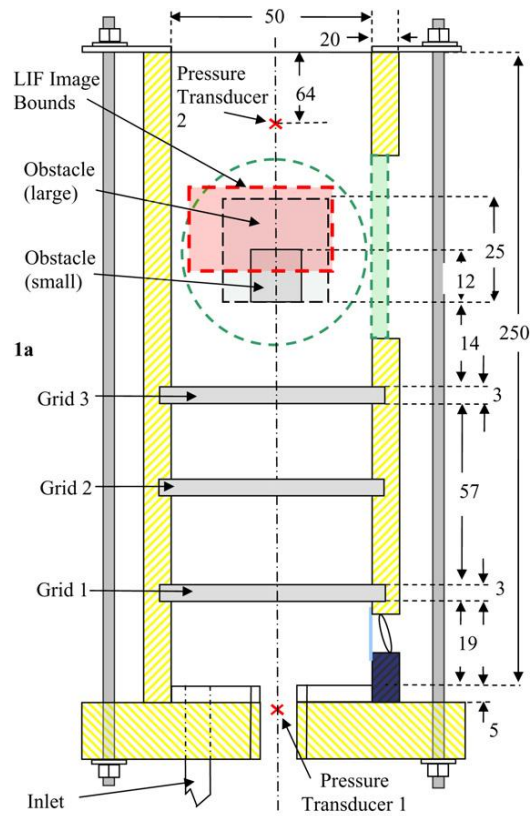
Figure 7.2 Schematic diagram of the latest 0.625 liters combustion chamber. (Dimensions in mm)
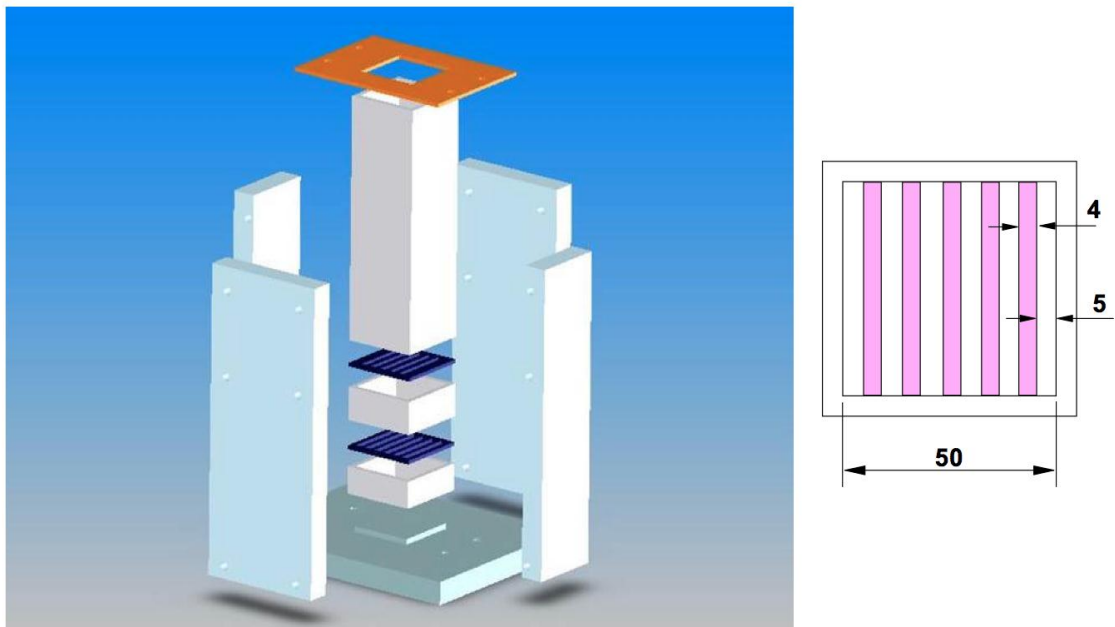

Figure 7.3 Solid diagram showing the baffles, and the internal and external structure of the setup for the latest chamber.

Horizontal grooves (stations) are cut into the sidewalls at locations of 20 mm (S1), 50 mm (S2) and 80 mm (S3) downstream of the ignition point in which the turbulence inducing baffle plates can be housed. For this investigation, the baffle plates are situated at various combinations of these locations in order to alter the turbulence generating characteristics of the flame and the flow properties. The plates are constructed from a 3 mm thick aluminum sheet placed perpendicular to the propagating flame front, and consist of five 4 mm wide strips evenly separated by six 5 mm wide spaces, rendering a blockage ratio of 40% as shown in Figure 7.3. A solid square obstacle of 12 mm or 24mm in cross section with a blockage ratio of 24% or 48% is centrally located at 96 mm from the ignition point running through-out the chamber, causing significant disruption to the flow. The influence of the individual obstacles in generating turbulence and flame propagation is detailed in the following section. Several configurations were extracted from Kent, Masri et al. (2005), Hall (2006 & 2008) and Masri et al. (2011) based on the number and the position of the baffle plates, and these are illustrated in Figure 6.4. Initially, the LES simulations were carried out using DFSD for the chemical reaction rate to establish the various shapes of obstacle modelling. Table 7.1 presents the details of the LES simulations, carried out for various configurations using various models. Gubba (2009) was able to validate the configuration Family 1, therefore, the present work mainly focuses on Family 2 and various shapes of solid obstacles. Table 7.2 presents a check list of the available experimental data used in this investigation to compare with the LES simulations.

All experiments conducted by Kent et al. (2005) and Masri et al. (2012) used liquefied petroleum gas (88% C3H8, 10% C3H6 and 2% C4H10 by vol.), which enters through a non-return valve in the base plate at a flow rate of ~20 g/min and equivalence ratio of 1.0. To ensure that all the products from previous combustion runs are cleared from the vessel, it is flushed with air before each test. The fuel air mixture then flows into the test rig for a long enough time such that more than three times the volume of the vessel is supplied to purge the flame chamber and to ensure the mixture is homogenous. A hinged flap closes the top of the vessel during filling. This flap, actuated via a pneumatic valve, is opened prior to ignition to allow the exhaust gases to escape, and remains open until the completion of the combustion process. The entire experimental sequence, from the initial filling of the vessel to the opening of the flap, the ignition of the mixture and the operation of the LIF components is automated using computer software.
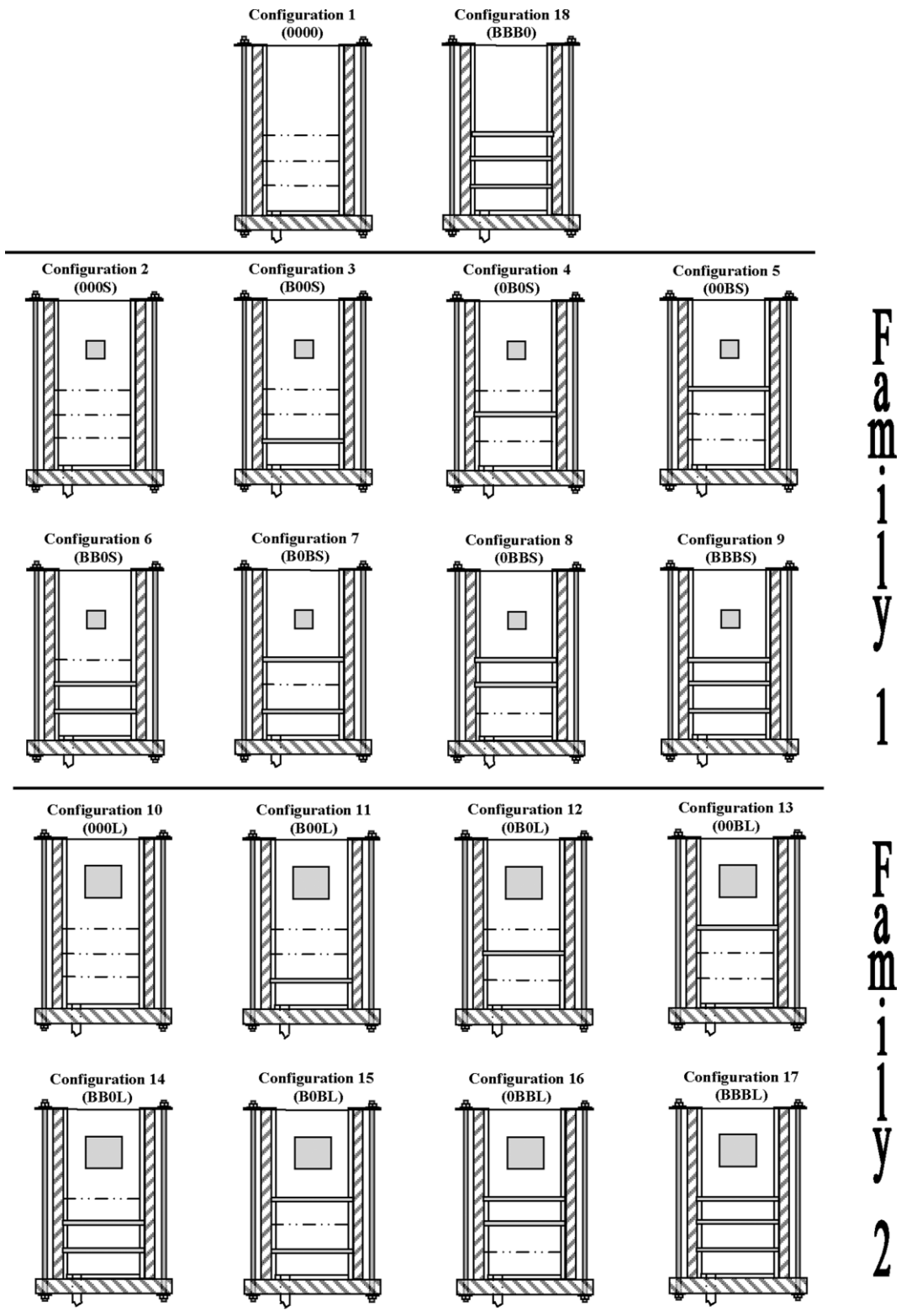
Figure 7.4 Illustration of various Families of configuration of baffle plates and two different sizes of obstacles.

7.2.1 Position of Baffles and Solid Obstacles

The introduction of baffle plates and obstacles into the flow inside the combustion chamber serves to increase the turbulence level and the flame propagation speed. The position and number of the baffle plates employed with respect to the square obstacle significantly alters the generated peak pressure, the flame speed and the structure (Kent et al., 2005, Masri et al., 2006 and 2012). From these experimental investigations, it is found that the addition of baffle plates increases the overpressure, speeds up the flame and causes a significant level of stretching in the flame front as it jets through the baffles. Higher turbulence levels increase the burning rates and hence the overpressures at an even faster rate than the flame speed. Hence a large increase in the overpressure can be gained through only a small increase in the flame speed. In the present work, the influence of the individual baffle plates and the square obstacle on the flow is discussed with particular relevance to how the solid obstructions placed inside the chamber change the turbulence level and the regime of combustion.

Baffle Plate One (S1) This plate is located at 20mm downstream from the ignition closed end. Due to the close proximity to the ignition point the flame speed is still relatively low, thus this obstacle only has a small effect on turbulence generation. Hence re-laminarisation of the flame front shortly after this obstruction can be observed. The main purpose of this baffle plate is to increase the initial propagation speed of the flame front, hence leading to a faster time to peak pressure.

Baffle Plate Two (S2) This plate is located at 50mm downstream from the ignition closed end. This serves both to increase the pressure and increase the propagation speed of the flame. In particular it affects the positioning of the flame front at peak overpressure.

Baffle Plate Three (S3) This plate is located at 80mm downstream from the ignition closed end. This is most effective at increasing the amount of turbulence generated within the combustion chamber. Flame accelerates at its greatest after hitting this baffle, thus increasing the amount of turbulence and the flame propagation speed.

Small Square Obstacle (S. Sq. Ob.) The small, solid square obstacle is located at 96 mm downstream from the ignition closed end. This is not a turbulence-inducing device as such but does serve to increase the blockage ratio and hence alter the development of the flame front. Rapid acceleration of the flame is recorded past this obstruction followed by the wrapping of the flame in the recirculation region, which enhances the mixing and distortion at the flame front.

Large Square Obstacle (L. Sq. Ob.) This large, solid square obstacle is used instead of the small, solid square obstacle also located at 96 mm downstream from the ignition closed end. This large device increases the blockage ratio even more, and rapid acceleration of the flame is recorded past the obstruction followed by the wrapping of the flame in the large recirculation region. However, there might be decreases in the overpressure for some of the cases because of the large blockage ratio.

Configuration	Obstacle Layout				LES Simulations			
	B1	B2	B3	OBS	Coarse	Med	Fine	V Fine
Cylinder	--	--	--	S			Y	--
Cylinder	--	--	--	L			Y	--
Triangle	--	--	--	S			Y	--
Triangle	--	--	--	L			Y	--
Wall/plate	--	--	--	S				--
Wall/plate	--	--	--	L				--
Family1								
1							Y	
2	--	--	--	S	Y	Y		--
				SQ OBS				
Family2								
10	--	--	--	L		Y		--
11	Y	--	--	L				--
12	--	Y	--	L				--
13	--	--	Y	L				--
14	Y	Y	--	L				--
15	Y	--	Y	L				--
16	--	Y	Y	L				--
17	Y	Y	Y	L	Y	Y	Y	Y
18	Y	Y	Y	--				

Table 7.1 Details of the LES simulation carried out for the possible configuration shown in Figure 7.4. Y indicates the presence of baffles, S and L indicate the presence of small and large sizes of obstacles.

Configuration	Overpressure	Flame Position	Velocity Measurements	OH Images
Cylinder	Y	--	--	--
Cylinder	Y	--	--	--
Triangle	Y	--	--	--
Triangle	Y	--	--	--
Wall/plate	Y	--	--	--
Wall/plate	Y	--	--	--
1	Y	Y	--	--
2	Y	Y	--	--
10	Y	--	--	--
11	Y	Y	Y	--
12	Y	Y	Y	--
13	Y	Y	Y	--
14	Y	--	--	--
15	Y	--	--	--
16	Y	Y	Y	--
17	Y	Y	Y	--
18	Y	Y	Y	--

Table 7.2 Check list of experimental data available to validate LES simulations.

7.2.2 Ignition System

Using a focused laser pulse to ionise the atoms in the chamber creates a spark which ignites the fuel/air mixture in the experimental chamber. The laser system used in the present experiment allowed for a precise and repeatable ignition point with an easily definable reference time (Hall, 2006). To avoid the surface interference and to attain a higher level of consistency, the laser beam is supposed to be focused just above the bottom of the combustion chamber. Two prisms are used to direct the laser beam to the focusing lens fitted into the Perspex wall as shown in Figure 7.5.

A Neodymium-doped Yttrium Aluminum Garnet (Nd:Y3Al5O12) laser is used to ignite the fuel/air mixture by focusing the infrared output onto the centre surface of the base plate. The Nd:YAG laser produces two simultaneous beams of varying wavelength, the first is the infrared spectrum and the second is a green beam (532nm). The primary role of the green beam is to track the path taken by the pulse for aligning purposes as the infrared spectrum is not visible to the naked eye. An external control console is used to adjust the intensity and the frequency of the laser pulse.
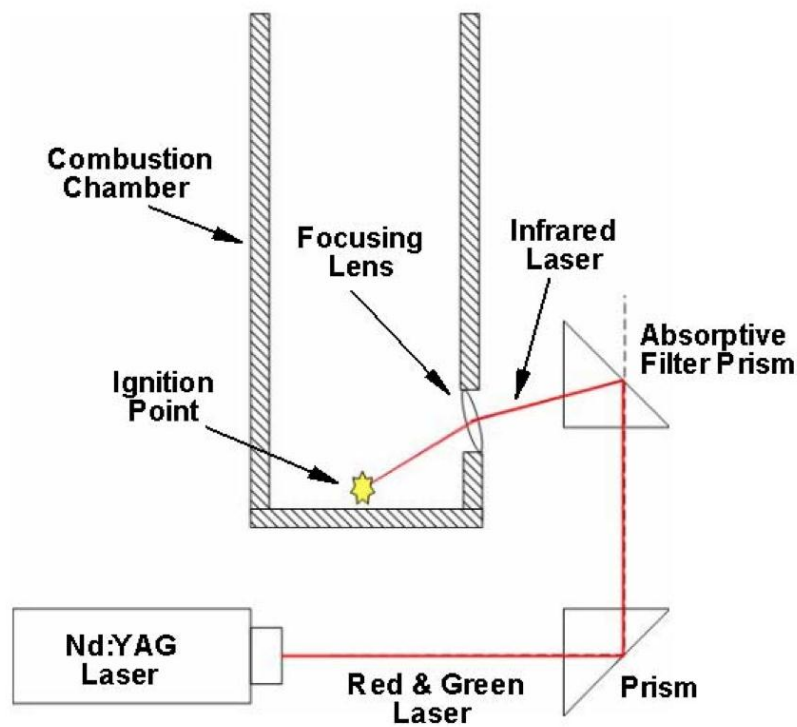
Figure 7.5 Layout of the Laser assisted ignition system. (Hall, 2006)

7.2.3 High Speed Imaging System

A Redlake high-speed digital camera is used to obtain images of the propagating flame. The full resolution of the camera (480x420 pixels) may be obtained at framing rates of up to 250 frames per second (fps). Due to the quick nature of the explosion event the camera was operated at 2000 fps with a shutter speed of 1/2000 seconds and an image resolution of 304x72 pixels. This resolution is convenient for the elongated chamber used in the present

study, with each pixel being about 0.8mm by 0.7mm respectively along the length and width of the chamber. After its origination, the flame takes approximately 13 ms to come out of the chamber (typically in the case of Configuration 1). MIDAS software is employed to records the flame images simultaneously with the pressure data, which is logged at a rate of 10 kHz. This ensures that, for the matching configurations, the same reference point with respect to the timing from the ignition point is used in both experiments.

7.2.4 Pressure Transducers

The pressure is measured using piezo-resistive pressure transducers with a range of 0-1bar and a response time of 0.1ms. These devices utilise quartz crystals that develop a charge relative to the pressure applied. The piezo-resistive sensor is particularly sensitive to rapid changes in pressure and hence makes it an ideal choice for this experiment. Two pressure transducers are employed to measure the pressure, one is positioned at the ignition end of the vessel and the other is positioned after the square obstruction from the ignition point. The pressure signals measured from both the transducers are confirmed to follow the same trend with slight variations. However, the overpressure details used in this work to compare LES simulations use the base pressure transducer, unless otherwise stated.

7.2.5 Laser Doppler Velocimeter

Hall (2006) employed the Laser Doppler Velocimeter (LDV) technique to extract the flow field measurements. LDV allows a direct qualitative analysis of particles in a flow as they enter the focal area. Each realisation of the LDV measures the instantaneous transverse and longitudinal components of the velocity. The root mean square (RMS) velocity can be calculated from these instantaneous velocity components, which indicates the turbulence intensity present in the flow.

The LDV system consists of an Argon Ion Laser, which produces the beams that will be directed into a separate box to turn the wavelength and focus the laser. After the laser has been filtered, a fibre optic cable is used to transfer the laser to the combustion chamber. The

LDV system requires two beams to focus inside the combustion chamber at the location of interest, perpendicular to the direction of propagation. Both wavelengths, 488nm (blue light) and 514.5nm (green light) are then scattered by the seeding particles, which are composed of Talcum Powder (Hydrous Magnesium Silicate – Mg_3 [Si_4O_{10}](OH)$_2$) in this case, and then received by the photo detector which is mounted at 180° to the emitter.

7.2.6 Laser Induced Fluorescence of OH

Planar Laser Induced Fluorescence from the hydroxyl radical, OH (LIF-OH) is performed using a typical arrangement, with a Pulsed YAG laser (Spectra-Physics DCR-2A) being used to pump a Pulsed Dye Laser (Spectra-Physics PDL-2). The beam is then passed through cylindrical optics to form a thin sheet of approximately 200μm thick which illuminates the viewing region. The laser is positioned 110mm downstream pointing through a 1-inch diameter quartz-viewing window with the CCD camera placed at a right angle, with the lens pointing through a second quartz-viewing window. The experimental test rig with CCD camera and viewing windows can be seen in Figures 7.6 and 7.7.

The exciting wavelength is 282.93nm with the LIF being collected at 310nm on a CCD camera using 648x595 pixels imaging an area of 28x23mm (Kent, Masri et al., 2005). The timing is such that the LIF measurement is made just when the flame front is crossing the imaging window. Since the OH is formed in the reaction zone of the flame and is rapidly quenched by cold un-reacted gases, it is a good indicator of the flame front position in flames where the reaction zone is thin (Abu-Gharbieh et al., 2001). Hence this technique is suitable for use with a premixed turbulent flame front, giving negligible perturbation of the flow whilst attaining high temporal and spatial resolution (Kaminski et al., 2000).
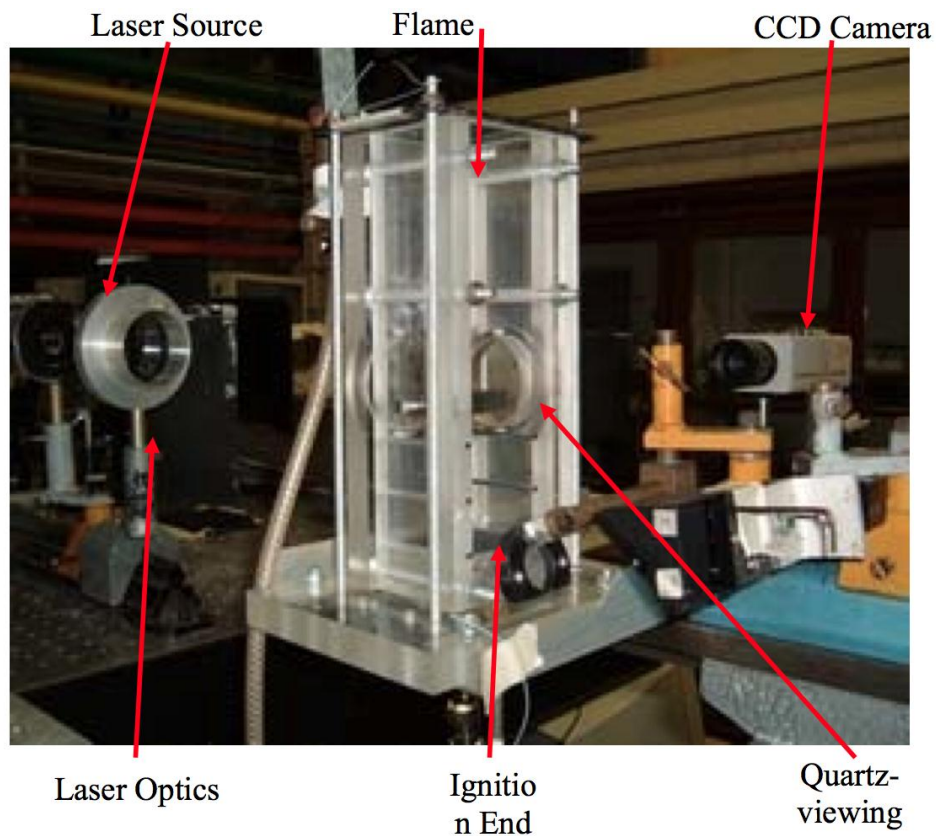
Figure 7.6 Experimental setup of LIF-OH (Kent et al. 2005)

Figure 7.7 Experimental rig of the turbulent premixed combustion chamber (Hall, 2008)

7.3 Experimental Procedure

The entire experimental sequence is controlled by a computer, operating all the equipment and solenoid valves in a predetermined sequence. The fuel/air mixture is directed to the combustion chamber either directly or by passing via the seeding vessel and finally straight out to the exhaust. The technical issue involved in directing the fuel/air mixture through the various way points as the experiment progresses, arises due to the seeding of the fuel before it enters the chamber. This may corrupt the outcome of the experiment. However, to avoid the risk of corruption of the results, two sets of two-way valves are used in series as shown in Figure 6.8, which are also operated by the computer. Both the ignition laser and the LDV system are also controlled by a computer to enable a base timeframe for the collection of the data.

7.3.1 Experimental sequence

As a typical experimental procedure is involved in co-ordinating several systems, such as the fuel direction system, the high speed imaging system, the pressure transducers, the Laser system for ignition and for flow measurements, the entire sequence is controlled and the data is collected by three computers.

Step 1: Before starting the experiment, the LDV system needs to be prepared by warming up, and will remain on indefinitely as long as the cold cooling water is continually supplied. The power output of the LDV can be controlled using an external console by setting the current to 25 amps to maintain a power of 4.5 W.

Step 2: Cooling of the ignition system should be initiated before firing the laser into the combustion chamber. The laser must be fired at the centre of the chamber approximately 2 mm above the lower surface to avoid interference and damage to the base Perspex plate. The frequency of the laser should be adjusted by an external control box, to ensure a spark is produced at every pulse.

Step 3: To ensure the fuel/air mixture supply into the combustion chamber, turn on the fuel at the gas bottle and the compressed air.

Step 4: Turn on the mass flow meter and confirm the pipes and valves are not leaking. A digital flow controller controls the quantity of the fuel/air mixture entering the combustion chamber. Sufficient time is allowed to settle the fuel/air mixture in order to achieve quiescent conditions before ignition.

The entire system works from three independent computers, a Mac and two PCs, which are not networked and must be operated simultaneously to collect the data for each run. The Mac is responsible for running the experiment from the programmed macro, while the first PC was connected to the LDV system and the second was connected to the pressure sensor and high speed imaging system. Both PCs are responsible for correlating all the results.
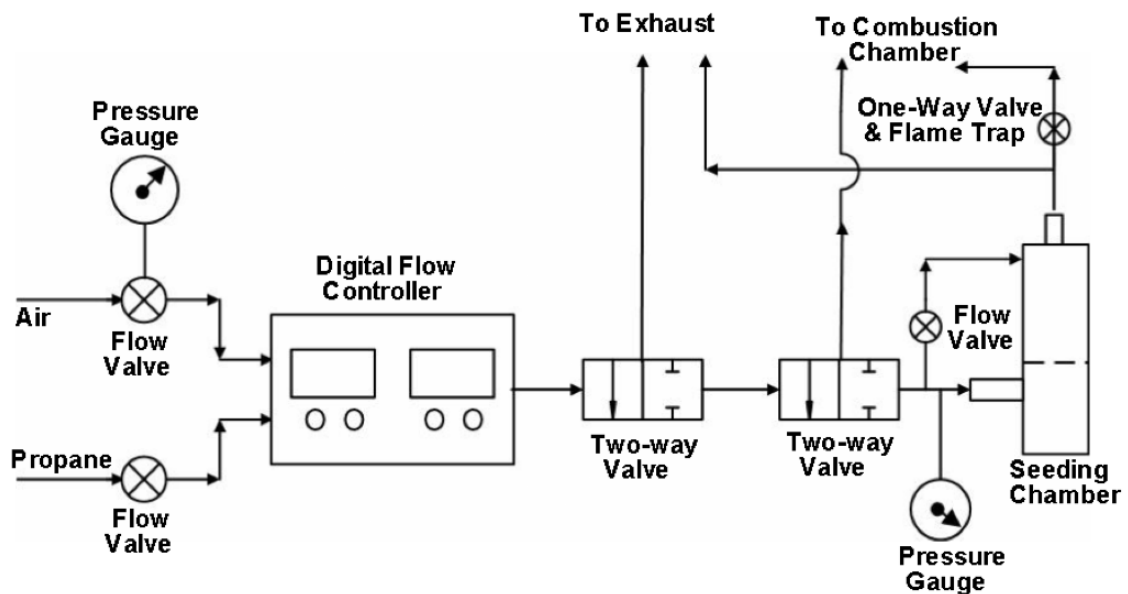

Figure 7.8 Two-way valve fuel/air direction system (Hall, 2006)

7.4 Numerical Domain

In order to simulate the turbulent premixed flame of the stoichiometric propane/air flame, in the combustion chamber shown in Figure 7.2, a computational domain with initial and boundary conditions is required. As described in the preceding chapter, in the case of compressible flows, the domain must extend in the direction normal to the outflow boundary to avoid pressure reflections. However, to avoid certain numerical instabilities, in general, the domain is extended in the other two directions as well. A typical computational domain, superimposed with the numerical combustion chamber and obstacles is shown for clarity in Figure 7.9. The combustion chamber has dimensions of 50 x 50 x 250 mm where the flame propagates over the baffles and solid obstacle surrounded by solid wall boundary conditions. To ensure that the pressure wave leaves the chamber smoothly, without reflections, the open end of the domain is extended to 250 mm in the z-direction with far-field boundary conditions. Similarly, the domain is extended to 325 mm in the x and y directions with large expansion ratios approximately equal to 1.25 outside the combustion chamber.

The simulations are carried out for the 3-D, non-uniform, Cartesian co-ordinate system for a compressible flow, having low Mach number. In order to examine the solution dependence on the grid resolution, simulations are performed with four different grid resolutions as detailed in Table 7.3. All the calculations are submitted to the Sun Grid Engine which is a high performance computing (HPC) cluster having 24 processors and with 35 GB RAM. Typical running times are also provided in Table 7.3 for clarity.

Grid	N_x	N_y	N_y	Grid Resolution in millions	Computational time in days
I	40	40	156	0.25	$\frac{1}{2}$
II	54	54	190	0.55	1
III	90	90	336	2.70	10
IV	90	90	448	3.62	30

Table 7.3 Grid resolutions applied to the present work, N_x, N_y and N_z are present nodes in the x, y and z directions.
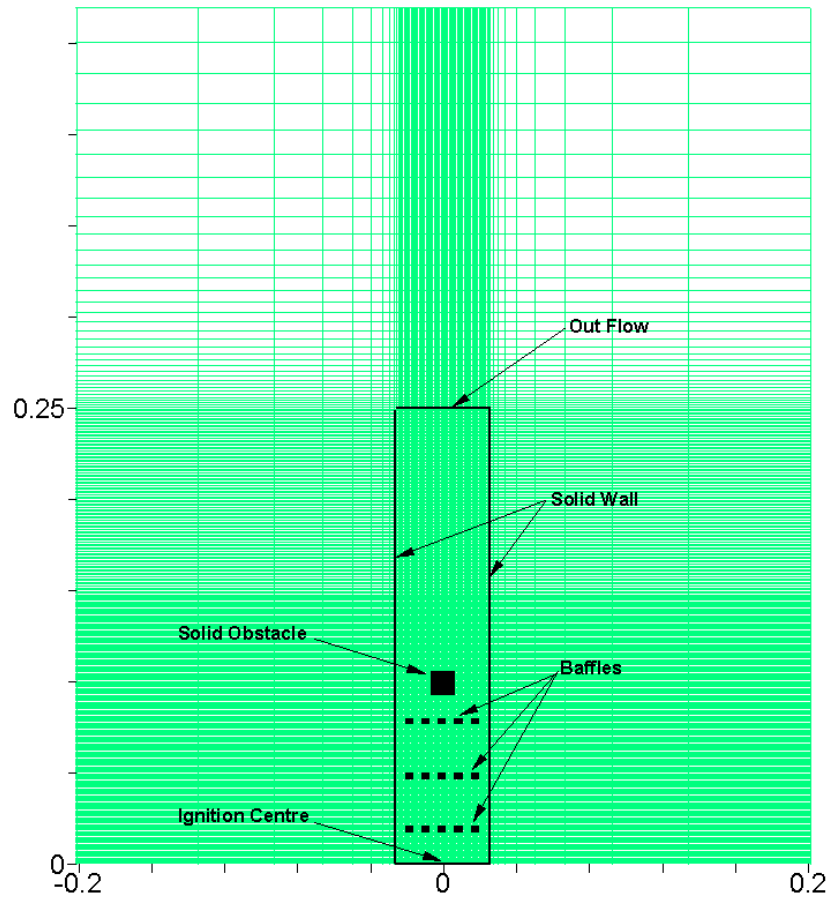
Figure 7.9 Illustration of the computational domain with the combustion chamber and obstacles superimposed over the Fine grid resolution in the above table.

7.4.1 Initial Conditions

Initially, i.e. at the time of starting the new simulations, the energy and reaction progress variables are set to zero everywhere in the computational domain. The initial velocity field is quiescent, with a random perturbation field to allow for the development of turbulence. In order to achieve the initial quasi-laminar flame phase corresponding to the experiments, ignition is modelled by setting the reaction progress variable to 0.5 within the radius of 4 mm (Bradley and Lung, 1987) at the bottom centre of the chamber most of the time. However, the radius of the ignition influence of the overpressure timing is shown in Chapter 8.

7.5 Summary

This chapter summarises the influencing factors in the design of the experimental combustion chamber and the challenges faced in the past due to large scale experimental test rigs. A novel chamber, recently developed through collaboration with The University of Sydney Combustion group, which can retain the combustion physics with good optical access has been discussed. Details of the individual obstacles used, and their influence in generating turbulence and overpressure of the propagating premixed flame, are also presented and discussed. Brief details of various measurement devices used such as the LDV and LIF-OH, and techniques such as ignition control and image capturing, were presented and discussed. A typical experimental sequence controlled by a computer has been illustrated through a flow diagram. Finally, the numerical domain, initial conditions and the various grid resolutions employed in the present simulations are described and justified for use in the current work.

Chapter 8   Results Validation and Discussions

8.1 Introduction

For modelling of industrial exploration, it is a common practice to validate model prediction against experimental data for the generated overpressure. This important parameters used by design engineer to improve the layout and arrangement of various components within an off and on shore plants. This is usually done to achieve a safer design against accidental explosion event. This is presented in the chapter together with other explosion parameters. This chapter presents results and discussions from the LES simulations of stoichiometric propane/air turbulent premixed flame, propagating over various solid obstacles in a vented explosion chamber. As described in chapter 6, model validation is carried out against experimental data published by Ibrahim et al. (2001), Kent et al. (2005), Hall (2009) and Masri et al. (2012). This chapter presents as follows:

- ❖ Results are presented and discussed from the LES simulations with the DFSD model (Eq. 5.16) for configuration 9 to identify the influence of solid obstacles on turbulence generation and flame characteristics. Further numerical optimisation studies are also presented for configuration 9.

- ❖ Grid independency test results using the DFSD model. Moreover, other numerical aspects such as filter width and model coefficient are presented and discussed.

- ❖ Results from the grid independent solution for the flow and flame structure during different phases of flame propagation from ignition to the completion of combustion.

- ❖ Study of the effects of outflow boundary conditions.

❖ Results for the velocity and length scales from the LES simulation in order to identify the regimes of turbulent premixed combustion of explosion in the current combustion chamber.

❖ Discussions on the effects of different shaped solid obstacles on the explosion phenomenon in the chamber are discussed.

❖ Finally, parametric studies are presented and discussed to examine the influence of the position and number of solid baffles in the flame structure and the generated overpressure.

8.2 Results of the DFSD Model for Explosion

In this section, results from LES simulations of turbulent premixed flames, propagating past solid obstructions built inside an open ended rectangular combustion chamber, are shown in Figure 6.2 are presented. Here, the model used is the Dynamical Flame Surface Density (DFSD) model. Various parametric studies have been carried out to establish confidence in using the LES methodology to simulate turbulent premixed flames. From the experimental studies of Kent et al. (2005), it has been identified that the overpressure and turbulence levels are very low in configuration 10 as section 8.6.1 and not much insight was extractable, when compared to a more complex configuration such as configuration 9 shown in Figure 6.4. Hence, this analysis has been carried out using the complex configuration 9 having three baffles and a small square solid obstacle as shown in Figure 6.2. Masri et al. (2012) identified that configuration 9 has yielded larger overpressure with a high stretched turbulent flame. This was due to the presence of multiple solid obstacles. For this reason, configuration 9 has been chosen, in the current work, to carry out parametric studies to optimize various parameters used with the LES-DFSD model, such as grid resolutions, filter width etc. Further to this, studies have been extended to simulate other flow configurations in order to examine the effects of different flow configurations on the flow and combustion characteristics in vented explosions.

8.2.1 Grid Independency Tests

The grid dependency, in numerical simulations, is a controversial and much debated topic (Klein, 2005) as it depends on many numerical and physical aspects, especially in LES. However, in numerical modelling, it is desirable to achieve substantial uniqueness of results, independent of the grid resolution employed. Hence, in the present investigation, LES simulations of turbulent propagating premixed flames have been carried out by refining the grid employed for configuration 9, as detailed in Table 7.3. Four tests cases have been considered with different total number of computational cells. Case I with 0.25 million, case II has 0.55 million, case III has 2.7 million and case IV has 3.6 million grid points in the computational domain as shown in Figure 6.9. All these simulations were carried out using the simple dynamic flame surface density model with the model coefficient, $\beta = 1.2$. The pressure-time histories of the overpressure near the closed ignition end of the chamber are considered here as a bench mark to assess the grid dependence of the LES results. Pressure-time histories for cases I, II, III and IV are presented together with the experimental data reported by Masri et al. (2012) in Figure 8.1.

From Figure 8.1, it is evident that grids I and II show an initial increase in overpressure at 5 and 6ms after ignition, respectively, while this instance corresponds to 8 ms for grid III and IV, which is in reasonable agreement with the experimental measurements. This initial increase in overpressure in the cases of grid III and IV correspond to the time where the flame is due to interact with the third baffle plate (see Figure 6.2). It can also be noticed, that the slope of the peak overpressure using grids III and IV is well calculated. Evidently, these calculations confirm the peak overpressures of 113 and 108 mbar, occurring at the small vitiating time i.e. 10.63 and 11.01ms for grids III and IV, respectively. Based on the peak overpressure and its time of incidence, LES results can be considered grid independent, beyond the grid resolution III. However, LES calculations with grid IV were found to under-predict and grid III found slice over predict to the experimental peak pressure of 111.98 mbar occurring at 10.7 ms after ignition, It is identified that this may be mainly due to the usage of a constant value for the model coefficient β However, grids III and IV are in good reasonable agreement with the experimental data in terms of the rate of pressure rise and overpressure trend. Further to this, the influence of the filter width on the grid independency is studied and discussed in the following section.
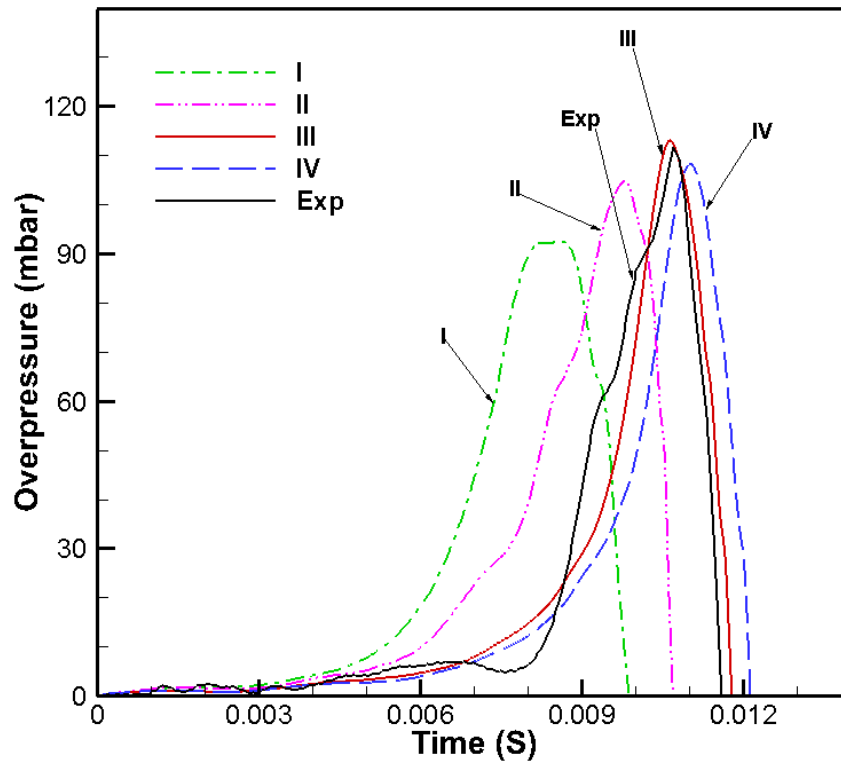
Figure 8.1 LES prediction of overpressure vs. time histories using four grids resolutions

detail in Table 7.3 are compared with experimental measurements

Scalars	I	II	III	IV
δx(mm)	2.0	1.47	0.75	0.75
δy(mm)	2.0	1.47	0.75	0.75
δz(mm)	1.0-2.0	1.0-1.75	0.75-1.0	0.48-0.75
$\bar{\Delta}$(mm)	3.17-4.0	2.60-3.12	1.5-1.65	1.29-1.5
$h/\bar{\Delta}$	0.32-0.5	0.39-0.56	0.5-0.6	0.37-0.5
L_f(mm)	0.294	0.294	0.294	0.294
$\bar{\Delta}/L_f$	10.8-13.6	8.78-10.6	5.1-5.61	4.40-5.10
Peak Overpressure (mb)	92.43	104.78	113.02	108.26
Time (ms)	8.54	9.8	10.63	11.01
Flame speed (m/s)	88.0	81.3	64.48	74.71
Flame position (cm)	13.9	19.12	16.25	16.81

Table 8.1 Detail of the numerical parameters applied and results deduced from LES

predications with four grids resolutions for the configuration shown in Figure 8.1.

8.2.2 Influence of Filter Width

The accuracy of the solution in LES is associated with several numerical and modelling parameters such as grid spacing h, filter width Δ, discretization schemes, solver, initial and the boundary conditions employed. For a given discretization scheme, solver, initial and boundary conditions, the remaining critical numerical parameters that affect the LES solution are the grid spacing and the filter width. Filtering the flow field for large eddies by choosing an appropriate and optimal filter width does resolve the maximum amount of turbulence kinetic energy, which is a unique concept and distinguishes LES from other modelling techniques such as RANS and DNS. In the present investigation, the box filter presented and discussed in equation (4.5) is used.

In a conceptual study, Pope (2004) hypothesizes that LES solution may reach an intermediate asymptote when the filter width lies within the inertial sub-range. The relationship between grid spacing and filter width has been studied as a ratio of $h/\bar{\Delta}$ by Vreman et al. (1996) and Chow and Moin (2003) for non-reacting cases. Their studies concluded that small values of $h/\bar{\Delta}$ correspond to excellent numerical accuracy and the higher values correspond to resolving a greater range of turbulence motions with less numerical accuracy. Vreman et al. (1996) and (Chow & Moin, 2003) and Moin (2003) identified that, with a specified SGS model for turbulence, $h/\bar{\Delta} \leq 0.25$ with second order spatial accuracy or $h/\bar{\Delta} \leq 0.5$ with sixth order spatial accuracy has given numerically accurate solutions. Examination of this fact in the case of reacting flows is computationally very expensive and requires an extensive experimentally validated DNS solution.

In the present work, numerical investigation has been made to examine the dependency of the numerical accuracy on the filter width. Two important ratios associated with the filter width, Δ have been selected. Firstly, the grid spacing of the filter width as discussed earlier and second is the ration of the filter width to the laminar flame thickness. Grid spacing, h in the present study is not uniform and generally varies in the direction of flame propagation i.e. z-axis. Therefore all the relevant estimates used here are calculated using the grid spacing in the flame propagating direction and are presented in Table 8.1.

For grids I, II, III and IV as shown Table 8.1, the $h/\bar{\Delta}$ ratio is plotted against filter width as shown in Figure 8.2. Correlating Figure 8.1 and Figure 8.2, elucidates the fact that the accuracy of the solution is improved in terms of overpressure inside the chamber, as $h/\bar{\Delta}$ ratio tends to zero with respect to filter width. Referring to the time traces of the overpressure shown in Figure 8.1 for all the four grids, the dependency of the numerical accuracy on grid spacing is very clear. Considering the $h/\bar{\Delta}$ ratio from Table 8.1 for grids I, II and IV, it can be noticed that, they are identical in range and the accuracy of solution IV is in close agreement with the experimental measurements. From the time history of overpressure for cases III and IV shown in Figure 8.1, it is evident that the solution is grid independent in terms of the occurrence of peak overpressure. However, the $h/\bar{\Delta}$ ratio for grid III is 0.5 to 0.6 and is different from the values from grid IV, which vary from 0.37 to 0.5. This analysis clearly shows the dependency of the numerical accuracy on the filter width. It is evident from Table 8.1, that even a small change in $h/\bar{\Delta}$ affects the accuracy of the solution. Clearly the $h/\bar{\Delta}$ ratio demonstrates improvement in the accuracy of the solution as the value of $h/\bar{\Delta}$ diminishes.
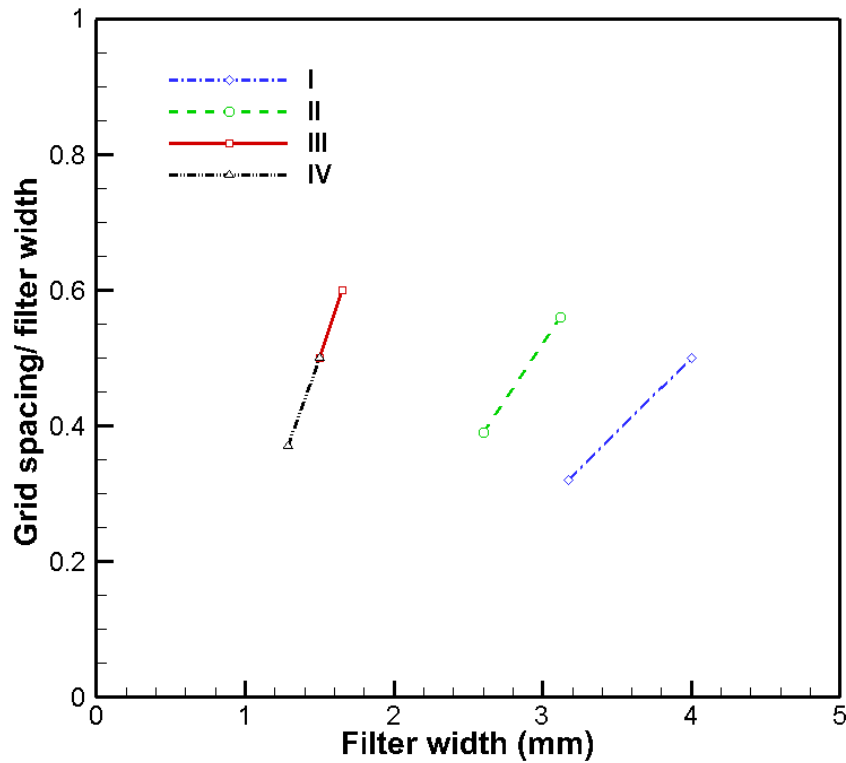

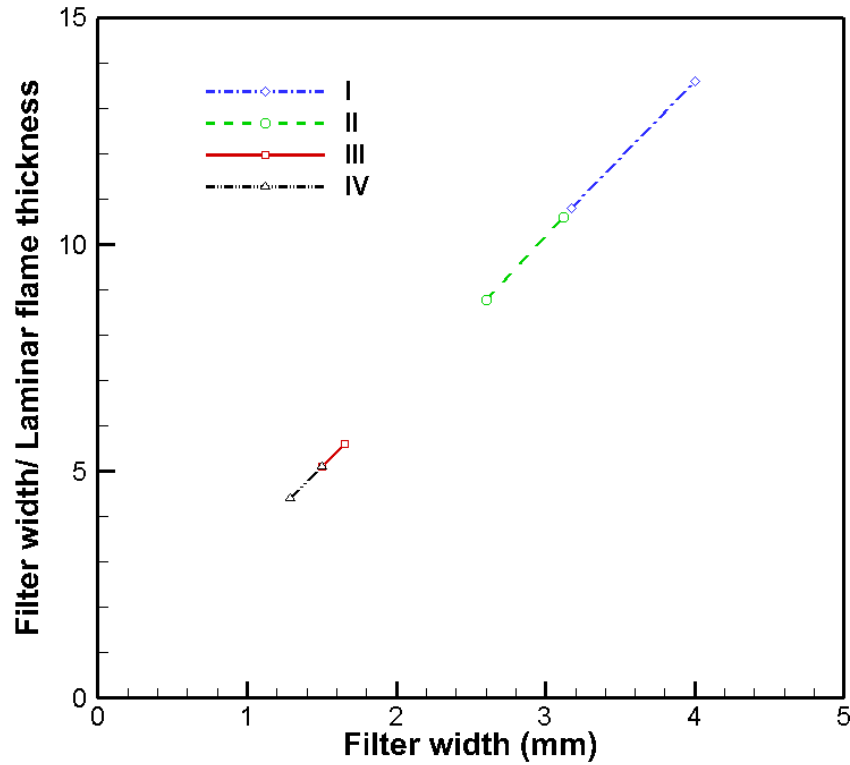Figure 8.2 Raito of grid spacing to filter width ($h/\bar{\Delta}$) vs. filter width.

Figure 8.3 Raito of filter width to laminar flame thickness $(\bar{\Delta}/L_f)$ vs. filter width.

Considering the second ratio shown in Table 8.1, i.e. the filter width to laminar flame thickness, $\bar{\Delta}/L_f$ for grid I, it ranges from 10.8 to 13.6, and for grid II it ranges from 8.78 to 10.6 compared to 5.10 to 5.16 for grid III and 4.40 to 5.10 for grid IV. Here L_f is the calculated strained laminar flame thickness and this is different from the unstrained laminar flame thickness, L_{f0} which is a specified input parameter ($L_{f0} = 0.3mm$). Figure 8.3 shows $\bar{\Delta}/L_f$ ratio with filter width for four grids employed in this simulations. By correlating Figure 8.3 with Figure 8.1, it should be noted, that the accuracy of the solution improved as the $\bar{\Delta}/L_f$ ratio diminishes. Further analysis can be carried by halving the mesh size (δ_{x2}, δ_{y2}, δ_{z2}, Δ_2) such that $\bar{\Delta}/L_f$ is also halved but remains larger than about 3.0. At $\bar{\Delta}/L_f \sim 3$, it is expected that the DNS limit is reached and this is not practical when dealing with real combustors. It should be pointed out at this stage that, as $\bar{\Delta}/L_f$ changes from 5.10 to 5.16 in grid III to 4.40 to 5.10 in grid IV, the total cost of solutions (CPU time in days) has doubled (Table 7.3). So it is essential to ensure that the filter width remains sufficiently larger than the strained laminar flame thickness. It can be seen from the estimates presented in Table 8.1 that L_f is more or less constant for propane/air flame and the filter width is one of the critical parameters, which controls the numerical accuracy.

Given an optimal and affordable grid resolution, one can obtain better numerical accuracy by reducing the filter width. However it should be noted here that the LES simulations under investigation are involved in "implicit filtering" (Schumann, 1989) and is difficult to achieve in practice without the refinement of the grid, as it is directly associated with grid resolution as given in equation 4.5. An alternative and more feasible approach is the explicit filtering (Chow and Moin, 2003) which involves decoupling the filter width from the grid resolution. For turbulent premixed combustion, the explicit filter width may be expressed in terms of the sub-grid scale flame and flow structures such as laminar flame thickness, flame speed and characteristic sub-grid scale velocity fluctuations.

Just to verify the above fact, different fixed filter width $\overline{\Delta}$ equal to 1mm, 2mm and 3mm are examined, in order to avoid the DNS limit. Nevertheless, four additional simulations have been carried out using grid III to verify the influence a fixed filter width on numerical accuracy by varying the value of $\overline{\Delta}$ from 1.0 to 3.0 mm with an interval of 1. Figure 8.4 shows the pressure-time histories from LES simulations using various filter coefficient values.

Figure 8.4 clearly indicates that, there is no significant improvement in the pressure-time history, by changing the value of the fixed filter width. It can be seen that, the pressure-time histories from the simulations using $\overline{\Delta}$ from 1 to 3 mm are overlapping, As explained earlier, this phenomenon is due to the implicit filtering approach used in the present simulations. From the above analysis, the ratios $h/\overline{\Delta}$ and $\overline{\Delta}/L_f$ have identified the filter width, as a key factor in assessing the numerical accuracy of LES. It is also identified that, in governing the numerical accuracy, filter width has a restricted role due to the type of filtering approach employed, which is directly linked to the grid resolution.
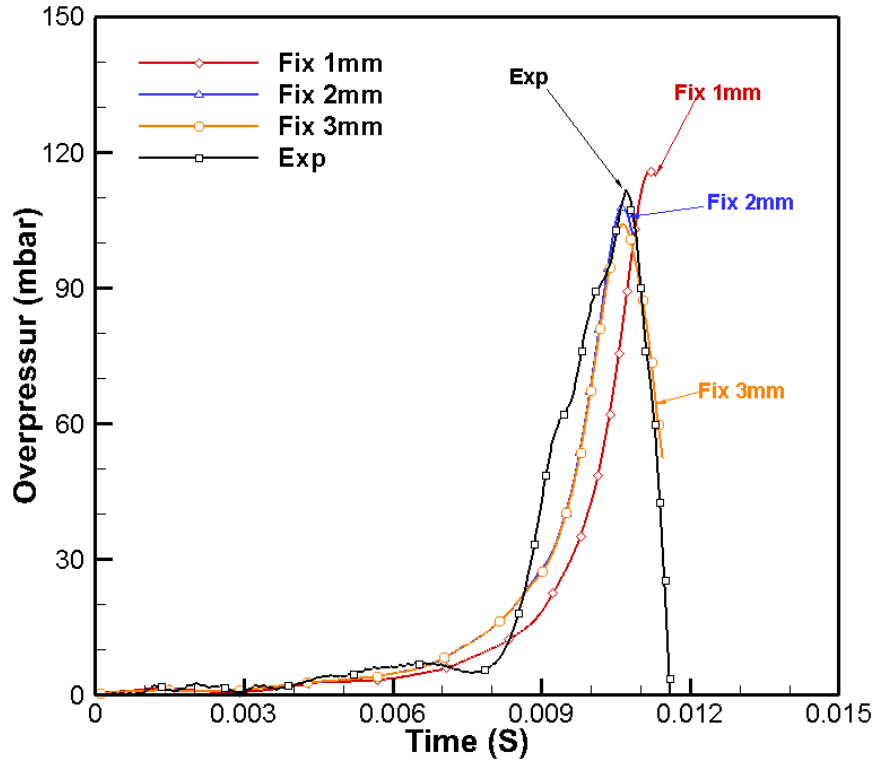
Figure 8.4 LES prediction of overpressure vs. time histories using various fixed filter width compared with experimental measurements

8.2.3 Sensitivity to the Model Coefficient *β*

To overcome the drawbacks of under-predicting the overpressure, a natural and first choice could be self-scaling or dynamic modelling of the model coefficient *β*. This coefficient is not considered to be universal and expected to be dependent on many physical and modelling parameters in the simple algebraic FSD model (equation 5.15). The dynamic calculation procedure, explained in section 5.2.2 has been implemented in the in-house LES code and examined for an additional run employing grid III for configuration 9. Boger's *β* constant, as described in Chapter 5 (Eq. 5.16) plays a major role in controlling the mean chemical reaction rate and thus influences flame dynamics. Four LES cases with *β* constants from 1.1 to 1.4 are considered here as detailed in Table 8.2. It is worth mentioning at this stage that the test filter to grid filter ratio (γ) is considered as 1.362 for all these cases. Table 8.2 also delineates LES predictions for these cases against experimental measurements.

Results from LES simulations using grid III with constant $\beta = 1.2$ and a dynamic model coefficient in the flame surface density equation are compared against the experimental measurements and discussed in this section. It should be noted here that, the LES results using the model coefficient from 1.1 and 1.4 shown in Figure 8.5 and Figure 8.6 are used to compare the present simulation. In order to assess the dynamic model, initial time histories of the overpressure are shown in Figure 8.5. The solid red line in Figure 8.5 represents overpressure with the model coefficient 1.2 and the rest of dotted and dashed represents overpressure from the model coefficient 1.1, 1.3 and 1.4, this is compared with the black square symbol line representing the experiments. It is evident from Figure 8.5 that the simulation with the model coefficient 1.3 and 1.4 predicted similar pressure trend and the rate of pressure rise was equal to that with constant model coefficient 1.2. A slightly higher peak overpressure i.e. 126.48 mbar at 9.92 ms is predicted with model coefficient 1.3 compared to 113.02 mbar at 10.64 ms in case of constant value for β. Though the overpressure trend is much increased and over predicted by approximately 12% and shows fast timing compared to the experiments.

Figure 8.5 shows overpressure time histories of both cases against the measurements. Figure 8.6 shows flame positions obtained from LES simulations against the experimental flame positions that are derived from the high speed video images. It is interesting to note that as the value of β increases, the overpressure trend in Figure 8.5 progressively increases. It should also be noted that with a higher value the flame propagates faster. This phenomenon is clearly confirmed by the predicted flame positions in Figure 8.6. As β constant is related to the SGS flame wrinkling level, an increase of this value is expected to increase the degree of flame wrinkling and thus increases the surface area of the propagating flame. As a result, the reaction zone thickness increases as it consumes more unburned mixture downstream of the chamber. It is also noticed that the flame front is becoming sensitive to the resolved turbulent motions as seen in the reaction rate images from LES predictions.
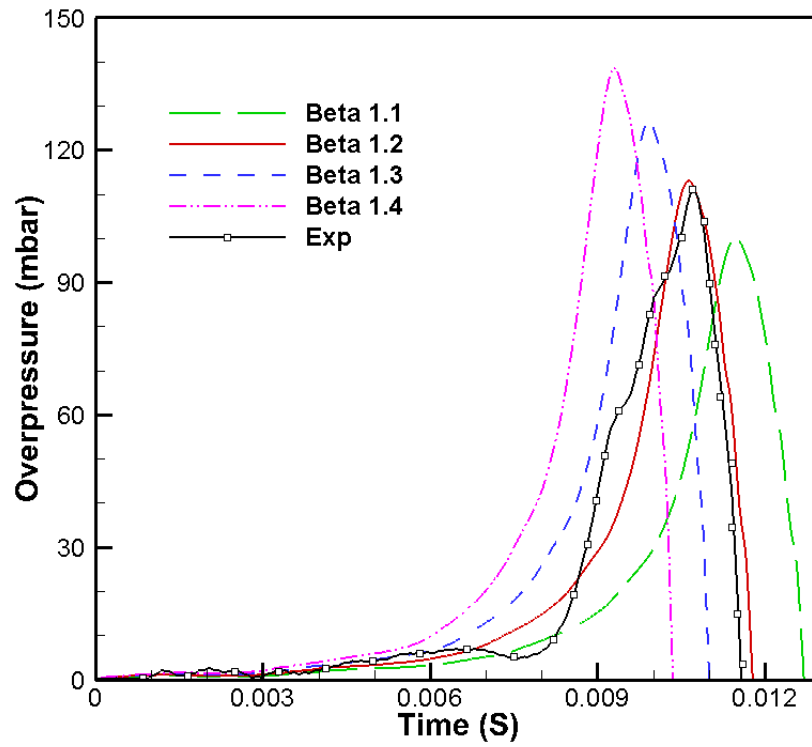
Figure 8.5 LES prediction of overpressure vs. time histories using two different Beta

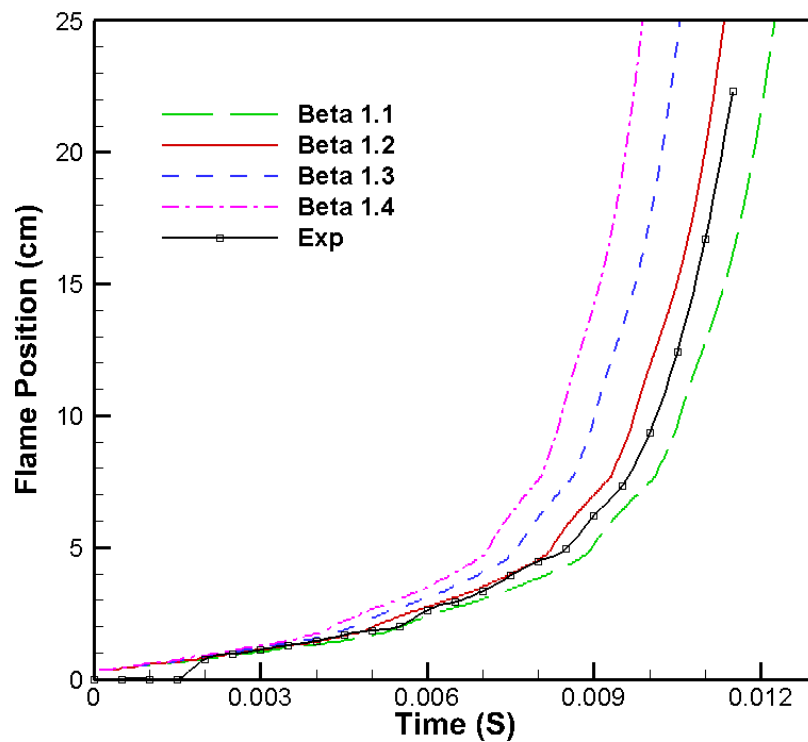constant value are compared with experimental measurements

Figure 8.6 Flame position vs. time histories of LES prediction using two different Beta

constant value are compared with experimental measurements

Figure 8.7 shows a sequence of reaction rate contours for two LES cases and images from experimental high speed video recordings at various stages of flame propagation after ignition. Individual reaction rate contour legends for LES is also shown in Figure 8.7 (a) and (b). From these, it is evident that, as the value of β is increased, the magnitude of reaction rate follows thus causing over prediction of flame speed. In Case C3 ($\beta = 1.3$) though the peak overpressure is in good agreement with the experiments, it is clear that the flame is much faster and leaves the chamber at an early stage. In Case C2 ($\beta = 1.2$), LES predictions are in better reasonable agreement i.e. the peak overpressure is within 0.9 % of experimental tolerance and with a correct flame position up to the flame venting phase. Hence, it is clear from these simulations that the β value constant is one of the key parameters on which flame is highly dependent or in other words; choosing a correct value for β will provide better results. Examining the results presented in Figure 8.5 LES prediction of overpressure vs. time histories using two different Beta constant value are compared with experimental measurements and Figure 8.7 indicates that a value of $\beta = 1.2$ is the best choice for the propagating turbulent premixed flame in the combustion chamber under study in the thesis.

Case	Model Coefficient (β)	Time (ms)	Peak Overpressue (mbar)	Flame Position (cm)
C1	1.1	11.47	100.20	15.95
C2	1.2	10.64	113.02	16.25
C3	1.3	9.92	126.48	16.55
C4	1.4	9.30	138.46	16.85
Exp	--	10.70	111.98	10.89

Table 8.2 LES prediction using various Model Coefficient against experimental measurements.
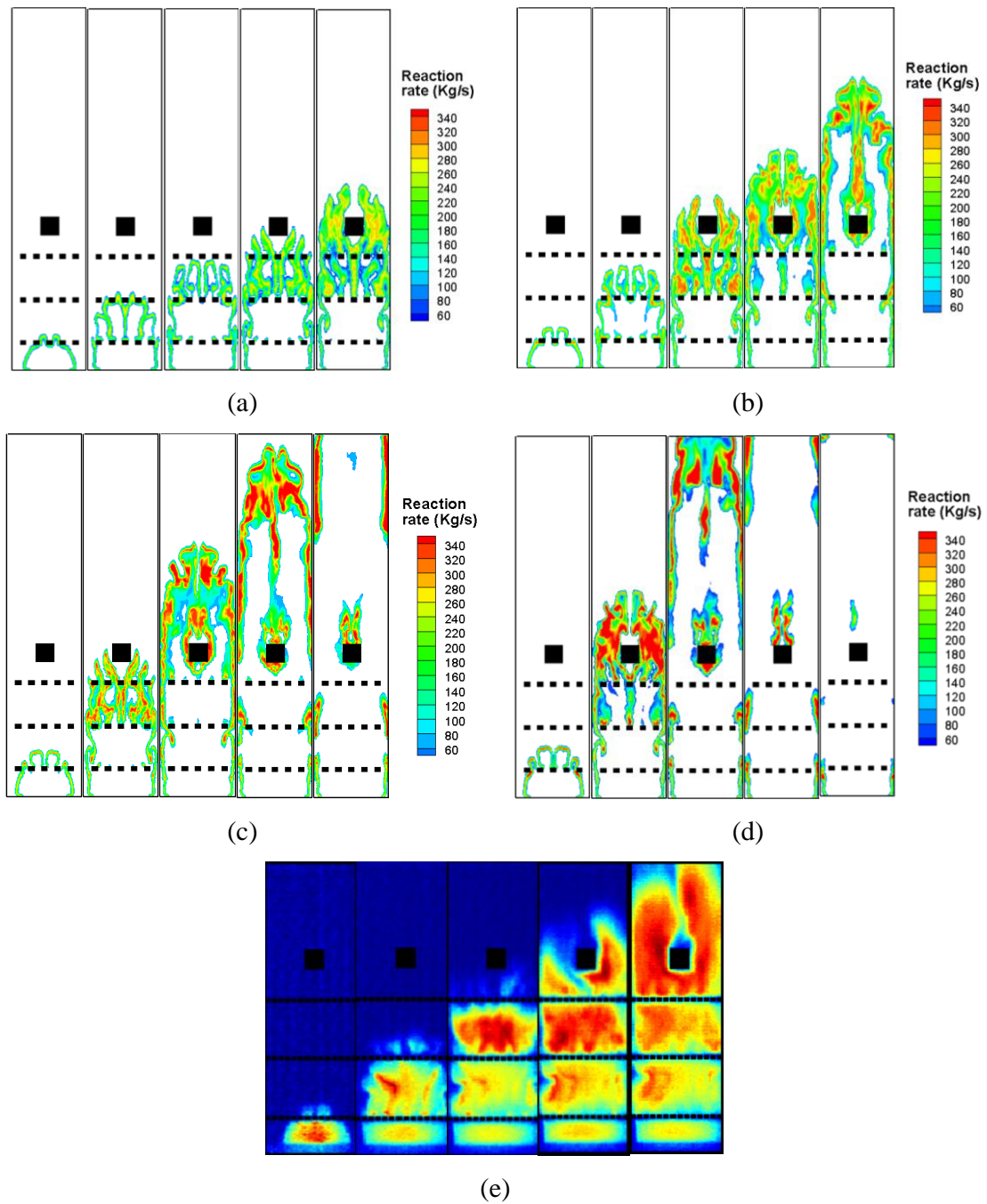
Figure 8.7 Sequence of experimental images to show flame structure at different times after ignition at 6, 9, 10, 10.5 and 11ms. (a) Case C1 with $\beta = 1.1$, (b) Case C2 with $\beta = 1.2$, (c) Case C3 with $\beta = 1.3$, (d) Case C4 with $\beta = 1.4$ and (e) experimental images from high speed video recordings

8.2.4 Configuration 9 Results

From the grid dependency tests, results of grid III with 90x90x336 grid points in the x, y, z directions, provides good agreement with experimental data and the solution is considered as grid independent. Hence, LES calculations using grid III are considered in the present section for further analysis of the flame structure, location and speed. In order to facilitate a detailed analysis of the flame structure and identify the regimes of combustion, the combustion chamber has been divided into five regions of interest as shown in Figure 8.8.
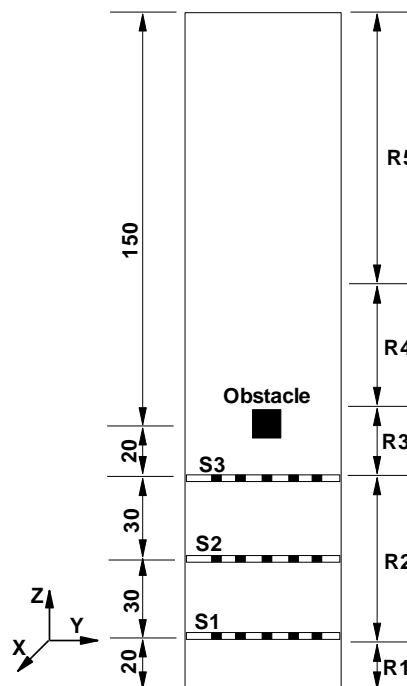

Figure 8.8 Region of interest along the combustion chamber. All dimensions are in mm.

8.2.4.1 Flame Characteristics and Generated Overpressure

Results from LES simulations together with experimental measurements are shown in Figures 8.1, Figure 8.9, Figure 8.10 and Figure 8.11. The time histories of the overpressure produced from using various grids are shown in Figure 8.1. As shown, grids III and IV provide reasonably accurate values for the overpressure and its trend with time. As discussed earlier, since there is no significant improvement beyond grid resolution III, further analysis is carried out using grid III only.

In order to validate the LES predictions, flame characteristics such as flame location, speed and structure are extracted from experimental video images Figure 8.9, Figure 8.10 and Figure 8.11 show comparisons between LES and experimental data for the flame position, speed with time, and flame speed with position respectively. From LES calculations, the flame position is obtained by locating the farthest point of the leading edge of the flame front, from the ignition bottom end (defined here as the most down stream location of the flame from the ignition point, where ($\tilde{c} = 0.5$). The flame speed is derived from the rate of change over successive images of the flame location at the leading edge of the flame furthest from the ignition point. It should be noted here that the experimental measurements are analyzed from high-speed video recorded (2000 fps) images, where there is a time limitation of 0.5 ms between two consecutive frames, which is considered here as the bin size for relevant LES estimates.
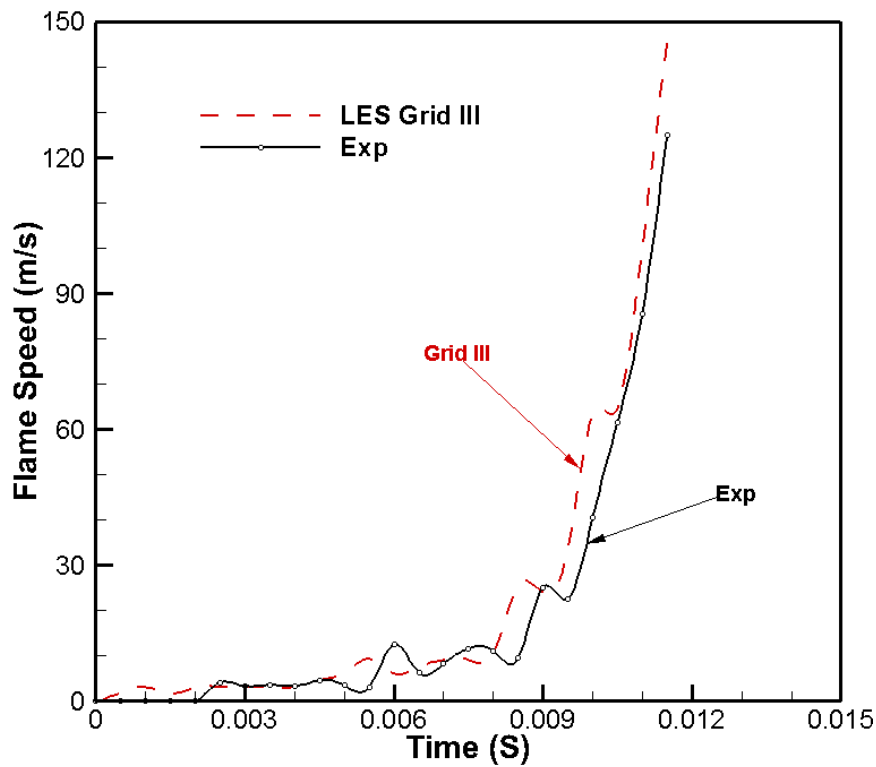

Figure 8.9 Flame speed versus time using LES simulations with Grid III compared with experimental measurements

From Figure 8.9, it can be seen that the flame position at various stages of the flame propagation is well predicted. Similarly from Figure 8.10 and Figure 8.11, it can be identified that the flame speed either with respect to time or flame position is well reproduced by grid III and is in very good agreement with experimental measurements. The calculated and measured data confirm that the peak overpressure occurs during the reconnection of the flame (see Figure 8.12 & Figure 8.13), downstream of the square obstacle in the blow down region. The higher pressure is induced by consuming the trapped mixture around the square obstacle as discussed later in this section. It should be noted, however, that the peak overpressure is slightly under predicted and there is a slight difference in the time of its occurrence.
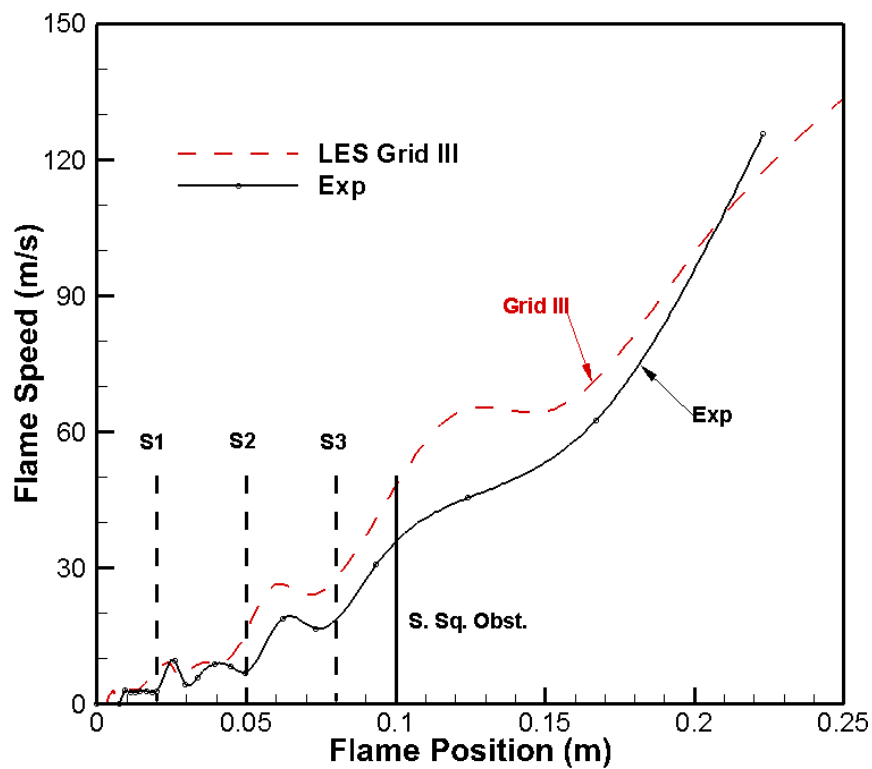

Figure 8.10 Flame speed versus flame position using LES simulations of Grid III compared with experimental measurements
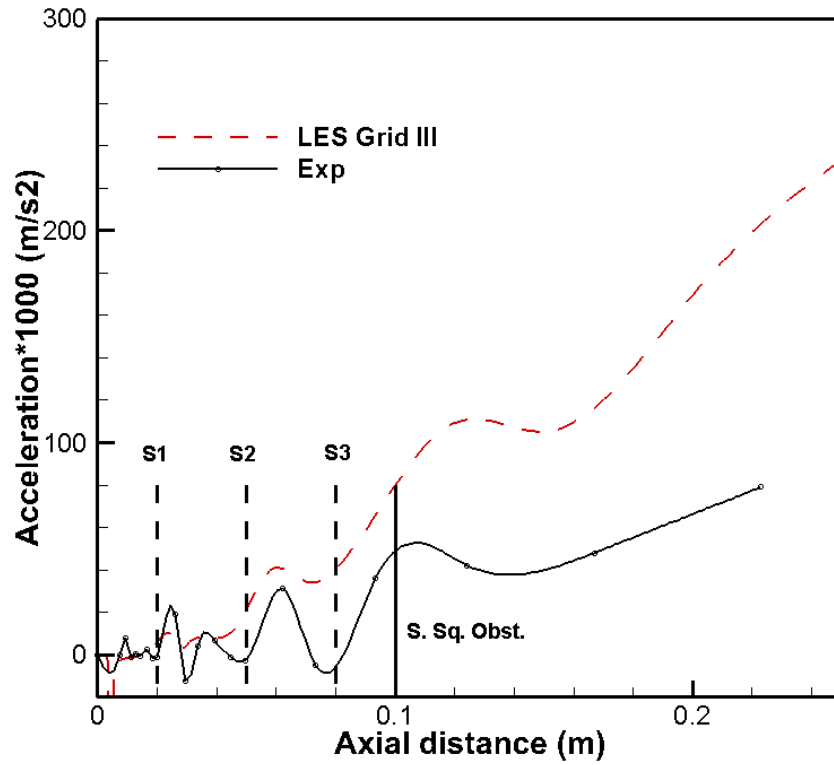
Figure 8.11 Flame acceleration versus flame position using LES simulations of Grid III compared with experimental measurements

Figure 8.12 and Figure 8.13 provide snap-shot sequence of the turbulent propagating flame at particular times from LES and experiments. It is worth mentioning at this stage, that experimental snap-shots are taken from the side end of the combustion chamber. However, numerical snap-shots are extracted from the central plane of the chamber in x direction shown in Figure 6.2 It can be observed from these snap-shots that the flame goes through different phases (or regimes) of turbulent premixed combustion, while interacting and propagating with solid obstacles inside the chamber. To identify these phases or regimes, the combustion chamber is divided into five regions of interest as shown in Figure 8.7 to examine the progress of flame characteristics from ignition at the closed end until the flame exits in the chamber at open end. Three possible realizations in every region are considered from LES predictions to demonstrate the flame structure, wrinkled nature, turbulence levels and other flame characteristics. Due to the limitation of frame speed in the case of the experimental video images, it is not possible to compare LES snap-shots exactly at the same time reference. As Figure 8.1 and Figure 8.9 demonstrate the simulation modeling and experiment result are similar, and deduce this experiment results are in the same region of Figure 2.7 and Figure 2.8. However, a minimum of one experimental video image is considered from each region as shown in Figure 8.13.

8.2.4.2 Regimes of Combustion in the Current Chamber

Region1 (R1): This region is extended to 20 mm from the ignition end of the chamber. In this region, the flame is thin and quasi laminar and propagates at almost the laminar burning velocity ~0.45m/s until it starts to approach the first baffle plate. This is confirmed from both numerical and experimental snap-shots shown in Figure 8.12(R1) & Figure 8.13(4.5ms) respectively.

Region 2 (R2): This region extends from 20 to 80 mm as shown in **Error! Reference source not found.**, downstream of the ignition point. Within this region the flame propagates through three baffle plates and traps a small amount of unburnt fuel/air mixture as it evolves from the baffle plates. The flame is then stretched further as it moves from one baffle plate after another. The entrapment of the flame around the baffles and its evolution through jetting can be noticed from numerical and experimental images as shown in Figure 8.12(R2) & Figure 8.13(6 ms) respectively. A progressive increase from 1.0 to 4 m/s of calculated turbulent has been noticed.

Region 3 (R3): This region extends from 80 to 112 mm downstream from the ignition closed end. This region has the square obstacle running through the chamber having a 12 mm side. As shown in numerical and experimental images in Figure 8.12(R3) & Figure 8.13(9.5 and 10.5 ms), the turbulent flame encounters the square obstruction and propagates at a speed of 7.5 m/s from the third baffle plate. This resulted in a highly stretched and distorted flame as it interacts with the solid square obstacle and achieves a maximum of 9 m/s of turbulent burning velocity. A rapid rise of overpressure from 40 to 70 mbar with a steep pressure gradient and a sharp increase in flame propagation speed from 15 to 50 m/s is observed during this interaction.

Region 4 (R4): Region 4 extends from 112 to 150 mm downstream of ignition point. This region may be viewed as start of the blow-down region, where flame starts exiting from the chamber. Due to the presence of square obstacle in region 3, a significant amount of unburnt fuel/air mixture is trapped around the obstacle as shown in Figure 8.12(R4) &

Figure 8.13(11 ms). The flame is stretched further and is reconnected within the recirculation zone. The reconnected flame has an increased surface area, which eventually consumes more unburnt mixture. As a result, the pressure and flame propagation speed are found to increase further to 103 mbar and 80 m/s respectively as the turbulent burning velocity increases to 10 m/s.

Region 5 (R5): This region covers the remainder of the chamber, where the blow-down phase continues and the flame propagates further to outside of the chamber. In this region the flame reconnects completely as shown in Figure 8.12(R5) & Figure 8.13(11.5 ms). The overpressure is found to increase and achieves its maximum of 110 mbar further in this region due to the burning of the remaining fuel/air mixture trapped inside the chamber. Experimentally, it is observed that the maximum overpressure reaches 138 mbar by consuming the trapped mixture around the solid obstacles. It is also found that the flame propagates at its maximum speed of around 140 m/s driving towards the chambers exit. The generated pressure oscillates while the remaining trapped mixture is burning in the chamber.

Relevant estimates from LES predictions at various instants of flame propagation within the above regions are calculated and presented. It is very interesting to note, that the level of agreement in the cases of flame position, propagating speed and the flame structure as shown in Figure 8.9, Figure 8.10, Figure 8.11, Figure 8.12and Figure 8.13 at different instants are very convincing and confirm the validity of the LES predictions. Further to this, various regimes of combustion are calculated based on non-dimensional groups and are identified on two standard combustion regime diagrams as discussed in the following section.
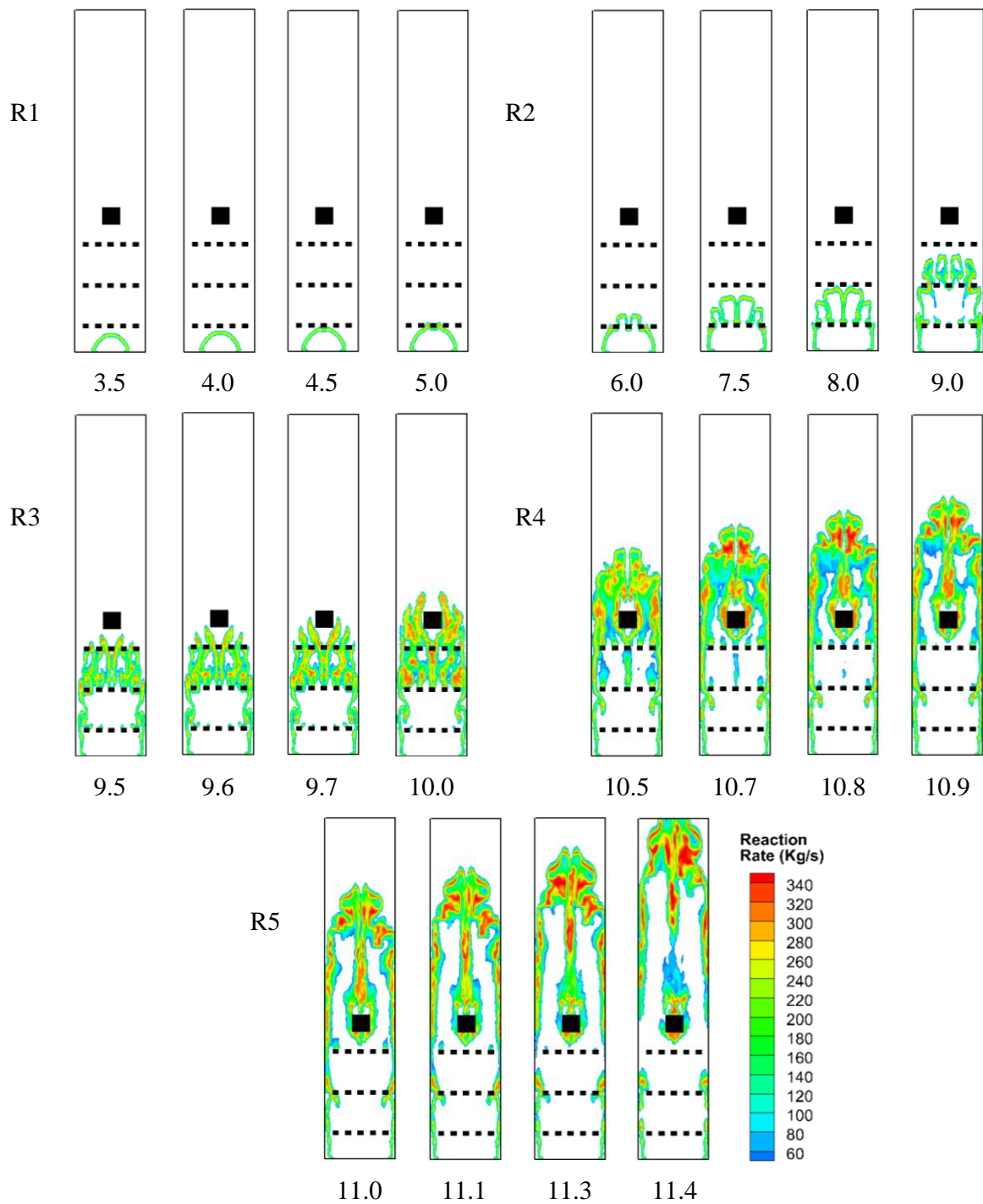
Figure 8.12 Flame structure derived from reaction rate contours from grid III, showing the flame propagation at different times after ignition within the five regions with each regions having four steps. The time stated mentioned at the bottom of each chamber is in ms.
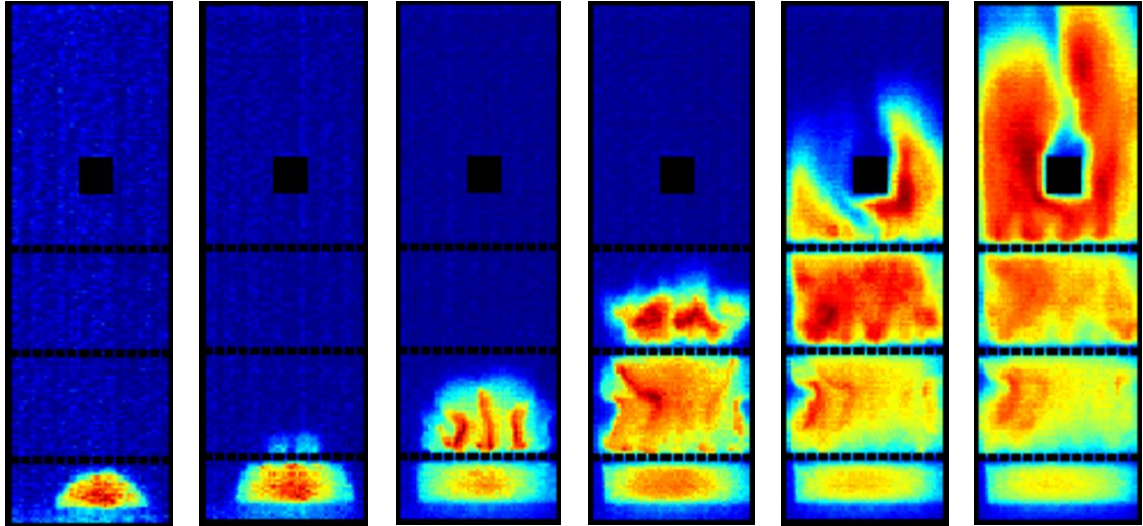
Figure 8.13 Sequence of experimental images to show flame structure at different times after ignition 4.5, 6, 8, 9.5, 10.5, 11 and 11.5 ms.

8.3 Influence of Ignition Sources

This section describes the influence of the ignition source on the overpressure trend and its timing in configuration 9. Three additional LES simulations using grid resolution III, with various ignition radiuses and initial progress variable values are carried out using the DFSD model. All simulations have been carried out using the test filter ratio (γ) of 1.362. The test filter ratio 1.362 was chosen, as Kirkpatrick et al. (2000) conducted parametric analysis while using 4 mm ignition radius in their numerical combustion chamber.

In the present analysis, four simulations were carried using 4 mm ignition radius of a hemi-sphere ignited from the bottom, a 2 mm ignition diameter of a full sphere ignited 2 mm up from bottom and 2.83 mm ignition diameter of full sphere ignited 2.83 mm up from the bottom with a reaction progress variable of 0.5, initialised at the start of the simulation. The basic idea for using different ignition start shapes and position to achieve the same iginiton as 4 mm of this analysis is to verify which ignition radius is appropriate to choose in order to achieve quasi-laminar phase of the premixed propagating flame. The peak overpressure and its incidence time are detailed in Table 8.3.
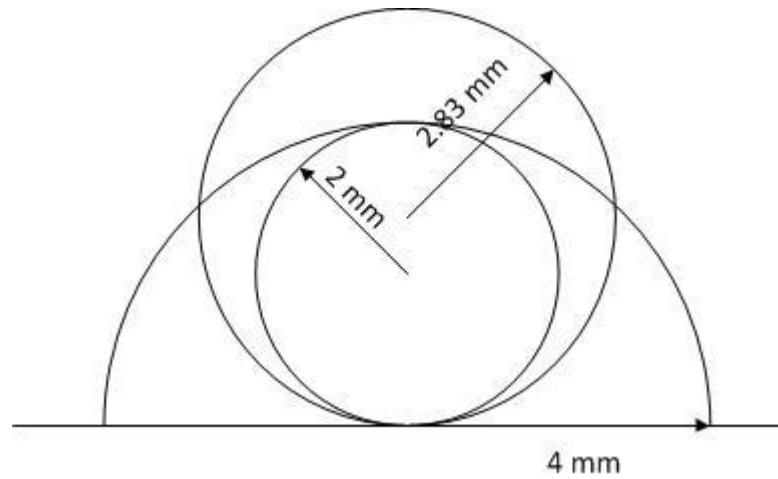
Figure 8.14 Sketch of the three kinds of ignition sources starting from the bottom of the combustion chamber.
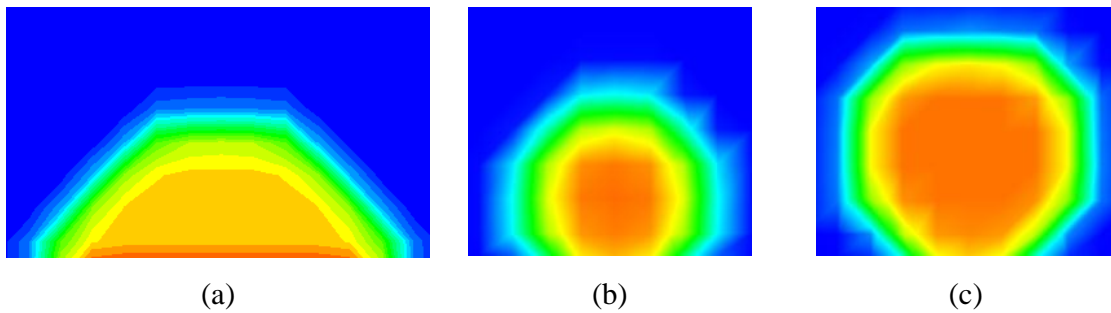

| (a) | (b) | (c) |

Figure 8.15 Three ignition sources at the bottom of the combustion chamber by LES simulation with (a) 4mm hemi-sphere, (b) 2mm sphere and (c) 2.83mm sphere.

Figure 8.14 and Figure 8.15 show the starting points of the ignition source of at the bottom closed end of combustion chamber. By choosing the 2mm radius of full shape of sphere ignition source at random, does not change the peak overpressure much except that the incidence timing is delayed nearly 2 ms as show in Table 8.3. After calculating the 4mm hemi-sphere area, the equilibrium of the same ignition area is the 2.83 mm radius of a full sphere.
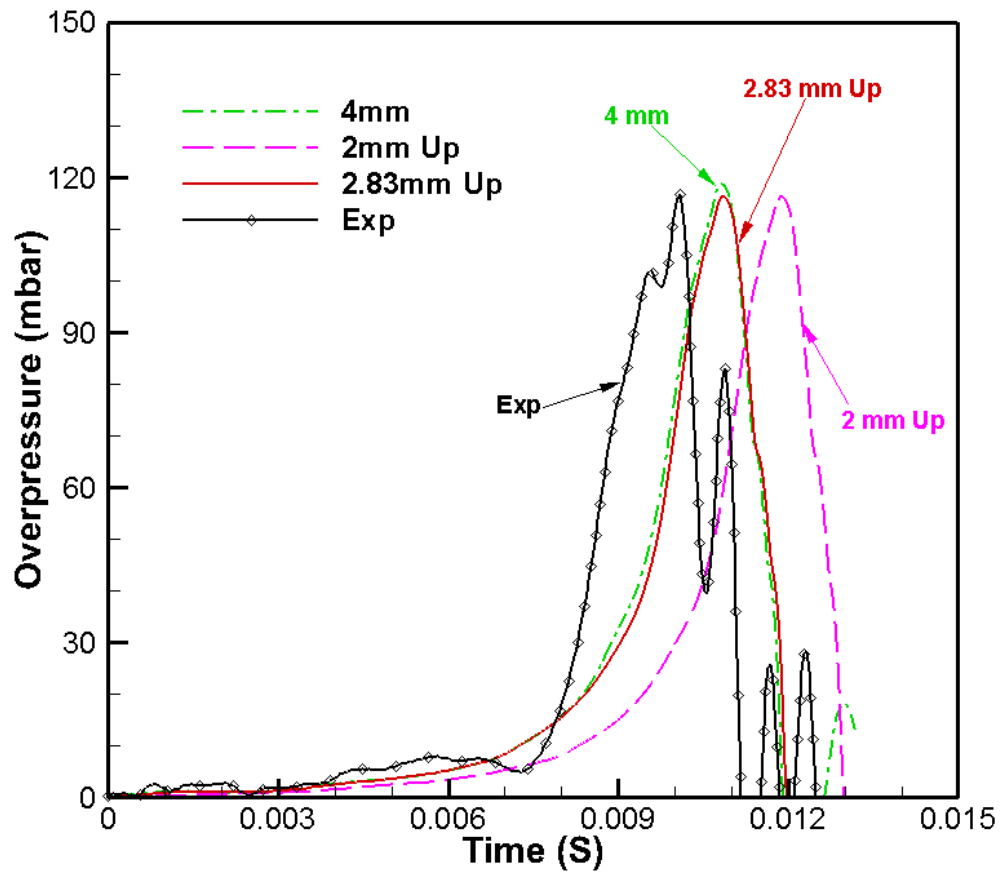
Figure 8.16 Comparison of predicted and measured overpressure time traced of LES
simulation of various ignition radios.

Radius of ignition (mm)	Ignition area (mm^2)	Peak overpressure (mbar)	Time of occurrence (ms)
2mm sphere	12.57	116.20	11.88
2.83mm sphere	25.16	116.25	10.86
4mm hemi-sphere	25.13	118.56	10.82
Experiment	--	116.73	10.08

Table 8.3 LES simulation applies various ignition sources values and experiment
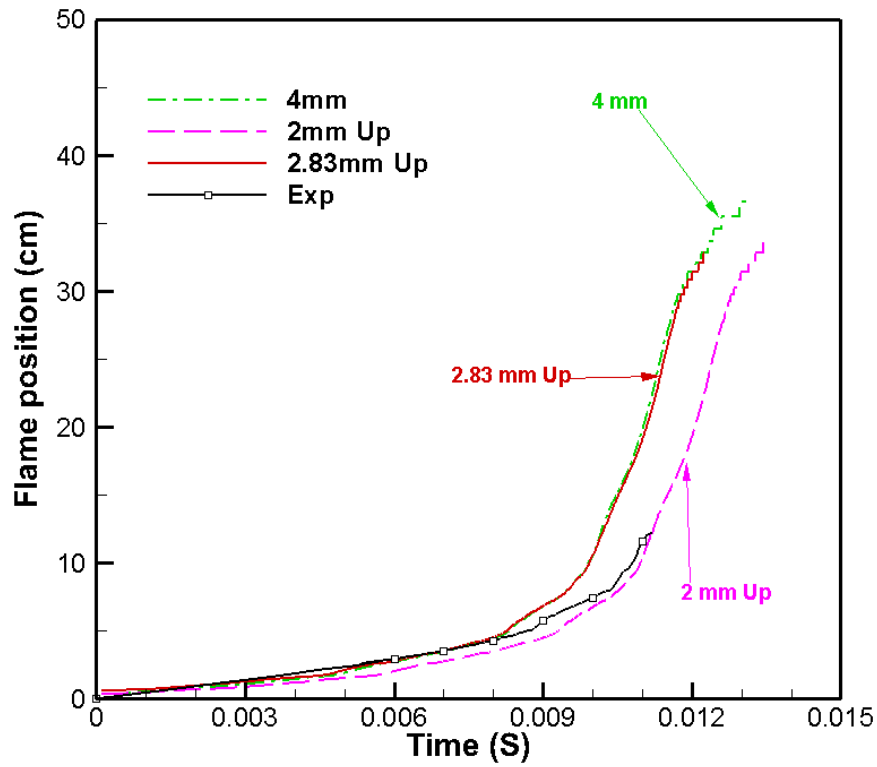measurement.

Figure 8.17 Comparison of predicted and measured flame position time traced of three LES simulations with different ignition sources.
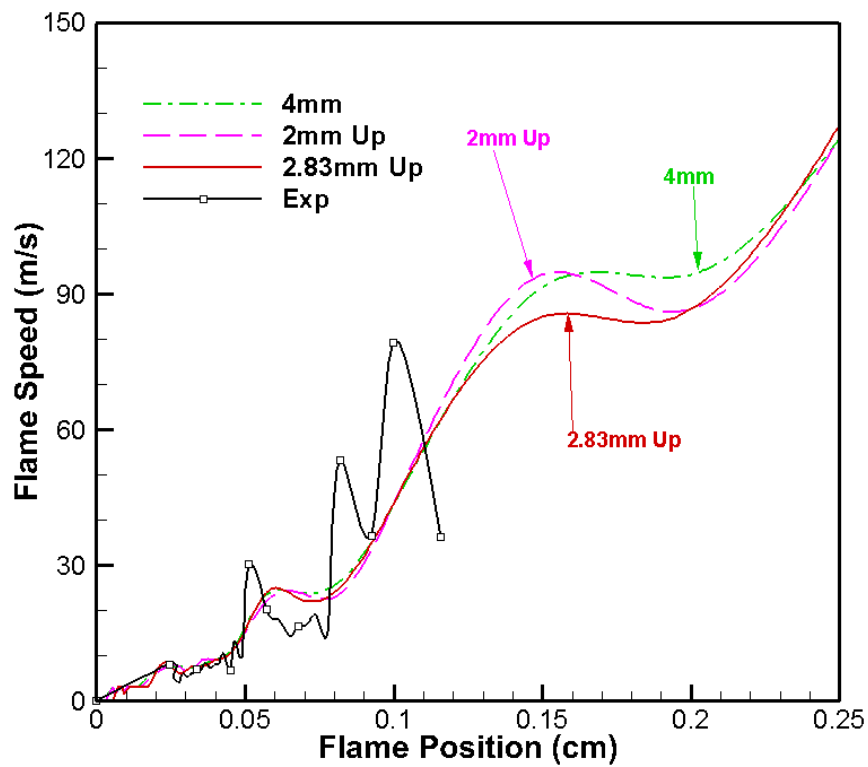

Figure 8.18 Derived flame speed verses flame positions from LES and experiments. Baffle and obstacle positions are marked to indicate the influence.

Figure 8.16 presents the pressure-time histories obtained from four LES simulations against experimental overpressure. It is very interesting to note from Figure 8.14, that the ignition radius 2mm up and 4mm of the hemi-sphere have a linear relation with respect to the incidence of peak pressure. The statistics of Table 8.3 represents the time of experimental peak overpressure in configuration 17, which roughly represents an ignition radius of about 5 mm. However, Figure 8.16 and Table 8.3 shows that there is no such significant influence on the magnitude of overpressure predictions.

Snap-shots of the reaction rate contours from LES simulations at peak overpressure time are presented in Figure 8.19. It reveals that irrespective of the ignition radius chosen, the contours represent similar propagating flame scenarios in the combustion chamber. Though Figure 8.17 shows very few differences at this instance in flame position, thickness, pockets, shape of recirculation zone and structure, it is quite encouraging that all LES simulations have predicted the overall flame characteristics very well. It can also be identified that, irrespective of the radius chosen to initialise ignition, overpressure predictions show a maximum of 1–2 % variation, which is quite encouraging in choosing the appropriate value of ignition radius to achieve the correct timing. It should also be noticed here, that the overpressure predicted by these simulations is about 116 mbar, which was predicted by the LES simulation, this is in very good agreement with experiments. The delaying of prediction peak timing of overpressure is probably due to the different ignition radius, which has an impact on the early stage, the quasi-laminar phase, of flame evolution..

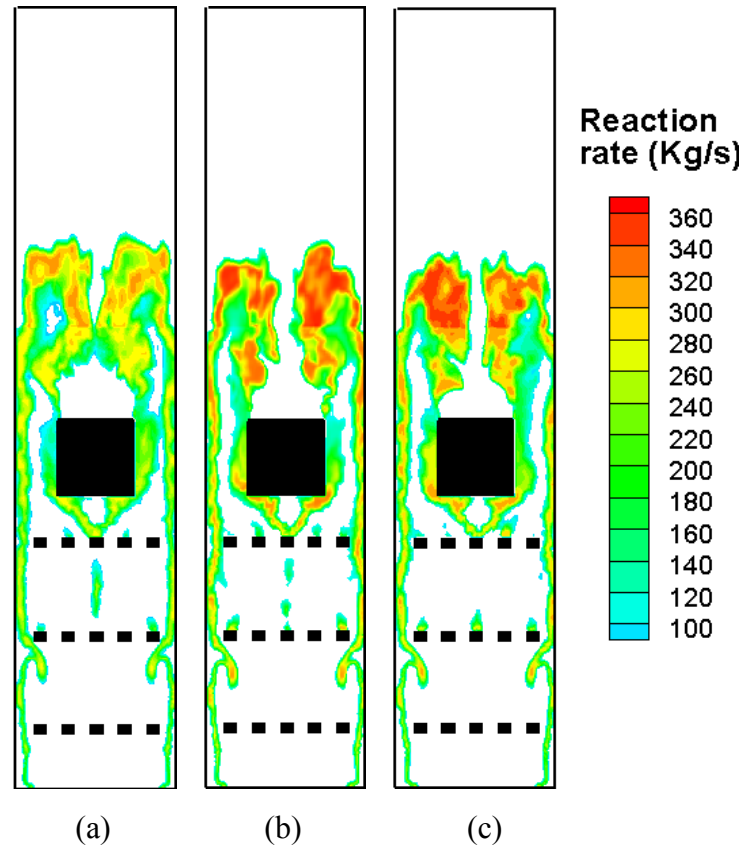(a)   (b)   (c)

Figure 8.19 Reaction rate contours peak overpressure incidence from LES simulations within ignition radius of (a) 4mm (b) 2mm (c) 2.83mm.

8.4   Effects of Outflow External Boundary

This section describes the effects of the outflow external boundary on overpressure trend and its timing in configuration 9. All additional LES simulations using grid III, with various external boundaries are carried out using the DFSD model. All these simulations were carried out using test filter ratio (γ) of 1.362. In the present analysis, four simulations were carried using 250, 300, 350 and 500 mm of outflow external boundary. The outflow external boundary distance can influence the position of the deflagrating flames when it reaches the end part of combustion chamber. The basic idea of this analysis is to verify which outflow external boundary is appropriate to have less effects in the combustion process inside the chamber. The peak overpressure and its incidence time are detailed in Table 8.6.

Figure 8.20 illustrates the four simulations computation domain of combustion chamber and obstacles superimposed over grid resolution III. Figure 8.20(a) is the outflow external boundary at 250mm from the ignition closed end. As aforementioned the combustion chamber's full length from ignition point to end outflow is 250mm, therefore the propagating flame will have no space between the exits outflow to the external boundary. Figure 8.20(b), (c) and (d) show the flame exits the outflow gradually and extend from 300mm, 350mm and 500mm, respectively, from the ignition closed end. It means that the lengths between flame exit and the outflow external boundary are 50mm, 100mm and 250mm, respectively.

(a)   (b)

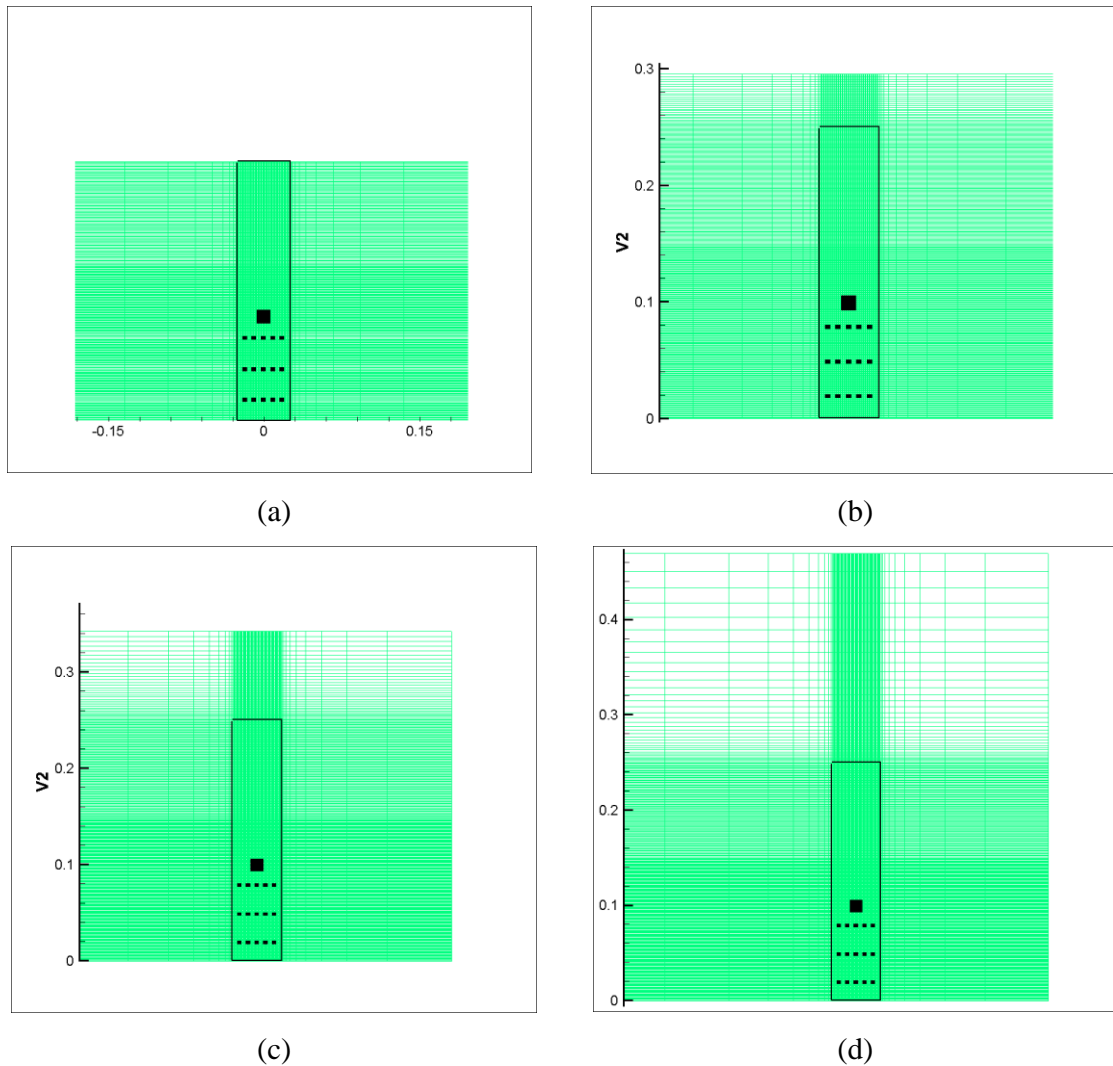(c)   (d)

Figure 8.20 Illustration of computational domain of combustion chamber and other obstacles and superimposed over grid resolution III of outflow external boundary by (a) 250mm (b) 300mm (c) 350mm (d) 500mm from the ignition close end.
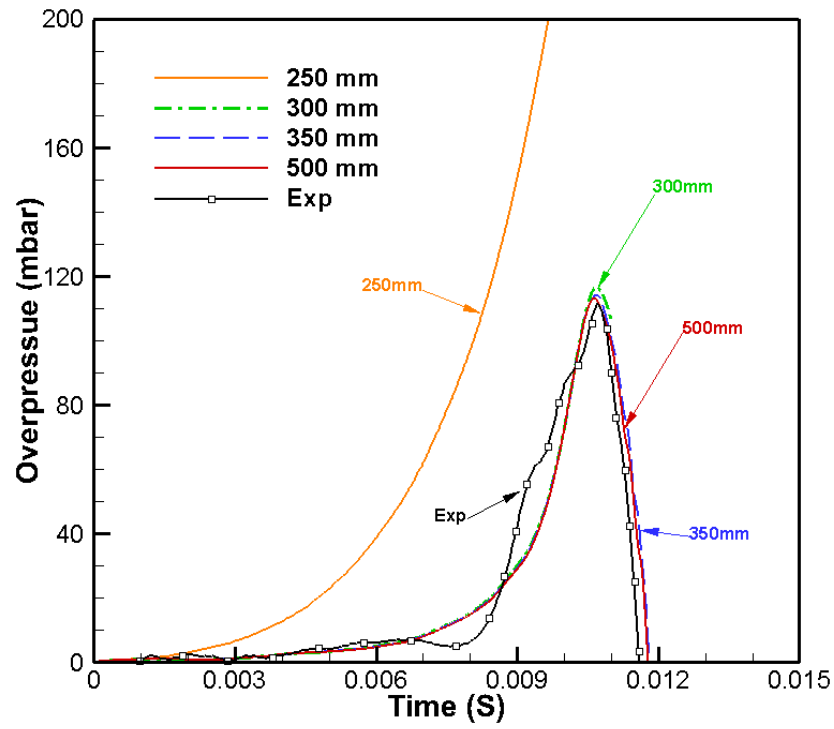
Figure 8.21 LES prediction of overpressure vs. time histories using various outflow external boundaries compared with experimental measurements.
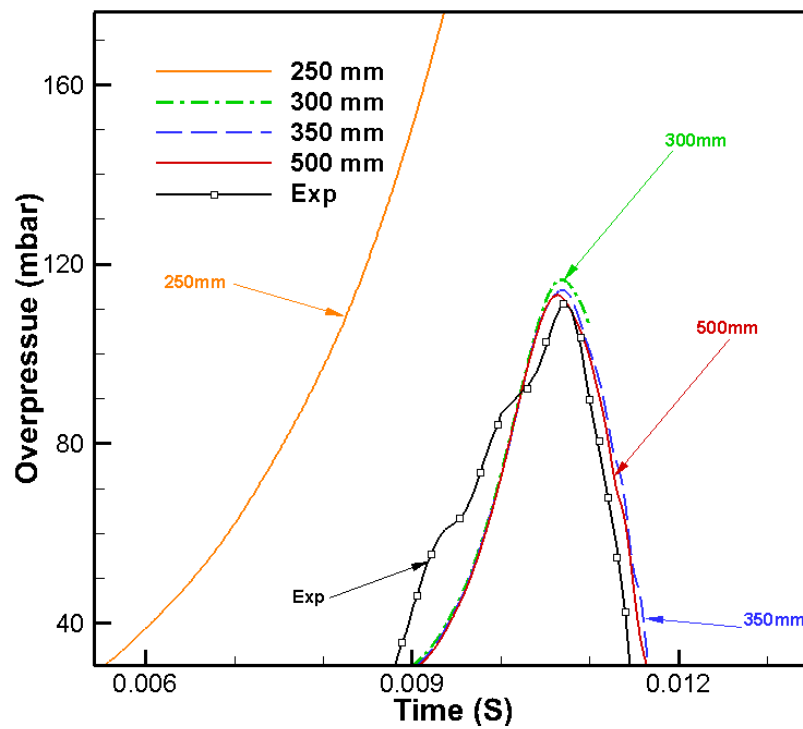

Figure 8.22 Zoom in Figure 8.21 showing the peak of LES prediction of overpressure vs. time using various outflow external boundaries compared with experimental measurements.

Analysis	Model-external boundary (mm)	Time (ms)	Overpressure (mbar)	Flame position (m)	Flame speed (m/s)
LES	250	9.71	< 200	0.0654	18.25
	300	10.67	116.62	0.1625	62.99
	350	10.69	114.11	0.1655	63.61
	500	10.64	113.02	0.1625	65.34
Experimental	--	10.70	111.99	0.1266	62.67

Table 8.4 Summary of the result for all ranges of outflow external boundary in fine grid simulations and experimental measurements.

Figure 8.21, Figure 8.23, Figure 8.24 and Figure 8.25 show the comparison of time histories of overpressure, flame position, flame speed and flame speed with flame position for LES simulations with experimental measurements, respectively. Comparisons of the predicted peak overpressures with outflow external boundary 250mm, 300mm, 350mm and 500mm models clearly shows the highest predictions with the 250mm formulation. This is mainly due to the limitation of external space by compressing the front of flame, which is captured by the 250mm formulation while calculating the SGS chemical reaction rate. The peak overpressure as presented in Table 8.4 and shown in Figure 8.21, is huge, more than 200 mbar at 9.71 ms using the outflow external boundary at 250mm, 116.62 mbar at 10.67 ms using the outflow external boundary of 300mm, 114.11 mbar at 10.69 ms using the outflow external boundary of 350mm and 113.02 mbar at 10.64 ms using the outflow external boundary of 500mm against the experimental measurements of 111.99 mbar at 10.70 ms. The peak pressure corresponds to the reconnection of the flame past the recirculation zone over the solid square obstacle and burning of the trapped un-burnt gases around the obstacle. This is again confirmed by the outflow external boundary 500mm and therefore considered as a reference to validate other model characteristics.

The peak pressure and its timing are slightly over-predicted despite the complex nature of the DFSD models. This might be due to the over sensitivity of the models to turbulent motions generated during flame propagation between the second and third baffle plates in the chamber. As well as the front propagation flames close to the end of the chamber and the outflow external boundary space push backwards against the flame propagation direction which generates more pressure. Amplification of the predicted LES from Figure 8.23 between 9 and 10 ms supports this observation. This observation can be combined with the experimental overpressure measurements presented in Figure 8.21. As Figure 8.21, the outflow external boundary of 250mm shows a steep increase in overpressure after 3ms, but the rest of the model show regular increasing. The short hump and shifting rain in the overpressure between 6 and 9 ms and can be attributed to jetting of the flame through the second baffle plate in the chamber. LES predictions using all model cases failed to predict this short hump and shifting as shown in Figure 8.21.
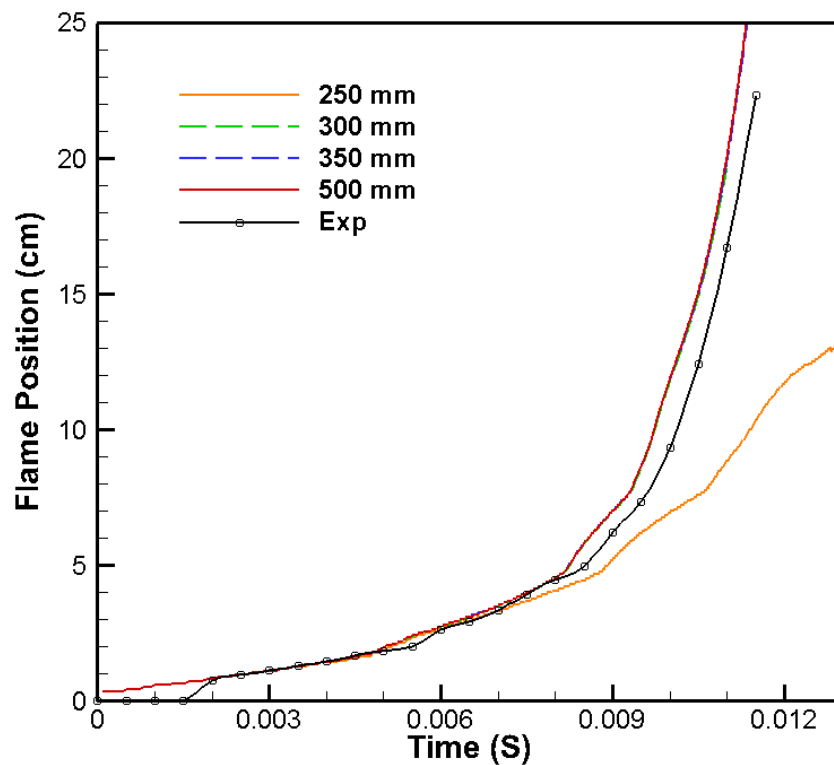

Figure 8.23 Comparison derived flame position vs. time histories using various outflow external boundaries are compared with experimental measurements.
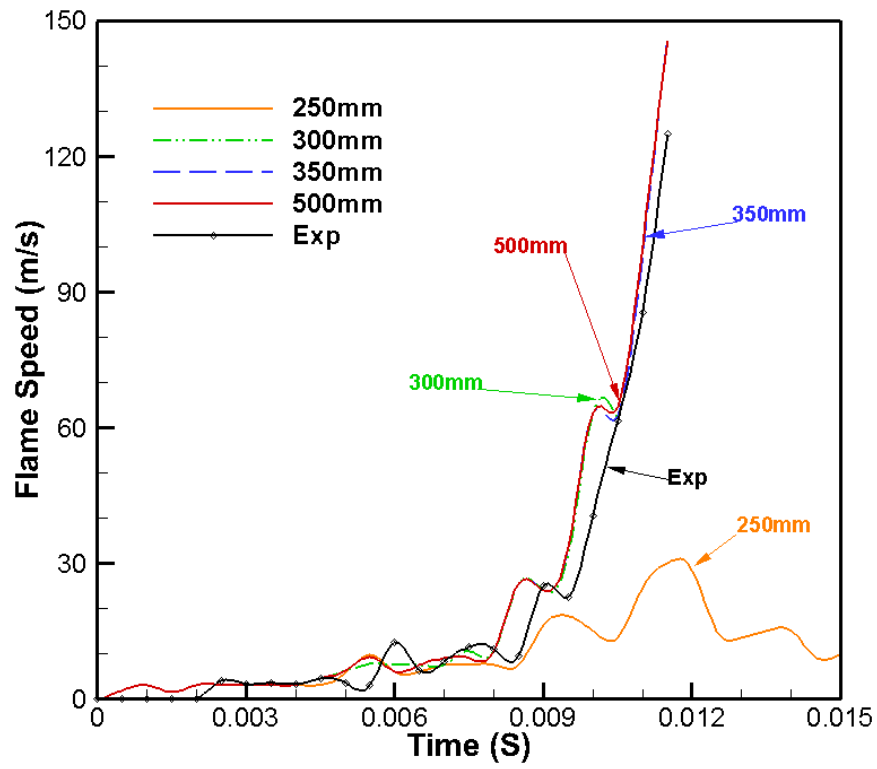
Figure 8.24 Comparison derived flame speed vs. time histories using various outflow external boundaries are compared with experimental measurements.
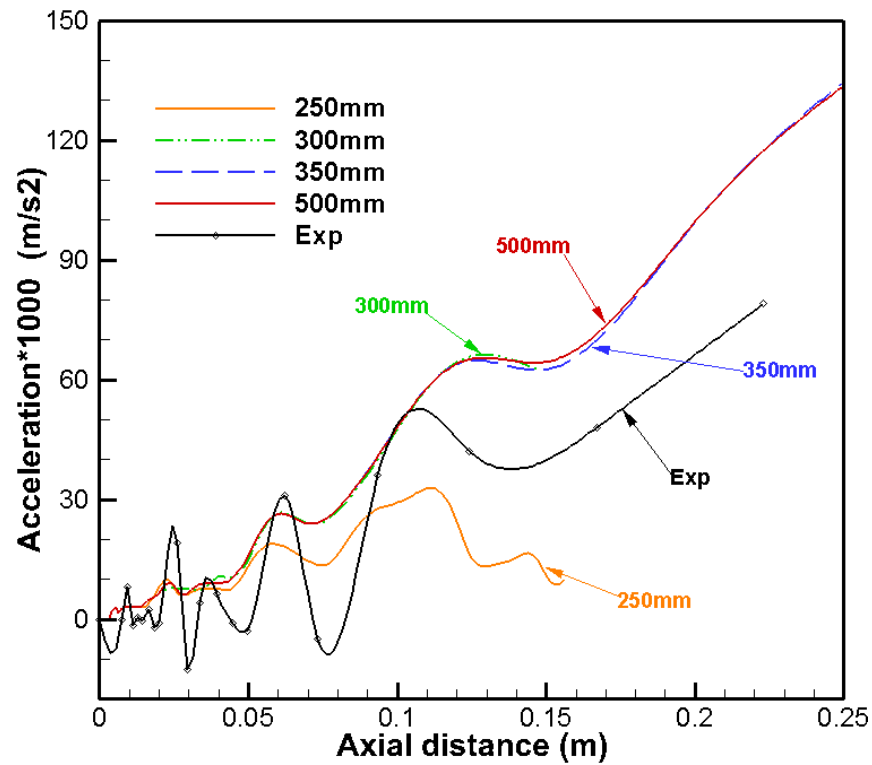

Figure 8.25 Comparison derived flame acceleration vs. axial distance using various outflow external boundaries are compared with experimental measurements.

Figure 8.23 shows the comparison of the flame position verses time histories, again the outflow external boundary is 250mm. Flames barely move forward after 8 ms and are slow moving to the end up to 12 cm. Another reason might be the drop off in flame speed followed by acceleration as shown in Figure 8.24 and Figure 8.25 after the flame encounters the square obstacle (~ between 10 and 11 ms); during this period the peak pressure occurs. However, there is no drop off in experimental flame speed as shown in Figure 8.24 and Figure 8.25, which might be due to the limitation of experimental data points derived from video images. Finally, ignition modelling used in the present study might have a significant influence in predicting the time of incidence of the peak over pressure and other flame dynamics. Identifying the influence of the ignition modelling on flame dynamics is another subject of interest.

8.5 Effect of Obstacle Structure

The probability of an explosion has major implications on the safety of personnel on a platform both in terms of potential loss of life and the possibility of escalation of the process, which could lead to a domino effect and more serious consequences. The mechanisms which enhance explosion overpressure, therefore, need to be established with some certainty in order to ensure that all aspects of safety in design (structure and processes) so that the protection of personnel is taken into account.

Configuration type	Summary Code	Dimensions (mm)	Blockage ratio (%)	Comment
Cylinder	C1	Diameter=4.87mm	9.7	
Cylinder	C2	Diameter=16.28mm	32.6	
Triangle	T1	Equal sides=6.28mm	12.6	Pointing Down
Triangle	T2	Equal sides=15.90mm	31.8	Pointing Down
Diamond	D1	Diagonals=6.15mm	12.3	
Diamond	D2	Diagonals=18.41mm	36.8	
Wall/Plate	W1	Width=10.26mm	20.5	3 mm Thick
Wall/Plate	W2	Width=27.44mm	54.9	3 mm Thick

Table 8.5 Various obstruction geometries investigated within the combustion chamber.

The studies described here represent only a very limited set of scenarios of actual explosion situations where generally, the flame spreads past the ignition points interacting with obstructions of various sizes and cross sections such as cylinders, triangle, diamond, wall/plate and sharp edges. The propagating flame front is likely to interact differently with these obstacles. The resulting overpressures and the amount of unreacted mixtures trapped behind various obstacles is also likely to be different. Previous research in this area focused on one types of obstacles and repeated walls (plates or rings within the test chamber) (Gubba et al., 2009). The common conclusion is that the existence of obstacles has a profound effect on the flame propagation speed due to the generation of turbulence and the modification of turbulence structures. Table 8.5 shows a detailed and systematic study of the effects of the obstruction geometry and blockage ratio, the flame propagation rate and the resulting overpressures. The experiment measurement uses the Figure 7.1 for the test rigs to demonstrate the flame in the larger combustion chamber but this LES simulation study uses Figure 7.2 as aforementioned to limit the time consuming and cost of it. The geometry of the obstacles is presented is proportional to the experiment test rigs.

8.5.1 The Single Solid Obstacle Size Influence

Corresponding to the experiment test rig, all obstacles has set up 68.81 mm away from the ignition point. Since, configuration cylinder, triangle, diamond and wall/plate has no baffles except for only a single solid obstacles running through the chamber at approximately 10 ms contact with the front of the propagation flame. The time series of overpressure from LES simulations using the DFSD model are briefly shown in Figure 8.26, Figure 8.27, Figure 8.28 and Figure 8.29, respectively.

Configurations		Blockage (%)	Peak overpressure (mbar)	Time (ms)
Cylinder		9.7	16.39	13.86
		32.6	23.72	14.48
	Increase	22.9	7.33	0.62
Diamond		12.6	17.80	14.23
		31.8	34.53	15.00
	Increase	19.2	16.73	0.77
Triangle		12.3	19.90	14.23
		36.8	23.92	14.95
	Increase	24.5	4.02	0.72
Wall/Plate		20.5	23.06	14.30
		54.9	56.50	13.44
	Increase	30.4	33.44	-0.86

Table 8.6 Various obstruction geometries of blockage ratio of peak overpressure and occurrence time with increased pressure and timing statistic.

Table 8.6, shows the effects of increasing the blockage ratio on the flame acceleration obtained for the four obstruction geometries cylinders, diamond, triangles and wall/plate, respectively. Figure 8.26 substantiates the LES prediction of single cylinder shape obstacle with 9.7% blockage ratio has peak overpressure of 16.39 mbar at 13.86 ms, but the higher blockage ratio with 32.6% has a higher peak overpressure of 23.72 mbar at 14.48 ms. So, for both of the peak overpressure and incidence timing has been increased by 7.33 mbar and 0.62 ms. With a 9.7% blockage ratio, the flame reached the obstacle at about 9 ms and exited the chamber at about 15 ms. This elapsed time taken by the flame front to travel from the ignition to the vent was lengthened to about 16 ms when the blockage ratio was increased to 32.6 %, relatively lower effects of obstacle blockage ratio were observed with the circular cross sections. Figure 8.30 shows the comparison of the LES prediction of peak overpressure against the blockage ratio of the experimental measurements by Ibrahim et al. (2001) with the large combustion chamber. The increase of the cylinder cross sections had little significant impact on the peak overpressure but on the small chamber the increase of blockage ratio increased by about 7.33 mbar.
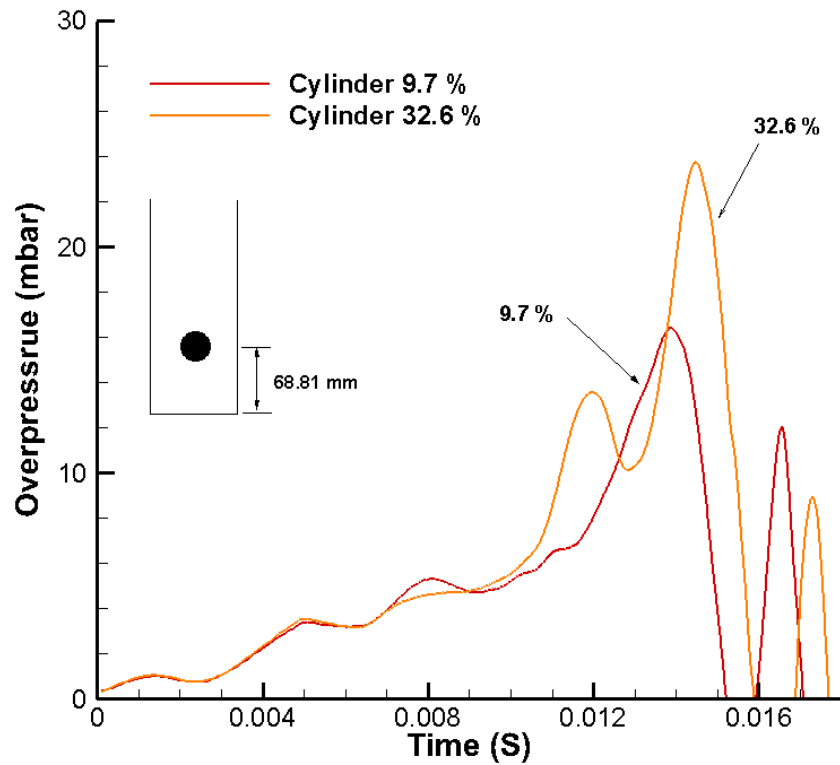
Figure 8.26 LES prediction of overpressure vs. time using the cylinder shape obstruction with two blockage ratio in the combustion chamber.

It was very interesting to notice, in Figure 8.26 and Figure 8.27 the LES simulations for the larger blockage ratios the raised the overpressure when the pressure reached about 11 or 12 ms, it has an initial peak showing then a decrease in the pressure by about half to one ms and then it raise to a peak for the cylinder and diamond shaped obstacles. The triangle shape obstacle in Figure 8.28 does not clearly show a peak at about 11 or 12ms, but it shows that the increased rose in pressure has slowed down to between 12 and 13 ms. However, the shape of diamond obstacle shows an increase of blockage ratio from 12.3% to 36.8%, the peak overpressure increased 16.73 mbar which its rhythm corresponds to the experiment measurement in the Figure 8.31. Meanwhile, the LES simulation of peak overpressure versus blockage ratio for the triangle obstacle shows an increased rhythm from 19.90 mbar to 23.92 mbar for the blockage ratio from 12.6% to 31.8% with experiment measurement from Figure 8.32.
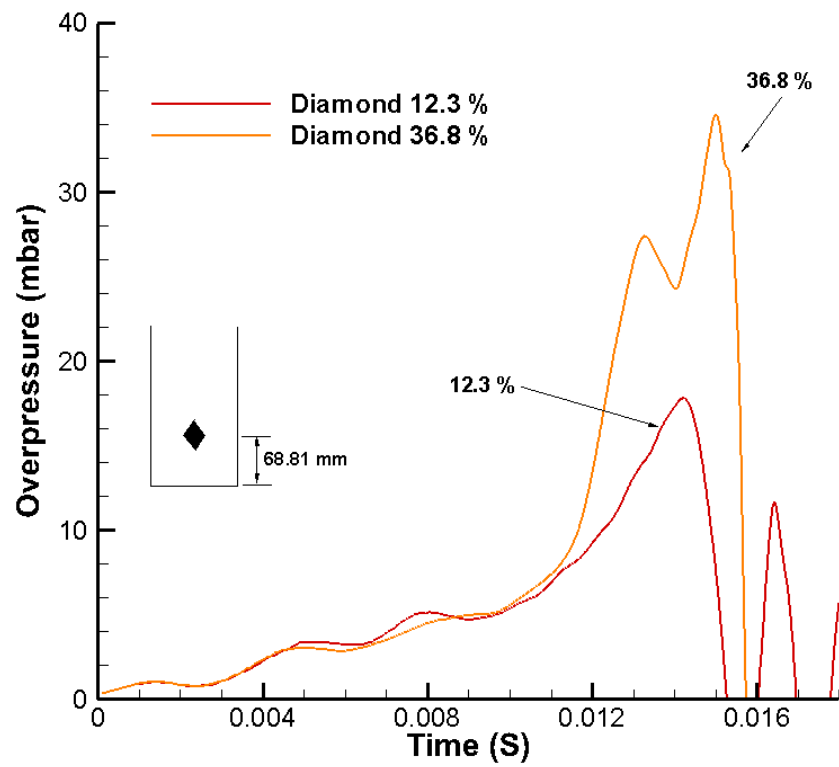
Figure 8.27 LES prediction of overpressure vs. time using diamond shape obstruction with two blockage ratio in the combustion chamber.
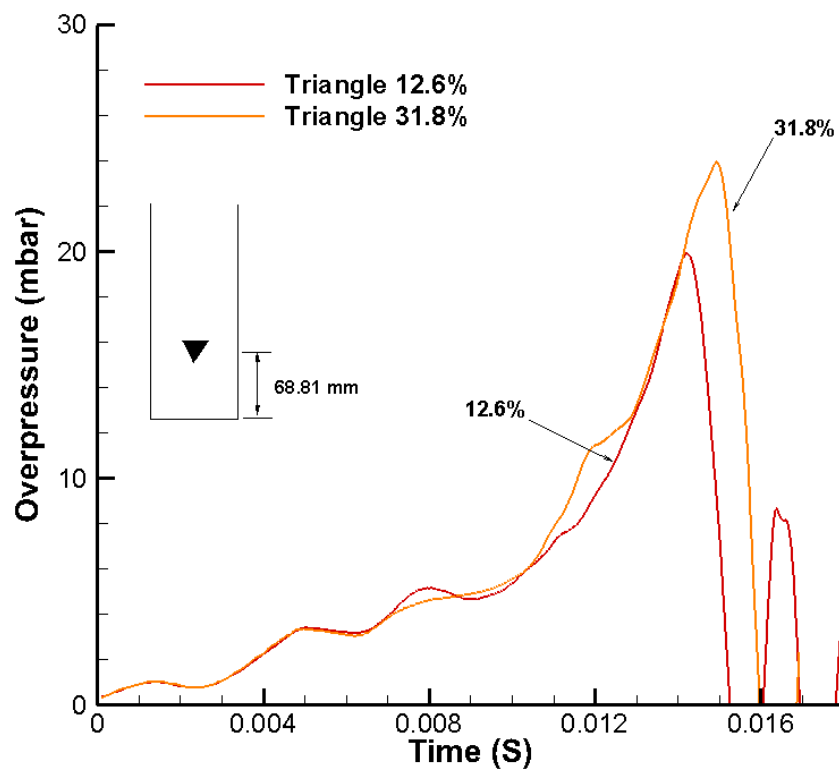

Figure 8.28 LES prediction of overpressure vs. time using diamond shape obstruction with two blockage ratio in the combustion chamber.
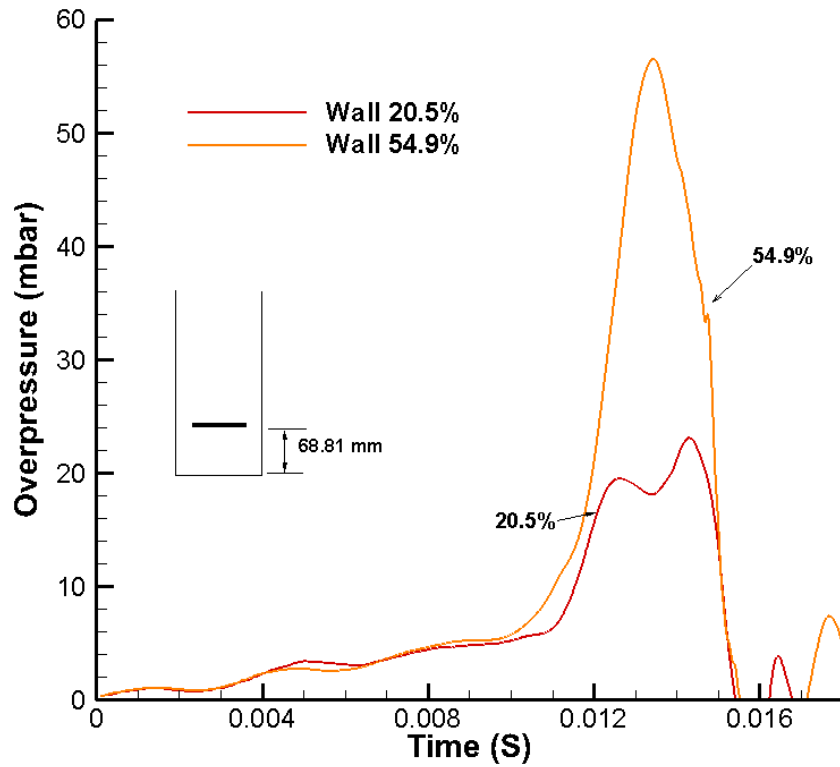
Figure 8.29 LES prediction of overpressure vs. time using wall/plate shape obstruction with two blockage ratios in the combustion chamber.

It is clear flame speed is increased by increasing the obstruction blockage ahead of the flame. The greatest effect of increasing blockage occurs when the wall/plates obstacle is used, in this instance there was an increase between 20.9% to 54.9% and an increase in overpressure of 34.44 mbar, this can be seen in Figure 8.29 and Table 8.6. The effect of increasing the blockage ratio appears after the flame impinges on the obstacles and it has a direct effect at about 10 to 11 ms. The flame acceleration is then enhanced as the flame reaches the recirculation zone behind the obstacle. This is consistent with the expectations that the level of turbulence behind the obstacle is high and therefore increases flame speed. This level of turbulence appears to depend on the obstruction conjuration as the flame acceleration behind the obstacle was different. Quantitative measurements of the level of turbulence generated by different blockage ratio obstacles will be the objective of future research.

Figure 8.30 Comparison LES prediction of peak overpressure vs. blockage using cylinder shape obstruction with two blockage ratio in the combustion chamber are compared with experimental measurements.

Figure 8.31 Comparison LES prediction of peak overpressure vs. blockage using diamond shape obstruction with two blockage ratio in the combustion chamber are compared with experimental measurements.
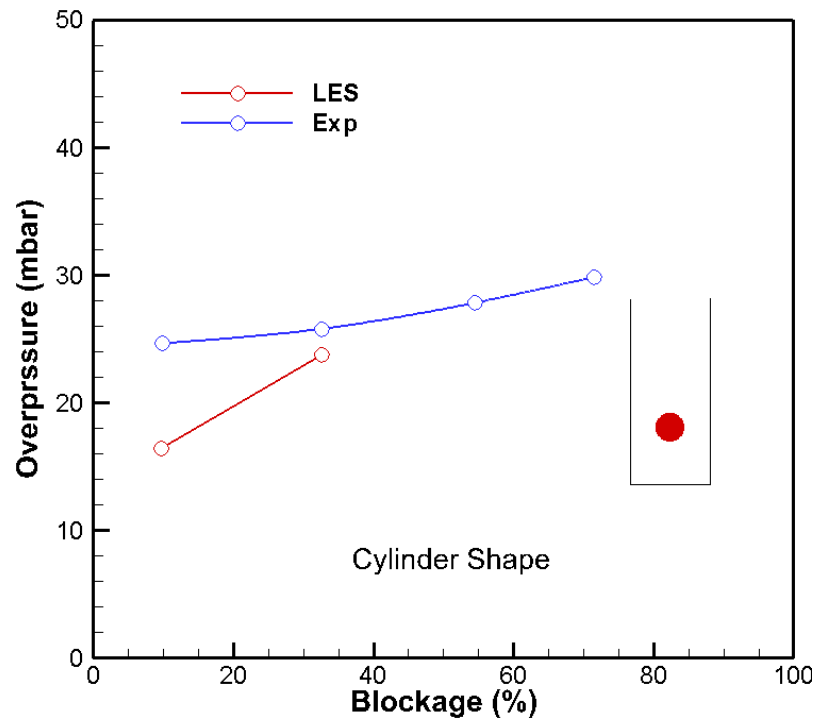
Figure 8.32 Comparison LES prediction of peak overpressure vs. blockage using triangle shape obstruction with two blockage ratio in the combustion chamber are compared with experimental measurements.
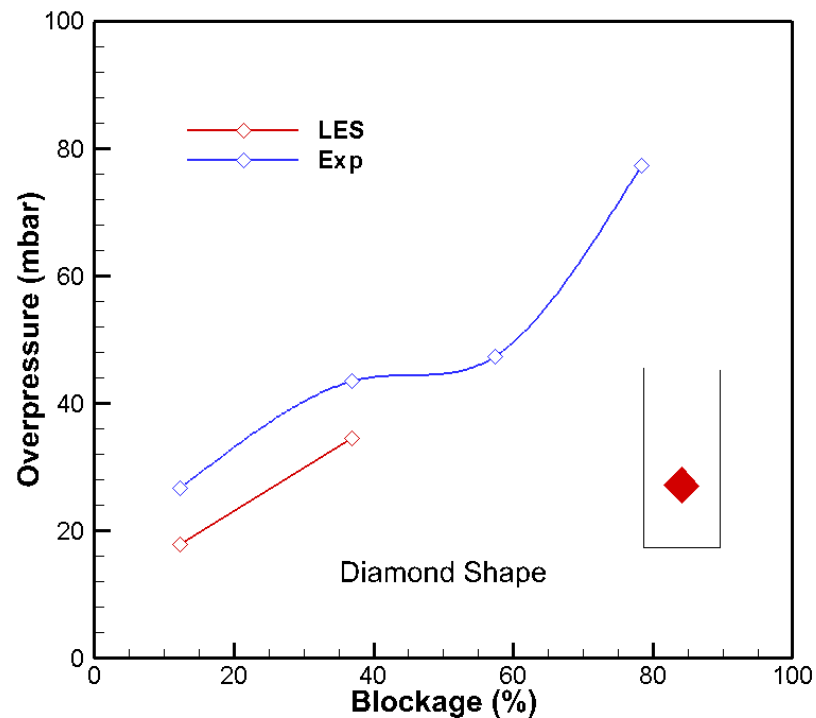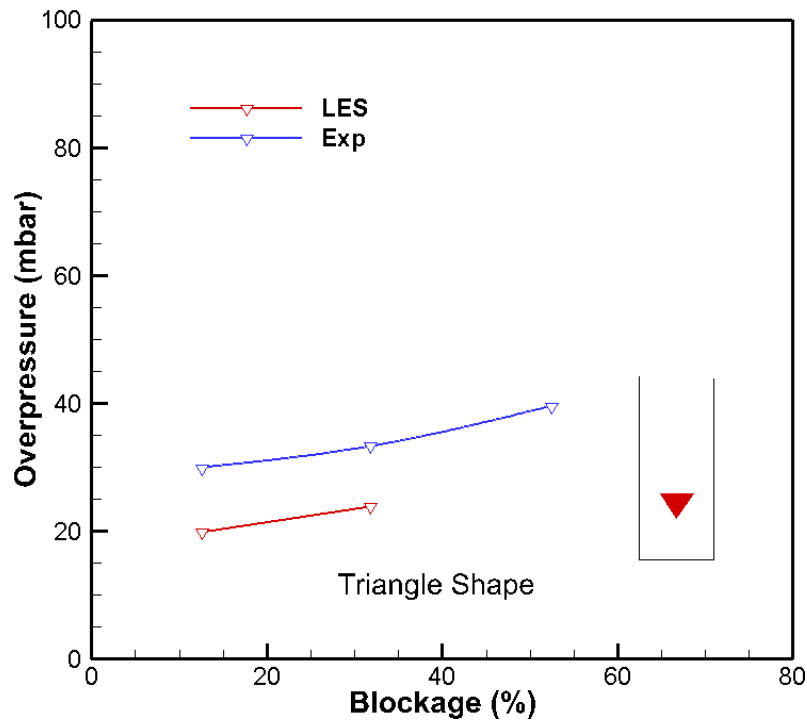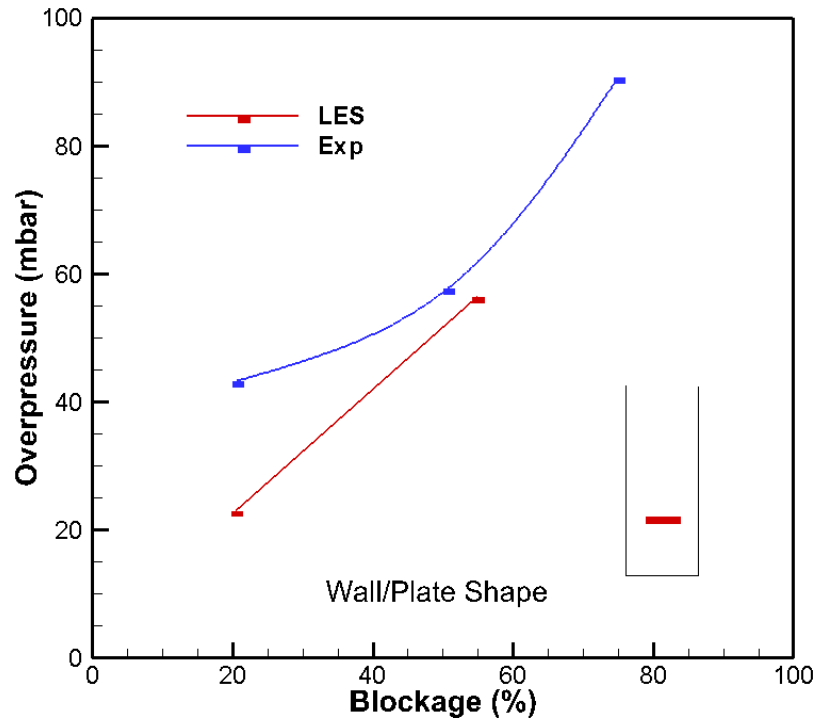

Figure 8.33 Comparison LES prediction of peak overpressure vs. blockage using wall/plate shape obstruction with two blockage ratio in the combustion chamber are compared with experimental measurements.

8.5.2 The Single Solid Obstacles Shape Influence

This section shows a typical sequence of LES simulation of the progress of flame interaction in an explosion with single shapes such as a cylinder, diamond, triangle and wall/plate cross-section obstacles, respectively. It can be seen that a very symmetrical flame develops after ignition sparked at the bottom-closed end of the box. It is important to distinguish between the direct and indirect effects the obstacles have on the flame. The indirect effects arise from the change in the overall flow field due to drag, turbulence production and volume reduction induced by the obstacle, whereas direct effects are those that occur when the flame impinges on the obstacle. The flow behind the obstacle is complex and its effect on the flow flame interaction is very sensitive to the geometry of the obstacle.

Figure 8.36, Images for the early stages of flame propagation are similar for all obstacles and are not all shown here due space limitations. Regardless of the obstacle used, the flame propagates in the shape of a hemisphere from the point of ignition. At about 5 ms after ignition, the flame began to elongate in the axial direction towards the obstacle. At the same time, the cover of the vent was blown off due to the positive pressure built up inside the box. The flame continued to grow and unburned mixture was vented through the opening at the top end. The pressure inside the tube increased slightly as the flame area continued to increase. At about 10 ms after ignition the flame reached the front end of the obstacle facing the ignition point. At almost the same time the flame reached the sidewalls and extinguished near the bottom end of the box. The geometry of the obstacles influenced the distortion of the flame front due to the formation of a vortex pair of different sizes behind the obstacle. Some unburned mixture was trapped behind the obstacle. The quantity of the trapped mixture of gas was found to be proportional to the vortex size and was found to be higher for wall/plate obstacles. The cylinder, diamond and triangle shaped obstacles have, respectively, a lower amount of trapped mixture gas. These pockets of gas mixture are the last to be consumed during the flame propagation.

The time taken to burn the trapped gas was shorter with the circular cross-section obstacle where the flame front entrained the vortex pair as soon as it passed the obstacle, as shown in

Figure 8.36. With the triangle shaped obstacle, the flame started to roll-up behind the obstacle at some distance downstream. The length of this vortex pair was found to be about 20, 25 and 62 mm, respectively, for the cylinder (C2), diamond (D2), triangle (T2) and wall (w2) shaped obstacles all of which have blockage ratios of around 31.8 to 54.9%. The difference in the vortex pair size is due to the distortion of the unburned gas flow preceding the flame front, which as already mentioned depends on the obstacle's geometry. The flow distortion resulted in a jet like flame front emerging from the clearance gap between the obstacle and sidewalls of the box. Flame reconnection behind the vortex was found to be faster with the cylinder shaped obstacle, as shown in Figure 8.36, and occurred at about 12.5 ms after ignition. The slowest flame reconnection was observed with the wall/plate and triangle shaped obstacles and occurred at about 13.7 and 13.8 ms, respectively.

Figure 8.34 and Figure 8.35 shows all the geometric obstacles of LES prediction of peak overpressure and incidence time against blockage ratio with comparisons of experimental measurement. Figure 8.34 clearly demonstrates the wall/plate (green line) has the highest of peak overpressure on both blockage the ratio of simulation and experimental. Again, the shape of the cylinder (red line) presented the lowest peak overpressure in all blockage ratios. Figure 8.33 shows all the geometric obstacles in respect of the incidence time of peak overpressure, because the volume of the combustion chamber has variations from the simulation to the experiment. Both results show that the timings are totally different, the LES incidence time is between 11 to 13 ms and the experimental in between 35 to 55ms. However, it shows that the incidence time in the prediction all go up by increasing the blockage ratio except the wall/plate obstacle. In the experimental measurement, incidence timing decreases by increasing the blockage ratio except for the cylinder blockage ratio which is 32.6% which increase and then decreases.

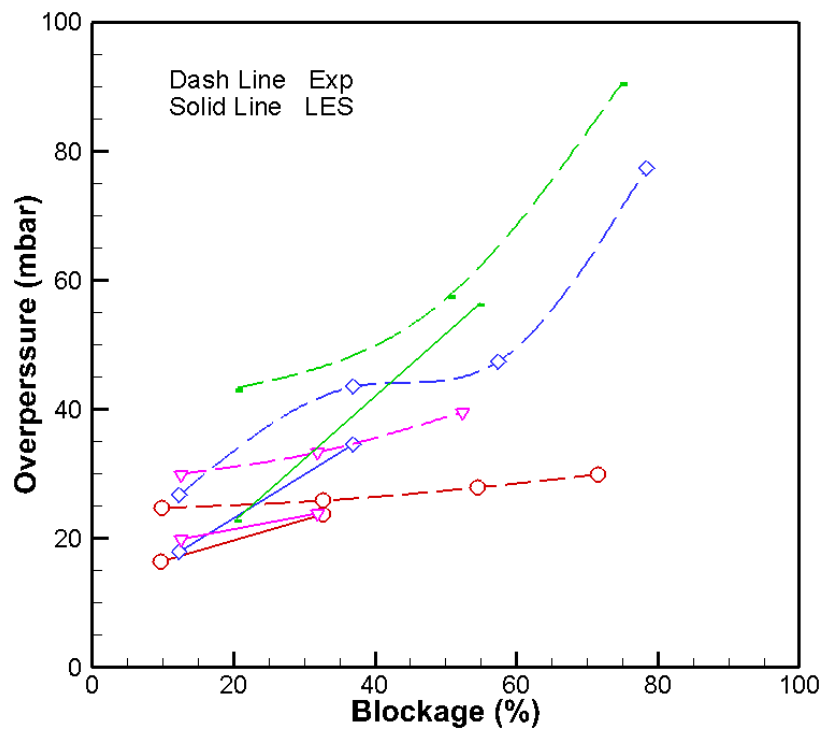Figure 8.34 LES prediction of peak overpressure vs. blockage using various shaped obstructions with two blockage ratios in the combustion chamber compared with various experimental measurements.
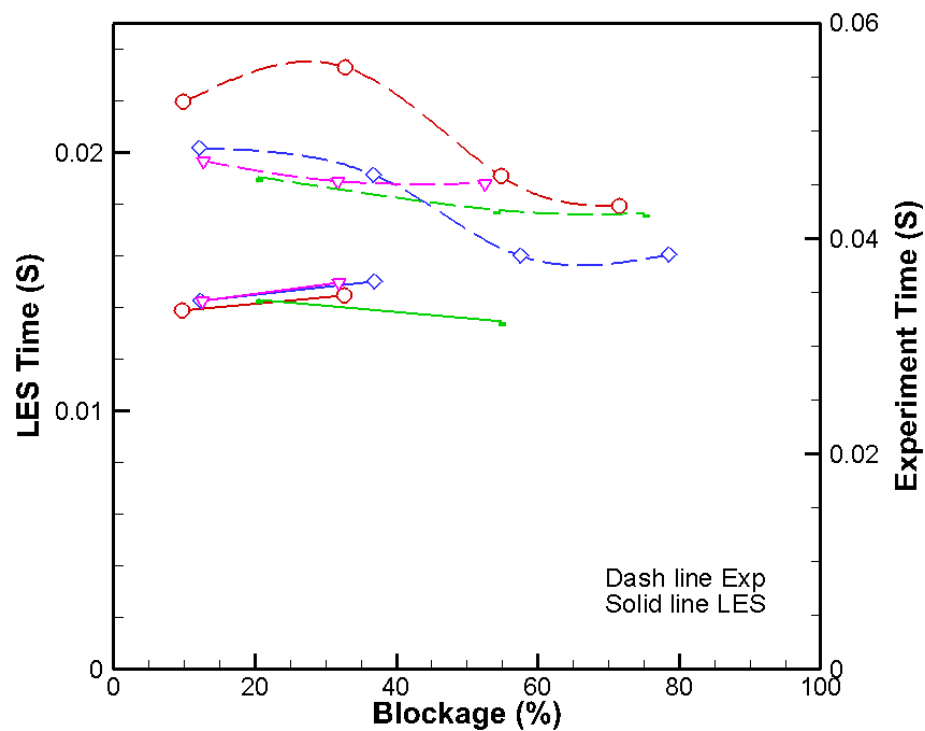
Figure 8.35 LES prediction of peak overpressure incidence time vs. blockage using various shape obstructions with two blockage ratio in the combustion chamber are compared with various experimental measurements.

169

(a)

(b)

(c)

(d)

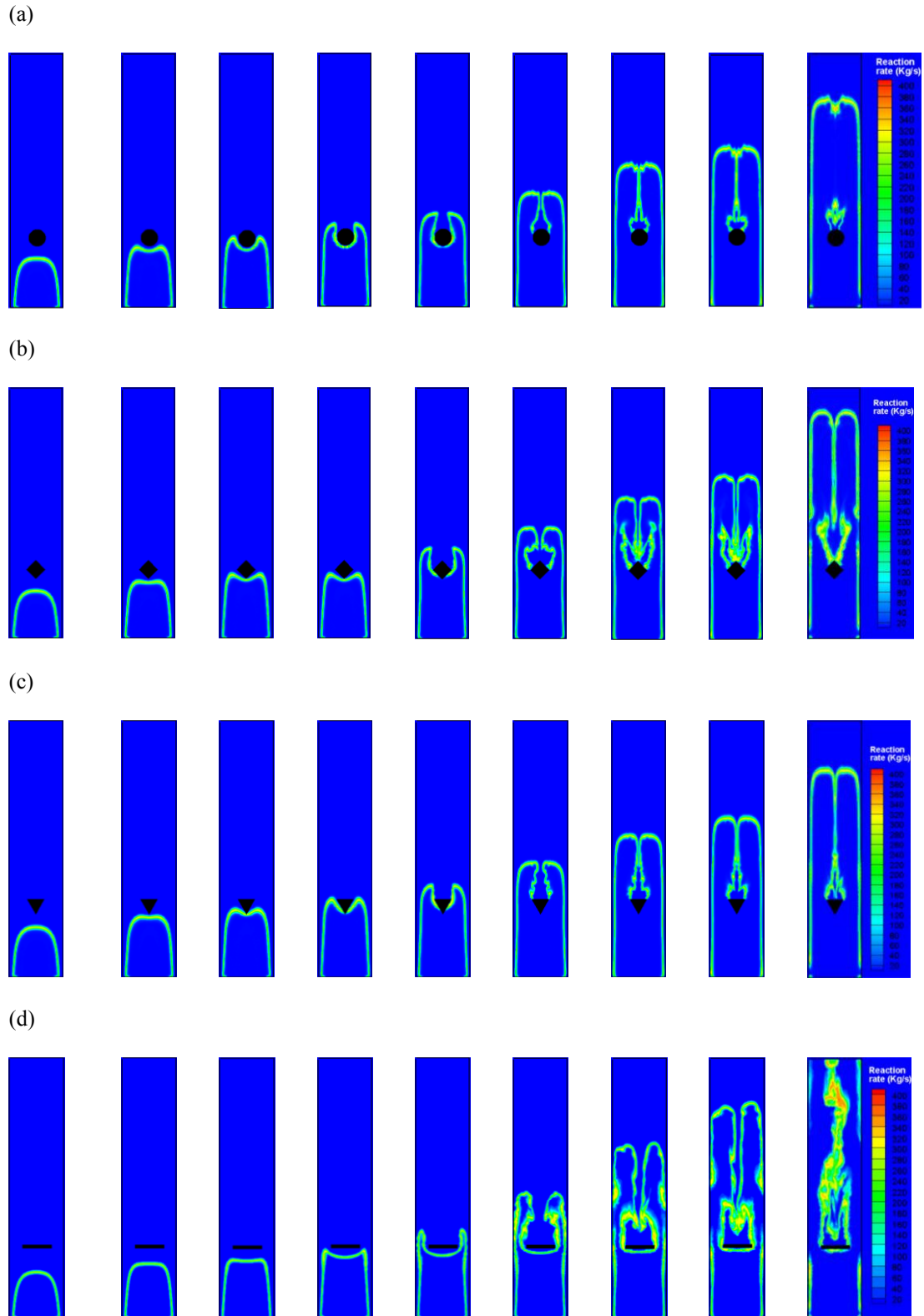Figure 8.36 Derived flame speed verses flame positions from LES and experiments. Baffle and obstacle positions are marked to indicate the influence. (a) Cylinder 32.6% (b) Diamond 36.8% (c) Triangle 31.8% and (d) Wall 54.9% with 9, 10, 10.5, 11, 11.5, 12.5, 13.5, 14 and 15ms.

8.6 Different Flow Configurations

The DFSD model discussed in the preceding sections of this chapter was identified to have been more effective in predicting turbulent premixed propagating flames. To establish a higher level of confidence in using this model, various flow configurations, shown in Figure 8.37, were numerically simulated for stoichiometric propane/air mixture which was ignited from stagnant condition. These configurations were classified into groups as shown in Figure 8.37 to facilitate ease of comparison and discussion. Furthermore, the base configuration 10 i.e. without baffles has also been simulated to validate the model by compare with to the experimental measurements. The primary objective of the present analysis is to validate and explain the DFSD model in predicting turbulent premixed propagating flame dynamics over a wide range of flow configurations. Secondly, the influence of the position of the individual baffle plate in generating overpressure, due to the interactions with deflagrating flames, with respect to the origin of ignition is examined.
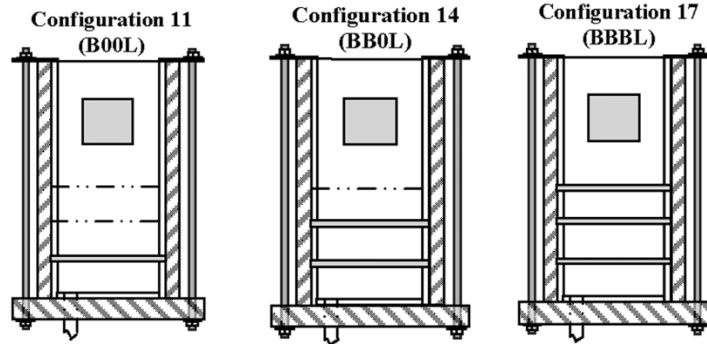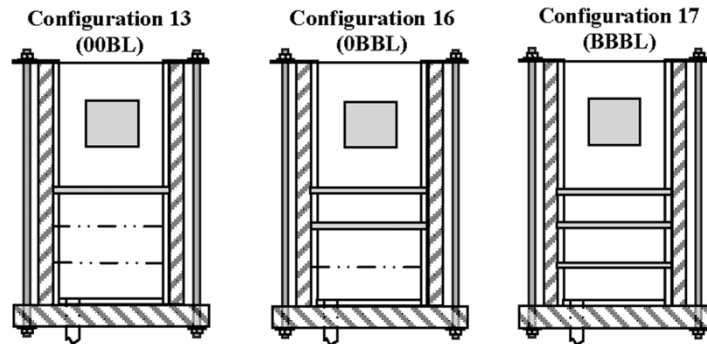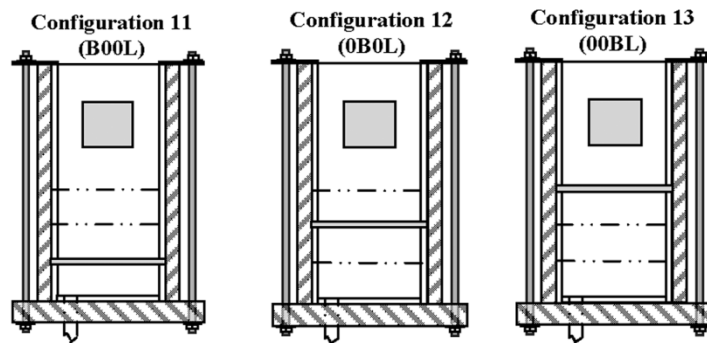
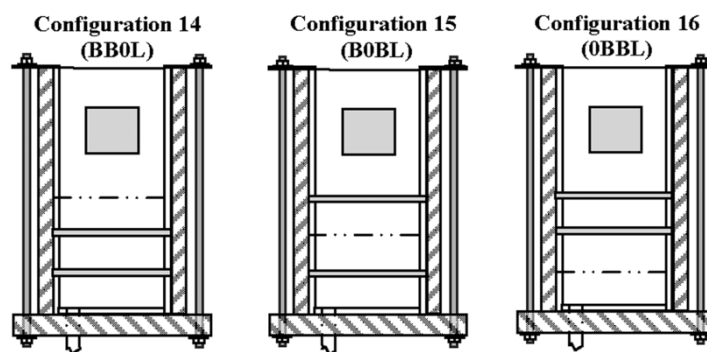Figure 8.37 Classification all Family 2 configurations into groups.

8.6.1 Flame Characteristics: Configuration 10 (Base Case)

Configuration 10 has no baffles except for a solid square obstacle running through the chamber at approximately 96 mm downstream of the ignition point. Since baffles are not presented in this chamber, the flame took longer than in any other configuration discussed in this work to encounter a solid obstacle and to reach the blow-down stage. This configuration is very interesting to analyze and could give some fundamental insight into the formation of flame pockets/traps, due to the obstruction of the flame propagation in the chamber. At time series of overpressure and flame positions from the LES simulations using the DFSD model are briefly shown against the experimental measurements in Figure 8.38. The overpressure trend is very encouraging, as it follows the pressure trend from ignition to blow-down in much the same way as for the experiment measurements, the LES prediction includes the time of pressure rise at about 13 ms, the rate of the pressure rise, peak pressure and its incidence time at 16.2 ms and finally the pressure reflections once the main flame left the chamber. However, the experiment measurement includes the time the pressure rose at about 11.5 ms slope of pressure rise, and peak pressure and its incidence time at 13.6 ms, which is much quick than the predication.

Figure 8.38 and Table 8.6 substantiates the LES predictions of peak overpressure of 55.78 mbar at 16.28 ms against the experiment measurements of 46.87 mbar at 13.64 ms, which is slightly over predicted by 19%. However, considering the overall DFSD model the prediction is natural and appropriate for flame turbulence. Figure 8.39 shows the sequence of images for the flame front from LES (reaction rate contours). It is evident from these images that the LES simulations using the DFSD model are capable to show turbulent flame fronts very accurately at various stages. For instance at 12 ms, the flame shape (finger shape) and its approach towards the square obstacle can be immediately noticed. Similarly, at 16.28 ms (peak overpressure incidence) LES captured the same shape of the experimental image i.e. the flame engulfs upstream from the square obstacle by trapping a certain amount of unburnt mixture which can be seen to burnt out before 16 ms. However, there is some unburnt mixture trapped in the recirculation zone which will burn after the main flame has left the chamber which causes pressure reflections.
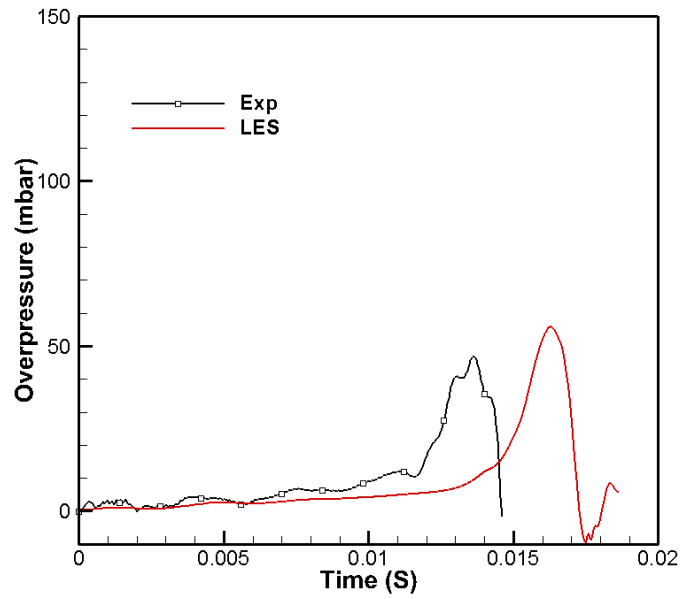
Figure 8.38 Time histories of overpressure vs. experiment measurement for configuration 10.

Group	Describe	Configuration	Present Code	Overpressure (mbar)		Incidence Time (ms)	
				Exp	LES	Exp	LES
1		11	B00L	61.01	82.41	13.20	12.37
		14	BB0L	78.23	93.29	9.60	11.03
		17	BBBL	117.09	118.56	10.00	10.82
2		13	00BL	81.53	70.69	13.00	13.65
		16	0BBL	117.70	103.17	11.40	12.41
		17	BBBL	117.09	118.56	10.00	10.82
	Base Configuration	10	000L	46.87	55.78	13.64	16.28
3		11	B00L	61.01	82.41	13.20	12.37
		12	0B0L	73.78	83.13	12.30	12.73
		13	00BL	81.53	70.69	13.00	13.65
4		14	BB0L	78.23	93.29	9.60	11.03
		15	B0BL	87.52	86.60	10.90	11.70
		16	0BBL	117.70	103.17	11.40	12.41

Table 8.7 List of the configurations with the peak overpressure obtained and the time taken to reach the peak from ignition as well as time in stages of the LES prediction and experiment measurements.

Figure 8.39 Series of flame images at 7.0, 12.5, 13.0, 13.5, 14.0, 14.5, 15.0, 15.5, 16.0, 16.5 and 17.0ms respectively after ignition.

8.6.2 Flame Characteristics: Group 1

This section provides the flame characteristics of the configurations in Groups 1 using the DFSD model according to the discussion in Figure 8.37. This fami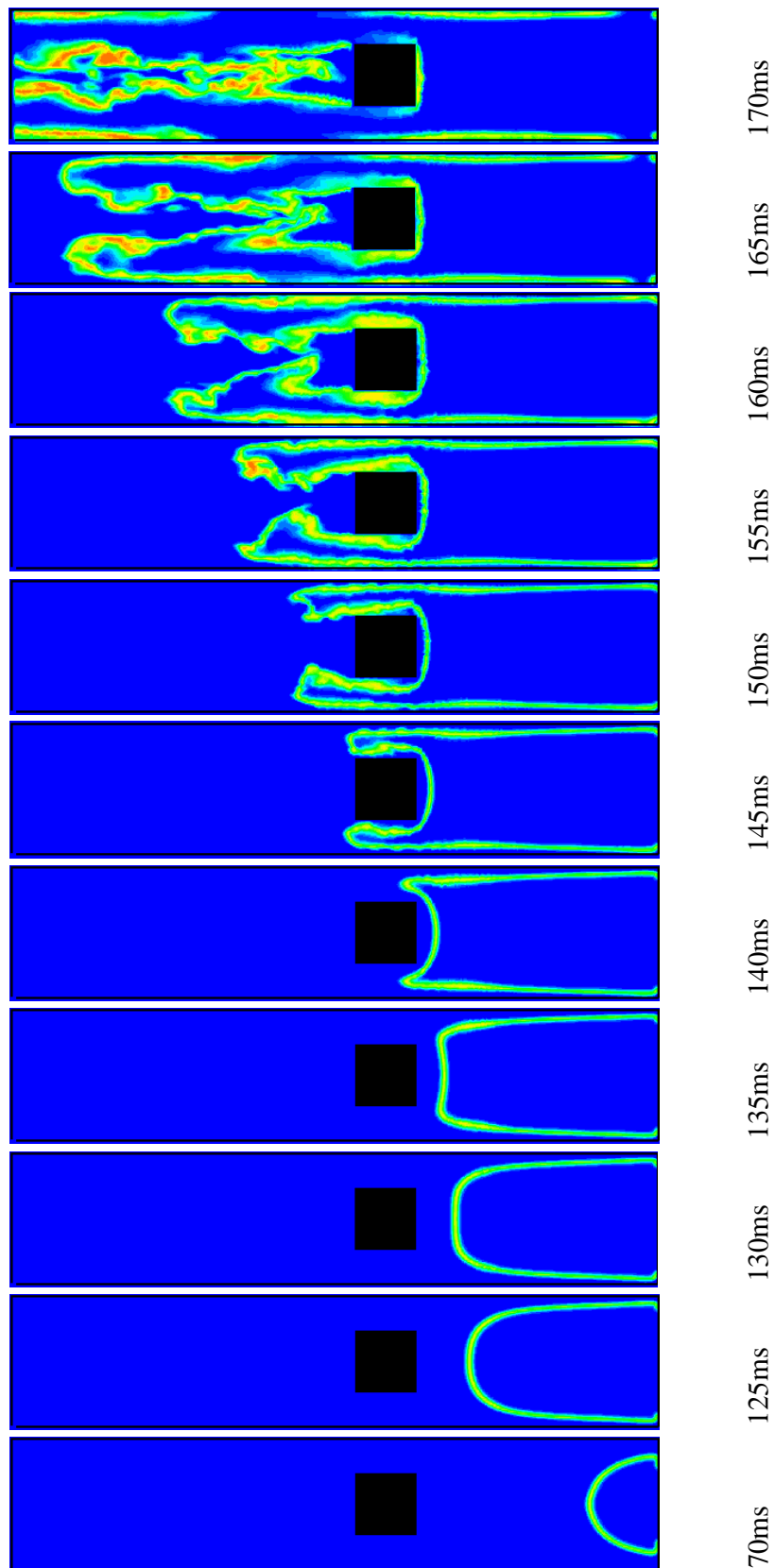ly consists of configurations 11-14-17 with a progressively increasing number of baffles from one to three and positioned nearest from the ignition point at the bottom as shown in Figure 8.37. It should also be noted here, that the detailed experimental results for configuration 14 are not available to compare with LES, however, only overpressure and its time of occurrence reported by Masri et al. (2009) are used here.

.

The time histories of the overpressure and flame positions from LES and experiments are plotted as shown in Figure 8.40 and Figure 8.41 respectively. It is evident from Figure 8.40 that the overpressure trend is in high agreement, only being slightly over predicted. Nevertheless, by comparing the LES simulations using the DFSD model we can see that there is good agreement in terms of magnitude, trend and timing. This is mainly due to the DFSD model employment, which is efficient in calculating unresolved flame surface density. Figure 8.40 highlights the impact of number of baffles and their positions with respect to the distance from the ignition bottom. Time elapsed after the first and second baffle from the ignition bottom and sharply increased in the pressure gradient due to the turbulence generated, this can be easily identified. Similarly, the flame position shown in Figure 8.38 was also well predicted except limitation of the experimental measurement for configuration 14.

Figure 8.42 and Figure 8.43 shows the flame speed and acceleration from the LES and experiments derived from flame the images. However, the limitation of the experimental measurement was hard to obtain for the flame speed and acceleration for the configuration 14. It can be noticed that the flame speed and acceleration from the LES matched accurately with the experimental measurements, except when the flame was located downstream of the acceleration for configuration 17. One main reason for this is due to the limitation in the resolution of the experimental measurements. Within blow down configuration 17, the flow conditions were highly turbulent and the flame propagates faster at approximately 80 - 100 m/s in this group. Hence, the available flame images within this region are limited, this

eventually controls the experimental data. It is very interesting to note that irrespective of the number of baffles and their positions, all configurations recorded a speed of around 100 m/s during the blow down phase.

A quantitative comparison at any given time gives the influence of baffles on overpressure and turbulence generation. In order to facilitate further discussion, the magnitude and incidence time of overpressure for four groups were plotted as shown inFigure 8.44. It is evident from Figure 8.44(a) that, as expected, the overpressure which was generated was higher in the case of configuration 17 since it had 3 baffles with an earlier and lower incidence of time in configuration 14 due to one baffle with a later incidence time. It is very interesting to note that the incidence of time in this group maintained a linear relationship while the overpressure had a non-linear relationship as seen in Figure 8.44(a). The magnitude of the overpressure increased from 50% and 75% due to the addition of one and two baffles in configuration 14 & 17 respectively when compared to the overpressure of configuration 11, which had one baffle at S3. However, the incidence of time decreased by 10.8% and 12.5% in configuration 14 &17 respectively, this is inline with configuration 14. One reason for the non-linear relationship of overpressure might be due to the position of the baffles from the ignition source, even though they had the same blockage ratio. This will be discussed further in the next section.

Figure 8.45 presents a cut view of the LES predicted reaction rate contours, showing the flame structure at 5.0, 7.0, 9.0, 10.0, 10.5, 11.0 and 12.0 ms after ignitions for the whole group. This facilitates qualitative and quantitative comparison of flame position and its structure at any given time. It can be seen that while using the flame surface density model, approximately 3 to 6 LES grid points are required to resolve the flame thickness however, using the DFSD model only requires a maximum of 3 grid points. The pockets or traps indicated in the case of configuration 17 can be clearly seen, while using the DFSD model in Figure 8.45(c) at 11.0 and 12 ms. Considering an instance at 7.0 ms from Figure 8.45(a) & (b), which illustrates the finger shaped flame structure, which is generally expected in chambers having l/d ratio greater than 3. Figure 8.45(b) at 10.5 and 11.0 ms shows a clear picture of entrapment of unburnt fuel/air mixture around the solid square obstacle within the recirculation zone. Similarly, Figure 8.45(c) at 11 and 12.0 ms shows the consumption of trapped mixture, once the main flame had left the chamber. The above reaction rate contours also show the consumption of unburnt mixture within the viscous boundary layer, as evidenced in experimental flame images in Figure 8.13.
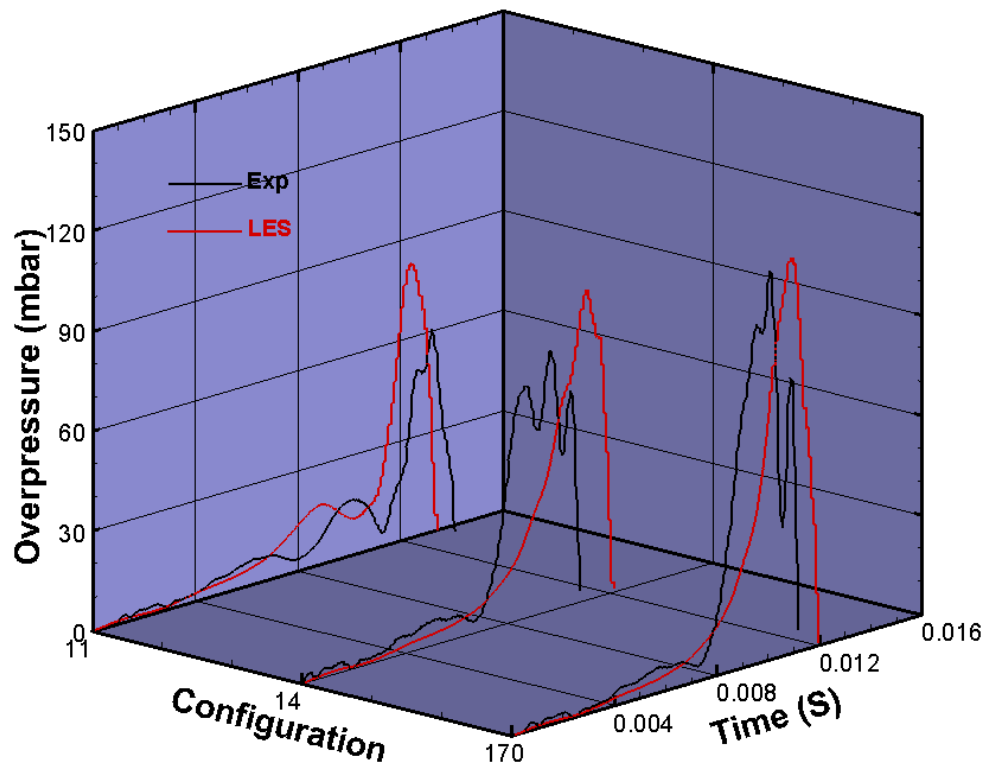
Figure 8.40 Comparison of LES predicted and experiment measured overpressure time traces of Group 1.
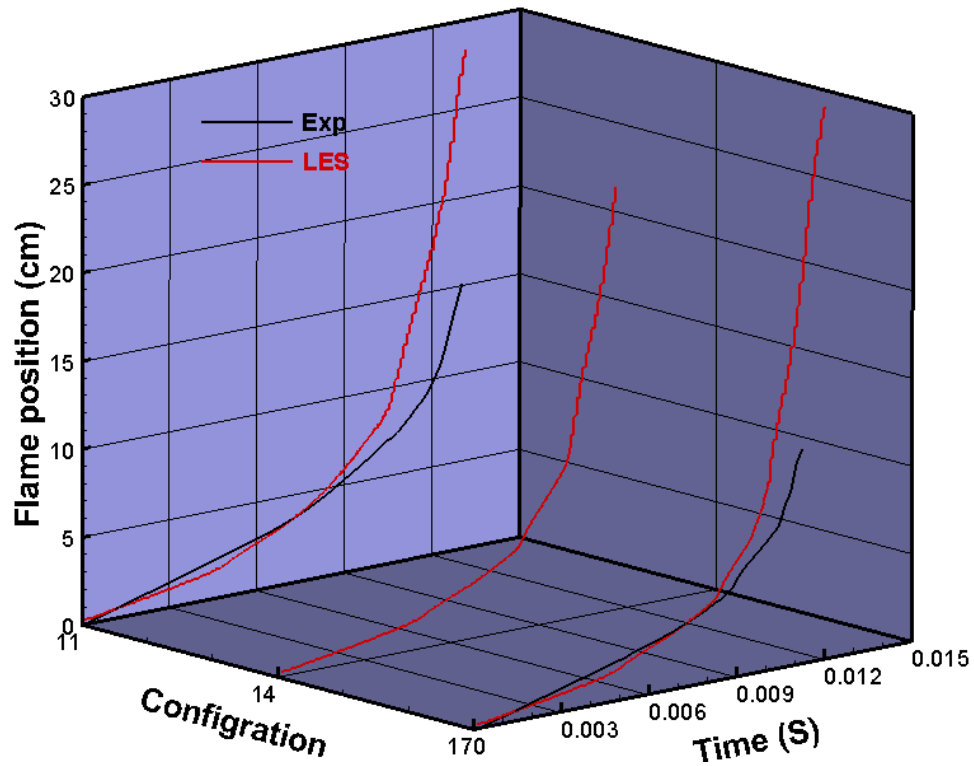
Figure 8.41 Comparison of LES predicted and experiment measured Flame position against time traces of Group 1.
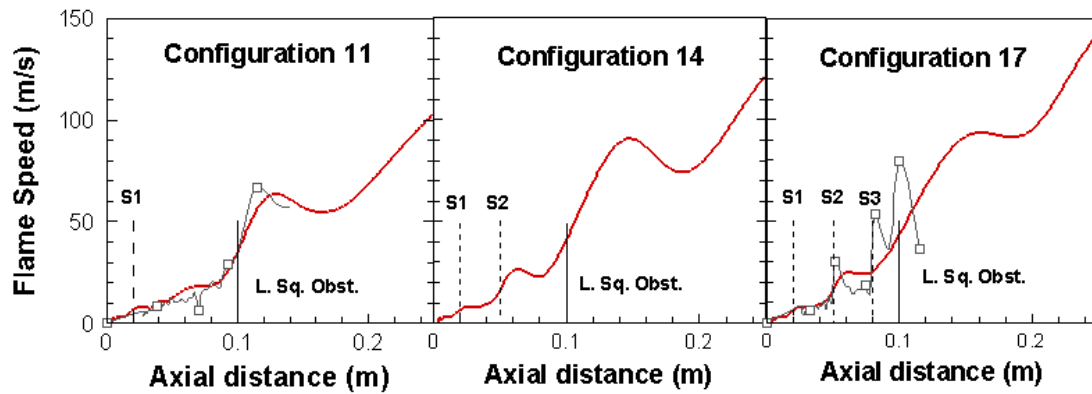
Figure 8.42 Comparison between predicted (Red solid line) and experiment (Grey lines with square symbol) of flame speed against axial distance. The location of baffle stations (S1, S2 and S3) and the large square solid obstacle are shown.
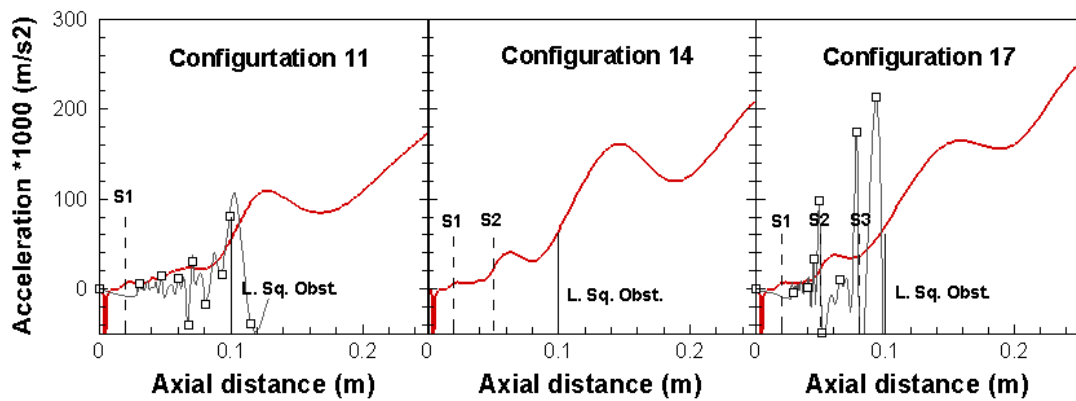
Figure 8.43 Comparison between predicted (Red solid line) and experiment (Grey lines with square symbol) of flame acceleration against axial distance. The location of baffle stations (S1, S2 and S3) and the large square solid obstacle are shown.
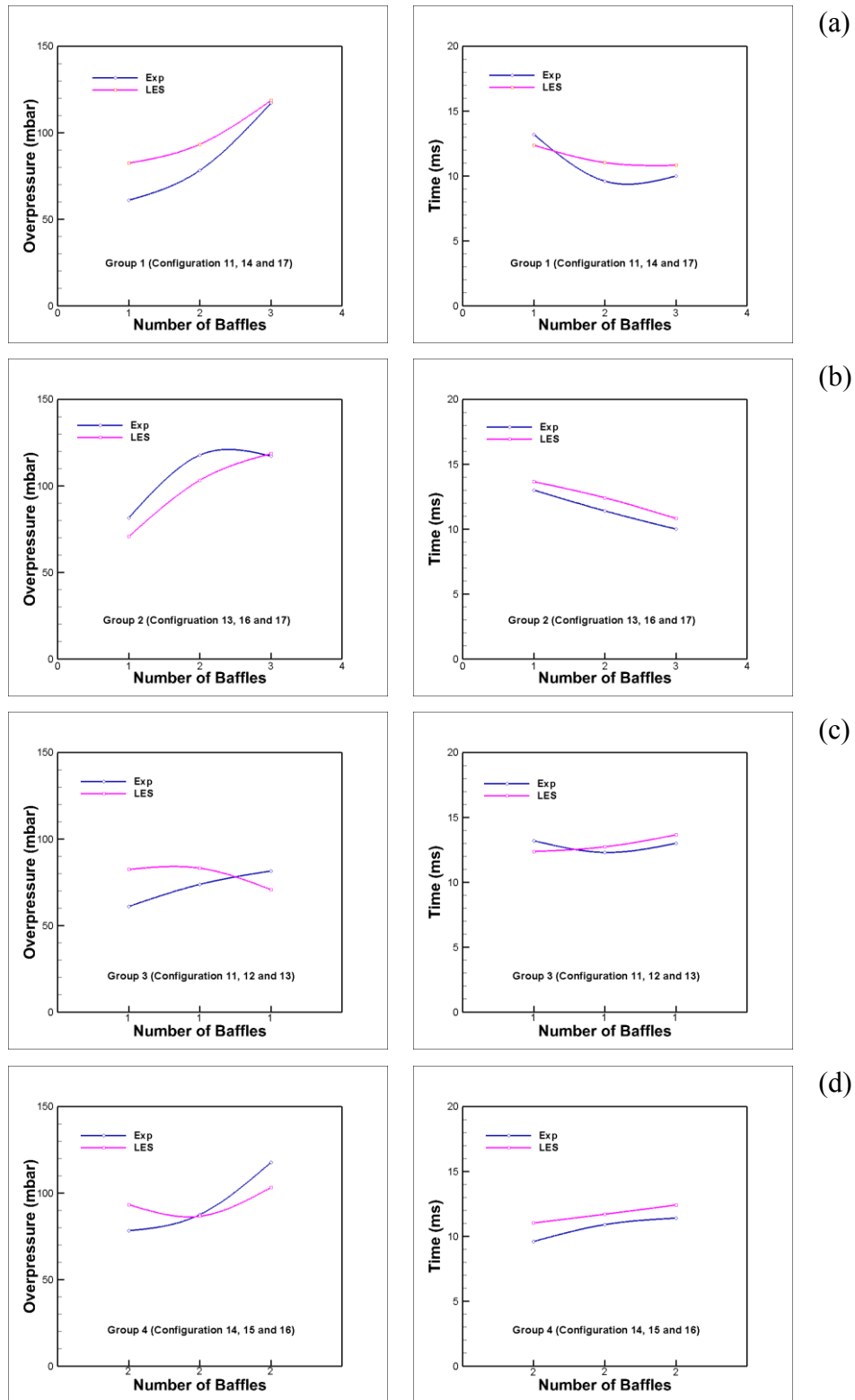
Figure 8.44 Variation of peak overpressure and its time of incidence compared with LES vs. Experiments for four groups (a) Group 1, (b) Group 2, (c) Group 3 and (d) Group 4.
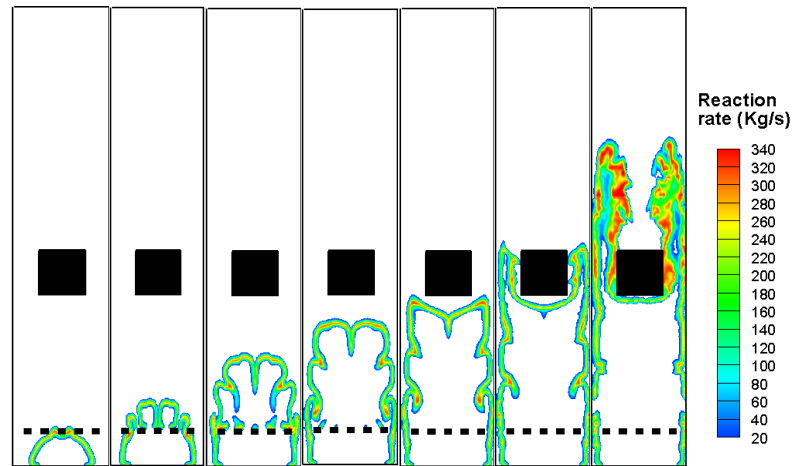
(a)
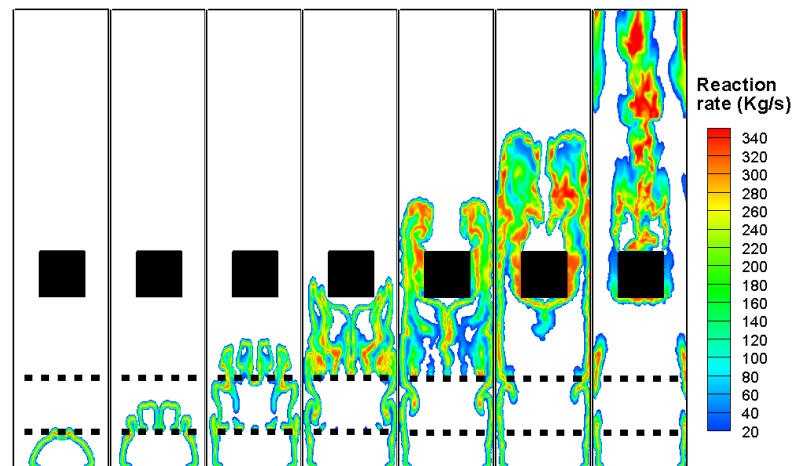
(b)
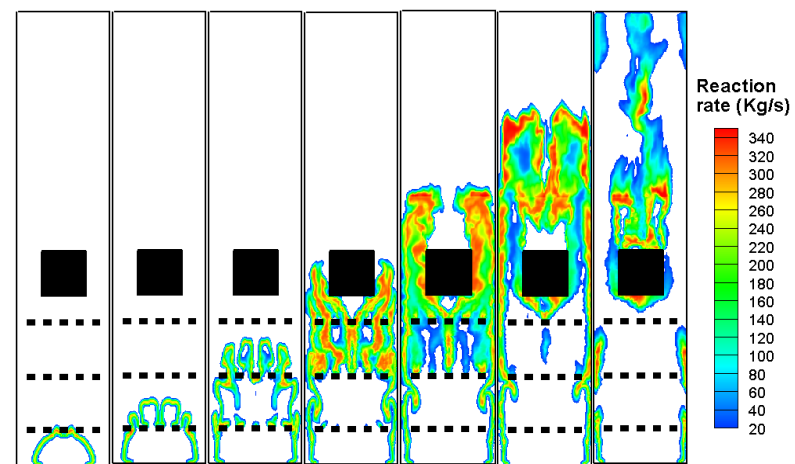
(c)

Figure 8.45 Predicted flame structure from three configurations at 5, 7, 9, 10, 10.5, 11 and 12.0ms after ignition (a) Configuration 11, (b) Configuration 14 and (c) Configuration 17.

8.6.3 Flame Characteristics: Group 2

The baffles in Group 2 progressively increase from one to three from the farthest side of the ignition bottom end as shown in Figure 8.37. The configurations involved in this group are 13-16-17 and are very similar to Group 1 in terms of number of baffles, however, they are very different in terms of their position with respect to the ignition source. This section does not describe the flame characteristics as it is a subset of the other groups.

Time histories of overpressure and flame position from LES and experiments for Groups 1 and 2 are plotted and shown in Figure 8.46 and Figure 8.47. Figure 8.46 shows that all the LES simulations have a slight delay in the incidence timing for the overpressures, and are also under predicted for the peak overpressure on configuration 13 and 16. However, Figure 8.46 demonstrates the impact of the number of baffles and their position with respect to the distance from the ignition bottom. The time elapsed in reaching the first baffle from the ignition bottom increased in the steepness of the pressure gradient due to the turbulence generated, this can by clearly identified. Meanwhile, the flame position shown in Figure 8.47 is comparable with the LES predictions with all the experimental measurement being slightly over predicted. Figure 8.47 and Figure 8.48 demonstrate that the flame speed and acceleration from LES and experiment derived from the flame images with all the configurations in this group. The experimental measurements of the flame speed and acceleration footprints are well tracked by LES predication simulations for configurations 13 and 16 respectively. However, configuration 17 is no mentioned here because this was covered the last section.

The overpressure and the incidence of time for the whole family of experiments is shown in Figure 8.44(b). It is evident that both the overpressure and time maintain a nonlinear relationship in this group. The overpressure increased from 46% and 68% in configuration 16 and 17 compared to the measured overpressure in configuration 13. However, the incidence times decreased by about 9-21%. To facilitate a comparative discussion, results for experimental groups 1 and 2 were plotted together and individual configurations were

mentioned as shown in Figure 8.49 . The following main points can be derived from Figure 8.49.

It is very interesting to note that, although the baffle plate in configuration 13 and 16 has the same blockage capacity, lower overpressure is generated in configuration 13 due to the position of the baffle from the ignition source. Similarly, configurations 16 and 14 have two baffles with the same blockage capacity and generated less overpressure than in configuration 14. This observation confirms that the blockage with the same capacity, nearer to the ignition source would generate less overpressure that at an earlier time, when compared with the blockage positioned far from the ignition source. In addition, it can also be observed that the timing of the peak pressure in configuration 13 & 16 is great when compared to configuration 11 & 14. Although the overpressure increases with the blockage ratio, the rate of this increase from configurations 16 to 17 and 14 to 17 is not the same, as observed in Figure 8.49.
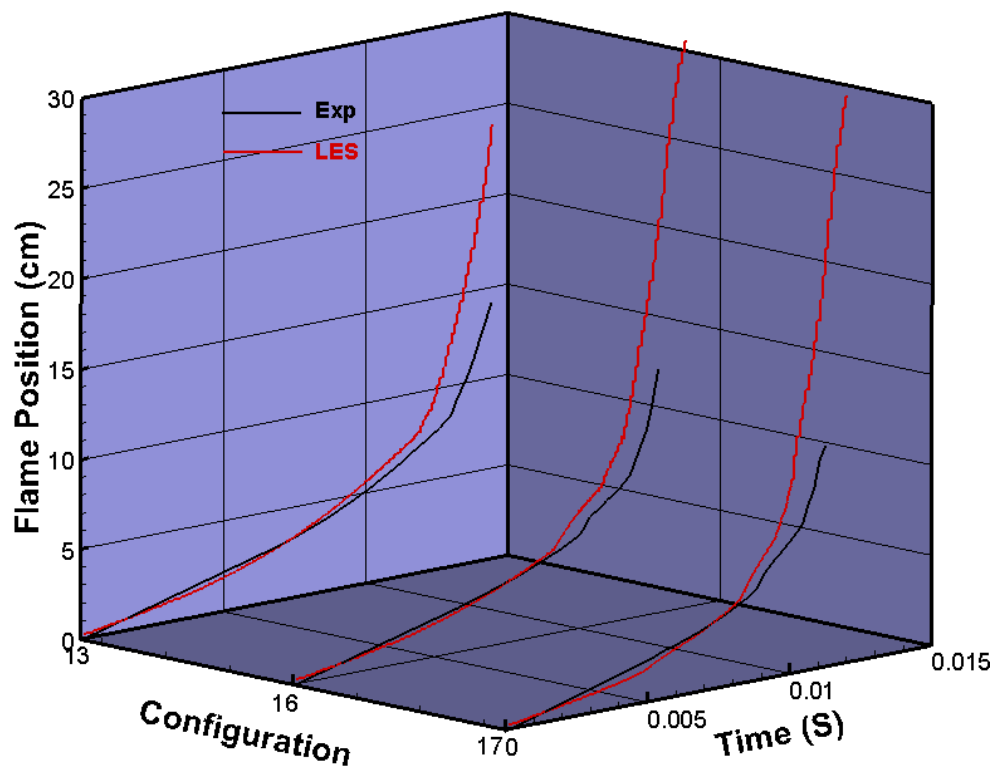
Figure 8.46 Comparison of LES prediction and experiment measured flame position against time traces of Group 2.
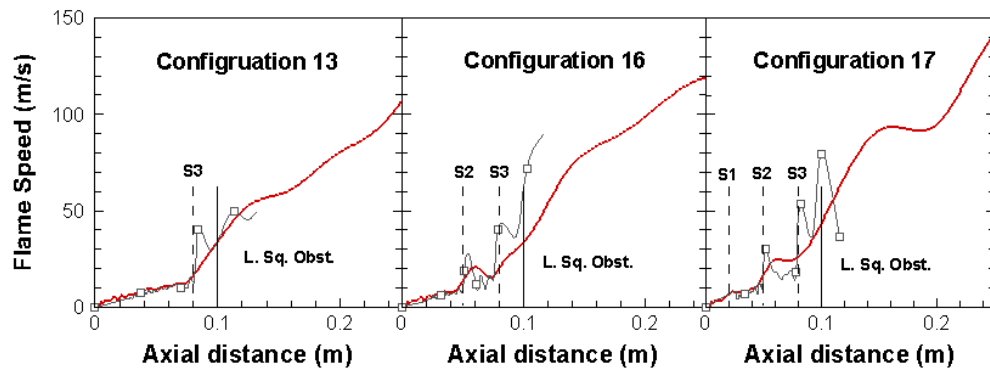
Figure 8.47 Comparison between predicted (Red solid line) and experiment (Grey lines with square symbol) of flame speed against axial distance. The location of baffle stations (S1, S2 and S3) and the large square solid obstacle are shown.
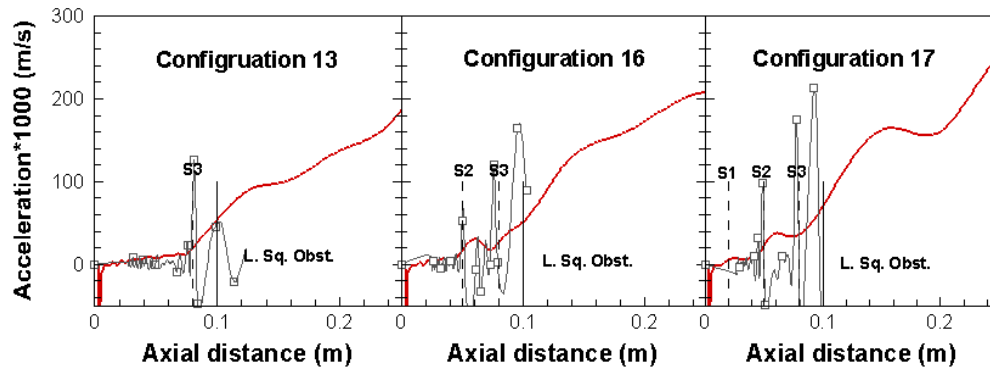
Figure 8.48 Comparison between predicted (Red solid line) and experiment (Grey lines with square symbol) of flame acceleration against axial distance. The location of baffle stations (S1, S2 and S3) and the large square solid obstacle are shown.
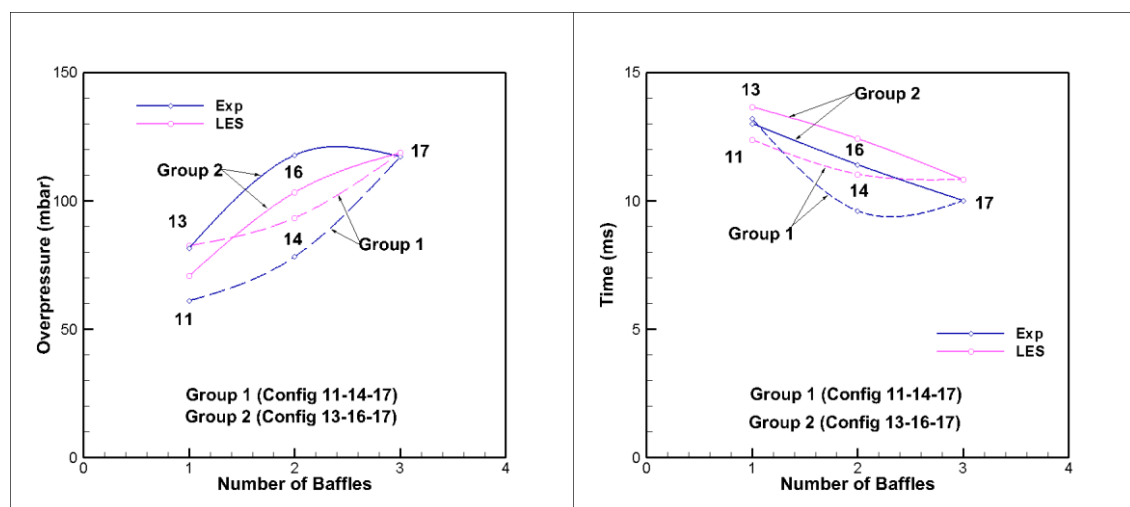
Figure 8.49 Variation of peak overpressure and its time of incidence compared from LES vs. experiments for Group 1 and 2.
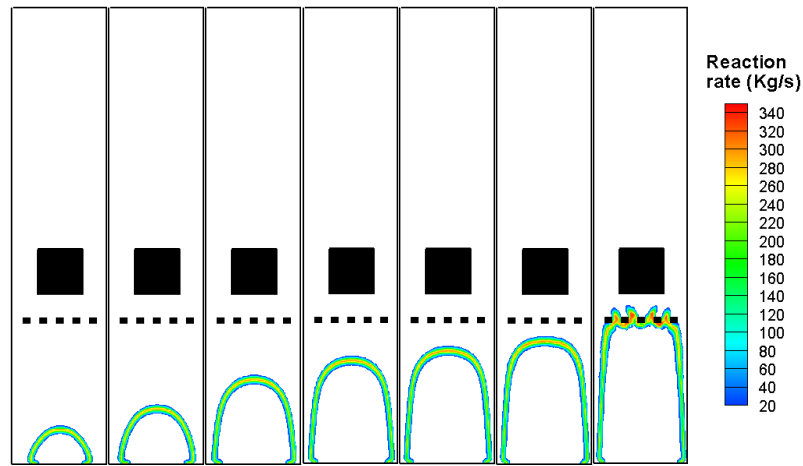
(a)
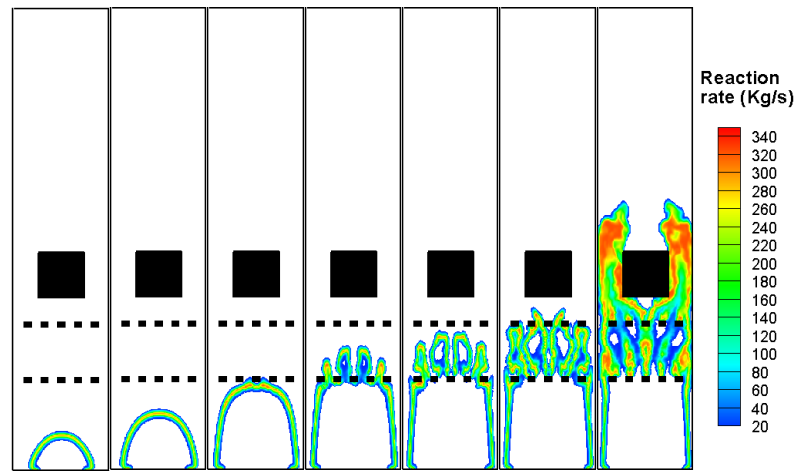
(b)
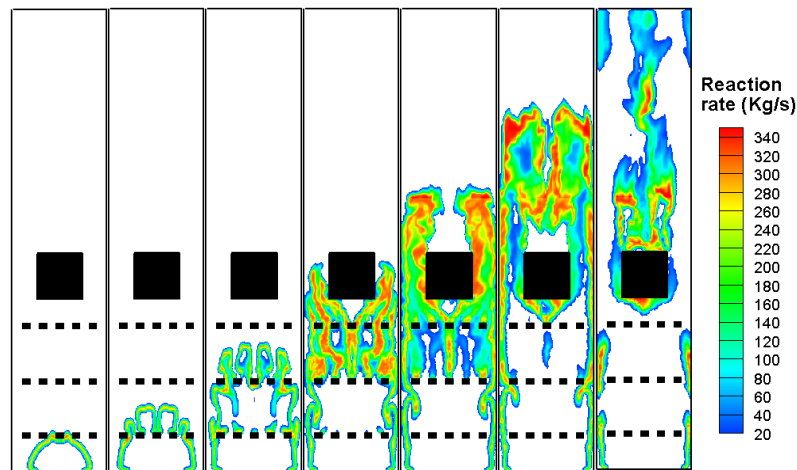
(c)

Figure 8.50 Predicted flame structure from three configurations at 5, 7, 9, 10, 10.5, 11 and 12.0ms after ignition. (a) Configuration 13, (b) Configuration 16 and (c) Configuration 17.

8.6.4 Flame Characteristics: Group 3

Group 3 has three configurations (11-12-13) with one baffle plate at different stations and a solid square obstacle at a fixed position as shown in Figure 8.37. This group has been extensively investigated mainly for two reasons. The first is consistency in the number of baffles used in individual configurations, which is very interesting for direct comparison. Secondly, the availability of experimental axial and radial velocity information using the LDV technique at a location downstream from square obstacle in all configurations facilitates the validation by the DFSD model in this work.

The time histories for overpressure for three configurations are shown in Figure 8.51. The experimental pressure trend collected near the ignition end of configuration 13 has been plotted together for comparison purposes. As discussed earlier in the case of the other groups, the DFSD formulations are very successful in predicting turbulent premixed flames in all the complex geometry of configurations. It is evident from Figure 8.51 that the time traces of overpressure from the LES for configuration 13 are very closely matched to the experimental measurements. It can be clearly seen that every stage of the flame propagation including interaction with the baffle plate and solid obstacle are reproduced very well. The time of peak overpressure occurrence is perfectly matched, however, the magnitude is slightly under predicted on configuration 11 and 12. It is also evident that the DFSD model is successful in predicting the pressure gradient at various stages of the flame propagation. Figure 8.52 presents the flame position against the time histories, it can be observed that the flame positions are slightly over predicted again with time for all configurations.

Figure 8.53 and Figure 8.54 show a comparison between experimental measurements and numerical predictions for flame speed and acceleration. Also the position of the baffle plates and the solid square obstacles are shown in Figure 8.53 and Figure 8.54, in order to identify the influence of the obstacles. Flame speed is calculated from the rate of change over successive images in the case of the experiments and as a first derivative of the flame position with respect to time in LES. It should be noted here that in the case of the experimental measurements there is a 2000 fps limitation on the high speed digital camera, which eventually controls the resolution of the measurements. Due to this limitation, the

drop in flame speed after the square obstacle is not captured correctly, however, predictions from LES are more continuous. For the purposes of clarity, experimental measurements are represented by square symbols in **Error! Reference source not found.** and Figure 8.54. At the location of the square obstacle, the highest flame speed is obtained for configuration 11 and this location also corresponds to the highest flame acceleration. It is interesting to note in configuration 13 that the slowdown in the flame speed and the reduced acceleration as the flame front travels a relatively longer distance which is further away from the baffle plate and the square obstacle.

Reaction rate contours from LES at seven important instants are plotted in Figure 8.55 to study the flame-obstacle interactions in this group. The instants chosen are 5, 7, 9, 11, 12, 13 and 13.5 ms in all configurations. This generally matches flame evolution, interaction with the baffle plate, interactions with the square obstacle, formation of the recirculation zone and blow-down of the flame from the chamber. The reaction rate contours at 5, 7 and 9 ms provide a great deal of information about the nature of flames. At these instants, configuration 12 & 13 have a perfectly identical structure, the shape is the same flame thickness and the reaction rate. Since configuration 11 has a baffle plate at S1, the flame interacted and jetted through the baffle, which eventually changed the flame shape. However, the flame position at 9 ms in configuration 11 is almost equal to the flame position in the other two configurations which had just started to propagate at a higher speed. At 11 ms, the flame in configuration 11 had a higher surface area to consume more mixture due to its interaction with the baffle plate at 5 ms. By this time in configuration 12, the flame had evolved through the baffle slits and started to form individual flame kernels. However, the flame in configuration13 was still smooth and had a finger shaped structure propagating in the axial direction proportional to gas expansion ratio.

Reaction rate contours at 12 ms are very interesting and we are able to delineate information about the flame entrapment around the square obstacle. By comparing configuration 11 and 12 at this instant, it is evident that, configuration 11 has more surface area with a smoother outer flame structure and wrinkled inner flame structure. The inner flame structure is responsible for trapping any unburned mixture. Although, it is a very similar scenario to configuration 12, having the smoother inner flame structure, which engulfs a lesser amount of mixture compared to configuration 11. Also, some flame islands can be observed in the

case of configuration 12 which are responsible for a slightly higher overpressure at any given time compared to configuration 11.

Comparing reaction rate contours at 13 ms from configuration 13 with contours at 12 ms of configuration 11 and 12 enhances the idea of how individual flow configuration traps unburned mixture around obstacles. It can be clearly observed that the mixture trapped in configuration 13 is a lot less compared to other configurations and the flame spreads within the boundary layer region around the square obstacle. One reason for this might be due to the gap between the baffle and square obstacle which affects the turbulence intensity of the flow within the chamber. At 13 ms from configuration 11 and 12, it can be observed that the flame position overlaps again and both configurations show similar natures of the flame i.e. consuming trapped mixture downstream of the square obstacles and overlapping of the two branches of flame separated as a result of the obstacles.

Figure 8.51 shows peak overpressure and their incidence times from LES and experiments. It is very interesting to know that in this family, overpressure from LES maintains a linear relationship. The experimental overpressure also maintains a linear relationship however, with a different slope. The incidence time in the case of LES and experiments does not maintain a linear relationship as such and LES incidence times showing a slight over prediction for configuration 12 and 13.

It is very interesting to know that configuration 13, having a baffle at S3 (away from the ignition bottom) recorded a higher overpressure of 70.69 mbar at 13.65 ms. Configuration 11 had one baffle at S1, near to the ignition bottom which recorded 82.41 mbar at 12.37 ms. Configuration 12 had one baffle at S2 and recorded an overpressure of 83.13 mbar at 12.73 ms in between the other two. This observation confirms the observation made in the case of group 3 i.e. the farther the baffles are from the ignition centre, the higher the overpressure is at a later stage. By closing the baffles at the ignition source or at the end reduces the magnitude of the overpressure at an earlier stage. However, the LES simulations for this group have some differences.
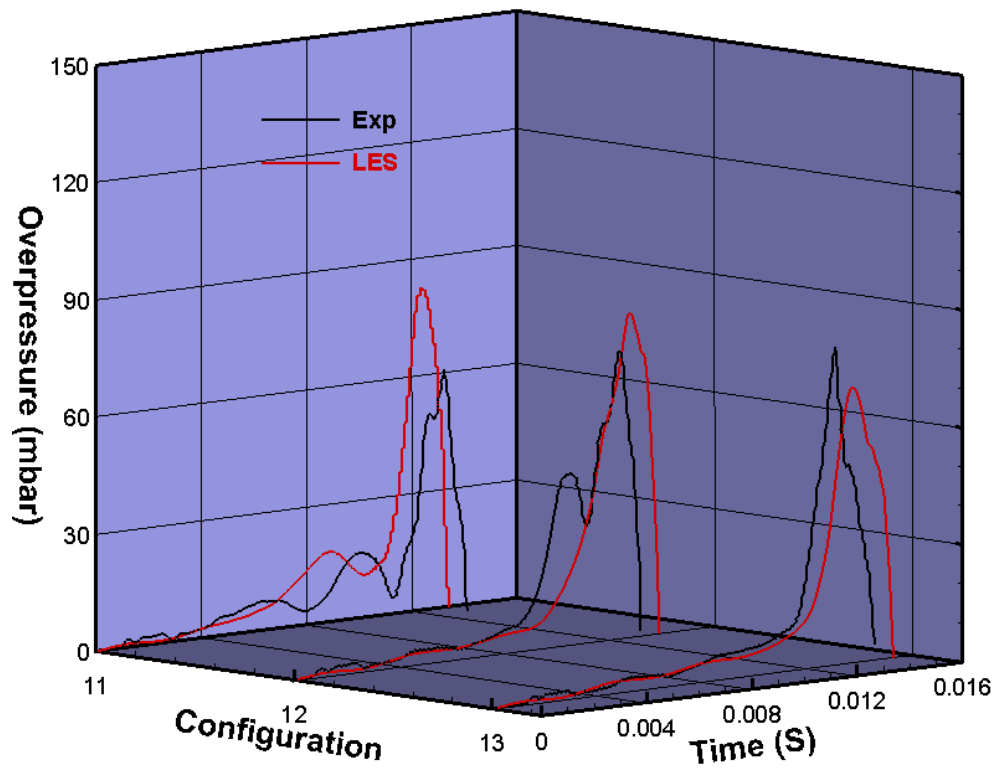
Figure 8.51 Comparison of LES predicted and experiment measured overpressure time traces of Group 3.
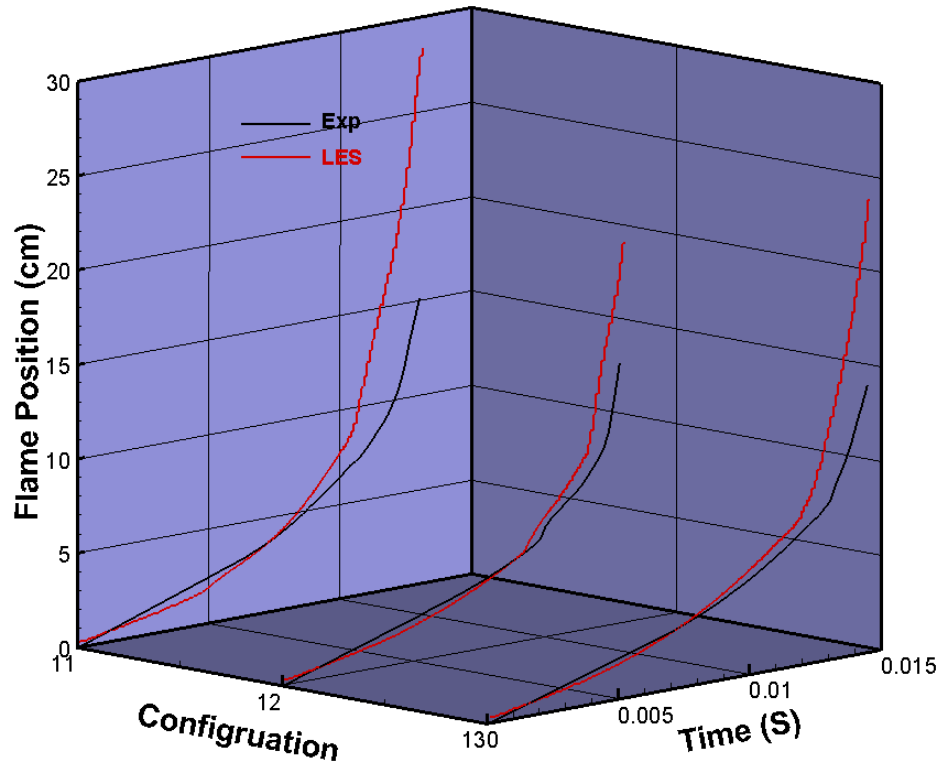
Figure 8.52 Comparison of LES predicted and experiment measured Flame position against time traces of Group 3.
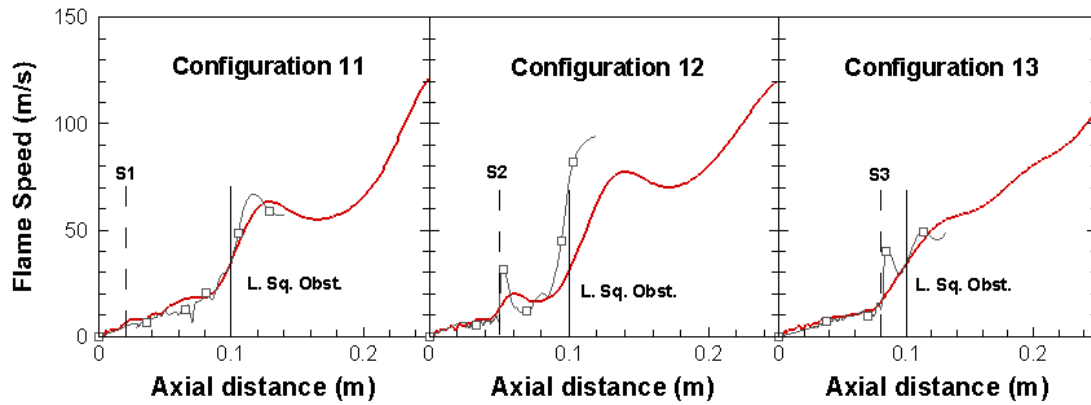
Figure 8.53 Comparison between predicted (Red solid line) and measured experiment (Grey lines with square symbol) of flame speed against axial distance. The location of baffle stations (S1, S2 and S3) and the large square solid obstacle are shown.
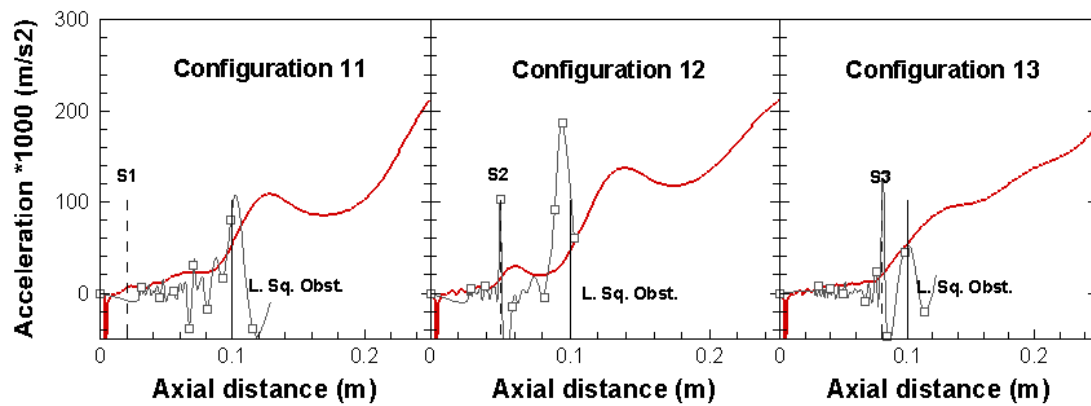
Figure 8.54 Comparison between predicted (Red solid line) and measured experiment (Grey lines with square symbol) of flame acceleration against axial distance. The location of baffle stations (S1, S2 and S3) and the large square solid obstacle are shown.
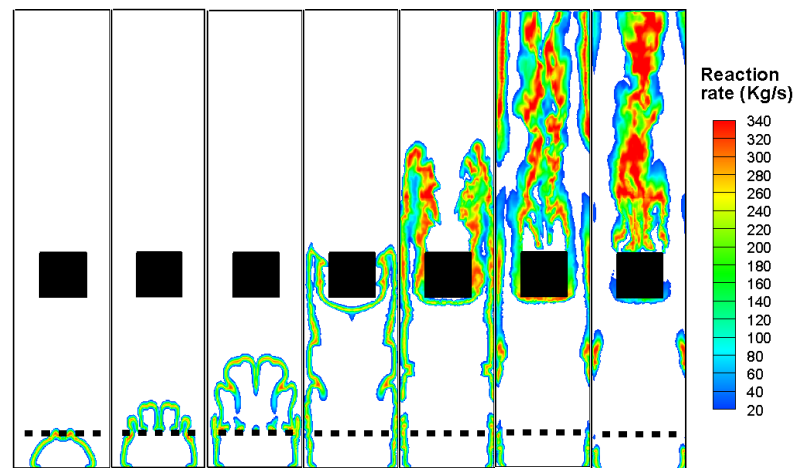
(a)
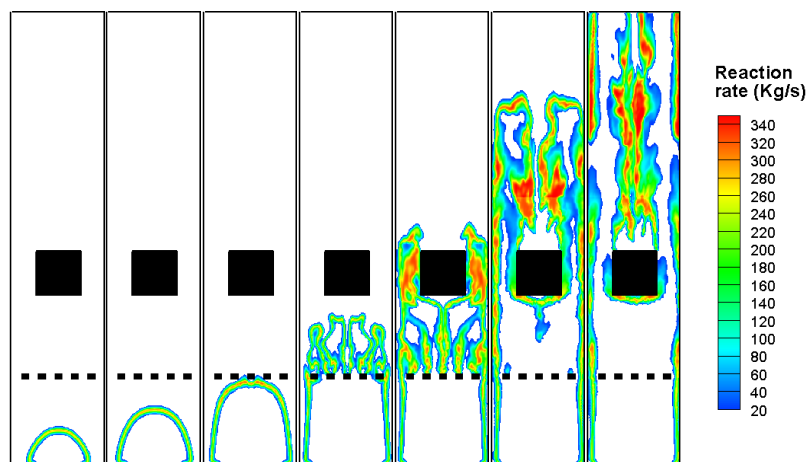
(b)
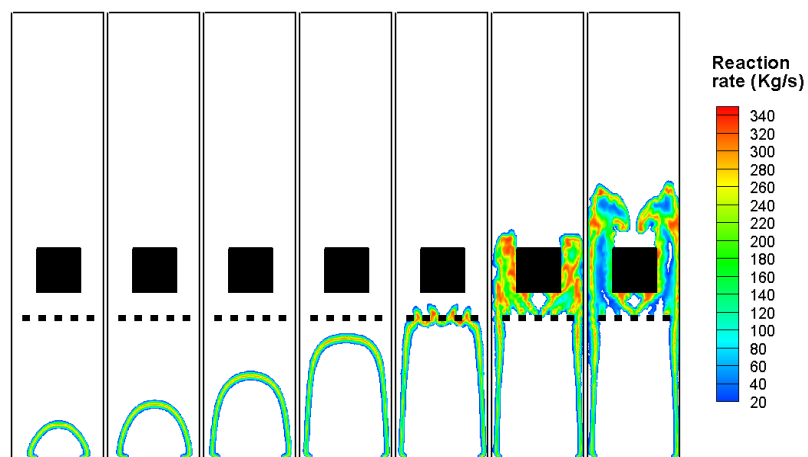
(c)

Figure 8.55 Predicted flame structure from three configurations at 5, 7, 9, 11, 12, 13 and 13.5ms after ignition. (a) Configuration 11, (b) Configuration 12 and (c) Configuration 13.

8.6.5 Flame Characteristics: Group 4

Group 4 has three interesting configurations (14-15-16) with two baffles positioned at different stations. Experimental measurements of flame positions and speed for configuration 14 and 15 are not available to compare. The time histories of overpressure for three configurations are shown in Figure 8.56. As discussed earlier in the case of other groups, the DFSD formulations are very successful in predicting turbulent premixed flames in all flow configurations. It is evident from Figure 8.56 that the time traces of overpressure from LES for all configurations very closely match the experimental measurements. It can be clearly seen that every stage of flame propagation including interacting with the baffle plate and solid obstacle is reproduced very well. The time of peak overpressure occurrence is perfectly matched, however, the magnitude is slightly under or over predicted. It is also evident that the DFSD model is successful in predicting the pressure gradient at various stages of the flame propagation.

Figure 8.56 shows a characteristic comparison of overpressure histories for three configurations, from experimental measurements and LES simulations. Due to the blockage of flow and interactions of the flame with the second baffle plate in configuration 14 and 15, a small hump in the pressure history is noticed at around 8 ms. It is clear that the rate of pressure rise and its trend including the first hump is predicted well except for configuration 14, where the computed rate of increase of pressure is slower than the measurements, indicating a faster decay of turbulence between the second baffle plate and the square obstacle. It is also worth noting here that the pressures reported here are measured close to the ignition end and these may be different if measured at the wall due to a possible pressure gradient within this chamber. From the experimental measurements, the overpressure is found to oscillate after the peak overpressure, while burning the remaining trapped mixture after blow down of the main flame. It has been found in our preliminary studies, that the DFSD model is able to predict the oscillating behaviour of the overpressure while burning the trapped fuel/air mixture as shown in the case of configuration 10 (Figure 8.38). However, this has not been repeated in order to verify for the present group of configurations presented in this section for two reasons. The first is, we are more interested in the flame-obstacle interactions. There is no scope in carrying out simulations once the flame has left the chamber. The second is the cost of the computational time.

A comparison of the flame position from the experiments and LES predictions is shown in Figure 8.57. In the case of the experiments, the flame position is extracted from high speed video images by locating the farthest location of the flame front from the ignition bottom end. From the LES calculations, the flame position is obtained by locating the farthest location of the leading edge of the flame front from the bottom end (defined here as the most down stream location of the flame, where $c = 0.5$ from the ignition point). While results for configuration 15 almost fully overlap, a slightly faster rate of propagation across the chamber is computed in configurations 14 and 16. This is evident only in the last few milliseconds of propagation where the flame experiences the highest levels of turbulence. Figure 8.58(left) presents the flame position, speed against time and speed against axial distance of the chamber. Evidently it can be observed that the flame position and speed with time and flame speed with position in Figure 8.58(right) for configuration 16 are predicted very well.
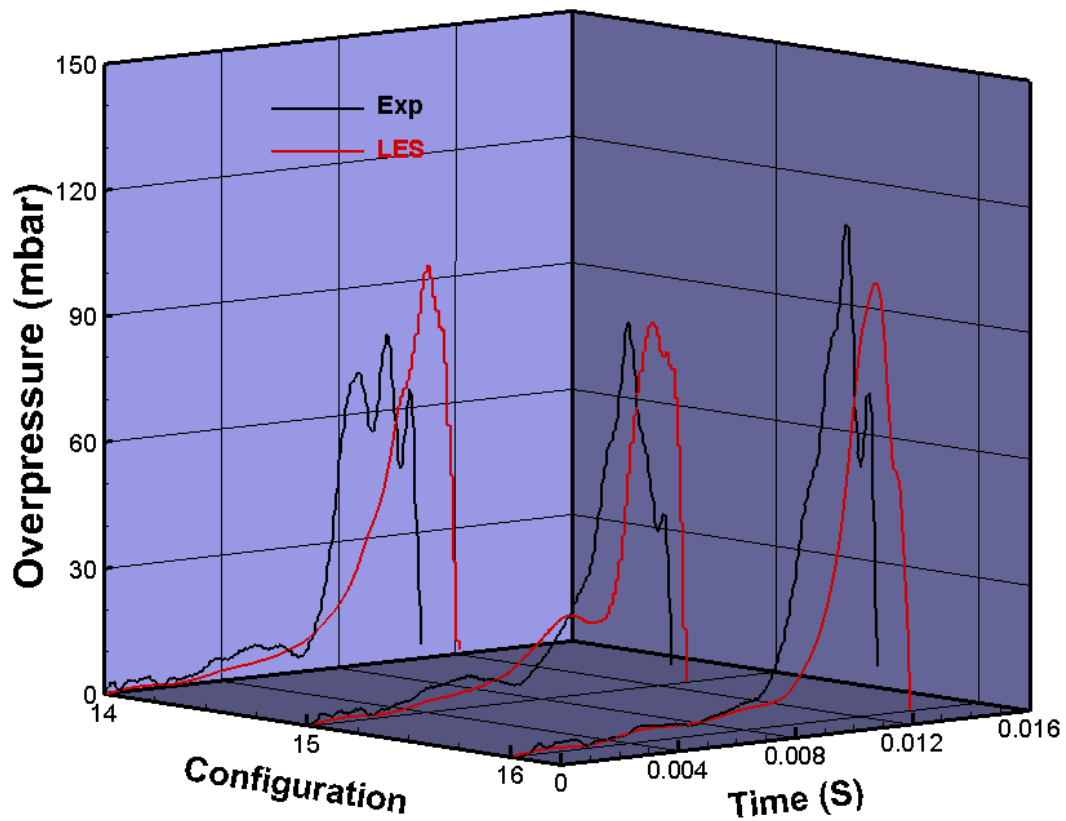

Figure 8.56 Comparison of LES predicted and experiment measured overpressure time traces of Group 4.
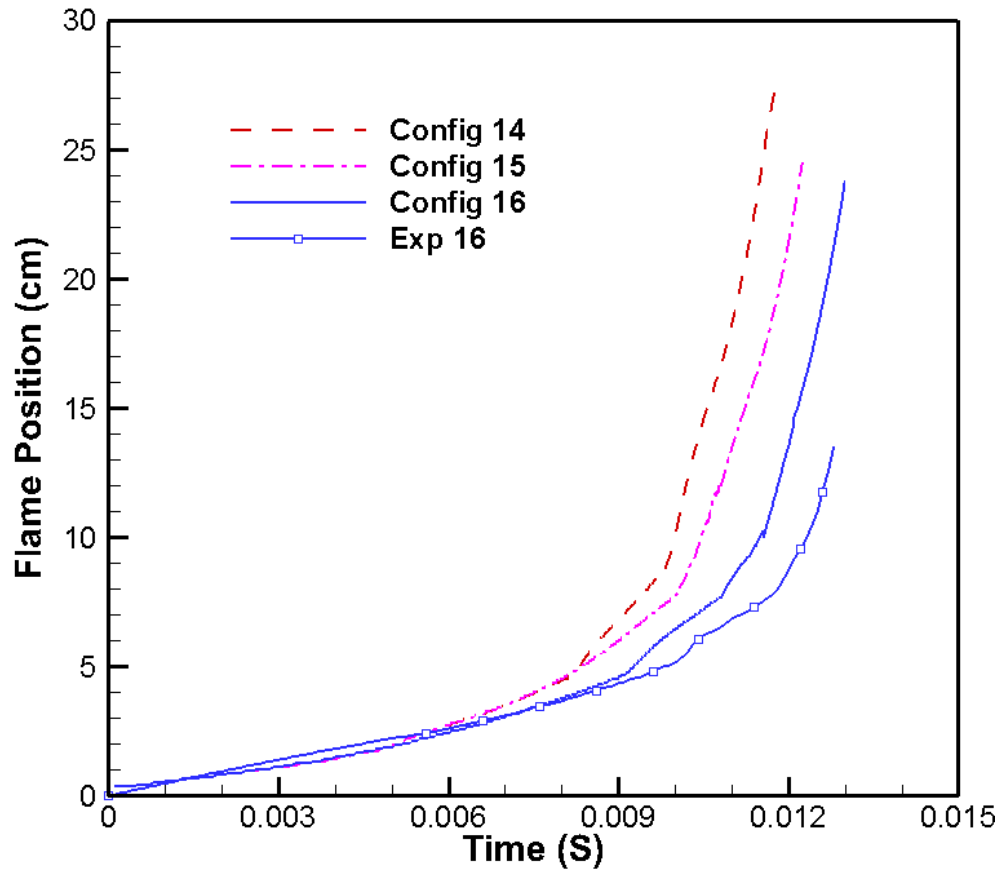
Figure 8.57 Comparison of LES predicted and experiment measured Flame position against time traces of Group 4.
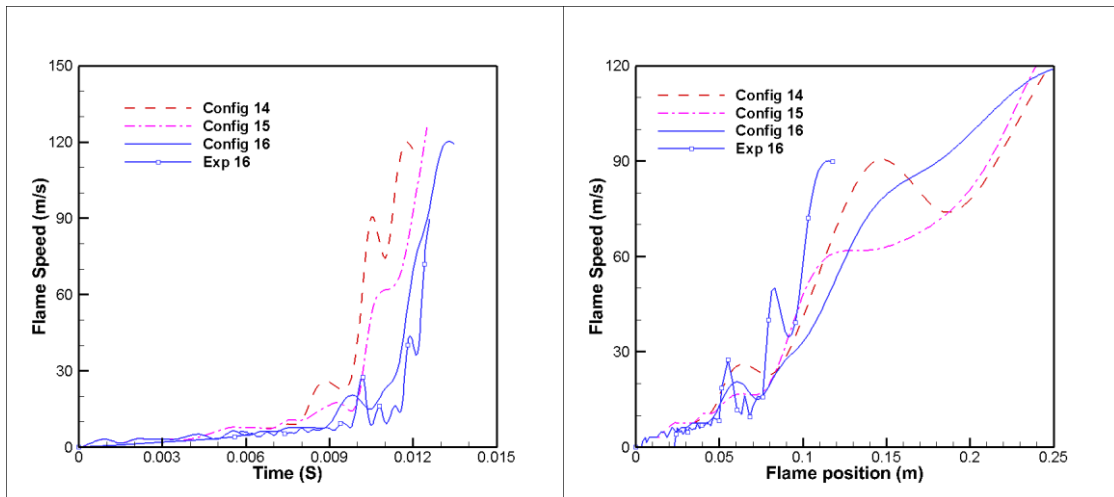

Figure 8.58 Flame characteristics of Group 4 Time traces of flame speed (left) and flame speed with axial location of chamber (right).

Figure 8.59 presents the predicted flame structure and data for the reaction rate, contributions of DFSD at strategic instants i.e. 5, 7, 9, 10, 10.5, 11, 12 and 12.5 ms after ignition. It is very interesting to note that using two baffles plates with a solid square obstacle having the same blockage capacity in all the configurations, the recorded and predicted overpressure is maximum in configuration 16 and minimum in configuration 15 as shown in Figure 8.56. Interestingly, LES predictions show a linear relation for generated overpressure and not by experiments. However, the predicted overpressure is very much in-line with the experiments. Neither experiments nor LES shows a linear relationship for the incidence of time. It is also evident from Figure 8.59 that, the flame exits the chamber faster in configuration 14 than in configuration 16. However, configuration 15 is in between the other two configurations in the case of the maximum overpressure and flame arrival time in the chamber. In case of configuration 16, though the flame has a laminar nature until it reaches the first baffle plates at S2, it quickly turns out to be highly wrinkled and turbulent due to jetting and contortion of the flame through the repeated obstacles. In this configuration the turbulent fluctuations are found to be progressively increasing and reach a maximum of 15.7 m/s at 11.5 ms. The laminar nature of flame front during the initial stages i.e. up to 9 ms caused a longer blow down time from the chamber at later stages. It should be noted that the baffles and square obstacle in configuration 16 are almost all evenly spaced from the bottom of the ignition centre. While in configuration 14, the flame is found to be highly turbulent during the initial stages followed by a faster decay at later stage.

The third configuration has two baffles at S1, near to ignition centre and S3, away from the ignition centre and close to the solid obstacle. It is noticed that once the flame is distorted after reaching the first baffle, the flame front is slightly wrinkled with a higher surface area. However, re-laminarisation (reduction in speed and turbulence levels) of the flame between S1 and S3 results in approaching the square obstacle at a later stage compared to configuration 14. This can also be observed by comparing the flame structure and its position between 10, 10.5 and 11 ms from Figure 8.59(a) and (b). Similarly, from configuration 14 it is noticed that due to the succession of the baffles close to the ignition centre at S1 and S2, the flame front is highly distorted and wrinkled before approaching the square obstacle. However, this configuration has recorded the lowest pressure due to sudden deceleration between S2 and the solid square obstacle shown in Figure 8.56. The flame deceleration after S2 is also confirmed by the experimental measurements. This is also evident in the calculations and hence, confirming that, the turbulence generated by the

baffle plates decay rather quickly, so the relative position and sequencing of obstacles is another important factor in explosions. It can be concluded that with reference to an observer at the exit of chamber, the loss/damage due to the overpressure is relatively low when solid obstacles are close to the ignition origin compared to when obstacles are at longer distance.
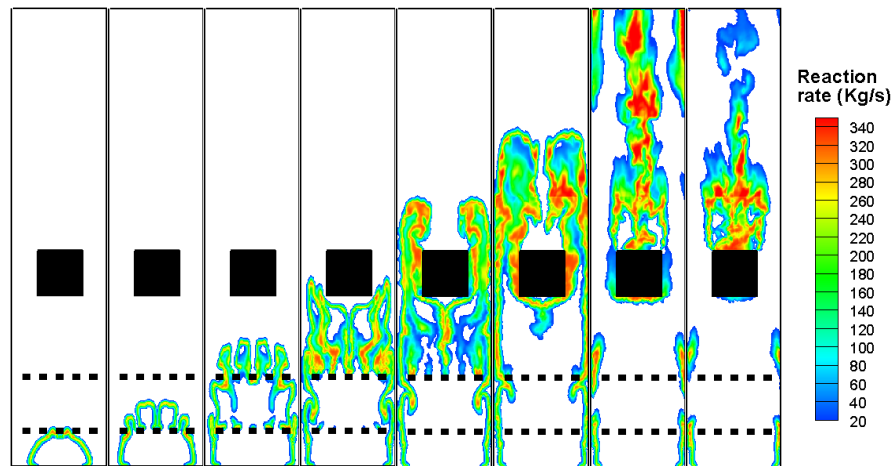
(a)
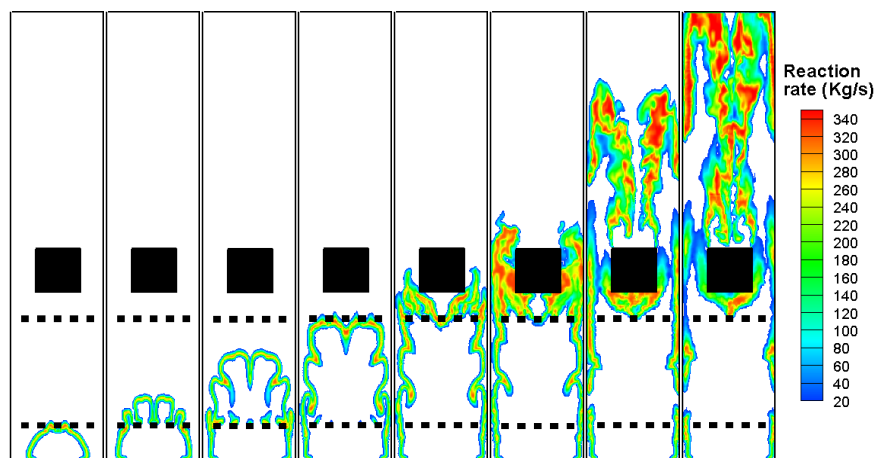
(b)
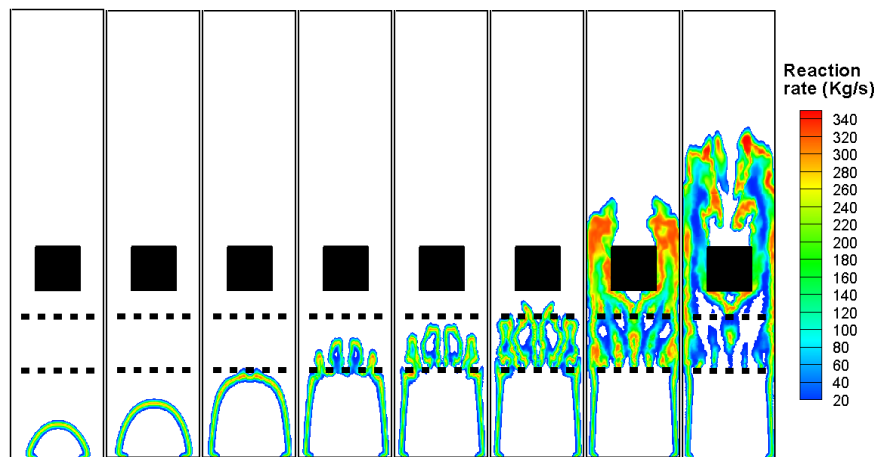
(c)

Figure 8.59 Predicted flame structure from three configurations at 5, 7, 9, 10, 10.5, 11, 12.0 and 12.5ms after ignition. (a) Configuration 14, (b) Configuration 15 and (c) Configuration 16.

Chapter 9   Conclusions and Recommendations for Future Work

Modelling of explosion deflagrating flames with the large eddy simulation technique, and using the Dynamical Flame Surface Density (DFSD) model which is based on the classical laminar flamelet theory is a prominent and well accepted choice in predicting turbulent premixed flames than with RANS modelling. The application of DFSD models in LES is very recent. These models are gradually gaining acceptance in the industry to compute and predict a variety of turbulent premixed combustion situations in complex combustion systems. However, there exists many issues such as their ability to accurately calculate flame surface density and their applicability across a range of combustion regimes, plus the values of the model coefficients used are to be clarified. Encouraged by the recent demand for eco-friendly combustion systems, advancements in the predictive capability of turbulent premixed combustion are considered to be essential, which enhances the fundamental understanding of the entire process and is the main motivation for this research. The studies presented in this thesis have achieved its main objectives:

The studies, carried out here, have increased confidence in using the LES technique for turbulent explosion flames. Propagating flames in a laboratory scale combustion chamber with built-in solid obstacles have been calculated using a newly developed LES-DFSD model. The calculations have been carry out by employing various grid resolutions to achieve a grid independent solution. Numerical investigations have been carried out to identify the influence of filter width and its coefficient on the predicted results. Achieved grid independent results were analysed to establish the quantity of the turbulent kinetic energy resolved using the LES technique. The laboratory scale combustion chamber has been divided into five regions of interest and a detailed analysis was carried out to verify the combustion regimes of the turbulent premixed combustion inside the chamber. The results from the LES-DFSD model are in good agreements with available experimental measurements, with only a few discrepancies, such as an under or over prediction of the magnitude of overpressure and its time of occurrence.

Another objective was to improve the DFSD model to make it more sophisticated, in order to enhance the predicting capabilities and to identify the drawbacks. Investigations identified that the model coefficient generally varied based on various numerical and physical parameters such as filter width, turbulence intensity and the chemistry of the mixture etc. Various parametric studies were carried out using the LES technique with different flow configurations. Also the influence of the ignition sources, the effect of the out flow external boundary and the effect of obstacle structure, have been examined and their effects on the predictions have been quantified. Although the understanding of overpressure prediction is partial, drawbacks were identified especially due to the resolved turbulent flame thickness on the LES grid.

The simulations have been performed for a series of simple to complex flow configurations which had a different number and position of solid baffles in a laboratory combustion chamber. The numerical results were validated against experimental data to establish the LES-DFSD model for turbulent explosion flames. The flow configurations used in this study were classified into four families based on the number and position of the solid baffles, and the influence of baffles with respect to the ignition end was analysed. For these experimental families, generated overpressure, flame characteristics and the reaction rate were generated and compared to available experimental data. The model predictions showed a clear agreement with experimental measurements for various configurations. However, present research has identified a slight under or over prediction of peak overpressure, which can be enhanced by accounting for the effects of flame curvature and strain into the DFSD equation.

9.1 Conclusions

The conclusions for the current work as Computational Modelling are presented in the following points:

➢ The grid independence tests conducted using four different grid resolutions have concluded that the employed grid can resolve most of the energy if it is sufficiently fine and is always independent of the filter width and grid resolution.

➢ The turbulent premixed regime of combustion identified in the present combustion chamber at various times after ignition at the leading edge of the flame is found to lie within the thin reaction zone, irrespective of classified regions and their interactions with obstacles. This finding supports the use of the laminar flamelet modelling concept that has been in use for the modelling of turbulent premixed flames in practical applications.

➢ The applicability of the DFSD model using grid independent results for turbulent explosion flames was examined by validating the generated pressure and other flame characteristics, such as flame structure, position, speed and acceleration against experimental data. This study concludes that the predictions DFSD model provides reasonably good results.

➢ As a first advancement, the model coefficient β has been evaluated using the wrinkling flame factor between the outer and inner cut-off scales, by assuming the wrinkled flame surface is a fractal surface. It was found that LES predictions were slightly improved in predicting a higher reaction rate, which eventually increased predicted overpressure.

➤ The agreement obtained confirms the applicability of the DFSD model to predict the dynamics of turbulent explosion flames in different flow configurations as can be found in engineering applications or chemical/fuel process/storage industries.

The combustion flame flow interactions for the current work are presented as following points:

➤ This investigation demonstrates the comparison of LES-DFSD model predictions with experimental measurements and the effects of placing multiple obstacles at various locations in the path of the deflagrating explosion premixed flames. As expected, it concludes that the increase in blockage ratio increases the overpressure, however, with the same blockage ratio, the position of the solid obstructions with respect to each other and the ignition end has a significant impact on the magnitude of the overpressure and spatial flame structure.

➤ It is identified that the overpressure representing the generated energy in any individual configuration is directly proportional to the number of baffle plates used in this study. The flame speed and the development of the reaction zone are clearly dependent on the number of obstacles used and their blockage ratio.

➤ Extensive flame flow interactions occur as the flame propagates past the baffle plate and the solid obstructions leading to the formation of disconnected flame islands with higher burning rates. However, there is no evidence to prove the presence of flame quenching due to elongation and stretching in the present study. This may be due to the small volume of the chamber used in this study.

➤ Large separation between the solid baffle plates allows sufficient residence time for turbulence decay, causing flow re-laminarisation and hence lowering overpressures with much smoother flame fronts.

➢ A higher pressure gradient develops along the length of the chamber with greater numbers of baffles or obstacles.

➢ It is identified that the trapped unburnt mixtures up and down stream of the obstacles are consumed once the main flame leaves the chamber, leading to subsequent oscillations in pressure.

➢ The location of the obstacles with respect to the ignition source has a direct impact on the overpressure and the structure of the reaction zone. Extending the distance between the baffles or between the baffles and the downstream obstacle allows turbulence to re-laminarise, although with the same blockage capacity, this phenomenon leads to lower overpressure and less distortion in the reaction zone. This new finding highlights the transient nature of the interaction between the propagating flame front and the local condition of the flow field.

9.2 Recommendation for Future Work

➢ Although the LES-DFSD model has improved overall predictions, it could be further improved by identifying or developing more refined models for the inner and outer cut-off scales. Particularly for the inner cut-off scale, although several models are available in literature, retrieving information dynamically from flow properties could be considered from LES filtering. The accurate prediction of overpressure with the LES-DFSD model could possibly be further improved by employing a rigorous model for flame stretch.

➢ The current in-house LES code can be further improved by implementing or adopting detailed chemistry via the look-up table concept. A simple and efficient method such as Intrinsic Low Dimensional Manifold (ILDM), based on laminar flamelet modeling, is suitable by generating a look-up table via pre-processing tools.

➢ It is recommended to study more complex flow configurations representing more real-life industrial applications.

➢ Consider of choosing non-carbonise content of production of the combustion fuels as hydrogen (H_2). This would limit air pollution and protecting the global environment.

➢ Chosen different ignition source locations and various cross section area shapes. These could have significant effect on the result of generated explosion in overpressure..

➢ Parallelisation of the LES code is highly recommended in future, which would eventually utilise the available computational resources efficiently and could easily be extendable to predict more complex combustion scenarios.

References

Abu-Gharbieh, R., Hamarneh, G., Gustavsson, T., & Kaminski, C. (2001). Flame front tracking by laser induced fluorescence spectroscopy and advanced image analysis. *Optics Express , 8* (5), 278-287.

Abu-Orf, G., & Cant, R. (2000). A turbulent reaction rate model for premixed turbulent combustion in spark-ignition engines. *Combustion and Flame , 122* (3), 233-252.

Abdel-Gayed, R. G., Bradley, D., & Lawes, M. (1987). Turbulent burning velocities: A general Correlation in terms of straining rates. *Proceedings of the Royal Society of London. Seriea A, Mathematical and Physical Sciences , 414*, 389-413.

Abdel-Gayed, R. G., Bradley, D., Hamid, M., & Lawes, M. (1985). Lewis number effects on turbulent burning velocity. *Symposium (International) on Combustion , 20* (1), 505-512.

Akkerman, V., Bychkov, V., Petchenko, A., & Eriksson, L. (2006). Flame oscillations in tubes with nonslip at the walls. *Combustion and Flame , 145* (4), 675-687.

Aluri, N., Reddy Muppala, S., & Dinkelacker, F. (2006). Substantiating a fractal-based algebraic reaction closure of premixed turbulent combustion for high pressure and the Lewis number effects. *Combustion and Flame , 145* (4), 663-674.

Aldredge, R., Vaezi, V., & Ronney, P. (1998). Premixed-flame propagation in turbulent Taylor-Couette flow. *Combustion and Flame , 115* (3), 395-405.

Angelberger, D., Veynante, D., Egolfopoulos, F., & Poinsot, T. (1998). *Large eddy simulation of combustion instabilities in turbulent premixed flames.* Stanford University, Center for Turbulence Research. Proceedings of Summer Program.

Butler, T., & O'Rourke, P. (1977). A numerical method for two dimensional unsteady reacting flows. *Proceedings of the Combustion Institute , 16* (1), 1503-1515.

Bauwens, C., Bauwens, L., & Wierzba, I. (2007). Accelerating flames in tubes-an analysis. *Proceedings of the Combustion Institute , 31* (2), 2381-2388.

Bardina, J., Ferziger, J., & Reynolde, W. (1980). Improved subgrid Scales models for large eddy simulations. *13th Fluid an Plasma Dynamics Conference*, (pp. 80-90).

Batty, M. (1985). Fractals-geometry between dimensions. *New Scientist , 105*, 31-35.

Bell, J., & Colella, P. (1989). A second order projection method for the incompressible Navier-stokes equations. *Journal of Computational Physics , 85*, 257-283.

Boughanem, H., & Trouvé, A. (1998). The domain of influence of flame instabilities turbulent premixed combustion. *Proceedings of the Combustion Institute , 27* (1), 971-978.

Boussinesq, J. (1877). Essai sur la thèorie des eaux courantes [Essay on the theory of flowing waters]. *Acadèmie des Sciences , 23* (1), 252-260.

Boger, M., & Veynante, D. (2000). Large eddy simulations of a turbulent premixed V-shaped flame. In *Advances in Turbulence VIII* (pp. 449-452).

Boger, M., Veynante, D., Boughanem, H., & Trouvé, A. (1998). Direct numerical simulation anallsis of flame surface density concept for large eddy simulation of turbulent premixed combustion. *Proceedings of the Combustion Institute , 27* (1), 917-925.

Borghi, R. (1990). Turbulent premixed combustion:Further discussions on the scales of fluctruations. *Combustion and Flame , 80* (3-4), 304-312.

Bray, K. (1990). Studies of the turbulent burning velocity. *Proceedings of the Royal Society: Mathematical and Physical Sciences , A431* (1882), 315-335.

Bray, K., & Cant, R. (1991). Some applications of Kolmogorov's turbulence research in the field of combustion. *Proceedings of the Royal Society: Mathematical and Physical Sciences , 434* (1890), 217-240.

Bray, K., & Moss, J. (1977). A closure model for the Turbulent premixed flame with sequential chemistry. *Combustion and Flame , 30*, 125-131.

Bray, K., & Peters, N. (1993). Laminar Flamelets in turbulent Flames. In P. a. Libby, *Turbulent reaction flows* (pp. 63-113). Academic press.

Bray, K., Champion, M., & Libby, P. A. (1989). Flames in stagnating turbulence. In R. Borghi, & S. Murphy, *Turbulent reacting flows* (pp. 541-563). New York: Springer.

Bray, K., Libby, P., & Moss, J. (1985). Unified modelling approach for premixed turbulent combustion- Part I: General formulation. *Combustion and Flame , 61* (1), 87-102.

Bray, K., Libby, P., Masuya, G., & Moss, J. (1981). Turbulence Production in premixed turbulent flames. *Combustion Science and Technology , 25* (3), 127-140.

Bradley, D. (2002). Problems of predicting turbulent burning rates. *Combustion Theory and Modelling , 6*, 361-382.

Bradley, D., & Lung, F. (1987). Spark ignition and the early stages of turbulent flame propagation. *Combustion and Flame , 69* (1), 71-93.

Bradley, D., Cresswell, T., & Puttock, J. (2001). Flame acceleration due to flame-induced instabilities in large-scale explosions. *Combustion and Flame , 124* (4), 551-559.

Bradley, D., Lau, A., & Lawes, M. (1992). Flame stretch rate as a determinant of turbulent burning velocity. *Philosophical Transactions of the Royal Society: Physical and Engineering Sciences , 338* (1650), 359-387.

Candel, S., & Poinsot, T. (1990). Flame stretch and the balance equation for the flame area. *Combustion Science and Technology , 70*, 1-15.

Cant, R., Pope, S., & Bray, K. (1991). Modelling of flamelet surface-to-volume ratio in trubulent premixed combustion. *Proceedings of the Combustion Institute , 23* (1), 809-815.

Castro, I., & Jones, J. (1987). Studies in numerical computations of recirculating flows . *International Journal for Numerical Methods in Fluids , 7*, 793-823.

Chan, C., & Li, X. (2005). Flame surface densityin turbulent premixed V-flame with buoyancy. *Flow, Turbulence and Combustion , 74*, 273-289.

Charlette, F., Meneveau, C., & Veynante, D. (2002). A power-law flame wrinkling model for LES of premixed turbulent combustion Part II: dynamic formulation. *Combustion and Flame , 131 (1-2)*, 181-197.

Charlette, F., Trouvé, A., Boger, M., & Veynante, D. (1999). A flame surface density model for large eddy simulations of turbulent premixed flames. *The Combustion Institute Joint Meeting of the British, German and French Sections.*

Chen, Y., Peters, N., Schneemann, G., Wruck, N., Renz, U., & Mansour, M. (1996). The detailed flamestructure of highly stretched turbulent premixed methane-airflames. *Combustion and Flame , 107* (3), 223-244.

Cho, P., Law, C., Hertzberg, J., & Cheng, R. (1988). Structure and propagation of turbulent premixed flames stabilized in a stagnation flow. *Porceedings of the Combustion Institute , 21* (1), 1493-1499.

Chow, F., & Moin, P. (2003). a further study of numerical errors in large-eddy simulations. *Jorunal of Computational Physics , 182* (2), 366-380.

Colucci, P., Jaberi, F., Givi, P., & Pope, S. (1998). Filtered density function for large eddy simulation of turbulent reacting flows. *Physics of Fluids , 10* (2), 499-515.

Colin, O., Ducros, F., Veynante, D., & Poinsot, T. (2000). Thickened flame model for large eddy simulations of turbulent premixed combustion. *Physics of Fluids , 12* (7), 1843-1862.

Cook, A., & Riley, J. (1994). A subgrid model for equilibrium chemistry in turbulent flows. *Physics of Fluids , 6* (8), 2868-2870.

Cook, A., & Riley, J. (1998). Subgrid-scale modeling for turbulent reacting flows. *Combustion and Flame , 112* (4), 593-606.

Duclos, J., Veynante, D., & Poinsot, T. (1993). A comparison of flamelet models for premixed turbulent combustion. *Combustion and Flame , 95* (1-2), 101-117.

Dandekar, K. V., & Gouldin, F. C. (1981). *Temperature and velocity measurements in premixed turbulent flames.* AIAA.

Damköhler, G. (1940). *Elektrochem, translation. N.A.C.A. Tech. Memo 1112. , 46*, 610.

Darabiha, N., Candel, S., & Marble, F. (1986). The effect of strain rate on a premixed laminar flame. *Combustion and Flame , 64* (2), 203-217.

Deardorff, J. (1970). Anumerical study of three-dimensional turbulent channel flow at large Renolds numbers. *Journal of Fluid Mechanics , 41* (02), 453-480.

Fureby, C. (2005). A fractal flame-wrinking large eddy simulation model for premixed turbulent combustion. *Proceddings of the Combustion Institute , 30* (1), 593-601.

Fureby, C., & Moller, S. (1995). Large eddy simulation of reacting flows applied to bluff body stabilized flames. *American Institute of Aeronautics and Astronautics , 33* (12), 2339-2347.

Fureby, C., Tabor, G., Weller, H., & Gosman, A. (1997). A comparative study of subgrid scale models in homogeneous isotropic turbulence. *Physics of Fluids , 9* (5), 1416-1429.

Fairweather, M., Ibrahim, S., Jaggers, H., & Walker, D. (1996). Turbulent premixed flame propagation in a cylindrical vessel. *Proceedings of the Combustion Institute , 26* (1-2), 365-371.

Fairweather, M., Hargrave, G., Ibrahim, S., & Walker, D. (1999). Studies of premixed flame propagation in explosion tubes. *Combustion and Flame , 116* (4), 504-518.

Ferziger, J. (1977). Large eddy simulation of turbulent flows. *American Institute of Aeronautics and Astronautics , 15* (9), 1261-1267.

Ferziger, J. (1993). Sub-grid scale modelling. In B. a. Galperin, *Large eddy simulations of complex engineering and geophysical flows* (pp. 55-78). Cambridge: Cambridge University.

Gubba, S., Ibrahim, S., & Malalasekera, W. M. (2011). Measurement and LES calculations of turbulent premixed flame propagation past repeated obstacles. *Combustion and Flame , 158* (12), 2465-2481.

Gubba, S., Ibrahim, S., Malalasekera, W., & Masri, A. (2009). An Assessment of Large Eddy Simulations of Premixed Flames Propagating past Repeated Obstacles. *Combustion Theory and Modelling , 13* (3), 513-540.

Gubba, S., Ibrahim, S., Malalasekera, W., & Masri, A. (2007). LES modelling of propagating turbulent premixed flames using a dynamic flame surface density model. In D. C. Roekaerts (Ed.), *ECCOMAS Thematic Conference on Computational Combustion.* Delft.

Gulati, A., & Driscoll, J. (1985). Velocity-density correlations and Favre averages measured in a premixed turbulent flame. *Combustion Science and Technology , 48* (5), 285-307.

Gülder, Ö. L., & Smallwood, G. (1995). Inner cutoff scale of flame surface wrinkling in turbulent premixed flames. *Combustion and Flames , 103* (1-2), 107-114.

Gao, F., & O'Brien, E. (1993). A large-eddy simulation scheme for trubulent reacting flows. *Physics of Fluids A , 5*, 1282-1284.

Germano, M., Piomelli, U., Moin, P., & Cabot, W. (1991). A dynamic subgrid-scale eddy viscosity model. *Physics of Fluids A: Fluid Dynamics , 3* (7), 1760-1765.

Givi, P. (1989). Model-free simulations of turbulent reactive flows. *Progress in Energy and Combustion Science , 15* (1), 1-107.

Ghosal, S., Lund, T., Moin, P., & Akselovll, K. (1995). A dynamic localization model for large eddy simulation of turbulent flows. *Journal of Fluid Mechanics , 286*, 229-255.

Gouldin, F. (1987). An application of fractals to modeling premixed turbulent flames. *Combustion and Flame , 68* (3), 249-266.

Gouldin, F. (1996). Combustion intensity and burning rate integral of premixedf lames. *Symposium (International) on Combustion , 26* (1), 381-388.

Gouldin, F., Bray, K., & Chen, J. (1989i). Chemical closure model for fractal flamelets. *Combustion and Flame , 77* (3-4), 241-259.

Gouldin, F., Hilton, S., & Lamb, T. (1989ii). Experimental evaluation of the fractal geometry of flamelets. *Proceedings of the Combustion Institute , 22* (1), 541-550.

Ibrahim, S., & Masri, A. (2001). The effects of obstrctions on overpressure resulting from premixed flame deflagration. *Journal of Loss Prevention in the process Industries , 14* (3), 213-221.

Huang, Y., Sung, H., Hsieh, S., & Yang, V. (2003). Large-eddy simulation of combustion dynamics of lean-premixed swirl-stabilized combustor. *Journal of Propulsion and Power , 19* (5), 782-794.

Hawkes, E. ((2000)). *Large eddy simulations of premixed turbulent combustion.* PHD Thesis, University of Cambridge, UK.

Hawkes, E., & Cant, R. (2000). A flame surface density approach to large-eddy simulation of premixed turbulent combustion. *Proceedings of the Combustion Institute , 28* (1), 51-58.

Hawkes, E., & Cant, R. (2001). Implications of a flame surface density approach to large eddy simulation of premixed turbulent combustion. *Combustion and Flame , 126* (3), 1617-1629.

Hall, R. (2006). *Flow field measurement in transient premixed flames.* BEng Thesis, University of Sydney, Australia.

Hall, R. (2008). *Influence of obstacle location and frequency on the propagation of premixed flames.* MEng Thesis, University of Sydney, Australia.

Hall, R., Masri, A., Yaroshchyk, P., & Ibrahim, S. (2009). Effects of position and frequency of obstacles on turbulent premixed propagating flames. *Combustion and Flame , 156*, 439-446.

Hentschel, H., & Procaccia, I. (1984). Relative diffusion in turbulent media: The fractal dimension of clouds. *Physical Review A , 29*, 1461-1470.

Hjertaer, B., Fuhre, K., & Bjorkhaug, M. (1988). Concentration effects on flame acceleration by obstacles in large-acale methane-air and propane-air vented explosions. *Combustion Science and Technology , 62* (4-6), 239-256.

Horiuti, K. (1997). A new dynamic two-parameter mixed model for large-eddy simulation. *Physics of Fluids , 9* (11), 3443-3464.

Kaminski, C., Hult, j., Richter, M., Nygren, J., Franke, A., & Alden, M. (2000). Development of high speed spectroscopic imaging techniques for the time resolved study of spark ignition phenomena. *SAE Technical Paper* , 2000-01-2833.

Kent, J., Masri, A., & Starner, S. (2005). A new chamber to study premixed flame propagation past repeated obstacles. *5th Asia-Pacific Conference on Combustion.* The University of Adelaide, Australia.

Kerstein, A. (1988). Fractal dimension of turbulent premixed flames. *Combustion Science and Technology , 60* (4), 441-445.

Kerstein, A. (1991). Linear-eddy modelling of turbulent transport. Part 6. Microstructure of diffusive scalar mixing fields. *Journal of Fluid Mechanics Digital Archive , 231*, 361-394.

Kerstein, A., Ashurst, W., & Williams, F. (1988). Field equation for interface propagation in an unsteady homogeneous flow field. *Physical Review A , 37* (7), 2728-2731.

Kim, W., & Menon, S. (2000). Numerical modeling of turbulent premixed flames in the thin-reaction-zones regime. *Combustion Science and Technology , 160* (1), 119-150.

Kim, W., Lienau, J., Slooten, P., Colket III, M., Malecki, R., & Syed, S. (2006). Towards modelling lean blow out in gas turbine flame holder applications. *Journal of engineering for gas turbines and power , 128*, 40-48.

Kirkpatrick, M. (2002). *A large eddy simulation code for industrial and environmental flows.* The University of Sydney, Australia.

Kirkpatrick, M., Armfield, S., Masri, A., & Ibrahim, S. (2003). Large eddy simulation of a propagating turbulent premixed flame. *Flow, Turbulence and Combustion , 70* (1-4), 1-19.

Klein, M. (2005). An attempt to assess the quality of large eddy simulations in the context of implicit filtering. *Flow, Turbulence and Combustion , 75* (1), 131-147.

Knikker, R., Veynante, D., & Meneveau, C. (2004). A dynamic flame surface density model for large eddy simulation of turbulent premixed combustion. *Physics of Fluids , 16* (11), L91-L94.

Knikker, R., Veynante, D., & Meneveau, C. (2002). A priori testing of a similarity model for large eddy simulations of turbulent premixed combustion. *Proceedings of the Combustion Institute , 29*, 2105-2111.

Kobayashi, H., Tamura, T., Maruta, K., Niioka, T., & Williams, F. (1996). Burning velocity of turbulent premixed flames in a high–pressure environment. *Symposium (International) on Combustion , 26* (1), 389-396.

Kronenburg, A., & Bilger, R. (2001). Modelling differential diffusion in nonpremixed reacting turbulent flow: application to turbulent jet flames. *Combustion Science and Technology , 166* (1), 175-194.

Lee, T., & Lee, S. (2003). Direct comparison of turbulent burning velocity and flame surface properties in turbulent premixed flames. *Combustion and Flame , 132* (3), 492-502.

Leonard, B. (1979). A stable and accurate convective modelling procedure based on quadratic upstream interpolation. *Computer Methods in Applied Mechanics and Engineering , 19*, 59-98.

Leonard, B. (1987). *SHARP simulation of discontinuities in highly convective steady flow* . NASA technical memorandum, 100240.

Libby, P., & Bray, K. (1981). Conuntergradient diffusion in premixed turbulent flames. *AIAA Journal , 19* (2), 205-213.

Lilly, D. (1992). A proposed modification of the Germano subgrid-scale closure method. *Physics of Fluids A: Fluid Dynamics , 4* (3), 633-635.

Lilly, D. (1967). The representation of small scale turbulence in numerical simulation experiments. *Proceedings of the IBM scientific computing symposium on enviromental sciences* , 195-210.

Lindstedt, R., & Vaos, E. (1999). Modeling of premixed turbulent flames with second moment methods. *Combustion and flame , 116* (4), 461-485.

Lindstedt, R., & Sakthitharan, V. (1998). Time resolved velocity and turbulence measurements in turbulent gaseous explosions. *Combustion and Flame , 114* (3-4), 469-483.

Lovejoy, S. (1982). Area-perimeter relation for rain and cloud areas. *Science , 216* (4542), 185-187.

Naitoh, K., Itoh, T., Takagi, Y., & Kuwahara, K. (1992). Large eddy simulation of premixed-flame in engine based on the multi-level formulation and the renormalization group theory. *SAE , 920590*.

North, G., & Santavicca, D. (1990). The fractal nature of premixed turbulent flames. *Combustion Science and Technology , 72* (4), 215-232.

Nottin, C., Knikker, R., Boger, M., & Veynante, D. (2000). Large eddy simulations of an acoustically excited turbulent premixed flame. *Proceedings of the Combustion Institute , 28* (1), 67-73.

Muppala, S., Aluri, N., Dinkelacker, F., & Leipertz, A. (2005). Development of an algebraic reaction rate closure for the numerical calculation of turbulent premixed methane, ethylene, and propane/air flames for pressures up to 1.0 Mpa. *Combustion and Flame , 140* (4), 257-266.

Murayama, M., & Takeno, T. (1989). Fractal-like character of flamelets in turbulent premixed combustion. *Proceedings of the Combustion Institute , 22* (1), 551-559.

Madina, C., & Givi, P. (1993). Direct and large eddy simulation of reacting homogeneous turbulence. In *Large Eddy Simulation of Complex Engineering and Geophysical Flows* (pp. 315-346). UK: Combridge University Press.

Maly, R. (1994). State-of-the art and future needs in S.I. engine combustion. *Proceedings of the Combustion Institute , 25(1)*, 111-124.

Malalasekera, W., Dinesh, K., Ibrahim, S., & Kirkpatrick, M. (2007). Large eddy simulation of isothermal turbulent swirling jets. *Combustion Science and Technology , 179* (8), 1481-1525.

Mandelbrot, B. (1975). On the geometry of homogeneous turbulence, with stress on the fractal dimension of the iso-surfaces of scalars. *Journal of Fluid Mechanics , 72* (2), 401-416.

Masri, A., & Ibrahim, S. (2007). Recent progress in the understanding of premixed flame propagation past obstacles. *Proceedings of the Third International Conference on Thermal Engineering: Theory and Applications.* Amman, Jordan.

Masri, A., Alharbi, A., Meares, S., & Ibrahim, S. (2012). A comparative study of turbulent premixed flames propagating past repeated obstacles. *Industrial and Engineering Chemistry Research , 51* (22), 7690-7703.

Masri, A., Ibrahim, S., & Cadwallader, B. (2006). Measurements and large eddy simulation of propagating premixed flames. *Experimental Thermal and Fluid Science , 30* (7), 786-702.

Masri, A., Ibrahim, S., Nehzat, N., & Green, A. (2000). Experimental study of premixed flame propagation over various solid obstructions. *Experimental Thermal and Fluid Science , 21* (1-3), 109-116.

Marble, F., & Broadwell, J. (1977). *The coherent flame model of non-premixed turbulent combustion.* TRW-9-PU.

Meneveau, C., & Poinsot, T. (1991). Stretching and quenching of flamelets in premixed turbulent combustion. *Combustion and Flame , 86* (4), 311-332.

Menon, S., & Jou, W. (1991). Large-eddy simulations of combustion instabilities in a axisymmetric ramjet combustor. *Combustion Science and Technology , 84*, 51-79.

Metghalchi, M., & keck, J. (1982). Burning velocities of mixtures of air with methanol, isooctane and indolene at high pressure and temperature. *Combustion and Flame , 48*, 191-210.

Metghalchi, M., & Keck, J. (1980). Laminar burning velocity of propane-air mixtures at high temperature and pressure. *Combustion and Flame , 38*, 143-154.

Mizobuchi, Y., Tachibana, S., Shinio, J., Ogawa, S., & Takeno, T. (2002). A numerical analysis of the structure of a turbulent hydrogen jet lifted flame. *29* (2), 2009-2015.

Moen, I., Donato, M., Knystautas, R., & Lee, J. (1980). Flame acceleration due to turbulence produced by obstacles. *Combustion and Flame , 39* (1), 21-32.

Moen, I., Lee, J., Hjertager, B., Fugre, K., & Eckhoff. (1982). Pressure development due to turbulent flame propagation in large-acale methane-air. *Combustion and Flame , 47*, 31-52.

Moin, P., Squires, K., Cabot, W., & Lee, S. (1991). A dynamic subgrid-scale model for compressible turbulence and scalar transport. *Physics of Fluids A: Fluid Dynamics , 3* (11), 2747-2757.

Moller, S., Lundgren, E., & Fureby, C. (1996). Large eddy simulation of unsteady combustion. *Proceedings of the Combustion Institute , 26* (1), 241-248.

Patel, S., & Ibrahim, S. (1999). Burning velocities of propagating turbulent premixed flames. *Proceedings of the 1st international symposium on Turbulence and Shear Phenomena* , 837.

Patel, S., Ibrahim, S., Yehia, M., & Hargrave, G. (2003). Investigation of premixed turbulent combustion in a semi-confined explosion chamber. *Experimental Thermal and Fluid Science , 27* (4), 335-361.

Patel, S., Jarvis, S., Ibrahim, S., & Hargrave, G. (2002). An experimental and numerical investigation of premixed flame deflagration in a semiconfined explosion chamber. *Proceedins of the Combustion Institute , 29* (2), 1849-1854.

Peters, N. (1988). Laminar flamelet concepts in turbulent combustion. *Proceedings of the Combustion Institute , 21* (1), 1231-1250.

Peters, N. (2000). The turbulent buring velocity for large-scale and small-scale turbulence. *Jorunal of Fluid Mechanics , 284* (1), 107-132.

Piana, J., Veynante, D., Candel, S., & Poinsot, T. (1997). Direct numerical simulation analysis of the G-equation in premixed combustion. In J. V. Chollet, *Direct and Large Eddy Simulation II* (pp. 321-330). Amsterdam: Kluwer Academic Publishers.

Piomelli, U., Zang, T., Speziale, C., & Hussaini, M. (1990). On the large-eddy simulation of transitional wall-bounded flows. *Physics of Fluids A: Fluid Dynamics , 2* (2), 257-265.

Piomelli, U., & Liu, J. (1995). Large-eddy simulation of rotating channel flows using a localized dynamic model. *Physics of Fluids , 7* (4), 839-848.

Piomelli, U., Yu, Y., & Adrian, R. (1996). Subgrid-scale energy transfer and near-wall turbulence structure. *Physics of Fluids , 8* (1), 215-224.

Piomelli, U., Moin, P., & Ferziger, J. (1988). Model consistency in large eddy simulation of turbulent channel flows. *Physics of Fluids , 31* (7), 1884-1891.

Pitsch, H. (2005). A consistent level set formulation for large-eddy simulation of premixed turbulent combustion. *Combustion and Flame , 143* (4), 587-598.

Pitsch, H. (2006). Large-eddy simulation of turbulent combustion. *Annual Review of Fluid Mechanics , 38*, 453-482.

Pitsch, H., & Duchamp de Lageneste, L. (2002). Large-eddy simulation of premixed turblent combustion using a level-set approach. *Proceedings of the Combustion Institute , 29* (2), 2001-2008.

Phylaktou, H., & Andrews, G. (1991). The acceleration of flame propagation in a tube by an obstacle. *Combustion and Flame , 85* (3-4), 363-379.

Poinsot, T., & Veynante, D. (2005). *Theoretical and numerical combustion* (2nd Edition ed.). PHILADELPHIAPA, PA, USA: Edwards.

Poinsot, T., Veynante, D., & Candel, S. (1991). Quenching processes and premixed turbulent combustion diagrams. *Journal of Fluid Mechanics , 228*, 561-606.

Poinsot, T., Candel, S., & Trouvé, A. (1995). Applications of direct numerical simulation to premixed turbulent combustion. *Progress in Energy and Combustion Science , 21* (6), 531-576.

Popat, N., Catlin, C., Arntzen, B., Lindstedt, R., Hjertager, B., Solberg, T., et al. (1996). Investigations to improve and assess the accuracy of computational fluid dynamic based explosion models. *Journal of Hazardous Materials , 45* (1), 1-25.

Pope, S. (1985). PDF methods for turbulent reactive flows. *Progress in Energy and Combustion Science , 11* (2), 119-192.

Pope, S. (2004). Ten questions concerning the large-eddy simulation of turbulent flows. *New Journal of Physics , 35* (6), 1-24.

Pope, S. (1988). The evolution of surfaces in turbulence. *International Journal of Engineering Science , 26* (5), 445-469.

Prasad, R., & Gre, J. (1999). An evaluation of flame surface density models for turbulent premixed jet flames. *Combustion and Flame , 116* (1-2), 1-14.

Sagaut, P. (2006). *Large Eddy simulation for Incompressible Flows* (3rd ed.). Springer.

Salvetti, M., & Banerjee, S. (1995). A priori tests of a new dynamic subgrid-scale model for finite-difference large-eddy simulations. *Physics of Fluids , 7* (11), 2831-2847.

Schumann, U. (1989). Large-eddy Simulation of turbulent diffusion with chemical reactions in the convective bounary layer. *Atmospheric Environment , 23* (8), 1713-1727.

Schumam, U. (1975). Sub-grid scale model for finite difference simulations of turbulent flows in plane channels and annuli. *Journal of Computational Physics , 18*, 376-404.

Smagorinsky, J. (1963). General circulation experiments with the primitive equations. *Monthly Weather Review , 91* (3), 99-164.

Spalding, D. (1971). Mixing and chemical reaction in steady confined turbulent flames. *Proceedings of the Combustion Institute , 13* (1), 649-657.

Sreenivasan, K., & Meneveau, C. (1986). The fractal facets of turbulence. *Journal of Fluid Mechanics , 173* (1), 357-386.

Starke, R., & Roth, P. (1989). An experimental investigation of flame behavior during explosions in cylindrical enclosures with obstacles. *Combustion and Flame , 75* (2), 111-121.

Ravikanti, S. (2008). *Advanced flamelet modelling of turbulent nonpremixed and partially premixed combustion.* PhD Thesis, Loughborough University, UK.

Ranga-Dinesh, K. (2007). *Large eddy simulation of turbulent swirling flames.* PhD Thesis, Loughborough University, UK.

Reveillon, J., & Vervisch, L. (1997). Dynamic sub-grid PDF modelling for non-premixed turbulent combustion. In *Direct and Large Eddy Simulation II* (pp. 311-320). Amsterdam: Kluwer Academic Publishers.

Richard, S., Colin, O., Vermorel, O., Benkenida, A., Angelberger, C., & Veynante, D. (2007). Towards large eddy simulation of combustion in spark ignition engines. *Proceedings of the Combustion Institute , 31*, 3059-3066.

Rogallo, R., & Moin, P. (1984). Numerical simulation of turbulent flows. *Annual view of Fluid Mechanica , 16* (1), 99-137.

Tabor, G., & Weller, H. G. (2004). Large eddy simulation of premixed turbulent combustion using flame surface wrikling modle. *Flow, Turbulence and Combustion , 72* (1), 1-28.

Thibaut, D., & Candel, S. (1998). Numerical study of unsteady turbulent premixed combustion: application to flashback simulation. *Combustion and Flame , 113* (1-2), 53-65.

Trouvé, A., & Poinsot, T. (1994). The evolution equation for the flame surface density in turbulent premixed combustion. *Journal of Fluid Mechanics , 278* (1), 1-31.

Vankan, J. (1986). A second order accurate pressure correction scheme for viscous incompressible flow . *SIAM Journal of Scientific and Statistical Computing , 7*, 870-891.

Veynante, D., & Vervisch, L. (2002). Turbulent combustion modeling. *Progress in Energy and Combustion Science , 28* (3), 193-266.

Veynante, D., & Poinsot, T. (1997). *Large eddy simulations of the combustion instabilities in turbulent premixed burners.* Centre for Turbulence Research Annual Research Briefs, Stanford University. pp.253-275.

Veynante, D., Piana, J., Duclos, J., & Martel, C. (1996). Experimental analysis of flame surface density models for premixed turbulent combustion. *Proceedings of the combustion Institute , 26* (1), 413-420.

Vreman, B., Geurts, B., & Kuerten, H. (1996). Comparison of numerical schemes in Large-Eddy Simulations of the temporal mixing layer. *International Journal for Numerical Methods in Fluids , 22* (4), 297-311.

Weller, H., Tabor, G., Gosman, A., & Fureby, C. (1998). Application of a flame-wrinkling LES combustion model to a turbulent mixing layer. *Proceedings of the Combustion Insititute , 1*, 899-907.

Werner, H., & Wengle, H. (1991). Large-eddy simulation of turbulent flow over and around a cube in a plate channel. *8th Symposium on Turbulent Shear Flows* (pp. 155-168). New York: Springer.

Williams, F. (1985i). *Combustion theory: the fundamental theory of chemically reacting flow systems.* Menlo Park, California, USA: Benjamin/Cummings Publications.

Williams, F. (1985ii). Turbulent Combustion. In J. Edited by Buckmaster, *The Mathematics of Combustion* (pp. 97-131). Phiadelphia: SIAM.

Yakhot, V. (1988). Propagation Velocity of Premixed turbulent flames. *Combustion Science and Technology , 60* (1), 191-214.

Zang, Y., Street, R., & Koseff, J. (1993). A dynamic mixed subgrid-scale model and its application to turbulent recirculating flows. *Physics of Fluids A: Fluid dynamics , 5* (12), 3186-3196.